amU
Aix Marseille Université

NNT : 2024AIXM0001

THÈSE DE DOCTORAT

Soutenue à Aix Marseille Université
le 16 juin 2025 par

Godefroy Vannoye

Development of real-time systems for neutrino detection with KM3NeT in the context of multi-messenger astronomy

Discipline
Physique et Sciences de la Matière

Spécialité
Physique des Particules et Astroparticules

École doctorale
ED352 : Physique et Sciences de la Matière

Laboratoire/Partenaires de recherche
Centre de Physique des Particules de Marseille
Université de Gênes

Composition du jury

Anna Franckowiak Professeure, Université de la Ruhr à Bochum	Rapporteure
Sergio Navas Professeur, Université de Grenade	Rapporteur
Alexis Coleiro Maître de conférences, Université Paris Cité	Examinateur
Alec Habig Professeur, Université du Minnesota à Duluth	Examinateur
Cristinel Diaconu Directeur de recherche, CNRS/Aix-Marseille Université	Président du jury
Damien Dornic Directeur de recherche, CNRS/Aix-Marseille Université	Directeur de thèse
Vladimir Kulikovskiy Chercheur, INFN Genova	Co-directeur de thèse

CENTRE DE PHYSIQUE DES PARTICULES DE MARSEILLE
CPPM

Università di Genova

Affidavit

I, Godefroy Vannoye, hereby declare that the work presented in this manuscript is my own work, carried out under the scientific supervision of Damien Dornic and Vladimir Kulikovskiy, in accordance with the principles of honesty, integrity and responsibility inherent to the research mission. The research work and the writing of this manuscript have been carried out in compliance with both the French national charter for Research Integrity and the Aix-Marseille University charter on the fight against plagiarism.

This work has not been previously submitted neither in France nor abroad in an identical or similar version to any other examination body.

Genoa, April 21st, 2025



This work is licensed under Creative Commons Attribution-NonCommercial-ShareAlike 4.0 International Public License.

This manuscript is LLM-free and written with organic human pain.

Liste de publications et participation aux conférences

Liste des publications réalisées dans le cadre du projet de thèse :

1. S. Aiello *et al.* [KM3NeT], "Search for Neutrino Emission from GRB 221009A using the KM3NeT ARCA and ORCA detectors," JCAP **08** (2024), 006 doi:10.1088/1475-7516/2024/08/006 [arXiv:2404.05354 [astro-ph.HE]].

2. S. Aiello *et al.* [KM3NeT], "Searches for neutrino counterparts of gravitational waves from the LIGO/Virgo third observing run with KM3NeT," JCAP **04** (2024), 026 doi:10.1088/1475-7516/2024/04/026 [arXiv:2311.03804 [astro-ph.HE]].

3. D. Dornic, G. Vannoye *et al.* [KM3NeT], "Implementation of the KM3NeT Online Core-Collapse Supernova neutrino search," PoS **ICRC2023** (2023), 1223 doi:10.22323/1.444.1223

4. S. Aiello *et al.* [KM3NeT], "Implementation and first results of the KM3NeT real-time core-collapse supernova neutrino search," Eur. Phys. J. C **82** (2022) no.4, 317 doi:10.1140/epjc/s10052-022-10137-y [arXiv:2109.05890 [astro-ph.HE]].

Participation aux conférences et écoles d'été au cours de la période de thèse :

1. "Monitoring the sky for the next Galactic Core-Collapse Supernova," LIA-ERIDANUS Virtual Workshop 2021, Novembre 2021, Communication orale, Conférence, https://www.youtube.com/watch?v=b__OAsGAE9s.

2. "Monitoring the neutrino sky for the next Galactic Core-Collapse Supernova with KM3NeT," Neutrino 2022, Juin 2022, Poster, Conférence, https://zenodo.org/records/6785410.

3. “First search for neutrino counterparts from gravitational wave sources with KM3NeT/ORCA,” Neutrino 2022, June 2022, Poster, Conférence, https://zenodo.org/records/6805229.

4. “Neutrino alert system of KM3NeT,” Second KM3NeT Town Hall Meeting, Septembre 2022, Communication Orale, Conférence, https://indico.cern.ch/event/1132669/.

5. “Monitoring the neutrino sky for the next Galactic Core-Collapse Supernova with KM3NeT,” Neutrinos in the Multi-Messenger Era, Novembre 2022, Poster, Conférence, https://agenda.irmp.ucl.ac.be/event/4681/.

6. “The Online Multi-Messenger Program of KM3NeT,” Neutrinos in the Multi-Messenger Era, Novembre 2022, Poster, Conférence, https://agenda.irmp.ucl.ac.be/event/4681/.

7. Transient Universe Summer School, Juin 2023, École d’été, https://indico.in2p3.fr/event/27295/.

8. “Implementation of the KM3NeT Online Core-Collapse Supernova neutrino search,” ICRC 2023, Juillet 2023, Poster, Conférence, https://pos.sissa.it/444/1223/.

Abstract

The last ten years saw the development of multi-messenger astronomy. Multi-messenger astronomy is the coordinated observation of signals of different nature but from the same source. Each messenger gives a different point of view on the mechanisms at play within a source. Neutrinos play a special role: they are neutral and interact weakly, and as such propagate in a straight line and are not absorbed. Their detection enables to probe the inside of celestial objects.

KM3NeT is a multipurpose cubic-kilometer neutrino observatory under construction in two different sites of the Mediterranean Sea. It consists of two detectors, ARCA and ORCA and is currently taking data with the first set of detection lines in operation. Although having different primary goals, both detectors can be used for neutrino astronomy over a wide energy range, from a few tens of MeV to PeV energies.

The KM3NeT Online Multi-Messenger Program, at present in the prototype phase, aims to detect neutrinos in real-time to communicate alerts and perform follow-up searches. This manuscript presents two parts of the program: the core-collapse supernova (CCSN) detection pipeline and the neutrino alert pipeline.

The observation of the neutrino burst coming from the next Galactic CCSN and its gravitational wave and electromagnetic counterparts will provide invaluable information on this phenomenon. By searching for an excess of coincidences above the optical background, KM3NeT is able to detect low energy neutrinos coming from CCSN. The sensitivity to Galactic and near-Galactic events is expected when data from the two infrastructures is combined. With its integration in the SNEWS global alert network and the ongoing work to compute, transmit and combine the neutrino light-curves of different detectors, KM3NeT will play a key part in notifying other telescopes in time. This manuscript presents the real-time detection capabilities of KM3NeT, the additional information that can be brought by light-curve computations and the follow-up of external alerts.

Alerts play a key role in the discovery and observation of celestial transients. In the neutrino astronomy field, they are one of the best strategies to identify likely astrophysical neutrinos and characterize their potential source by

performing follow-up observations in all the electromagnetic spectrum. This manuscript presents the current capabilities of the detectors to reconstruct and classify astrophysical neutrinos in real-time and the two planned parallel selections: one based on pure neutrino properties and the other relying on the multi-wavelength characteristics of the celestial objects inside the provenance region of neutrinos.

Résumé

Les 10 dernières années ont vu émerger le domaine de l'astronomie multimessager. L'astronomie multimessager consiste à coordonner l'observation de signaux de différentes natures venant d'une même source. Il existe quatre signaux messagers : les rayons cosmiques, les photons, les neutrinos et les ondes gravitationnelles. Chaque messager apporte un point de vue différent aux mécanismes ayant lieu dans les objets célestes.

KM3NeT est un télescope à neutrino sous-marin basé sur la détection de photons Cherenkov. Deux détecteurs, ARCA et ORCA, sont actuellement en construction sur deux fonds marins de la Méditerranée. Les détecteurs prennent déjà des données avec des configurations partielles. Bien qu'ils aient des objectifs différents, les deux détecteurs peuvent être utilisé pour de l'astronomie neutrino à travers une grande gamme d'énergie, de quelques dizaines de MeV au PeV.

Le programme d'analyse multimessager en temps réel de KM3NeT, à ce jour au stade de prototype, aspirent à détecter des neutrinos en temps réel pour transmettre des alertes et effectuer des recherches de contreparties. Ce manuscrit présente deux parties du programme : le pipeline de détection de supernova à effondrement de cœur (abrégé en CCSN de la traduction en anglais) et le pipeline d'alertes neutrinos.

L'observation de neutrinos venant de la prochaine supernova galactique et les ondes gravitationnelles et rayonnements électromagnétiques associés permettra d'obtenir de précieuses données sur ce phénomène. En recherchant un excès de coïncidences au dessus du bruit de fond optique, KM3NeT est capable de détecter des neutrinos basse énergie venant de CCSN. La combinaison des deux détecteurs assure une sensibilité à des évènements galactiques et quasi galactiques. Grâce à son intégration au sein du réseau d'alerte SNEWS and le travail en cours pour calculer, transmettre et combien les données temporelles de neutrinos, KM3NeT jouera un rôle clef dans la notification des autres télescopes. Ce manuscrit présente les capacités de détection en temps réel de KM3NeT, les informations additionnelles que peuvent apporter les données temporelles et le suivi des alertes externes.

Les alertes jouent un rôle clef dans la découverte et l'observation des phénomènes transitoires célestes. Dans le domaine de l'astronomie neutrino, les

alertes sont l'une des meilleures stratégies pour identifier des neutrinos probablement astrophysiques et caractériser leur potentiel source grâce à des observations de suivi dans tout le spectre électromagnétique. The manuscrit présente les capacités actuelles de KM3NeT pour reconstruire et classifier les neutrinos astrophysiques en temps réel et les deux sélections prévues : l'une basée seulement sur les propriétés du neutrino et l'autre sur les caractéristiques multi longueurs d'onde des objets célestes dans la région d'origine du neutrino.

Résumé étendu

Astronomie multimessager

Les 10 dernières années ont vu émerger le domaine de l'astronomie multimessager. L'astronomie multimessager consiste à coordonner l'observation de signaux de différentes natures venant d'une même source. Il existe quatre signaux messagers : les rayons cosmiques, les photons, les neutrinos et les ondes gravitationnelles. Chaque messager apporte un point de vue différent aux mécanismes ayant lieu dans les objets célestes.

Deux observations récentes ont marqué un tournant dans l'astronomie multimessager. Le 17 août 2017, la collaboration LIGO/Virgo observe un signal d'onde gravitationnelle (GW170817) provenant de deux étoiles à neutrons. Quelques secondes plus tard, les télescopes gamma Fermi et INTEGRAL partagent la détection d'un sursaut gamma, lançant la course à l'observation dans toutes les longueurs d'onde de l'objet détecté. Les différentes observations apportées permirent d'identifier l'évènement comme une kilonova. La localisation apportée par LIGO/Virgo et Fermi ainsi que les observations optiques sont visibles dans la figure 1, partie gauche. Le second évènement marquant est un neutrino détecté le 22 juillet 2017 par la collaboration IceCube en coïncidence avec le blazar TXS 0506+056 en état de forte émission gamma. À nouveau, une campagne mondiale d'observations est lancée pour caractériser le blazar en question. Les observations gamma de Fermi et la direction d'origine du neutrino sont montrées figure 1, partie droite.

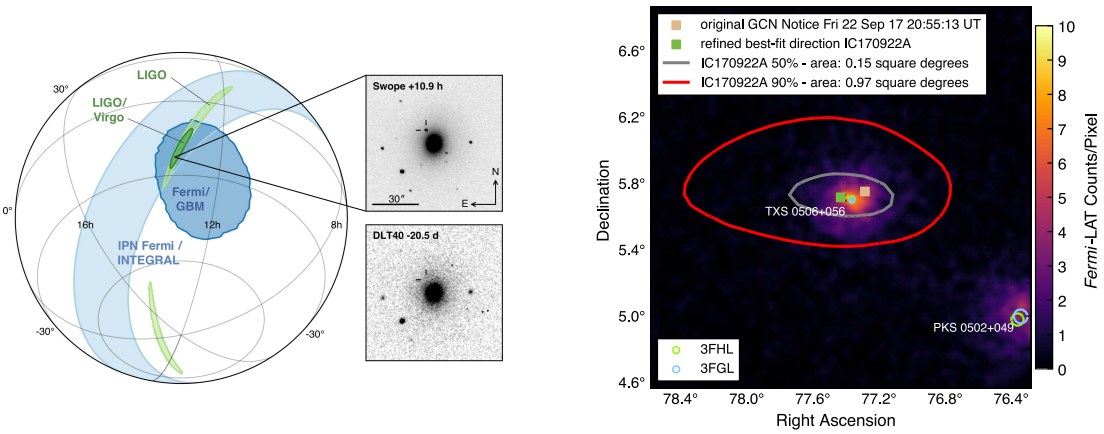

Figure 1. : Localisation apportée par LIGO/Virgo et Fermi et observations optiques pour GW170817 (à gauche). Observation gamma de Fermi et cône d'incertitude de la direction du neutrino en provenance de TXS 0506+05 (à droite).

Les neutrinos jouent un rôle particulier dans l'observation d'objets célestes.

Les neutrinos sont abondants dans l'univers et sont présents dans de nombreux phénomènes cosmiques, tels que les réactions nucléaires ou les désintégrations de particules énergétiques. Ils n'interagissent que faiblement et peuvent se propager en ligne droite – contrairement aux rayons cosmiques déviés par les champs magnétiques – et sans être absorbés – contrairement aux rayons gamma. Les neutrinos permettent donc de sonder les mécanismes internes des objets célestes.

Le flux de neutrinos sur Terre s'étend sur plusieurs ordres de grandeur, comme le montre figure 2, partie gauche. Les neutrinos cosmiques observés à ce jour sont ceux en provenance du Soleil, en provenance de supernovæ à effondrement de cœur et ceux compris entre 10 TeV et 10 PeV, mesurés par la collaboration IceCube. Le flux de neutrinos cosmiques à haute énergie est visible figure 2, partie droite.

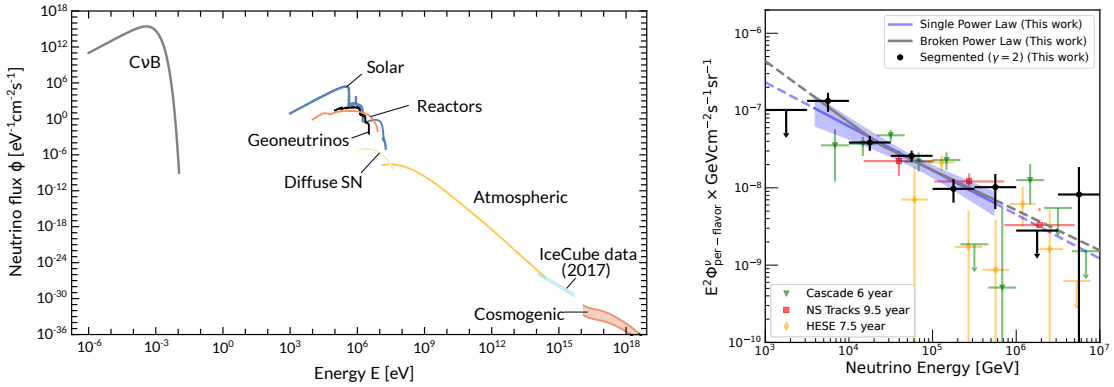

Figure 2. : Flux de neutrinos sur Terre en fonction de l'énergie (à gauche). Flux astrophysique de neutrinos en fonction de l'énergie (à droite).

Le détecteur à neutrinos KM3NeT

KM3NeT est un télescope à neutrino sous-marin basé sur la détection de photons Cherenkov. Deux détecteurs sont actuellement en construction sur deux fonds marins de la Méditerranée. ARCA, au large de la Sicile (Italie) à 3500 m de profondeur, est optimisé pour la détection de neutrinos aux énergies supérieures au TeV. ORCA, au large de Toulon (France) à 2500 m de profondeur, est lui optimisé pour les neutrinos d'une dizaine de GeV.

Le design des détecteurs KM3NeT est modulaire. Le module optique (*Digital Optical Module* en anglais, ou DOM) est une sphère résistante à la pression qui contient 31 photomultiplicateurs et de l'électronique embarquée. Les DOMs sont reliés verticalement par 18 pour former des unités de détections (*Detection Units* ou DUs). Une DU est attachée au fond marin et sa verticalité est assurée par une bouée. Plusieurs DUs réparties sur le fond marin forment un quadrillage 3D de photodétecteurs. Lorsqu'un neutrino interagit avec le milieu du détecteur, des

particules secondaires induisent un rayonnement bleu nommé Cherenkov. C'est à partir de ce rayonnement que l'énergie et la direction du neutrino peuvent être reconstruits. L'espacement entre les DOMs et les DUs diffèrent pour ARCA et ORCA, afin de correspondre à la gamme d'énergie visée.

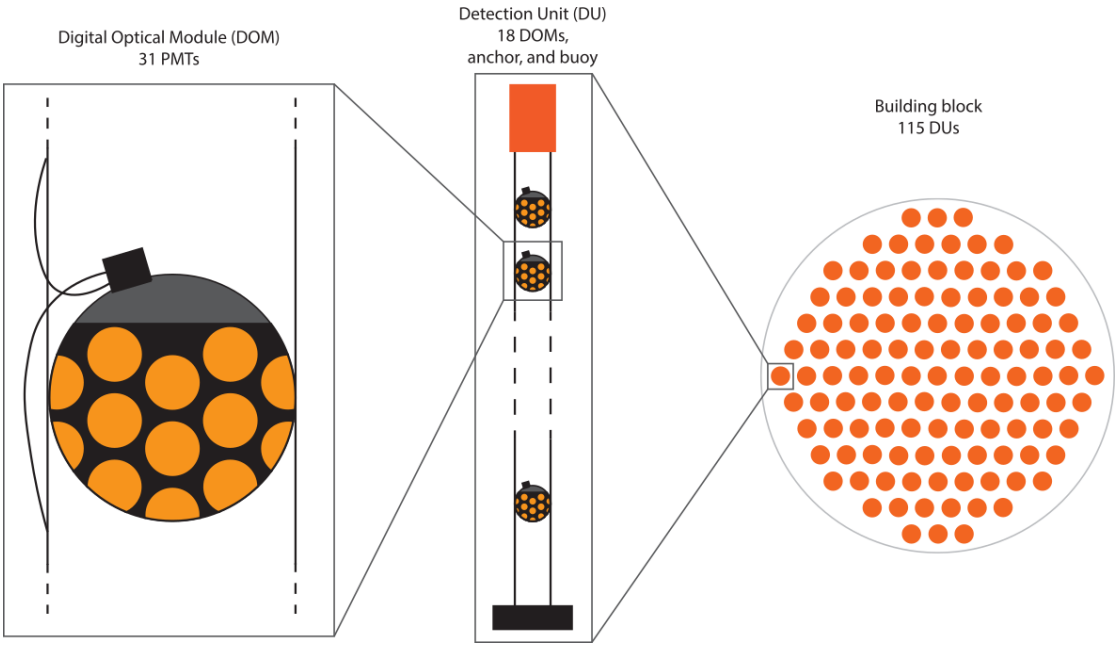

Figure 3. : Schémas décrivant le détecteur KM3NeT à différentes échelles : DOM à gauche, DU au milieu et détecteur vu du dessus à droite.

Détection en temps réel de neutrinos de supernova à effondrement de cœur

Supernova à effondrement de cœur Une supernova à effondrement de cœur (*core-collapse supernova* ou CCSN) est un phénomène explosif qui met fin à la vie de certaines étoiles (au-dessus de 10 masses solaires). Lors d'une CCSN, une quantité massive (3×10^{53} erg) d'énergie est libérée, majoritairement sous la forme de neutrinos d'une dizaine de MeV. Les neutrinos parviennent à s'échapper avant les photons, qui restent piégés par l'opacité du milieu quelques minutes à quelques heures. Le profil temporel théorique des neutrinos (en rose et rouge), ondes gravitationnelles (en bleu) et de la lumière visible (en noir) est illustré figure 4. Arrivant sur Terre préalablement aux photons, les neutrinos qui arrivent sur Terre peuvent donc servir de système d'alerte. Grâce à la mise en place d'une détection en temps réel, voire d'une localisation en temps réel de la CCSN, il est possible d'organiser une observation complète des émissions électromagnétiques. Cela est

d'autant plus important que la génération actuelle de détecteurs de neutrinos n'est sensible qu'à une CCSN galactique ou dans les voisinages. Or le taux estimé de CCSN galactiques est d'environ 1.5 par siècle. La rareté de cet événement rend d'autant plus importante l'automatisation du système d'alerte.

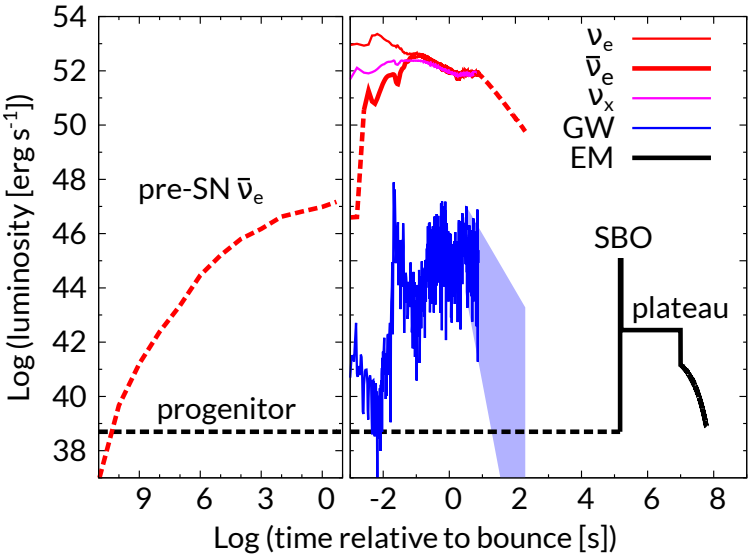

Figure 4. : Évolution temporelle théorique des différents messagers émis par une supernova à effondrement de cœur.

Détection de neutrinos de supernovæ avec KM3NeT KM3NeT détecte les neutrinos de supernovæ principalement par la désintégration bêta inverse d'anti-neutrinos électroniques sur les protons de l'eau ($\bar{\nu}_e + p \rightarrow e^+ + n$). Les positions individuelles des positrons ne peuvent pas être reconstruites à cause de la géométrie des détecteurs, optimisée pour le GeV et au-delà. La stratégie mise en place est la recherche d'un excès de coïncidences entre photomultiplicateurs au-dessus du bruit de fond optique des détecteurs. Les principales sources de bruit de fond sont les désintégrations radioactives du ^{40}K, la bioluminescence et les muons atmosphériques. Un veto est appliqué sur tous les photomultiplicateurs pour supprimer le bruit lié à la bioluminescence. Pour diminuer les autres sources de bruit optique, des coïncidences sont recherchées entre les photomultiplicateurs. La multiplicité est définie comme le nombre de photomultiplicateurs inclus dans une coïncidence. Une illustration du signal et des sources de bruit de fond et une distribution en multiplicité du bruit de fond sont montrées figure 5.

La distribution en multiplicité d'un signal de supernova et la sensibilité des deux détecteurs ARCA et ORCA est visible figure 6. En optimisant les propriétés des coïncidences et la gamme de multiplicité, KM3NeT est capable de détecter

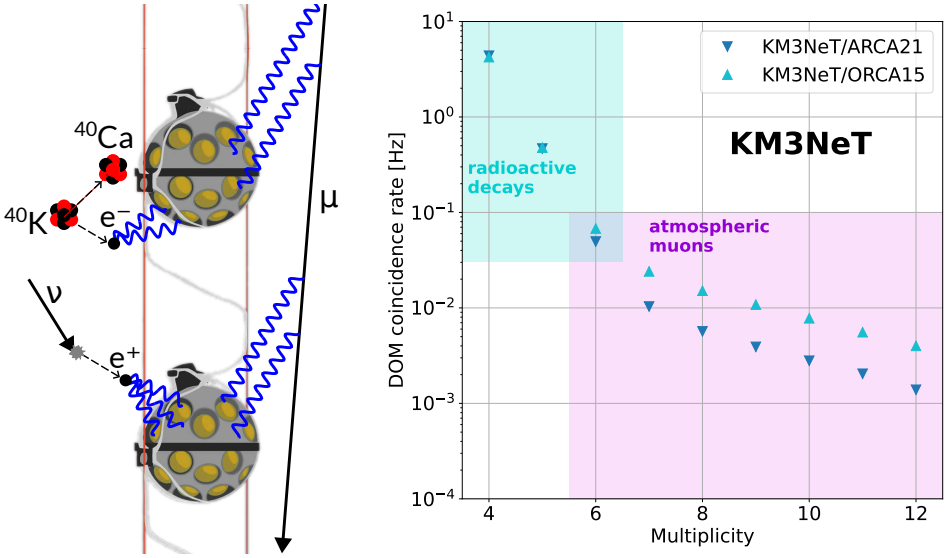

Figure 5. : Illustration du signal de neutrinos de supernova et du bruit de fond optique (à gauche). Distribution de la multiplicité des coïncidences dues au bruit de fond optique pour ARCA21 et ORCA15 (à droite).

une CCSN dans 95 % de la Voie Lactée, et est sensible jusqu'au Grand Nuage de Magellan.

Pipeline CCSN en temps réel de KM3NeT Le pipeline CCSN en temps réel fait partie de la plateforme d'analyse multimessager en temps réel de KM3NeT. Un diagramme du pipeline est donné figure 7. Le pipeline est composé de plusieurs modules, qui sont organisés en plusieurs sections. En bleu, le pipeline de recherche en temps-réel de CCSN calcule en temps réel un taux de fausse alarme à partir des données des deux détecteurs. Si le taux à un instant t est inférieur à un seuil donné, une alerte est transmise. En rouge, le pipeline quasi-temps réel est déclenché soit intérieurement par un taux de fausse alarme suffisamment bas, soit extérieurement par une observation pertinente d'un autre détecteur (par exemple d'onde gravitationnelle). Le cas échéant, l'intégralité des coïncidences détectées est récupérée afin d'augmenter la statistique et de produire une courbe temporelle de neutrinos à haute résolution temporelle. En jaune, le pipeline déclenché calcule une pertinence statistique à partir d'évènements passés en réponse à une observation d'un autre détecteur. Lors de ma thèse, j'ai été chargé de développer et maintenir le pipeline CCSN de KM3NeT.

Estimation adaptative du bruit de fond Pour ne pas surcharger les systèmes d'acquisition de données lors des périodes de bioluminescence, un veto est appliqué sur les photomultiplicateurs au-dessus du kHz. Cela provoque une variabilité du

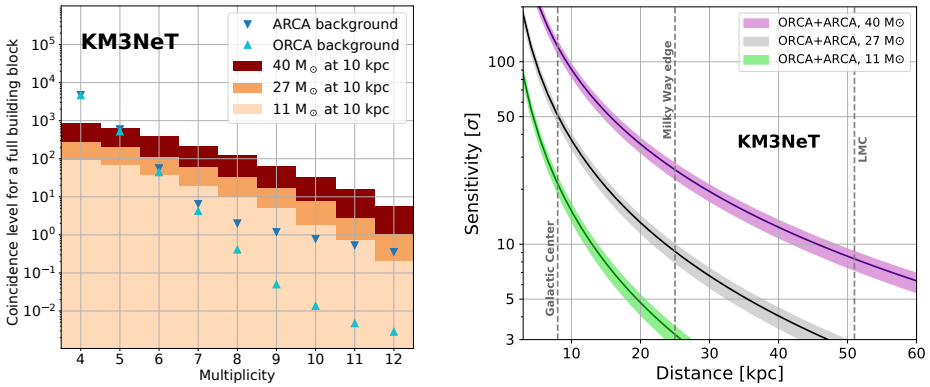

FIGURE 6. : Nombre attendu d'évènements en fonction de la multiplicité (à gauche). Sensibilité en fonction de la distance de la supernova (à droite).

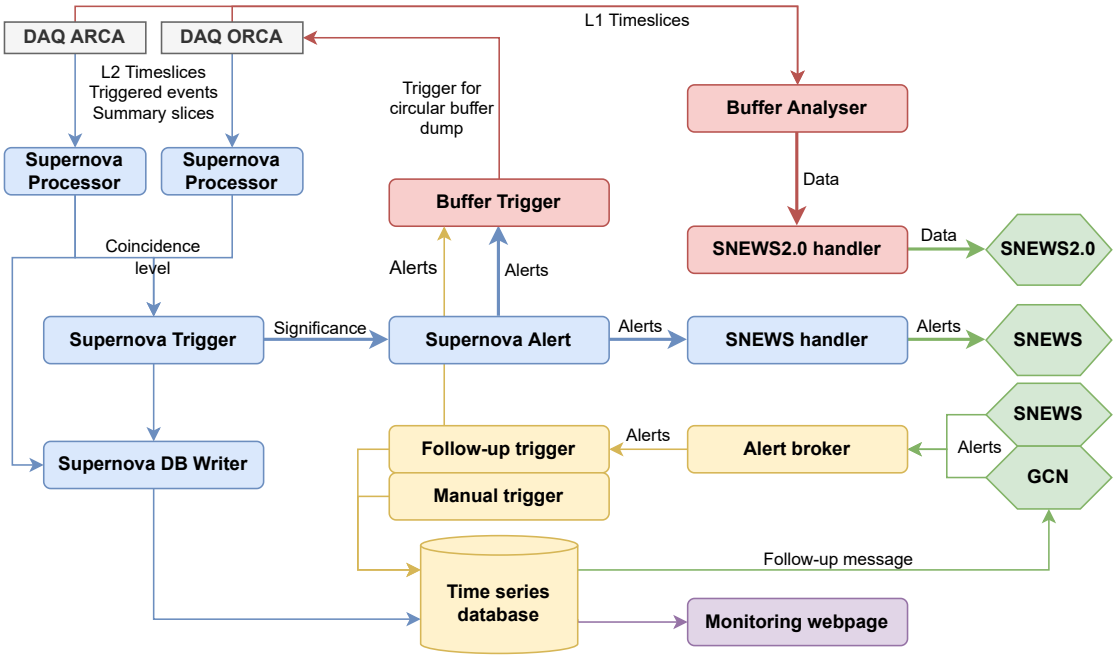

FIGURE 7. : Diagramme du flux de données du pipeline CCSN.

nombre de photomultiplicateurs, ce qui entraîne une variabilité du taux de bruit de fond optique. Ce phénomène est particulièrement présent avec le détecteur ORCA, en raison de sa location où la bioluminescence est fréquente.

Pour caractériser la réponse du détecteur, 20 mois de données de ORCA (de décembre 2021 à juillet 2023) ont été analysées. Un diagramme de dispersion du nombre de coïncidences en fonction du nombre de photomultiplicateurs, les deux normalisés par le nombre de DOM actifs, est montré dans le graphique de gauche de figure 8. Une analyse de la distribution du taux de fausse alarme montre que le détecteur est proprement caractérisé par une parabole dont les paramètres sont évalués tous les mois. Un exemple de parabole est visible dans le graphique de droite de figure 8.

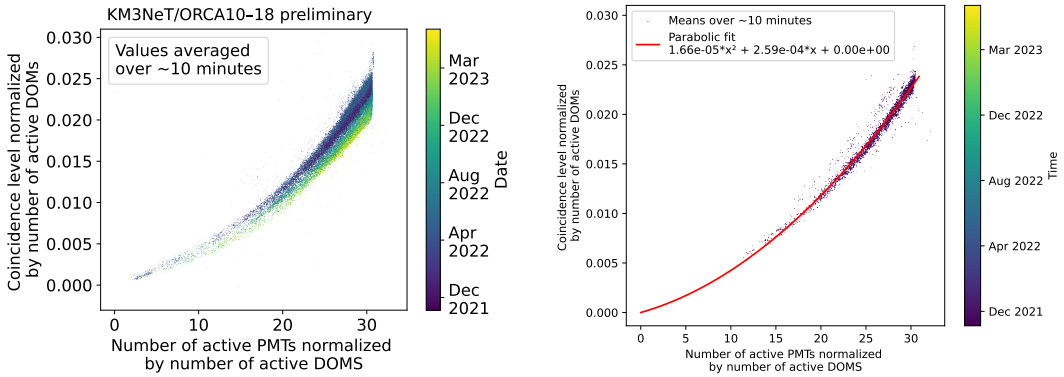

Figure 8. : Diagramme de dispersion du nombre de coïncidences en fonction du nombre de photomultiplicateurs, les deux normalisés par le nombre de DOM actifs, pour la période de décembre 2021 à juillet 2023 (à gauche). Exemple de parabole associée à 1 mois de coïncidences (à droite).

Recherche de contreparties neutrinos MeV En parallèle du développement du pipeline CCSN temps réel, des contreparties neutrinos ont été recherchées a posteriori pour deux familles d'évènements.

La première recherche a été faite pour les ondes gravitationnelles observées lors de la troisième session d'observation des détecteurs LIGO/Virgo (O3), qui a eu lieu en 2019 et 2020. Durant O3, le détecteur ORCA a eu trois configurations différentes : ORCA2, ORCA4 et ORCA6. ARCA ne prenait pas de données pendant cette période. La recherche est faite pour ORCA4 et ORCA6, afin d'avoir un volume de détection suffisant.

L'analyse consiste à rechercher, dans une fenêtre de 2 s après la détection de l'onde gravitationnelle, un excès de coïncidence au-dessus du bruit de fond attendu. Le délai de 2 s est choisi pour prendre en compte une éventuelle différence de temps de propagation entre les neutrinos et l'onde gravitationnelle. Pour les deux

géométries de ORCA, le bruit de fond est estimé à partir de données tirées au hasard. Pour chaque onde gravitationnelle, la coïncidence maximale de la fenêtre de 2 s est sélectionnée, et comparée à une distribution de Poisson au bruit de fond attendu. La valeur-p et les limites supérieures de détection associées sont calculées. Deux limites en particulier sont reportées dans les deux graphiques de figure 9 : l'énergie totale émise en neutrino si l'évènement associé est une CCSN $E^{iso,90\%}_{tot,\nu}$ et la fluence en neutrinos Φ.

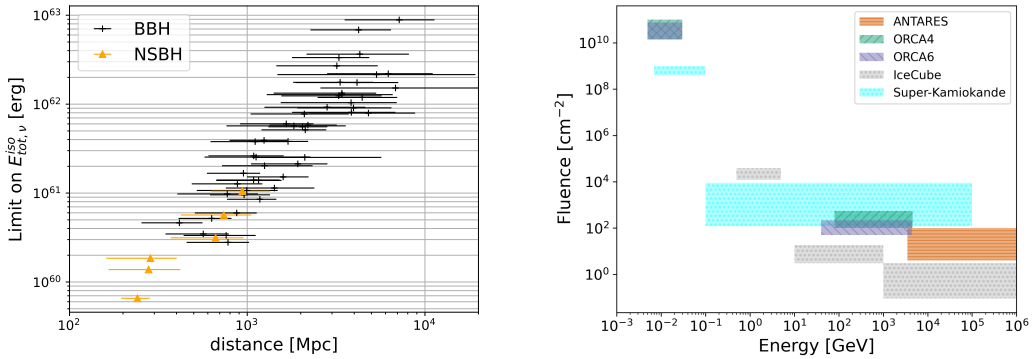

Figure 9. : Limites hautes sur l'énergie émise en neutrinos en fonction de la luminosité de distance de la source (à gauche). Limites hautes sur la fluence totale en neutrinos pour ORCA4, ORCA6, ANTARES, IceCube et SuperKamiokande. Les résultats des analyses à haute énergie sont aussi présents (à droite).

Une deuxième analyse est effectuée suite à la détection de GRB 221009A, le sursaut gamma le plus lumineux jamais observé. L'analyse est identique à celle réalisée pour O3. Seules les fenêtres de recherches changent : T_{90}, qui correspond à la fenêtre de temps dans laquelle se trouve 90 % de l'émission gamma, et $[-50\,s, 5000\,s]$, qui englobe des photons très haute énergie détectés par le détecteur LHAASO. Les distributions en temps du nombre de coïncidences pour les deux fenêtres de temps sont rapportées figure 10. Aucun excès comparé au bruit de fond attendu n'a été trouvé.

Alertes neutrinos avec KM3NeT

L'envoi d'alertes neutrinos est une stratégie efficace pour la découverte et la caractérisation de sources. C'est notamment à partir d'une alerte du détecteur IceCube que le blazar TXS 0506+056 fut identifié et observé. Mais le nombre d'alertes dans la communauté multimessager va exploser dans les années à venir, dû à la fois aux détecteurs qui augmentent en sensibilité et aux nouveaux détecteurs. C'est pour cela que l'intérêt scientifique de chaque alerte doit être maximisé.

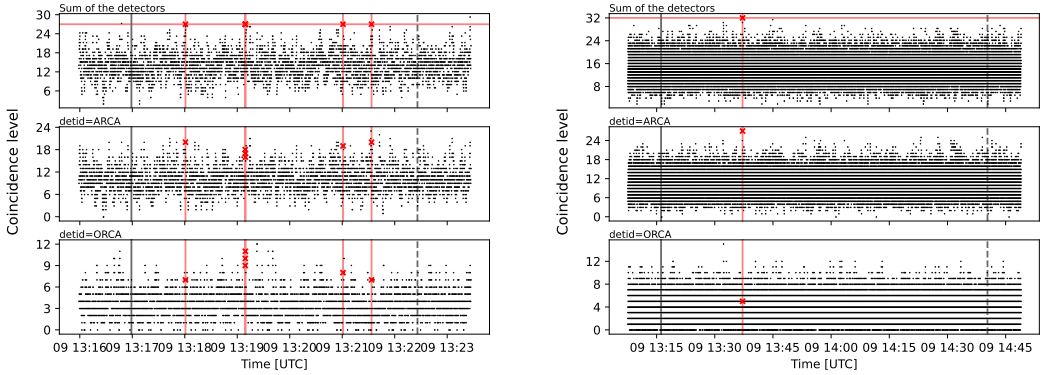

FIGURE 10. : Distributions temporelles du nombre de coïncidences dans la fenêtre T_{90} (à gauche) et $[-50\,\text{s}, 5000\,\text{s}]$ (à droite). Les maximums sont indiqués par des croix rouges.

KM3NeT présente plusieurs qualités pour l'envoi d'alertes. La large gamme d'énergie permet de sonder plusieurs populations de sources. La localisation dans l'hémisphère nord apporte une complémentarité à IceCube. Enfin, l'excellente résolution angulaire dû au milieu aqueux permet de facilité le suivi par des télescopes optiques et d'autres parties du spectre EM.

Le diagramme présentant la plateforme d'analyse multimessager en temps réel de KM3NeT est présenté figure 11. Les évènements sont reconstruits et classifiés en temps réel sur les rivages de chacun des détecteurs. En moins de 10 s, les propriétés des neutrinos, tous types d'interaction confondus, sont obtenues et communiquées à une plateforme commune aux deux détecteurs. Néanmoins, la majorité des évènements reconstruits est due aux muons atmosphériques, qui doivent être filtrés préalablement à l'envoi alertes.

De manière générale, les sélections faites sur les évènements pour l'envoi d'alertes sont faites uniquement sur les propriétés des neutrinos. Une nouvelle méthode est proposée : diminuer les conditions sur les propriétés des évènements, et prendre en compte les propriétés des potentielles sources dans la sélection. Une sélection seulement sur les propriétés neutrinos est tout de même mise en place pour ne pas biaiser envers certaines sources.

Une sélection est appliquée sur les évènements pour réduire leur flux de 15 Hz à 1 par jour. Passé cette sélection, la recherche de données astronomiques suivante est effectuée. Une recherche d'objets dans le cône d'incertitude du neutrino est faite dans les catalogues 4FGL (gamma), RFC et NVSS (radio) et Swift et eROSITA (rayon X). Pour chaque objet, la variabilité est récupérée à partir de données publiques si possible. Deux exemples de courbes de lumière, l'une en gamma à partir du télescope Fermi (à gauche) et l'autre en visible à partir du télescope ZTF

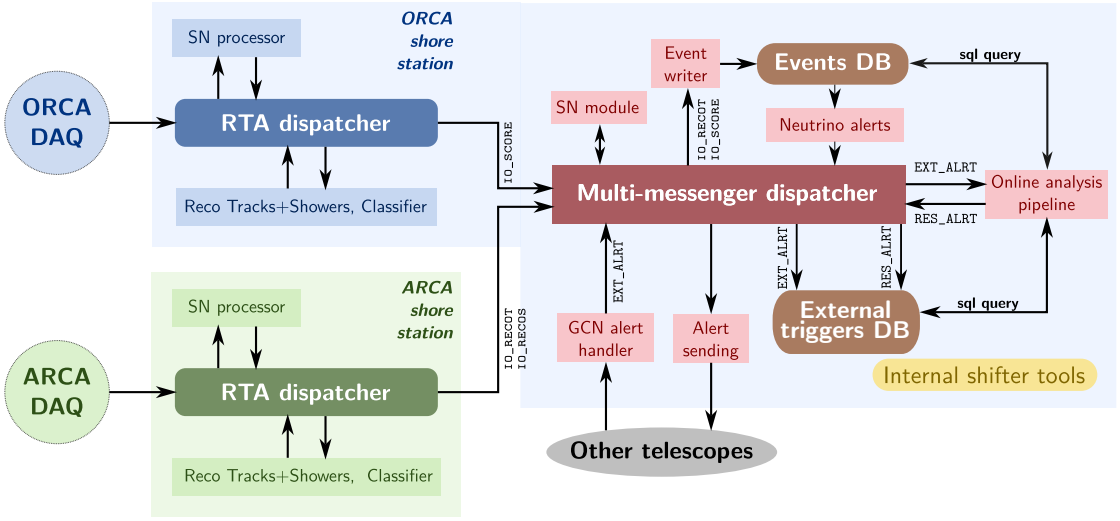

FIGURE 11. : Diagramme décrivant le flux de données de la plateforme d'analyse multimessager en temps réel de KM3NeT.

(à droite), sont montrées figure 12. La sélection est ensuite faite pour sélectionner les objets les plus lumineux en radio et X.

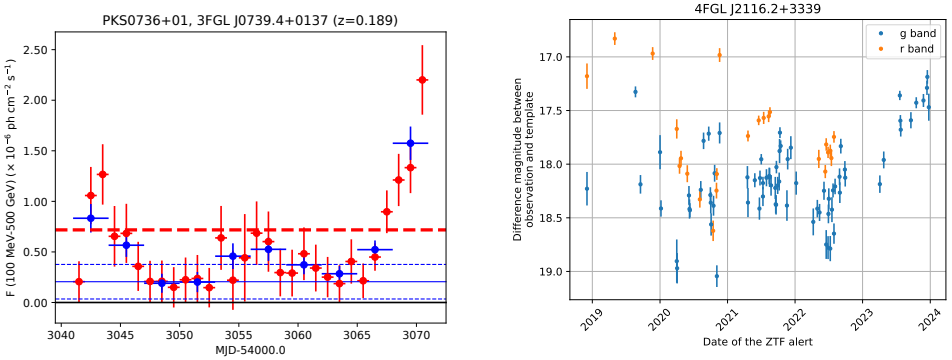

FIGURE 12. : Courbes de lumière pour 3FGL J0739.4+0137 dans le domaine gamma (à gauche) et pour 4FGL J2116.2+3339 dans le domaine optique (à droite).

À ce jour (début 2025), le système d'alerte neutrinos de KM3NeT est en phase de prototype. Cependant, le module de sélection pour les évènements de type trace à haute énergie et le module de recherche dans des catalogues sont tous les deux prêts.

Contents

Affidavit 2

Liste de publications et participation aux conférences 3

Abstract 5

Résumé 7

Résumé étendu 9

Contents 18

1. Multi-messenger context for neutrino detection with KM3NeT 21
1A. Multi-messenger astronomy 22
1A.1. Cosmic rays 22
1A.2. Photons 26
1A.3. Neutrinos 29
1A.4. Gravitational waves 32
1A.5. Connection between the different messengers 34
1A.6. Historical multi-messenger observations 37
1B. KM3NeT: a neutrino telescope in the Mediterranean Sea 42
1B.1. Principle of water Cherenkov detectors 42
1B.2. Experimental setup of KM3NeT 49

2. Real-time detection of neutrinos from a core-collapse supernova 61
2A. Origin and detection of CCSN neutrinos 63
2A.1. Supernova neutrinos 63
2A.2. Detection of MeV neutrinos with KM3NeT 76
2B. The KM3NeT CCSN online pipeline 85
2B.1. Real-time CCSN search pipeline 87
2B.2. Adaptive background expectation 92
2B.3. Quasi-online pipeline 101
2B.4. Transmitting data to the SNEWS network 103
2B.5. Triggered follow-up searches 105

2C. Searches for MeV neutrino burst counterparts 111
2C.1. GW from LIGO/Virgo O3 111
2C.2. GRB 221009A: the Brightest γ-ray burst Of All Times 121

3. Neutrino alerts within the KM3NeT Online Program **127**
3A. Real-time strategies for multi-messenger transient observations . . 129
3A.1. Observation facilities 129
3A.2. Communication methods 134
3A.3. Prospects for the near future of astronomy alerts 136
3B. The KM3NeT Online Multi-Messenger Program 136
3B.1. Online GeV-PeV event processing 137
3B.2. Automatic follow-up pipeline 141
3C. KM3NeT neutrino alerts 147
3C.1. Context within the multi-messenger landscape 147
3C.2. Strategy for the KM3NeT neutrino alerts 150
3C.3. Pure neutrino alert selection 154
3C.4. Multi-wavelength correlation 160

Bibliography **171**

Remerciements **188**

Chapter 1.

Multi-messenger context for neutrino detection with KM3NeT

Contents

1A. Multi-messenger astronomy 22
1A.1. Cosmic rays 22
1A.1.1. Composition and energy spectrum 22
1A.1.2. Origin of cosmic rays 24
1A.1.3. Acceleration mechanisms 24
1A.2. Photons 26
1A.2.1. Multi-wavelength astronomy 26
1A.2.2. *Double bump* spectral energy distribution 28
1A.3. Neutrinos 29
1A.3.1. Neutrino flux 31
1A.3.2. Diffuse flux of cosmic neutrinos 32
1A.3.3. Known sources of cosmic neutrinos 32
1A.4. Gravitational waves 32
1A.5. Connection between the different messengers 34
1A.5.1. Leptonic and hadronic models 34
1A.5.2. Gamma-rays absorption 36
1A.6. Historical multi-messenger observations 37
1A.6.1. SN 1987A 37
1A.6.2. GW170817 39
1A.6.3. TXS 0506+056 39

1B. KM3NeT: a neutrino telescope in the Mediterranean Sea 42
1B.1. Principle of water Cherenkov detectors 42
1B.1.1. Neutrinos interaction 42
1B.1.2. Cherenkov radiation and light propagation 44

1B.1.3. Event signatures 46
1B.2. Experimental setup of KM3NeT 49
1B.2.1. The multi-PMT Digital Optical Module 50
1B.2.2. Detectors layouts 51
1B.2.3. Background to the neutrino detection 54
1B.2.4. Description of the data acquisition software 55
1B.2.5. Event reconstruction 58
1B.2.6. Past and current status of the KM3NeT detectors 59

1A. Multi-messenger astronomy

> Be clearly aware of the stars and infinity on high. Then life seems almost enchanted after all.
>
> *Vincent Van Gogh*

Multi-messenger astronomy is the coordinated observation of signals of different nature but from the same source. The use of wavelength outside the visible range led in the 20th century to huge new possibilities of observation. Observations in the 21st century go further with the combination of cosmic rays, photons, neutrinos and gravitational waves. Each messenger gives a different point of view on the mechanisms at play within a source.

1A.1. Cosmic rays

At the beginning of the 20th century, the scientific community believed that the natural ionization of the air was caused by radioactive elements from the ground. Victor Hess made a series of ionization measurements with hot air balloons. He discovered the ionization rate to increase with the altitude, thus disproving the hypothesis. Many measurements led to the conclusion that the ionization was due to charged particles coming from space: cosmic rays (CRs).

1A.1.1. Composition and energy spectrum

Cosmic rays are very high-energy ionized nuclei. Protons are the main component of the cosmic ray flux (around 90 %). The remaining are helium nuclei ($\approx 9\,\%$) and heavier nuclei ($\approx 1\,\%$). When interacting with the atmosphere, CRs produce secondary particles. The secondary particles can either propagate,

decay, or interact with the atmosphere. The result is a cascade of particles called an Extensive Air Shower (EAS).

EAS are particularly useful to probe the spectrum of high-energy cosmic rays. Below few 100 TeV, the flux is high enough for direct measurements in space or with high-altitude balloons. Above 1 PeV, the flux goes lower than a few tens of particles per square meter per year. However, EAS can be detected by ground based observatories to indirectly measure the cosmic ray flux.

Cosmic rays span over 10 orders of magnitude in energy, from around 1 GeV to approximately 100 EeV. The differential cosmic ray flux (rate of particles per unit area per unit energy) is presented Figure 1.1. The flux is multiplied by $E^{2.6}$ to compensate for the fast drop in energy and better visualize the different components.

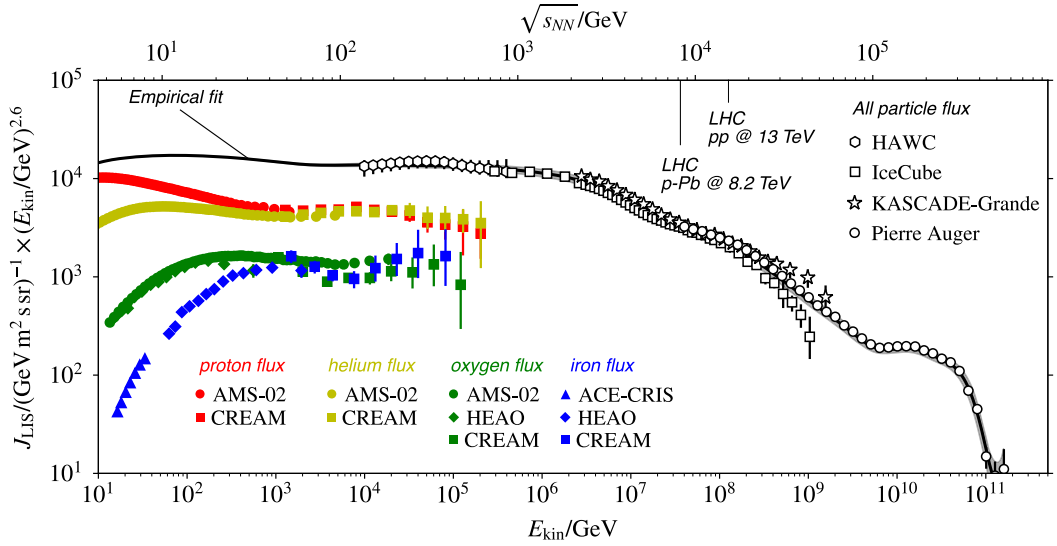

Figure 1.1.: Measurement of the cosmic-ray flux as a function of energy. The colored points are measurements of specific elements of the flux, while points are measurements of the full particle flux. The flux is multiplied by $E^{2.6}$ to better visualize the different components. [1]

The energy spectrum follows a segmented power law with differential spectral indexes between 2.7 and 3.3. Two transitions regions are present. Around 3 PeV, the slope steepens at a point called the *knee*. The *ankle* is the zone at about 3 EeV where the spectrum flattens. Those two transitions are poorly understood. The knee is thought to come from transitions between different classes of CR sources or propagation effects. The ankle could come from the transition from galactic to extragalactic origin.

A cutoff, usually called *toe*, is also present around 50 EeV. One possible explication is the Greisen-Zatsepin-Kuzmin (GZK) effect. Above 50 EeV, cosmic rays scatter off the photons of the Cosmic Microwave Background (CMB) and lose energy. Another explication is simply that it is the maximum energy an extragalactic source can accelerate cosmic rays to.

1A.1.2. Origin of cosmic rays

The origin of cosmic rays is still an open question today. Cosmic rays are charged particles and as such are deflected by magnetic fields. This makes it difficult to pinpoint directly to their sources. However, some necessary conditions can constrain the possible sources.

Michael Hillas proposed in 1984 a criterion to find the minimum conditions required on sources to accelerate cosmic rays. A particle is only accelerated while confined in the magnetic field of the source. Yet the particle escapes if its Larmor radius is larger than the size of the source. The maximum CR energy thus depend on the Lorentz factor γ of the source, the CR charge q, the source magnetic field intensity B and the characteristic source size R such as

$$E_{max} = \gamma\, q\, B\, R \tag{1.1}$$

The so-called *Hillas criterion* is shown Figure 1.2. The dashed red lines show the lower limits on magnetic field and size for the energy at the knee, ankle and GZK cutoff. Known celestial objects that would respect those constrains are added on the plot. The possible galactic sources are neutron stars, white dwarves, micro-quasars, supernova remnants and galactic disk and halo. Extra-galactic sources include active galactic nuclei (AGN), gamma-ray bursts (GRB), blazars, radiogalaxy lobes, galaxy clusters, starburst galaxies and intergalactic medium.

1A.1.3. Acceleration mechanisms

The simplest hypothesis for the acceleration of cosmic rays is the presence of variable magnetic fields. They can induce variable electric fields that accelerate particles over many interactions. However, the exact acceleration mechanism is poorly understood.

The idea was proposed by Enrico Fermi: the particles interact with many magnetized interstellar clouds. With each cloud, the particles gain some energy by a factor $\Delta E/E$. The principle is illustrated in the first line of Table 1.1. The resulting energy factor is proportional to the cloud velocity squared $\beta^2 = v^2/c^2$

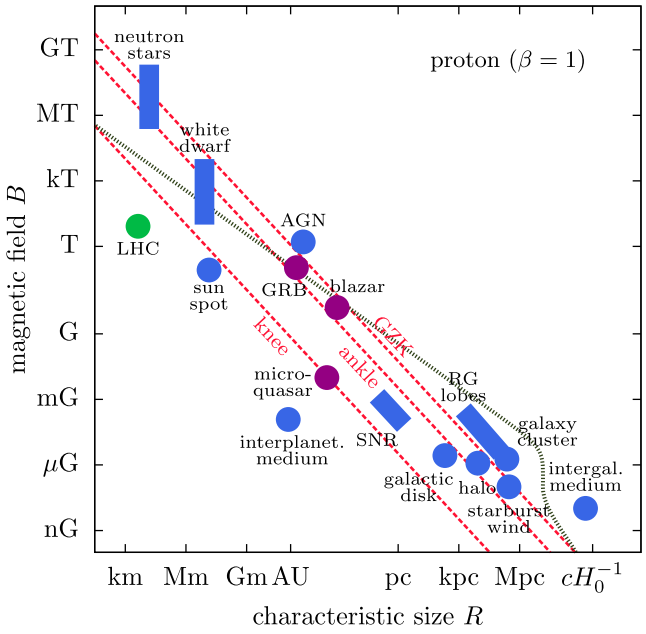

Figure 1.2.: Hillas plot describing the upper limits a source can accelerate a proton to as a function of its magnetic field and characteristic size. The red lines indicate the different energy regime of the CR spectrum: knee, ankle and GZK effect. [2]

Table 1.1.: Summary table for the two Fermi acceleration mechanisms. [3]

Mechanism	Principle	$\left\langle \frac{\Delta E}{E} \right\rangle$
Fermi 2nd order	Interaction of particles with the magnetized interstellar clouds	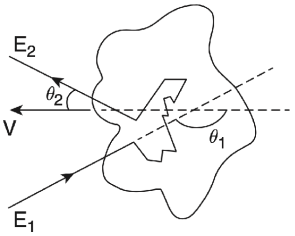 $\approx \frac{4}{3}\beta^2$
Fermi 1st order	Interaction of particles with a large plane shock front	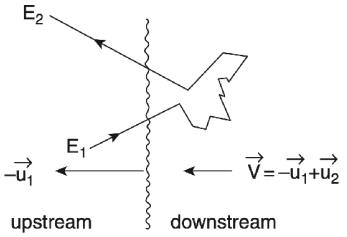 $\approx \frac{4}{3}\beta$

(thus Fermi 2nd order). With an interstellar cloud velocity in the order of $\beta \approx 10^{-4}$, the process is two inefficient to properly accelerate cosmic rays.

The Fermi 1st order mechanism describes the interactions of particles with a large plane shock front. An illustration is shown second line of Table 1.1. With this, the energy factor is linear and can explain cosmic ray energies up to the knee. The main accelerators associated to the mechanism are supernova remnants, which present a shock front as described. Above the knee, multiple hypothesis have been proposed such as magnetic reconnection [4], relativistic shocks [5], shear flows of matter [6] and others.

1A.2. Photons

Observation of the sky was mostly made through human history with visible light. However, the discovery of the full electromagnetic spectrum led to new observations and discoveries. The electromagnetic spectrum spans 20 orders of magnitude. The energy E of a given photon or radiation is often given as a frequency f or a wavelength λ. Those three values are connected through the Planck-Einstein equation:

$$\mathrm{E} = hf = \frac{hc}{\lambda}, \tag{1.2}$$

where h is the Planck constant and c is the speed of light in vacuum.

The electromagnetic spectrum is split into multiple ranges for historical reasons. In increasing frequency, the spectrum includes radio waves, microwaves, infrared, visible light, ultraviolet, X-rays and gamma-rays. Each part of the spectrum has different production mechanisms, such as synchrotron radiation, black-body radiation, electronic transitions or radioactive decays.

1A.2.1. Multi-wavelength astronomy

The physics processes associated with each wavelength and the Earth atmosphere absorption constrain how to make observations. The atmospheric opacity as a function of wavelength is presented Figure 1.3.

The first observation of a celestial object outside of the visible range was made at radio frequencies in the early 1930s. While investigating possible interference for long-range communication, Karl Jansky discovered a repeating signal. With a period of a sidereal day, the signal was likely to come from a “fixed” astronomical object passing in front of the antenna at each Earth rotation [7]. The radio emission origin was identified as the constellation of

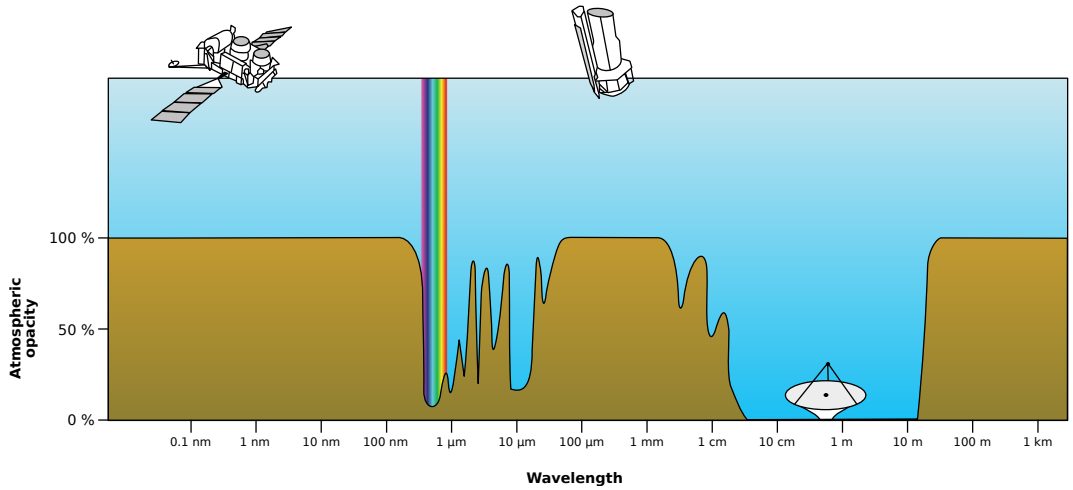

Figure 1.3.: Atmospheric opacity as a function of wavelength. Some observation devices are also represented at the appropriate frequencies.

Sagittarius in the Milky Way.

Radio observations from Earth are limited to wavelengths between 5 cm and 10 m. Above, the ionosphere reflects long-wavelength radio waves. Below, water vapor from the atmosphere can interfere observations. The angular resolution θ of a telescope can usually be approximated as

$$\theta = \frac{\lambda}{D} \tag{1.3}$$

where λ is the observed radiation wavelength and D the size of the telescope. As such, single dish radio telescopes are often tens or hundreds or meters in size. However, the high wavelength of radio waves facilitates the combination between different radio telescopes. Radio interferometry uses interference to use separated telescopes as a single one. The effective telescope size is thus increased, and the associated angular resolution improved. Very long baseline interferometry (VLBI) can even push this principle to reach an effective antenna the size of the Earth. VLBI was used to create incredibly detailed images of celestial objects, such as the first image of a black hole [8] or a detailed radio image of the Galactic center [9].

Infrared astronomy developed itself much later, thanks to two reasons: the success of radio astronomy in the 1950s and 1960s and infrared detector development by experimental physicists. Ground-based infrared telescopes are limited in sensitivity. Indeed, green house gases absorb the incoming infrared

radiation and emit thermal radiation. As such, most infrared telescopes are located at high elevation and dry places or in space. The main advantage of infrared radiation is its capacity to go through dense regions of gas and dust without being absorbed. This allows to probe further celestial objects, like the core of active galaxies.

The atmosphere is opaque for X-rays and gamma-rays. The first observations of astrophysical X-ray sources was made with rockets and high altitude balloons. But the short time flight of rockets and high atmosphere absorption with balloons led to dedicated X-ray astronomy satellites. X-rays are usually split in two categories. Hard X-rays are defined as photons with higher energy than 5–10 keV, whereas soft X-rays are less energetic.

Gamma-rays are defined as photons with an energy higher than 100 keV. The discovery of astrophysical gamma-rays came in the 1960s from military defense satellite. The partial nuclear test ban treaty prohibited the US and Soviet Union to test nuclear tests in the atmosphere. Satellites made to detect flashes of gamma-rays from Earth started recording gamma-ray bursts from deep space. Today, thousands of gamma-ray sources are recorded in the high-energy regime ($100\,\mathrm{MeV} < \mathrm{E} < 100\,\mathrm{GeV}$) and hundreds are recorded in the very high-energy one ($100\,\mathrm{MeV} < \mathrm{E} < 100\,\mathrm{GeV}$). They were observed with space telescopes, arrays of Cherenkov telescopes on the ground and high-altitude extended detector arrays.

1A.2.2. *Double bump* spectral energy distribution

Astronomical sources are often characterized according to their electromagnetic *spectral energy distribution* (SED). The SED is the distribution of energy output as a function of wavelength. A distribution of flux or flux density as a function of wavelength is also usually called a SED. Most objects being able to accelerate cosmic rays share a typical SED shape. A first bump spreads from radio to X-ray, with a peak usually between optical and X-ray. A second bump peaks in the high-energy part of the spectrum. An example is shown Figure 1.4, where the SED of Markarian 421 (Mrk 421), a blazar, is shown. The observation data points for different wavelength are gathered [10], and the two bumps are hand-drawn for illustration.

The first bump is associated with synchrotron radiation. Synchrotron radiation is emitted when relativistic charged particles are accelerated in a direction perpendicular to their movement. The phenomenon is common in astrophysical environments containing a strong magnetic field. Most radiation emitted usually comes from the electron, as its mass is much lower than other

charged particles. Assuming a power law distribution of particles with index α_l, compatible with the cosmic rays observations, the flux density is written

$$F(\nu) \propto \theta_s^2 \, R \, K \, B^{1+\alpha} \, \nu^{-\alpha}, \tag{1.4}$$

where θ_s and R are respectively the angular radius and the size of the source, K is the particle density and B is the magnetic field. The spectrum follows a power law of index α, which is related to the index of the power law particle distribution such as $\alpha = (\alpha_l - 1)/2$.

Equation 1.4 is divergent at small frequencies: $\alpha_l \approx 2$ so $F(\nu) \propto \nu^{-1/2}$. This is solved by the higher cross-section of photons at low frequencies. The matter present around the astrophysical source absorbs the synchrotron radiation, which becomes optically thick. Using thermodynamic consideration, the brightness temperature of the radiation must be equal to the effective kinetic temperature of the emitting matter. After some computation [11], this gives

$$F(\nu) \propto \theta_s^2 \, B^{-1/2} \, \nu^{5/2}, \tag{1.5}$$

with θ_s and B respectively the angular radius and the magnetic field of the source. The flux density in the thick regime no longer depends on the particle density K, as more density leads both to more emission and absorption.

The synchrotron emission for the two regimes is presented Figure 1.5. For low frequency, the source is optically thick and the flux density follows a power law of index 5/2. Above the self-absorption frequency ν_t where $F_{\text{thick}}(\nu_t) = F_{\text{thin}}(\nu_t)$, the source is optically thin. The flux density follows a power law of index $-\alpha$, and measurements in multiple wavelengths allows for estimating the slope and consequently inform on the acceleration processes. Additionally, flux measurement in both regimes is important to constrain both the particle density K and the magnetic flux B.

The origin of the second bump visible Figure 1.4 in the gamma-ray range is still the subject of many discussions. The two models, leptonic and hadronic, will be further discussed in section 1A.5.

1A.3. Neutrinos

Neutrinos were postulated by Wolfgang Pauli to explain the observed continuous energy spectrum in beta decay. Over the 20th century, neutrinos were detected and their properties studied. Three types of neutrinos were discovered, each associated with a charged lepton during interactions. The

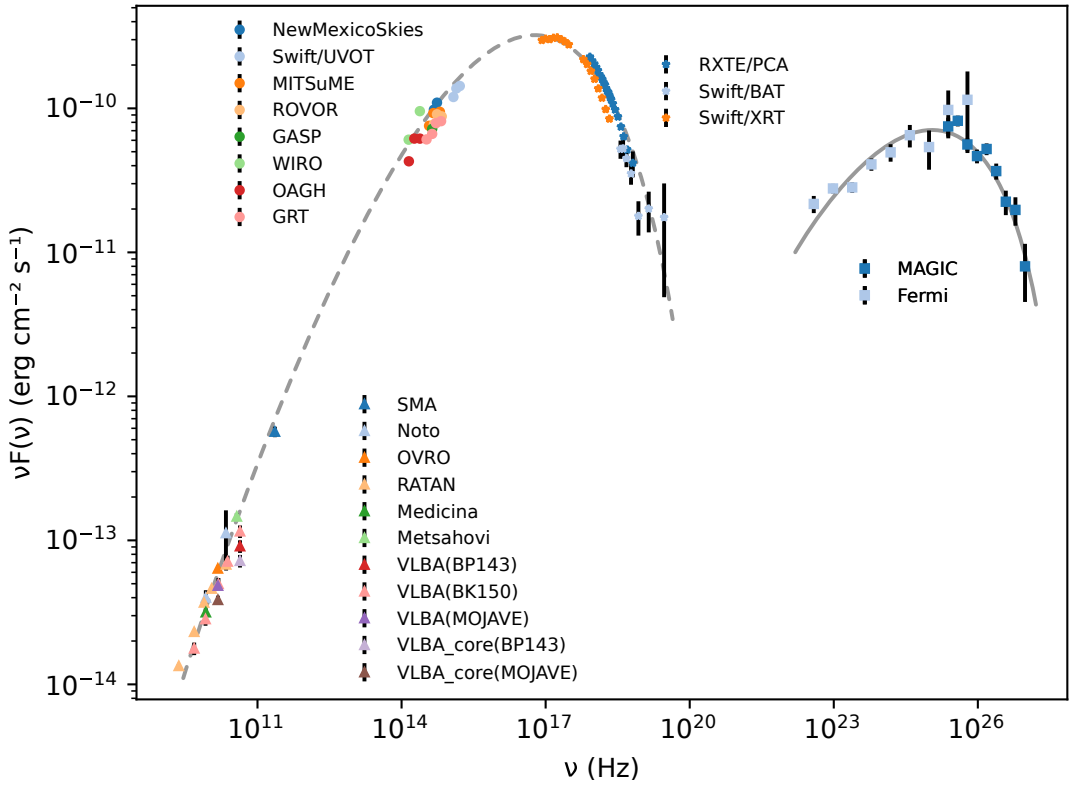

Figure 1.4.: Spectral energy distribution of Mrk 421 with data from [10]. The gray lines are hand-drawn for illustration purpose. The following convention is used for the observation data points: triangles for radio, circles for optical, stars for X-ray and squares for γ-ray.

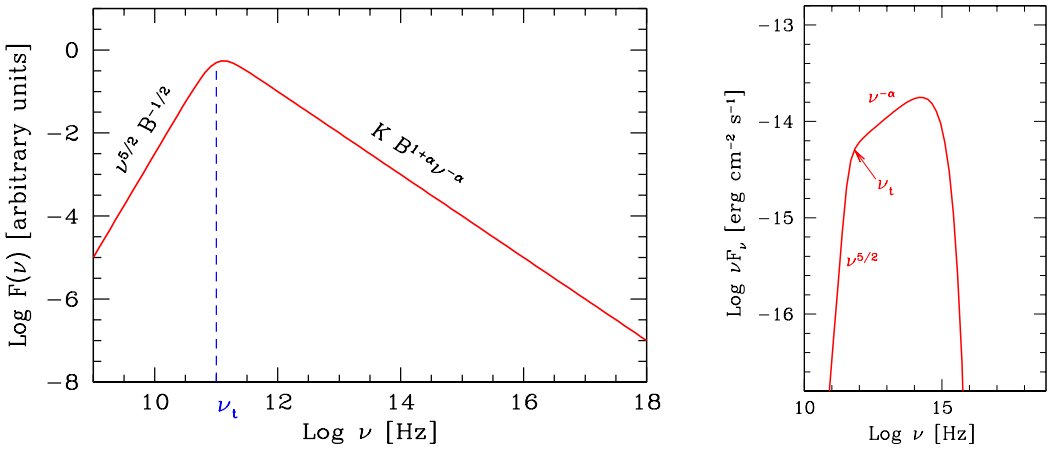

Figure 1.5.: Analytical flux (left) and spectral energy distribution (right) from synchrotron radiation. [11]

electron, muon and tau neutrinos differ in a property called *flavor*. They are neutral elementary particles that only interact through the weak interaction.

Neutrinos are particularly interesting both in particle physics and in astronomy. Originally thought to be massless in the Standard Model, the neutrinos were proven to be massive when neutrino oscillations were brought to light. A neutrino created with a given flavor can after propagation interact with a different flavor. This is the oscillation phenomenon. For astronomy, neutrinos are interesting for two reasons. They are abundant in the Universe and take place in many cosmic phenomenon, such as nuclear reactions or high-energy particles decays. Secondly, the low cross section and neutral charge allows them to leave dense environments and propagate in a straight line. Contrary to gamma-rays, they are not absorbed and contrary to cosmic rays, they are not deflected by magnetic field. As such, they offer a great probe to the inner mechanisms of celestial objects.

1A.3.1. Neutrino flux

Neutrinos can be produced by many sources through many processes. Figure 1.6 shows the whole neutrino and antineutrinos spectrum, from 10^{-6} eV to 10^{18} eV [12].

Between µeV and meV, a high flux of neutrinos from the cosmic neutrino background (CνB) is expected. The CνB are neutrinos which decoupled from matter one second after the Big Bang. No measure of them has been made yet, as their cross-section with matter is extremely small. The MeV range contains many contributions. The main one is solar neutrinos, which are created during the different nuclear fusion reactions. Reactor neutrinos come from the different fission reactors made by humans. Geoneutrinos originate from the radioactive decays from elements inside the Earth. Finally, all neutrinos emitted from core-collapse supernovae during the lifetime of the Universe contribute to the diffuse supernova flux.

Above 0.1 GeV, the neutrino flux comes mainly from the atmosphere. Cosmic rays interacting with the atmosphere create a cascade of secondary particles. Part of those particles are or decay to neutrinos afterward. As a result, the atmospheric muon flux follows a power law similar to the cosmic ray one.

The most energetic part of the spectrum is composed from astrophysical and cosmogenic neutrinos. Astrophysical neutrinos (from 10 TeV to 10 PeV) are presented in the next section. Cosmogenic neutrinos are expected from the interaction of cosmic rays with the CMB. They have to this day not been detected, but multiple experiments are in construction to probe this energy

region.

1A.3.2. Diffuse flux of cosmic neutrinos

The IceCube collaboration announced in 2013 the detection of neutrinos originating from outside the Solar System [14]. The neutrinos detected had energies between 30 TeV and 1.5 PeV. With more exposure, IceCube was able to measure the diffuse flux from astrophysical neutrinos. Figure 1.7 presents the latest results for the astrophysical energy spectrum. The energy spectrum follows a single power law with a spectral index of $2.58 \pm 0.10 \pm 0.09$

Multiple cosmic sources are proposed to explain this high-energy diffuse flux. Neutrinos most likely originate from sources which also produce cosmic and gamma-rays (see section 1A.5). Most commonly proposed sources are blazars and gamma-ray bursts, but recent study show some correlation with tidal disruption events (TDE) [15] and radio-loud active galactic nuclei [16].

1A.3.3. Known sources of cosmic neutrinos

To this day, only four sources of cosmic neutrinos have been confirmed (not counting solar neutrinos). The multi-messenger observations of SN1987A (a core-collapse supernova) and TXS 0506+56 (a blazar) are presented section 1A.6. Additionally, the IceCube collaboration measured two steady sources of neutrinos. NGC1068, also know as Messier 77, is an nearby active galactic nucleus. An excess of 79^{+22}_{-20} neutrinos was found in association with it, with a significance of 4.2σ [17]. Finally, the galactic plane is gamma-ray source and was hypothesized to be a neutrino source as well. A diffuse high-energy neutrino emission was identified with 4.5σ significance [18]. However, the use of shower-like events for the analysis restricted the angular resolution, and no precise source was found.

1A.4. Gravitational waves

Gravitational waves (GW) were deducted as a consequence of the theory of general relativity formulated by Albert Einstein. A bit less than a hundred years later, the LIGO-Virgo collaborations announced the first detection of a gravitational wave signal [19].

Gravitational waves are deformations of spacetime which propagate at the speed of light. They are emitted by non-spherically symmetric system of moving large masses. However, the current generation of gravitational wave

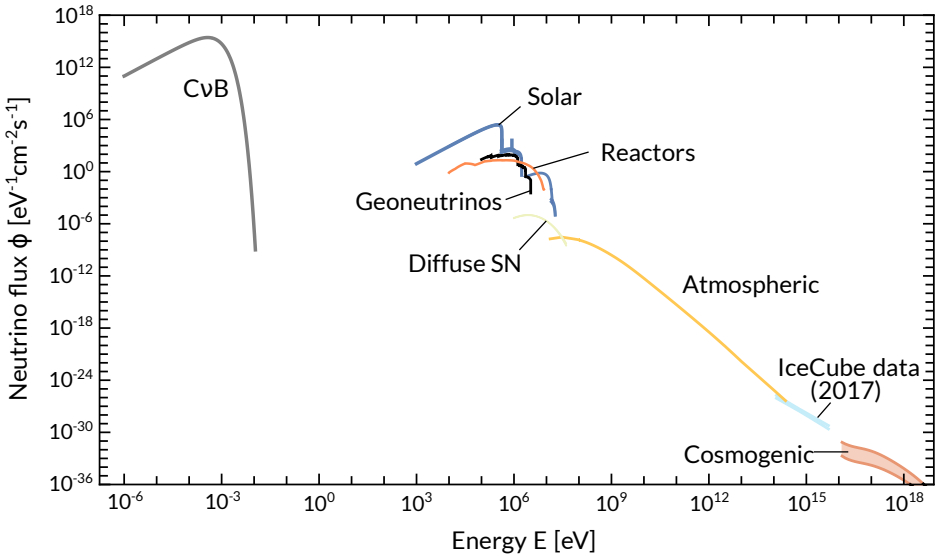

Figure 1.6.: Neutrino flux as a function of energy on Earth, integrated over directions and summed over flavors. The plot does not differentiate neutrinos and anti-neutrinos. [12]

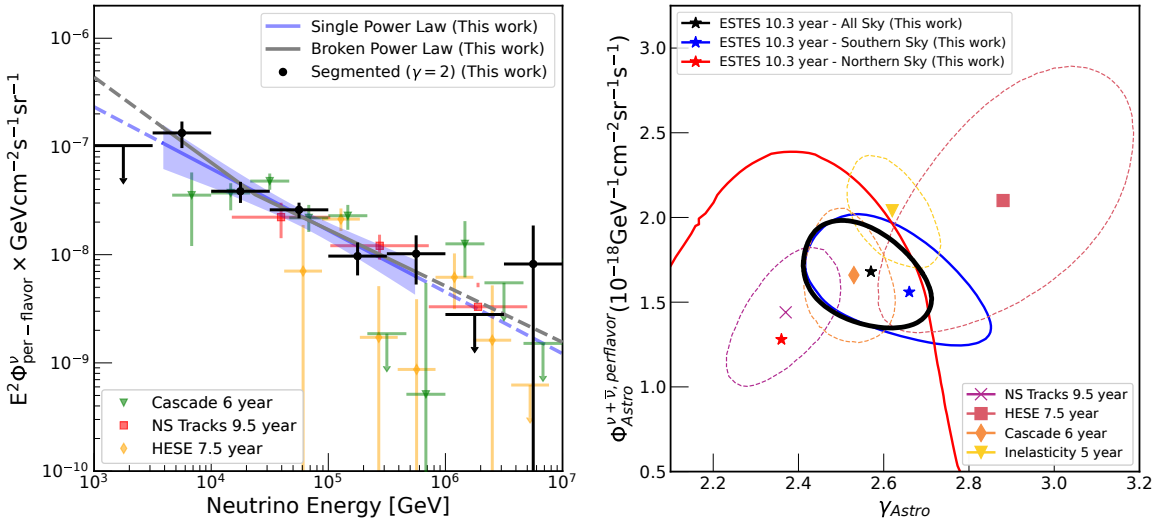

Figure 1.7.: Per flavor astrophysical neutrino flux as a function of energy (left) and confidence intervals for the measurements of the flux normalization and power law spectra index (right). [13]

detectors is only compatible to a limited set of objects. GW are observed with L-shaped interferometers. A LASER is split into two beams, which each propagate in an arm of a given length, reflect back and interfere together. When a GW crosses one of the beams, the arm length is slightly changed and the interference pattern changes. In order to be sufficiently sensitive, the arms are multiple kilometers long. The current major detectors are all based on Earth: two LIGO sites in the USA, Virgo in Italy and KAGRA in Japan. Together they form the LVK collaboration.

The current capabilities of the LVK collaboration is:

- binary mergers of two neutron stars (BNS), one neutron star and a black hole (NSBH) and black hole-black hole (BBH), up to 1 Gpc;
- non symmetrical galactic burst events, such as a core-collapse supernova.

A coarse localization of the GW sources is also possible by using the arrival times at different detectors.

The LVK real-time alert system sends automatic notices to the astronomy community. This led to the multi-messenger observation of a kilonova in 2017, described in more details section 1A.6. Gravitational waves are a unique messenger, as they carry gravitational information about the sources.

1A.5. Connection between the different messengers

1A.5.1. Leptonic and hadronic models

As described subsection 1A.2.2 and shown in Figure 1.4, most potential high-energy sources share a double bump SED. Synchrotron emission is the most common explanation as a source for the first bump. But the second bump, in the gamma-ray part of the electromagnetic spectrum, can originate from two mechanisms: leptonic and hadronic emission.

The leptonic model relies on Self-Synchrotron Compton (SSC). Particles (mostly electrons) moving in the magnetic field of the source produce photons through synchrotron emission. The photons energy spectrum peaks between the infrared and the X-rays. The emitted photons and parent particles can in turn interact together. Inverse Compton scattering describes the energy transmission from high-energy particles to low-energy photons. The mean energy $\Delta E/E$ gained by the photon depends on its initial energy in the particle

rest frame [20]:

$$\text{for } E_{\text{photon}} \ll mc^2 \text{ (Thomson regime)}, \frac{\Delta E}{E} \propto \gamma^2 \tag{1.6}$$

$$\text{for } E_{\text{photon}} \gg mc^2 \text{ (Klein-Nishina regime)}, \frac{\Delta E}{E} \lessapprox \gamma \tag{1.7}$$

with γ the Lorentz factor of the particle. Frequent situations give a Lorentz factor $\gamma = 10^2$–10^3. For electrons with $\gamma \approx 1000$ (0.5 GeV), optical photons with $\nu_0 = 4 \times 10^{14}$ Hz become gamma-rays of the MeV energy-scale. In some environments where electrons reach ultra-relativistic energy, the Lorentz factor can reach $\gamma \approx 10^9$. Infrared to X-ray photons can in this instance be boosted up to GeV or TeV energies.

The hadronic model describes the production of high-energy photons from interacting protons. Accelerated protons can interact either with other nucleons or with radiation from the medium. Most proton-nucleon interactions are inelastic, with a cross section almost energy independent. The main interaction product is pions:

$$p + p \rightarrow \begin{array}{l} p + p + \pi^0 \\ p + n + \pi^+ \end{array}, \quad p + n \rightarrow \begin{array}{l} p + n + \pi^0 \\ p + p + \pi^- \end{array} \tag{1.8}$$

Pions can also be produced when protons interact with low-energy photons γ present near the source. The process is called photoproduction and occurs mainly through the Δ^+ resonance:

$$p + \gamma \rightarrow \Delta^+ \rightarrow \begin{array}{l} p + \pi^0 \\ n + \pi^+ \end{array} \tag{1.9}$$

The associated cross section is much lower than the proton-nucleon one. However, a high density of radio to ultraviolet photons are present in astrophysical environments. This can lead the photoproduction process to contribute much more to pion production than proton-nucleon interactions.

If the source is sufficiently transparent, the interact products can escape. Indeed, neutrons and neutral pions are not confined by the magnetic field. Charged pions have a larger Larmor radius than the proton and can thus also escape.

Neutral pions decay to produce gamma-rays:

$$\pi^0 \rightarrow \gamma + \gamma \tag{1.10}$$

The energy spectrum of the gamma-rays produced by π^0 decay follows a bell shape between 100 MeV and few GeV. It is usually called the *pion bump* [21]. In the hadronic model, the pion bump is responsible for the second bump visible in a typical SED.

The charged pions start a decay chain which produces muon and electron neutrinos and anti-neutrinos:

$$\pi^{\pm} \rightarrow \mu + \nu_{\mu}, \quad \mu \rightarrow e + \nu_{\mu} + \nu_{e}. \tag{1.11}$$

The former equation does not take into consideration particle or anti-particle. The neutrons can also decay into proton through the weak interaction:

$$n \rightarrow p + e^{-} + \bar{\nu}_{e} \tag{1.12}$$

The energy escaping the astrophysical source is therefore shared between high-energy protons (cosmic rays), gamma-rays and neutrinos. With the hadronic model, a strong relationship exists between those three messengers. As such, gamma-ray measurements can lead to important information on cosmic rays and constrain the neutrino flux. Moreover, the observation of neutrinos in coincidence with gamma-rays is a "smoking-gun" to identify a source as containing hadronic processes.

1A.5.2. Gamma-rays absorption

Gamma-rays have however some probability to be absorbed between their emission and arrival on Earth. Two photons can under go a process called pair-production:

$$\gamma + \gamma \rightarrow e^{+} + e^{-} \tag{1.13}$$

This process is possible when the energy in the center of momentum exceeds twice the electron mass. The maximum contribution to the gamma-ray absorption is the Cosmic Microwave Background (CMB). The CMB starts to interact with photons at an energy of 100 TeV. Another radiation at play the the Extragalactic Background Light (EBL). The EBL is the integrated diffuse radiation of all light emitted throughout the Universe history. From the current measurements of the EBL, a gamma-ray distance horizon can be computed.

Figure 1.8 shows the distance-energy phase space where the Universe becomes opaque to photons (black area). Above a given energy, photons and cosmic rays can no longer propagate, respectively because of the EBL and the GZK effect. The most distance high-energy Universe can thus only be studied through neutrinos and gravitational waves.

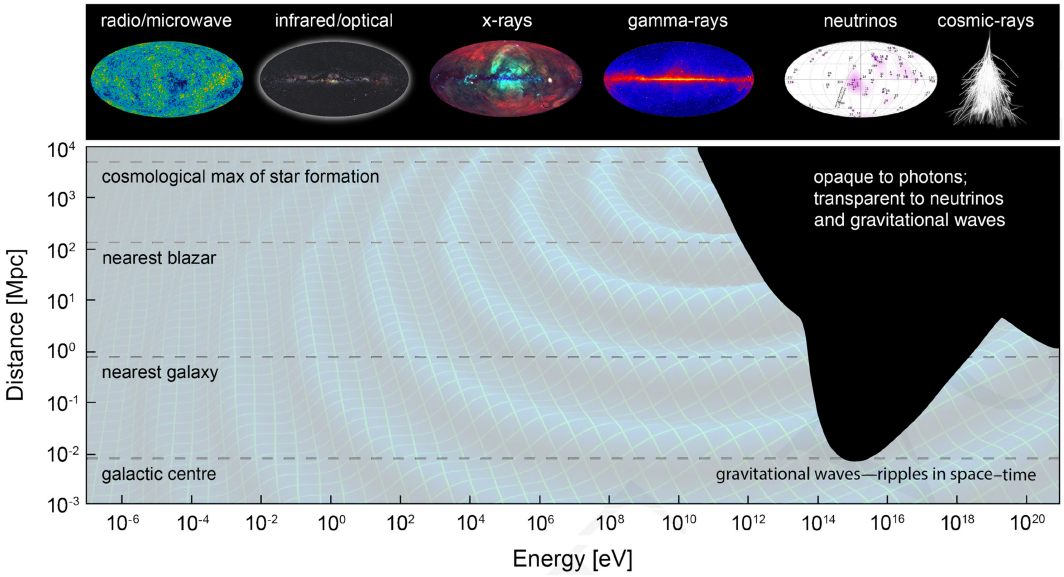

Figure 1.8.: Distance horizon at which the Universe becomes opaque to photons. Above the plots are views of the full sky in different wavelengths and neutrinos. [22]

1A.6. Historical multi-messenger observations

To this day, three transient events have been observed (excluding solar flares) in a multi-messenger capacity: a core-collapse supernova in 1987, a kilonova in August 2017 and a gamma-ray flare from a blazar in September 2017.

1A.6.1. SN 1987A

On February 24, 1987, a magnitude 5 object appeared in the Large Magellanic Cloud [23]. It was identified to be a supernova, the first modern one to be close enough to be visible to the naked eye. It is named SN1987A, following the supernova naming scheme (year and letter for order within the year). The observation of associated gamma-ray lines confirmed the radioactive origin of visible light emission.

A few days after the supernova discovery, four neutrino detectors reported a burst of neutrinos: two water Cherenkov, Kamiokande II [24] and IMB [25] and two scintillation detectors, Baksan [26] and LSD [27]. 25 neutrinos were detected few hours before the optical signal from Kamiokande, IMB and Baksan. This is the first observation of extra-solar neutrinos. This observation is

compatible with the Core-Collapse Supernova (CCSN) models, where neutrino escape before photons. The time distribution of the neutrino events are visible Figure 1.9. The events seen by LSD were a few hours before. They are generally considered as not related to the CCSN neutrinos, even if their origin is still debated.

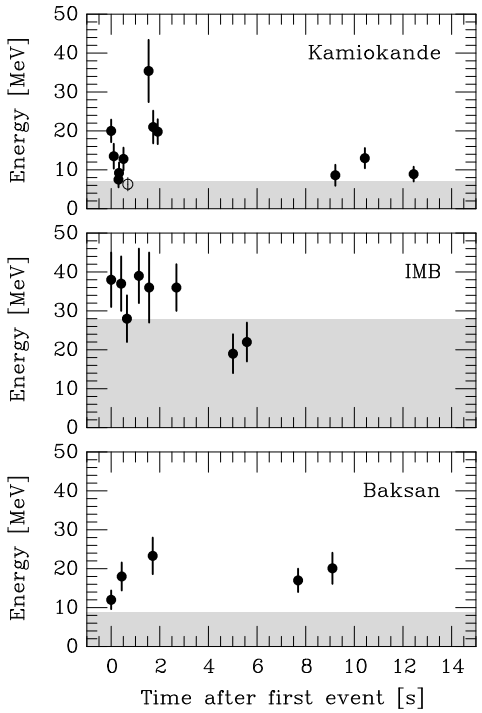

Figure 1.9.: SN1987A neutrino observations from Kamiokande II, IMB and Baksan. [28]

The observations of neutrinos from SN1987A could have been missed due to many different reasons [29]. The Kamiokande detector was switched off for routine calibration two minutes after the neutrinos' arrival. February 23 was celebrated as Soviet Army and Navy Day in many Soviet Union institutions. The Artyomovsk Scintillation Detector, for example, was not in operation. But the Baksan Neutrino Observatory director decided to leave the detector running. Finally, a few hours before the neutrino arrival, the magnetic tape recording the IMB data was almost full. As a result, the energy threshold was increased to lower the data writing rate. A graduate student was fortunately showing the facility to their partner the Sunday 22 night. Noticing the full magnetic tape, he exchanged it which lowered the threshold to allow the detection.

1A.6.2. GW170817

On 2017 August 17, the Fermi gamma telescope and the gravitational wave detector LIGO both issued independent GCN Notices. GCN Notices are a tool part of the NASA General Coordinates Network (GCN). They are real-time, machine-readable alerts that are usually submitted automatically by observation facilities. The Fermi notice announced the detection of a gamma-ray burst (GRB) and LIGO the detection of a binary neutron star coalescence. The two events were separated only by two seconds. Because of the coincidence, a GCN Circular (rapid astronomical bulletins) was distributed to push for a global follow-up.

Overall, more than 50 facilities over the world performed observations [30]. A timeline of all observations is shown Figure 1.10. A bright optical transient was found 11 hours after the merger [31]. The object was identified to be a kilonova thanks to the red and blue component from r-process nucleosynthesis.

The scientific impact of GW170817 was huge. The observations were used to investigate the equivalence principle or the Lorentz invariance, to measure cosmological constants, to better understand nucleosynthesis, and many other subjects. GW170817 is currently the only GW detection associated with an electromagnetic observation.

1A.6.3. TXS 0506+056

A bit more than one month after the observation of GW170817, the IceCube neutrino telescope reported a high-energy neutrino [15]. The reconstructed origin from the 290 TeV neutrino was coincident with the known gamma-ray blazar TXS 0506+056. At the time of the neutrino detection, the blazar was in a flaring state, as reported by the Fermi telescope. A GCN Circular was issued few hours after the automatic Notice. A multi-wavelength observation campaign started to characterize the SED and variability of the associated blazar. The IceCube neutrino containment region and observation by Fermi and Magic are presented Figure 1.11.

The IceCube collaboration performed archival searches for neutrinos in the direction of TXS 0506+056. The results showed neutrinos in excess to background in the blazar direction [32]. The association reaches a 3.5σ significance. The neutrinos were found to be mostly emitted at the beginning of 2015. The IceCube results are shown in the top plot of Figure 1.12. However, at the time of the neutrino excess TXS 0506+056 was not in a flaring state, as seen on the bottom plot of Figure 1.12.

Nevertheless, the 2017 neutrino detection was the first multi-messenger

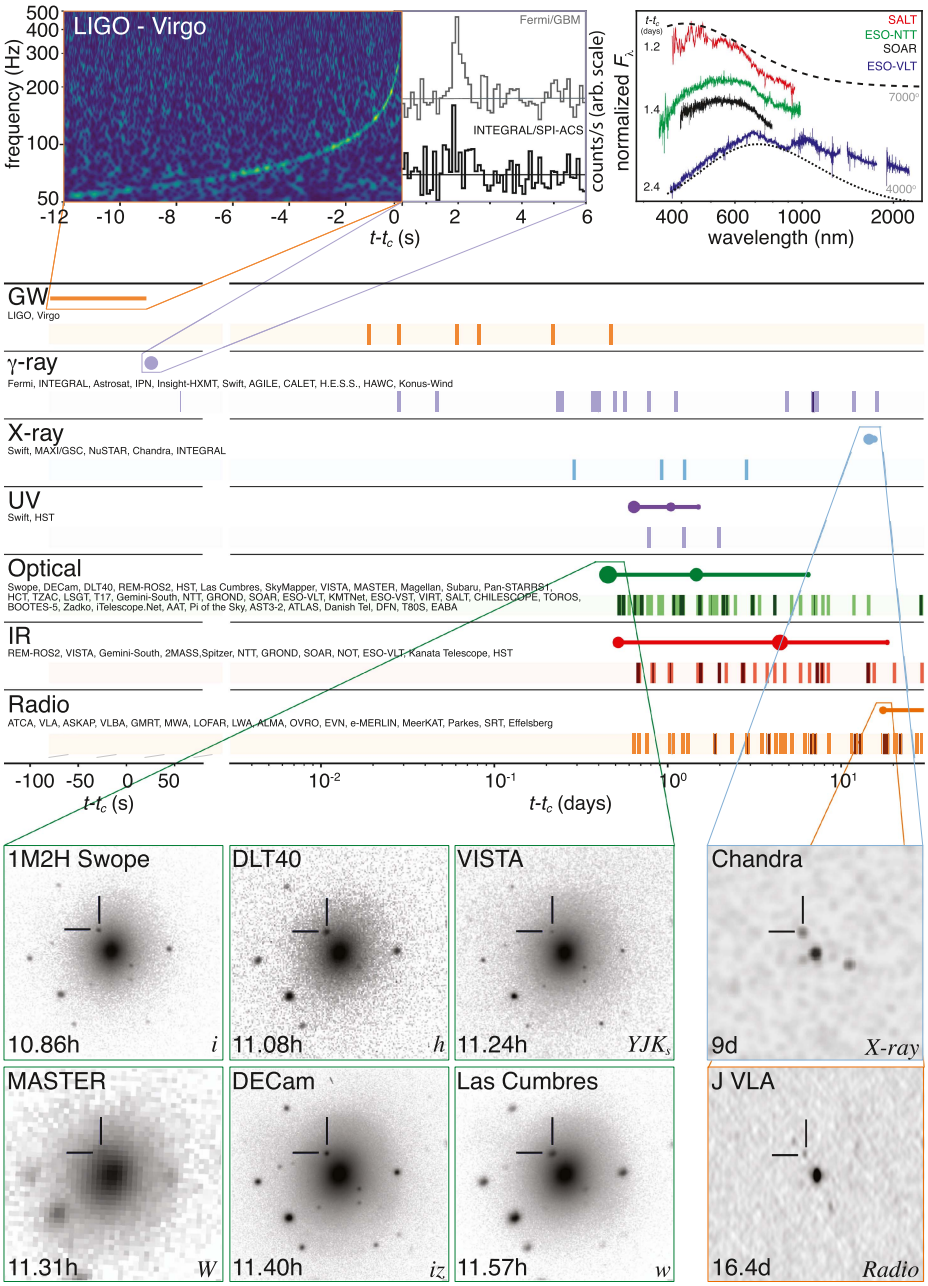

Figure 1.10.: Timeline of the discovery of GW170817 and follow-up observations. Every dash is an information reported in a GCN Circular. Observations are shown in full circles, with the size approximately proportional to the brightness. Horizontal lines indicate the source being detectable by at least one telescope. The insets are pictures of the first detections in the gravitational-wave, gamma-ray, optical, X-ray, and radio bands. The associated SED is shown in the top right. [30]

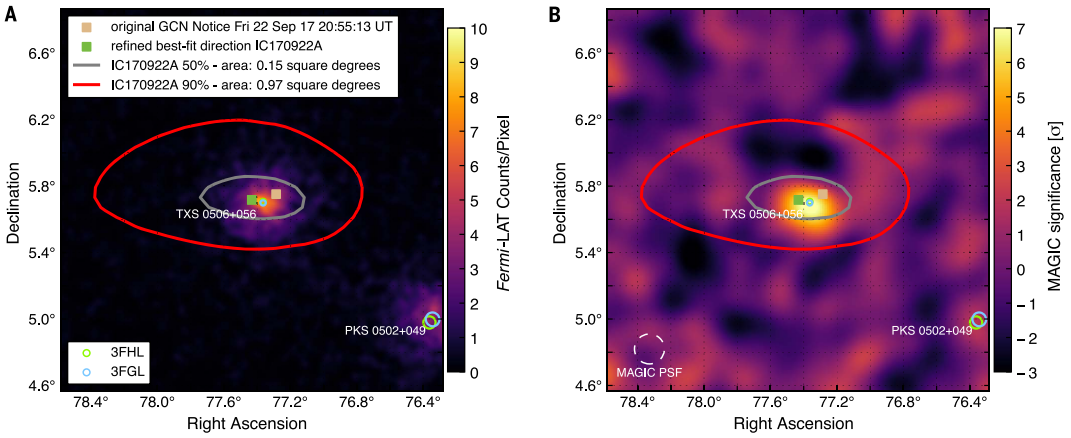

Figure 1.11.: Fermi-LAT (left) and MAGIC (right) observations of the IceCube event associated with TXS 0506+056. [15]

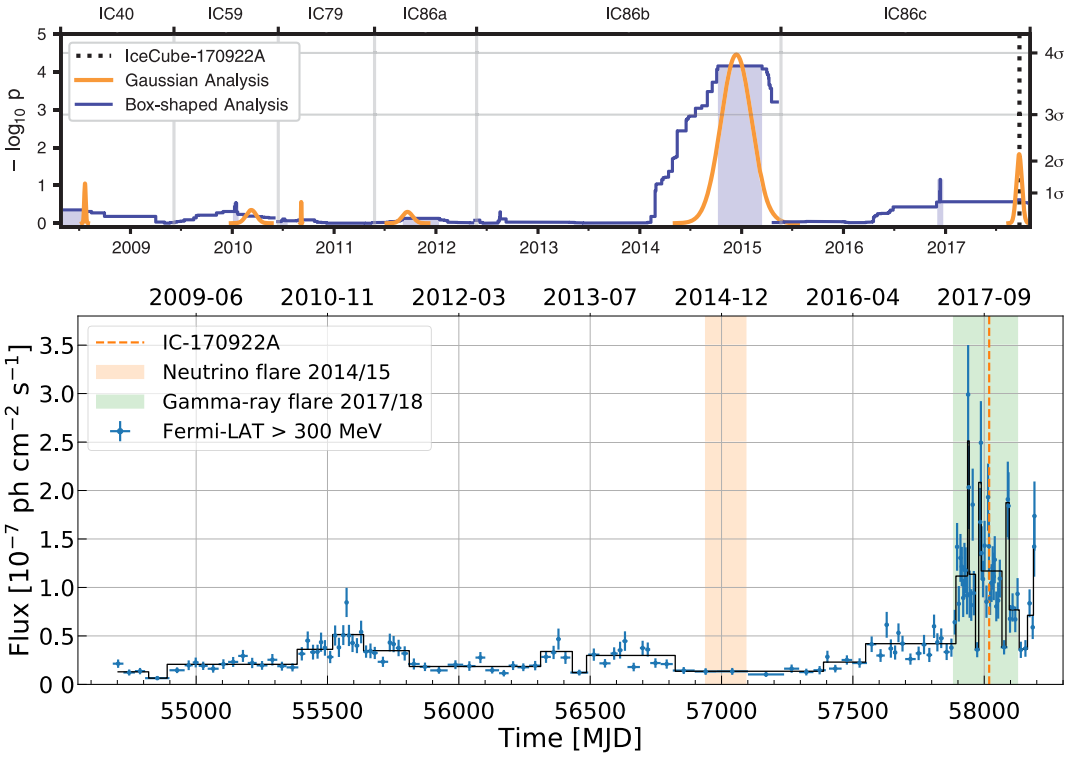

Figure 1.12.: Results for the time-dependent search of neutrinos with IceCube (top) and gamma emission measured by Fermi-LAT (bottom), both in the direction of TXS 0506+056. [32] [33]

observation with high-energy neutrinos. It reinforced the hypothesis of blazars as a neutrino source candidate, even if more observations are needed. Overall, the two 2017 multi-messenger observations showed the importance of real-time detection and communication. The KM3NeT detector, presented thereafter, will play a key part in multi-messenger observation.

1B. KM3NeT: a neutrino telescope in the Mediterranean Sea

C'est en ayant la tête sous l'eau qu'on peut voir des poissons.

Clotilde Vannoye

1B.1. Principle of water Cherenkov detectors

In the 1960s, Moisey Markov proposes the idea to indirectly detect neutrinos by installing detectors "in an underground lake or deep in an ocean" [34]. After a neutrino interaction, some products can induce an electromagnetic radiation called Cherenkov radiation. This light can be captured by an array of photosensors to reconstruct the neutrino properties. Using an naturally occurring medium as the interaction and light propagation medium enables the construction of detectors with a big instrumented volume for a fraction of the cost of one filled artificially.

1B.1.1. Neutrinos interaction

Neutrinos interact with matter only through the weak interaction. The Standard Model describes the weak interaction as the exchange of a so-called *weak boson*. Weak bosons are the W^+ and the W^-, respectively positively and negatively charged, and the Z^0, which is neutral. Two types of weak interactions are defined according to the charge of the exchanged boson.

Charged-current (CC) interactions $\nu_l + N \rightarrow l + X$ (1.14)

Charged current interactions see the production of a charged lepton l. The neutrino flavor is conserved, *ie* an incoming electron/muon/tau neutrino will always result in a produced electron/muon/tau.

Neutral-current (NC) interactions $\nu + N \rightarrow \nu + X$ (1.15)
In neutral current interactions, neutrinos are scattered elastically at low-energy and inelastically at high-energy and keep propagating after depositing energy.

The three main categories of mechanisms at GeV energy and above are quasi-elastic scattering, resonance production and deep inelastic scattering [35].

Between 100 MeV and 2 GeV, neutrinos interact mainly through quasi-elastic scattering. At this energy range, neutrinos scatters off entire nucleons. As such, the N and X in Equation 1.14 and Equation 1.14 stand respectively for a neutron and a proton in the case of an incoming neutrino. For an incoming anti-neutrino, the N stands for a proton and the X for a neutron.

For energy between 500 MeV and 10 GeV, a neutrino can excite the nucleon N, which in return produces a baryon resonance where $X = N^*$. The baryon resonance decays into one or multiple pions.

For higher energy than 5 GeV, the predominant neutrino interaction is deep inelastic scattering. In DIS, neutrinos interact with the inner structure of the nucleon N. This results in a final set of hadrons X which is often not stable and further decays.

Figure 1.13 gives an overview of the neutrino cross section as a function of neutrino energy between 100 MeV and 100 GeV. The three main mechanisms, quasi-elastic scattering (QE), resonant pion production (RES) and deep inelastic scattering (DIS) are identified as well.

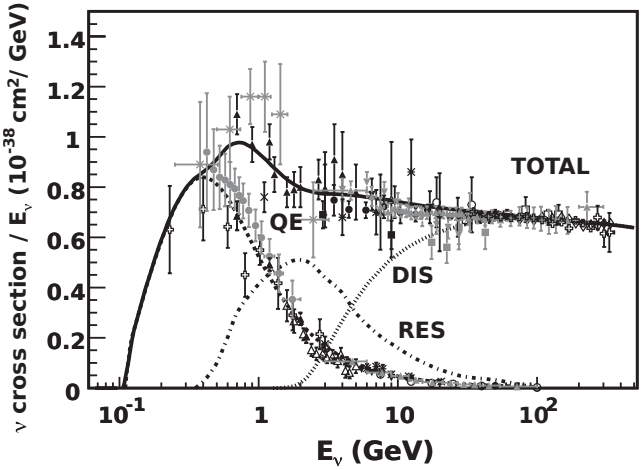

Figure 1.13.: Total neutrino CC cross section divided by neutrino energy as a function of neutrino energy. The contribution of the processes (QE for quasi-elastic scattering, RES for resonant pion production and DIS for inelastic scattering) are also indicated. [35]

For higher energy than 500 GeV, the amount of cross-section measurements is limited. Models describe the neutrino cross-section to grow linearly with the neutrino energy until reaching 10 TeV. Above, the cross section is approximated as a power law. Figure 1.14 shows the theoretical prediction for DIS, along with some measurements in the TeV to PeV range from the IceCube neutrino telescope [36]. Additionally, the FASER collaboration published in May 2025 the first measurement of muon neutrinos cross section in the 100–1000 GeV energy range [37]. The results are shown Figure 1.15.

1B.1.2. Cherenkov radiation and light propagation

The resulting particles from the neutrino interactions (charged lepton and/or hadrons) often propagate at a relativistic speed. When a charged particle propagates in a dielectric medium at a speed v greater than the velocity of light in that medium (c/n with c the speed of light and n the refractive index of the medium), an electromagnetic radiation called Cherenkov radiation is emitted. The light emission is due to the return to the ground state of molecules polarized along the charged particle path. If $v > c/n$, the spherical light wavefront interferes constructively in a cone shape light signal. An schematic representation of the emission of Cherenkov light is drawn Figure 1.16. The phenomenon is analog to the Mach wave of objects going faster than the speed of sound.

The angle θ between the particle direction and the light emission can be derived from the geometrical relations visible Figure 1.16:

$$\cos(\theta) = \frac{c/n}{\beta c} = \frac{1}{\beta n}, \tag{1.16}$$

with β the ratio between the particle velocity v and the speed of light c. In water where $n \approx 0.35$, the Cherenkov angle for relativistic particles ($\beta \approx 1$) is $\theta \approx 42^\circ$ and independent of the particle energy.

The number of emitted Cherenkov photon N per unit path length dl and unit wavelength interval dλ can be derived from the Frank-Tamm formula [38]:

$$\frac{\mathrm{d}^2\mathrm{N}}{\mathrm{d}l\mathrm{d}\lambda} = \frac{2\pi\alpha q^2}{\lambda^2}\left(1 - \frac{1}{\beta^2 n^2}\right), \tag{1.17}$$

where α is the fine structure constant and q is the charge of the particle. A shorter wavelength is associated to a higher number of photons. As such, Cherenkov radiation is observed to be blue, with most of the radiation being

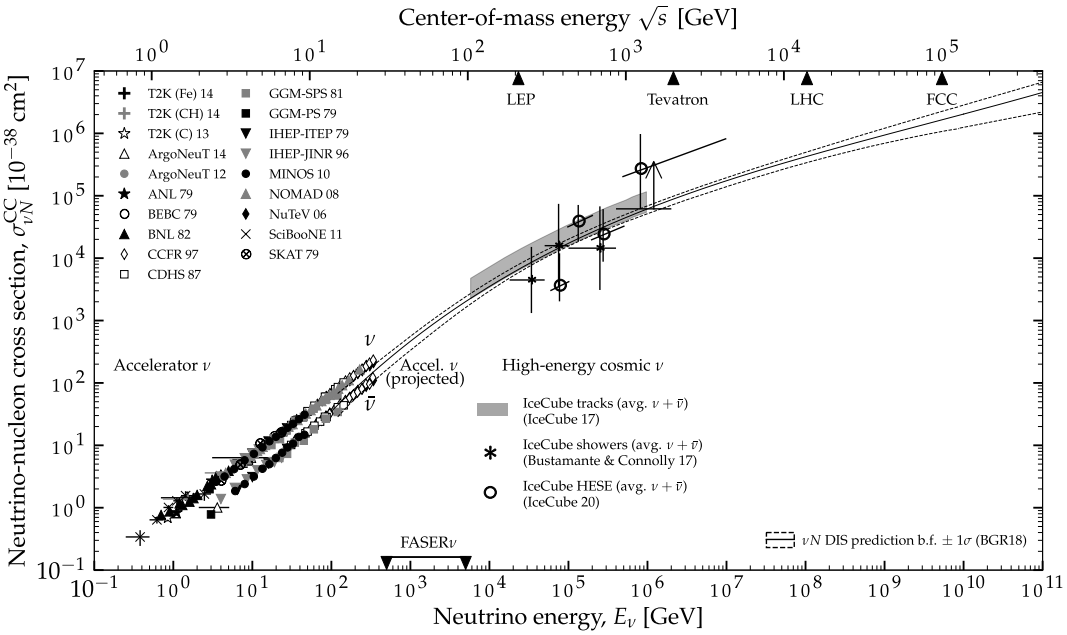

Figure 1.14.: Neutrino CC cross section as a function of neutrino energy. Measurements from accelerators are shown in the GeV to TeV range. Measurement from the IceCube neutrino detector are also presented. [36]

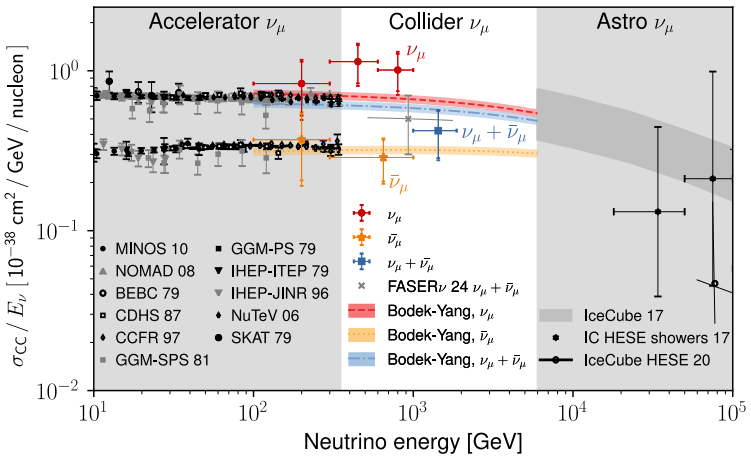

Figure 1.15.: Neutrino CC cross section divided by neutrino energy as a function of neutrino energy. The latest results from the FASERν experiment are shown in color. [37]

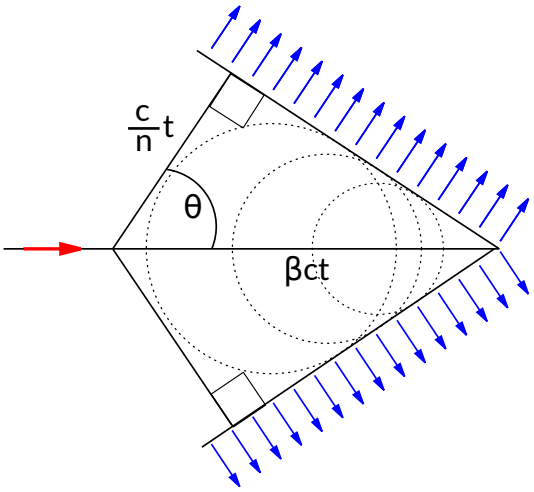

Figure 1.16.: Sketch describing the geometry of Cherenkov radiation. The red arrow represents the direction of propagation of the particle and the blue arrows indicate the wavefront direction of the emitted photons.

in the ultraviolet spectrum.

The amount of Cherenkov light in a perfectly transparent medium at a distance r is proportional to r^{-1}. This differs from a spherical emission, proportional to r^{-2}, thanks to the constructive interference at play. For real transparent medium such as water and ice, an exponential absorption term $e^{-r/\lambda_{abs}}$ needs to be added. The absorption length λ_{abs} is defined as the distance after which $1/e$ of the initial light remains. In the Mediterranean Sea, the average absorption length of 440 nm photons is approximately 67 m [39]. Additionally, light can scatter with molecules (Rayleigh scattering) and with dust (Mie scattering) present in the medium. The scattering results in a smearing on the arrival time of photons on detectors. Finally, the wavelength dependency of the refractive index results in small changes in the propagation time between photons of different energy. This causes an additional arrival time smearing. The resulting total photon arrival time uncertainty is in the order of the nanosecond.

1B.1.3. Event signatures

The interaction of neutrinos above GeV energy in water presents two main event topologies. Track-like events see the propagation of a muon in a straight line for long distances (at least few hundreds meters). Conversely, shower-like events contain particles that propagate in an spherical or obloid shape for

tens of meters. The event topology depends on the neutrino flavor and the interaction type.

Track-like events The ν_μ CC and some ν_τ CC interactions result in an hadronic shower and a propagating muon. A muon can propagate for several kilometers depending on its initial energy. For example a TeV muon can travel for up to around 4 km. As such, the Cherenkov light emitted along the path of the muon can be leveraged to retrieve with great performance the incoming direction of the neutrino. Additionally, the long propagation length of muons enables the detection of muons originating outside the detector volume. This increases the overall detector efficiency.

Shower-like events ν_e CC, some ν_τ CC and all NC interactions are characterized by hadronic and electromagnetic showers. A particle shower, sometimes called cascade, consists of incoming particles interacting to produce multiple new particles with lower energy, which in turn interact and produce new particles, *etc*. For example, the high-energy electron produced in a ν_e CC interaction leads to an electromagnetic cascade of photons and electrons through bremsstrahlung and pair-production. The observable signal comes from the Cherenkov radiation of the charged particles in the shower. Shower-like events are usually contained within the detector, and the total Cherenkov emission is mostly proportional to the initial neutrino energy. As such, shower are a great channel for low uncertainty energy reconstruction.

Tau neutrino The ν_τ CC interaction leads to the formation of a hadronic shower along a tau particle. Compared to the muon lifetime of 2.2×10^{-6} s, the tau lifetime is 2.9×10^{-13} s and cannot propagate for distances as long. However, tau particles above 500 TeV can propagate for tens of meters and induce the associated track. If the tau decays into a muon, the two tracks are indistinguishable. But if the tau decays into an electron or into hadrons, a second shower is produced. The specific topology of two distinguishable showers is named *double bang*. If the tau energy is too low, the two showers can become indistinguishable.

A summary of the different neutrino signatures is presented Table 1.2.

Table 1.2.: Detector signatures for different neutrino interaction. Every particle symbol is written without taking into consideration particle or anti-particle.

Interaction	Particle signature		Detector signature
ν_μ CC	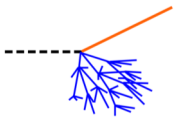	hadronic shower and μ track	track-like
ν_τ CC	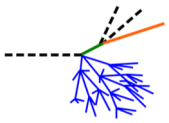	hadronic shower and μ track ($\tau \rightarrow \mu + \nu_\mu + \nu_\tau$)	
	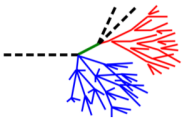	hadronic and EM shower ($\tau \rightarrow e + \nu_e + \nu_\tau$)	shower-like
	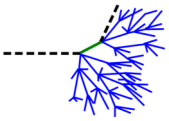	hadronic shower ($\tau \rightarrow$ hadrons)	
ν_e CC	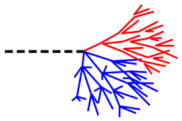	hadronic and EM shower	
ν NC	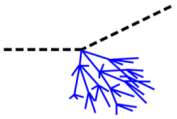	hadronic shower	

1B.2. Experimental setup of KM3NeT

KM3NeT (Kilometer-Cube Neutrino Telescope) is a European research infrastructure designed mainly for the detection and study of neutrinos [40]. It consists of two Cherenkov detectors distributed on two sites deep in the Mediterranean Sea. The feasibility of a deep sea neutrino detector was demonstrated by the first-generation neutrino telescope ANTARES [41]. ANTARES was operating for 15 years and its dismantlement took place in February 2022, of which I took an active part.

KM3NeT follows a modular design. A Digital Optical Modules (DOM) consists of a sphere hosting 31 photo-multiplier tubes (PMTs). The DOM design is further described in subsection 1B.2.1. A Detection Unit (DU) is a vertical line comprised of 18 DOMs. Multiple DUs are installed inside the sea to build the 3D array of photosensors. A building block is the name given to 115 DUs. More details on the layout of the DUs and building blocks is given in subsection 1B.2.2 The KM3NeT detectors are currently under construction, but the modular design allows for data taking to have started with partial detectors.

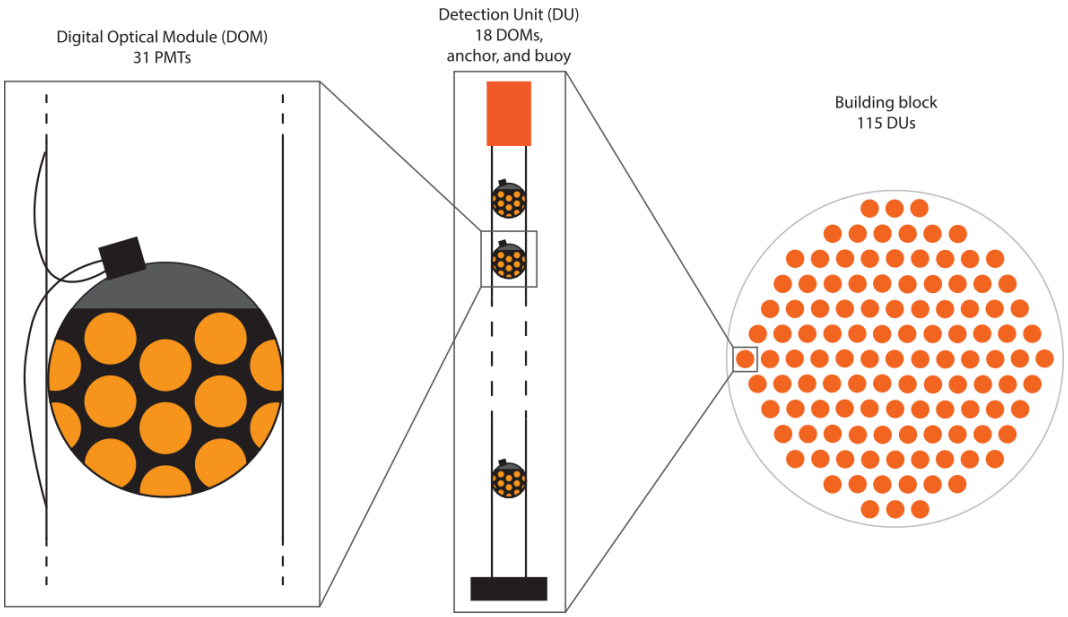

Figure 1.17.: Schematic of the KM3NeT detector layout at different scales. [42]

1B.2.1. The multi-PMT Digital Optical Module

The Digital Optical Module (DOM) is a pressure-resistant glass sphere. Inside are distributed 31 photo-multipliers (PMTs), calibration instruments and embedded electronics for power and data acquisition. A picture and 3D render of a DOM are presented Figure 1.18. A complete description of all elements inside the DOM, as well as design considerations and productions details is done in [43].



Figure 1.18.: Picture of an upside-down DOM (left) and DOM schematic (right) with a cutout showing the internal electronics. [43]

PMTs are 3 inch in diameter and are spread such as 19 PMTs are in the downward facing hemisphere and 12 PMTs are in the upward facing one. The PMT segmentation allows for a higher photocathode area and better photon counting compared to a single bigger PMT. The impact of a single PMT failure is also reduced. Furthermore, the multi-PMT design enables the rejection of environmental background (subsection 1B.2.3) and the detection of neutrino energies down to the tens of MeV (CCSN chapter).

A series of calibration instrument is also present inside the DOM. Accelerometers provide tilt, pitch and yaw to measure the DOM orientation. An acoustic system is used to measure the DOM positions. Triangulation is made with piezoelectric acoustic sensors at the bottom of each DOMs and acoustic emitters disposed at the seabed. Finally, each DOM contains a LED pulser called

nanobeacon. The nanobeacon emits fast light pulses during calibration runs for time calibration of neighbor DOMs.

The power and electronics boards are located in the top part of the DOM. They are attached to a mushroom-shaped aluminum structure which dissipates heat into the sea at the top of the DOM. DOMs are connected together with so-called vertical electro-optical cables (VEOCs) [44]. The VEOC connects to the top of the DOM through a pressure-resistant breakout box. VEOCs are polyethylene tubes containing two copper wires for power and optical fiber for data. They are filled with mineral oil to balance the inside pressure with the one present in the sea. As such, the cable does not need a thick sheath. The resulting VEOC diameter is only 6 mm, thus reducing the overall weight.

1B.2.2. Detectors layouts

The structural connection between the DOMs is assured by synthetic Dynema ropes. The ropes are attached on each side of the DOM with a titanium collar enclosing the glass sphere. The lowest DOM is attached to an anchor resting on the seabed. A buoy is attached to the top of the DU to ensure the verticality.

By varying distances between DOMs and between DUs on the seabed, multiple neutrino energy ranges can be explored. KM3NeT is made of two detectors with two different geometries. KM3NeT/ARCA is the sparser detector and aims to instrument a kilometer-cube of water for the study of TeV neutrinos and above. KM3NeT/ORCA is more dense to optimize the detection of neutrinos in the GeV to TeV energy range. A representation of both ARCA and ORCA to scale can be seen Figure 1.19. The Eiffel and Pisa tower are added to get a sense of scale.

KM3NeT/ARCA is located around 100 km offshore Portopalo di Capo Passero, at the southeast of Sicily, Italy. Once the construction of the two building blocks planned is finished, around 1 km^3 (or 1 Gton) of seawater will be instrumented. Each anchor rests at a depth of 3500 m and is spaced horizontally 36 m from each other. Every DOM is spaced 90 m from each other, with the lowest one 70 m above the seabed. ARCA is optimized for the detection of neutrinos with energy above hundreds of TeV. Its main science goal is the discovery of neutrino sources, notably thanks to its excellent angular resolution [42]. The location (called KM3NeT-It) and layout of the 230 DUs of ARCA are shown Figure 1.20.

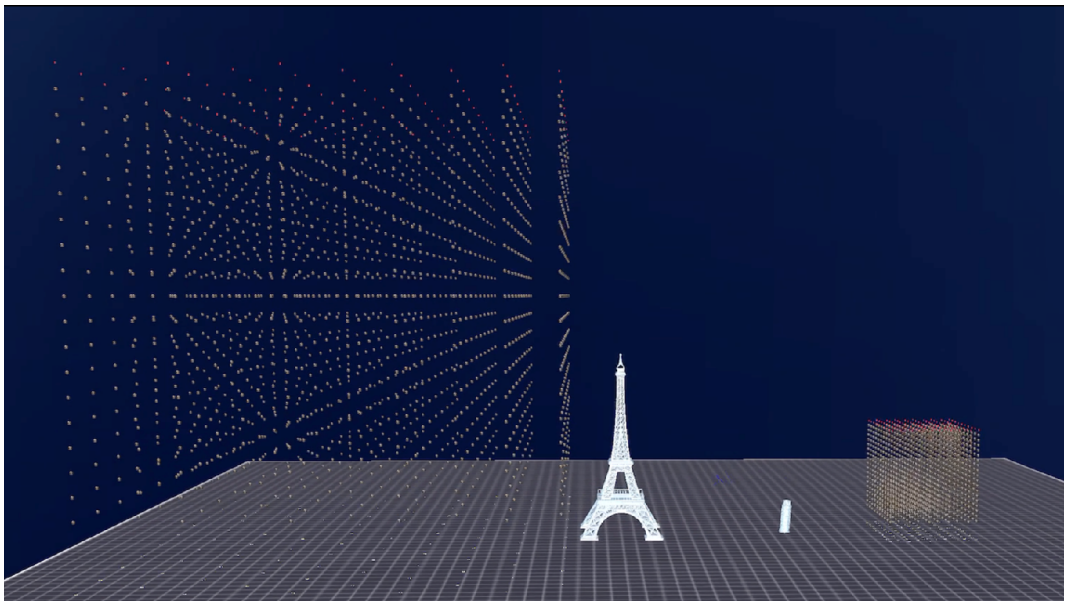

Figure 1.19.: 3D representation of the ARCA (most left) and ORCA (most right). The Eiffel and Pisa tower are added to show a sense of scale. [45]

KM3NeT/ORCA is located 40 km south from Toulon, France. The site is 10 km west of the former location of the ANTARES telescope, at a depth of 2450 m. ORCA is more densely instrumented with DOMs distributed 20 m horizontally and 9 m vertically from each other. The lowest modules are positioned around 9 m above the seabed. Overall, the total volume of ORCA will be around 7 Mton with one building block. The geometry of ORCA is optimized for neutrinos in the 1–100 GeV energy range. At this energy range, most neutrinos come from the interaction of cosmic rays with the atmosphere. Atmospheric neutrinos can be used to study the oscillation phenomenon. The main science goal of ORCA is the determination of the neutrino mass hierarchy. However, ORCA can also be used for astronomy studies, as demonstrated by [46] and [47]. Figure 1.21 shows the location of the ANTARES and KM3NeT/ORCA detectors (KM3NeT-Fr site) as well as the planned layout of the 115 DUs.

Overall, the two KM3NeT detectors can probe a wide range of neutrino energy, from the tens of MeV to PeV. In addition to the two main science goals described above, a rich variety of physics domains can be probed. Some examples are given in the following. Cosmic rays can be studied through the produced muons reaching the detector [48]. Beyond standard model physics can be inquired as well by searching for irregularities in oscillation

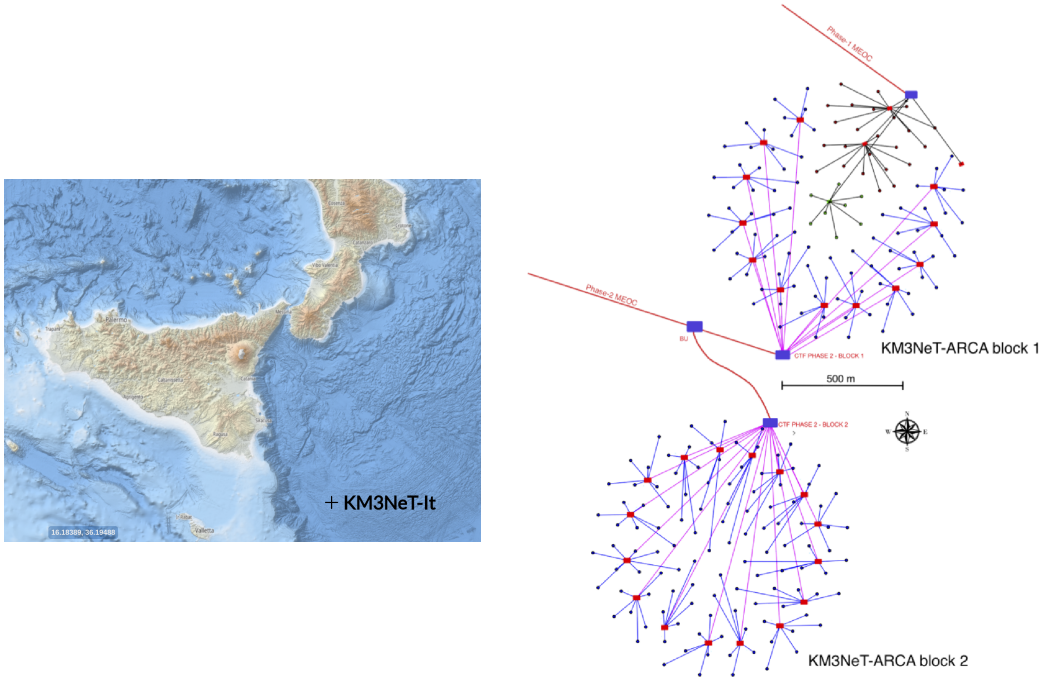

Figure 1.20.: Location of the KM3NeT/ARCA location (left) and KM3NeT/ARCA seafloor layout (right).

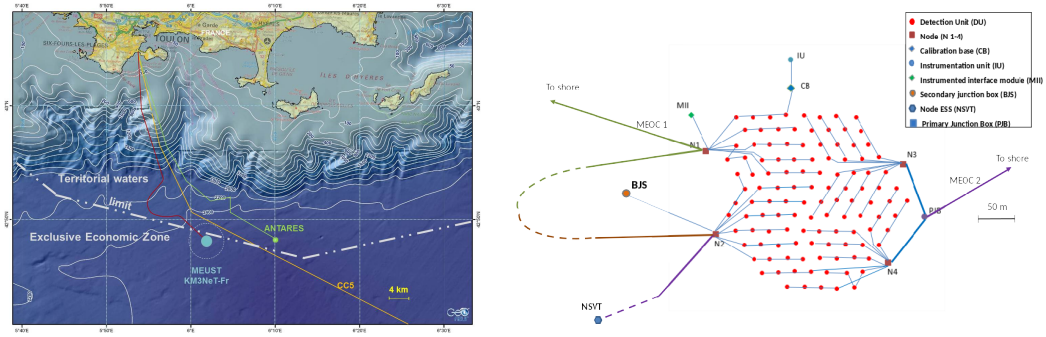

Figure 1.21.: Location of the KM3NeT/ORCA location (left) and KM3NeT/ORCA seafloor layout (right).

patterns [49]. It is also possible to indirectly search for dark matter by looking for an excess of neutrinos near dark matter reservoir, like the Sun or the Galactic Center [50].

1B.2.3. Background to the neutrino detection

Multiple phenomena can cause light emissions which can act as a background to the neutrino detection.

Two background sources are specific to using the seawater as detection medium: radioactive decay of salt and bioluminescence. The majority of photons measured by the PMTs comes from the decay of ^{40}K isotopes which are present naturally in the salt. Electrons and gamma are produced respectively *via* β-decay and electron capture and induce light. Radioactivity causes a constant background in every PMT with a hit rate of about 7 kHz. Bioluminescence is the emission of light by living organisms. In the sea, it is distributed over a range of organisms, from bacteria to fish. The amount of emitted light depends on the seasons and the sea current. Bioluminescence can lead to localized increases up to the MHz range. However, filtering those two background sources is relatively easy thanks to the DOM design. The light emission from radioactivity is very localized. Bioluminescence is non-coherent. As such, it is possible to only select light detected by multiple PMTs or even multiple DOMs in a very short window of time. In order to not saturate the data acquisition system, PMTs with rates above 20 kHz are vetoed.

When cosmic rays interact with the atmosphere, muons are produced and propagate towards the Earth surface. Building the detectors deep in the sea reduces the muon flux compared to the surface, but the majority of events registered comes from atmospheric muons. The muons look identical to the one produced by neutrino interaction. As such, they completely erase all muon neutrino detection possibilities. However, atmospheric muons cannot propagate through the Earth, whereas neutrinos can. Figure 1.22 illustrates this: for $\cos\theta < 1$, that is for events coming from below the horizon, the atmospheric muon flux is null and the neutrino on is not. Selecting up-going or horizontal muons is thus a effective way to select neutrinos. Some down-going atmospheric muons can nevertheless be mis-reconstructed as up-going ones, and still play a part in this background.

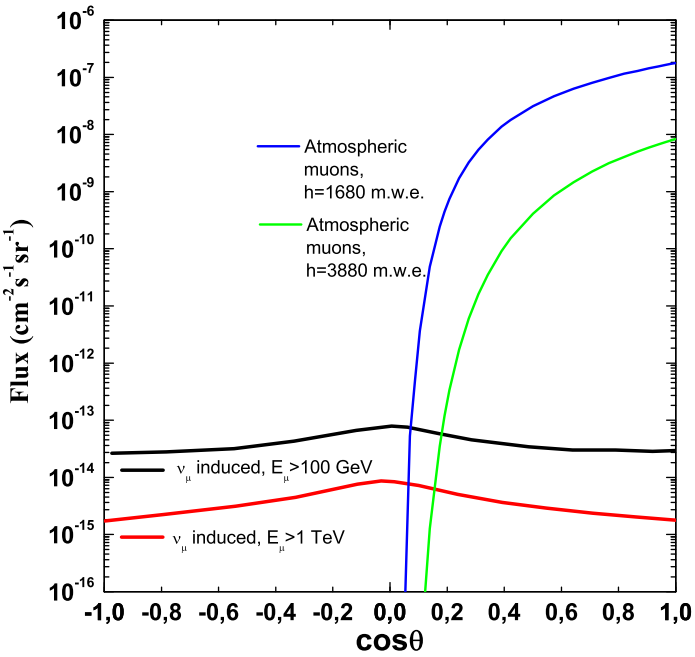

Figure 1.22.: Flux as a function of the zenith angle for atmospheric muons at different depths and neutrinos at different energies. [51]

1B.2.4. Description of the data acquisition software

KM3NeT follows the *all-data-to-shore* data acquisition (DAQ) concept. Once the PMT signal is digitized, no data reduction is made at the DOM level and all data is sent to be processed.

Inside a DOM, a hit is defined as a PMT voltage raising above a given threshold. The threshold is tuned to have an amplitude equivalent of 0.3 photoelectrons. The crossing time of the threshold and the time-over-threshold (ToT) of the pulse digitized with nanosecond accuracy. All hits are grouped in segments of 100 ms called *timeslices* and sent to shore. The nanosecond accuracy is ensured by the White Rabbit protocol. Additionally, acoustic data is transmitted for positioning.

The KM3NeT *Trigger and Data Acquisition System* (TriDAS) runs on each shore station to process the hit data. All incoming optical data is collected by the *data queue*. The data queue distributes the data to an array of *data filters*. The data filters select specific sets of hits depending on their topology, in order to select only physics events. The selected filtered events are called *triggered events*. The filtered data is sent to a common data dispatcher server (also called Control Host server). The *data writer* subscribes to the dispatcher to

retrieve the event and write them to disk. The operation is orchestrated by the *Control Unit*, a software responsible for assuring the communication between all the detector components, the TriDAS modules and the KM3NeT central database. An overview of the TriDAS components is presented Figure 1.23.

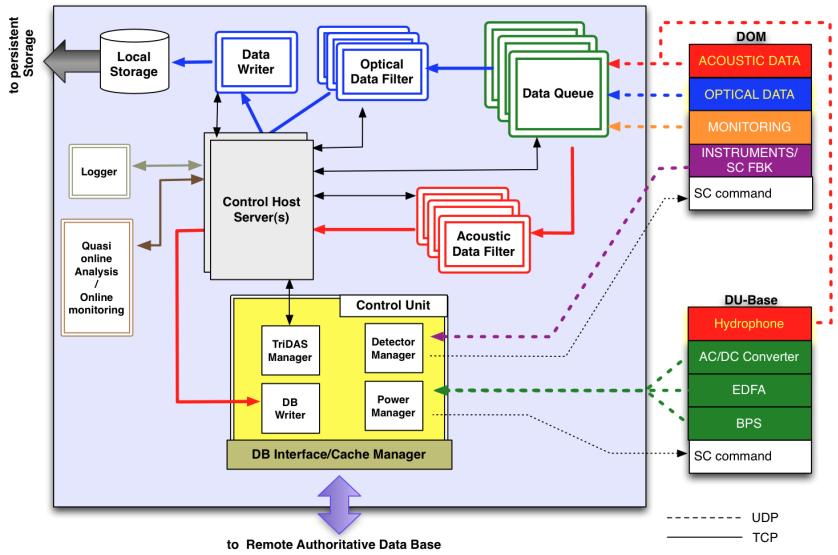

Figure 1.23.: Diagram of the KM3NeT Trigger and Data Acquisition System (TriDAS). [52]

The data filtering happens in multiple steps. Hits are first filtered to build coincidences within single DOMs. The following coincidences are defined:

- L0 hits are simply the hits measured by individual PMTs;
- L1 coincidences are L0 hits which are inside a 25 ns time window;
- L2 coincidences are L0 hits which are within 10 ns, on at least two different PMTs and whose PMTs are within 90 ° of each other.

From the built coincidence, the triggered events are made to select causally connected hits or coincidences. Hits are causally connected if they respect the relation

$$|\Delta T| < \frac{|\Delta r|}{c/n} + T_{extra} \tag{1.18}$$

where ΔT and Δr are respectively the time difference and distance between hits or coincidences. Indeed, two photons emitted from a same source and

propagating at a velocity c/n would follow this relation. T_{extra} is an additional time window to account for the delay due to photon scattering.

Three trigger criteria are used with the KM3NeT detectors, each optimized for a given event topology. The trigger algorithms run in parallel, so a same physics event can be tagged by multiple triggers.

3D muon The trigger aims to detect track-like events from propagating muons. The following is required:

- a minimum number of causally connected L2 coincidences on a minimum number of DOMs (5 and 5 for ARCA21);
- all within a maximum distance (820 m for ARCA21);
- all within an infinite cylinder of a given diameter (120 m for ARCA21).

A scan is performed to test for all possible cylinder directions with a given granularity.

3D shower The trigger aims to detect shower-like events. The spacing between DOMs is bigger for both detectors than the distance of the light propagation. As such, showers can be considered as point which emit light isotropically from the neutrino interaction. The trigger requires the following:

- a minimum number of causally connected L2 coincidences on a minimum number of DOMs (5 and 5 for ARCA21);
- all within a sphere of a given diameter (250 m for ARCA21).

MX shower This trigger aims to relax the condition of the the 3D shower trigger to lower the sensitivity to showers. The requirement is:

- a minimum number of L0 hits causally connected to a single L2 coincidence;
- all within a sphere of a given diameter.

In addition to the triggered events, a summary of the detector state is also built in slices of 100 ms. The triggered events, summary slices and a subset of L2 coincidences (for CCSN real-time search) are transmitted to the DAQ dispatcher to be written and stored. Online analyses like real-time event reconstruction can subscribe to the dispatcher to receive the data in parallel.

1B.2.5. Event reconstruction

Event reconstruction is either done in real-time within the online analyses, or performed later with refined calibration data in a processing server farm. Reconstruction algorithms are designed assuming a specific topology, but all triggered events are reconstructed with all algorithms [53].

Track reconstruction aims to estimate the direction and energy of ultra-relativistic muons. The muon propagation can be approximated as a straight line. It is described by five independent parameters: muon position associated with a given time, plus the propagation direction of the muon.

The first step of the direction reconstruction algorithm is a set of pre-fits. For an equal distribution of direction, a χ^2 test is made to compare the measured and expected arrival time of photons on the DOMs. In those tests, a condition on causal connection between hits is added to reduce the bias from optical background. A subset of those directions is ranked by quality and used as starting value for the reconstruction. The direction reconstruction itself is a maximum likelihood search starting from the subset of directions tested. The probability density function is estimated semi-analytically.

The energy estimator relies on the output of the direction reconstruction. It uses the spatial distribution of presence and absence of hits on PMTs within a given cylinder around the muon trajectory.

Shower reconstruction also follows two steps: the estimation of the neutrino interaction vertex followed by the estimation of direction and energy.

The vertex estimation is built from a so-called *M-estimator*. The M-estimator score function contains the measured hit times and the expected hit times assuming a spherical wavefront. The vertex position is found by minimizing the M-estimator starting from the hits center of gravity.

The energy and direction shower reconstruction is made from the presence and absence of PMTs and a log-likelihood estimator using the Poisson probabity of a non-hit on the given PMTs.

The performance of those reconstruction algorithms is presented Figure 1.24 for the full KM3NeT/ARCA detector. For tracks, the angular resolution should go lower than 0.1 ° for 100 TeV and above. For showers, the median angular resolution would be around 1.5 ° with an energy uncertainty between 5 and 10 %.

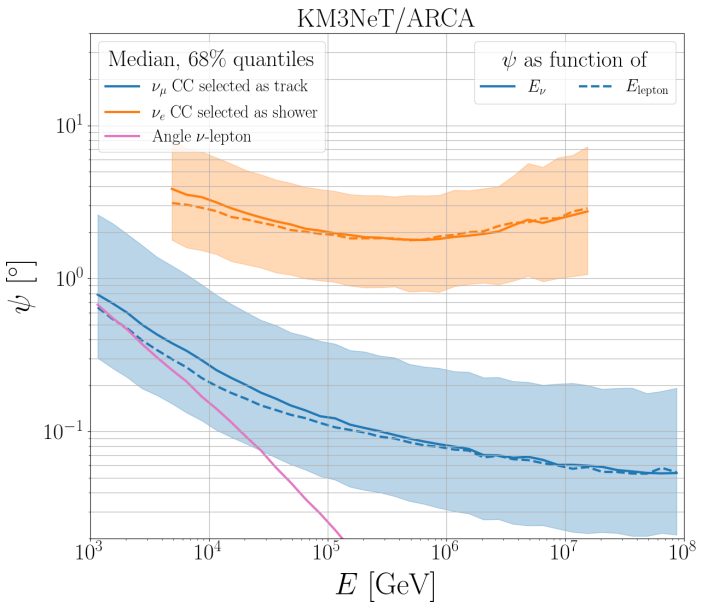

Figure 1.24.: KM3NeT/ARCA angular resolution for ν_μ CC events selected as track and for ν_e CC events selected as shower for 230 DUs.

1B.2.6. Past and current status of the KM3NeT detectors

The first DUs of the ARCA and ORCA detectors were respectively deployed in December 2015 and September 2017. At the beginning of my PhD, in October 2021 (left plots of Figure 1.25), 9 ARCA DUs and 6 ORCA DUs were deployed. At the time of writing, both detectors have grown more than three times their size, with 32 and 24 DUs respectively. The completion of all three building blocks is currently planned for 2028. But the growing detectors have already good detection capabilities and can be used to perform numerous analyses.

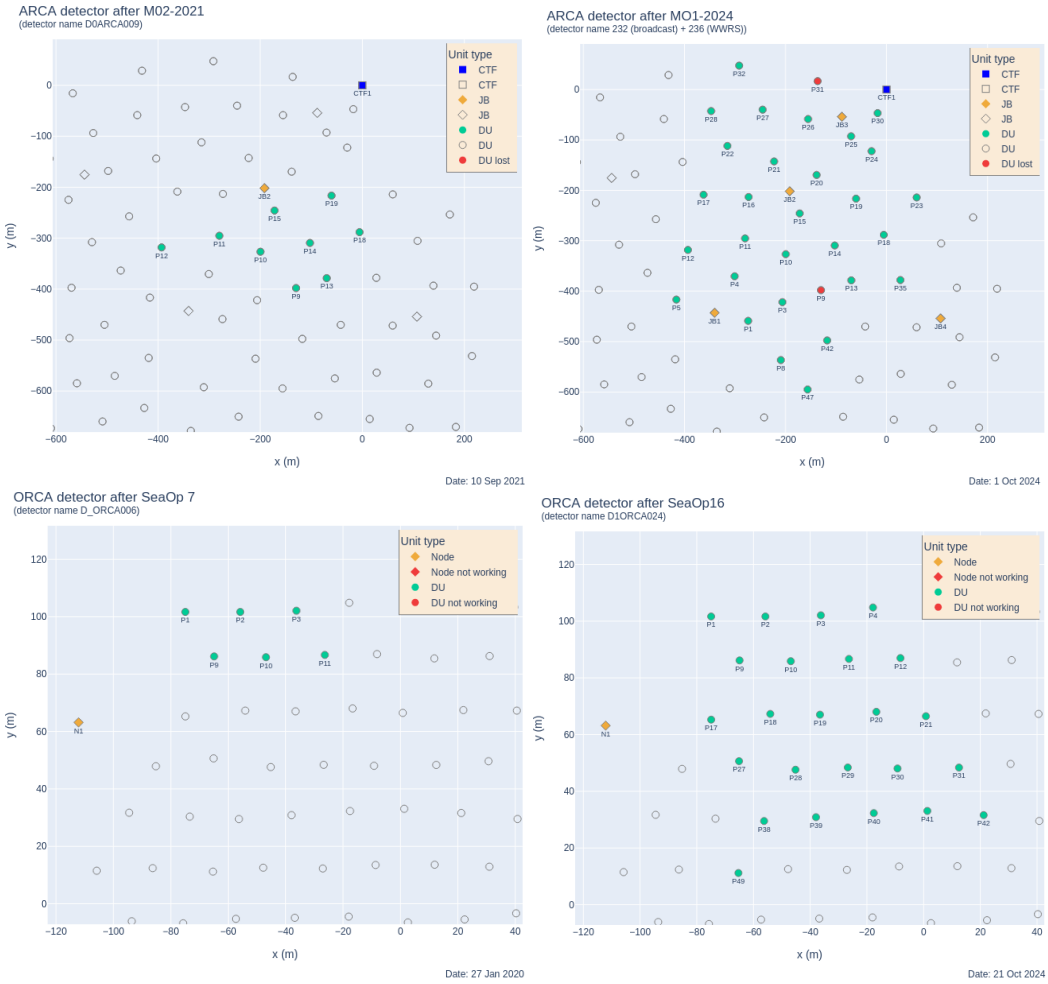

Figure 1.25.: Detector footprint with deployed DUs at a given date. Top figures show KM3NeT/ARCA and bottom figures show KM3NeT/ORCA. The footprint on the left correspond to October 2021 and the ones on the right to October 2024.

Chapter 2.

Real-time detection of neutrinos from a core-collapse supernova

Introduction

This chapter presents the KM3NeT detection capabilities for a core-collapse supernova (CCSN) neutrino burst, the implementation of the CCSN online and real-time pipeline and the searches for neutrino counterparts to two types of events.

KM3Net is able to detect the electron anti-neutrinos emitted in the MeV energy range by collapsing stars at the end of their lives, also called CCSN. The origin and detection strategy of CCSN neutrinos is described section 2A. The combination of the detectors is sensitive to a Galactic event, estimated to happen once per century. A fast and automatic system is needed to ensure its detection.

The KM3NeT CCSN online pipeline aims to achieve this, among other functions. The system went from a prototype on one detector to a working system on both detectors, with proper background characterization. Additional functions such as the automatic retrieval of data with higher statistics (quasi-online pipeline) and the automatic search for counterparts to external triggers were developed from scratch. The development took place in a complex context of detector construction and data-taking and processing commissioning. The description of the CCSN online pipeline is made section 2B.

Offline searches for MeV neutrino burst were also conducted in parallel of the CCSN online pipeline development. The first analysis was a search for neutrino counterparts to the gravitational waves event of the LIGO/Virgo third observing run. The second analysis was performed on an unexpected and exceptional event: GRB 221009A, the brightest GRB ever recorded. They are both presented section 2C.

Contents

2A. Origin and detection of CCSN neutrinos 63
2A.1. Supernova neutrinos 63
2A.1.1. First observations of supernovae 63
2A.1.2. Supernovae types 64
2A.1.3. Mechanisms of Supernovae 64
2A.1.4. Neutrino emission of core-collapse supernovae 70
2A.1.5. Electromagnetic and gravitational wave emission 73
2A.1.6. Motivations for the real-time detection of CCSN neutrinos 75
2A.2. Detection of MeV neutrinos with KM3NeT 76
2A.2.1. Interaction of MeV neutrinos in water 76
2A.2.2. Detection strategy 77
2A.2.3. Description of the optical background 79
2A.2.4. Optical background filtering 79
2A.2.5. Detection sensitivity 81

2B. The KM3NeT CCSN online pipeline 85
2B.1. Real-time CCSN search pipeline 87
2B.1.1. Coincidence level computation and detector combination 87
2B.1.2. Quality score 88
2B.1.3. Significance computation for constant background . . . 89
2B.1.4. Significance combination 90
2B.1.5. CCSN alerts 91
2B.2. Adaptive background expectation 92
2B.2.1. Previous AB method 93
2B.2.2. New AB method and application to 1.5 year of data . . 95
2B.2.3. Refined AB method with monthly fits 95
2B.2.4. Effect of the refined AB method on the zscore 96
2B.3. Quasi-online pipeline 101
2B.3.1. Goals of the quasi-online pipeline 101
2B.3.2. Implementation of the quasi-online pipeline 102
2B.4. Transmitting data to the SNEWS network 103
2B.4.1. SNEWS 103
2B.4.2. Data transmission 104
2B.5. Triggered follow-up searches 105
2B.5.1. Design of the database 105
2B.5.2. Principle of the search 105
2B.5.3. Significance computation 107
2B.5.4. Results report 108

2C. Searches for MeV neutrino burst counterparts 111
2C.1. GW from LIGO/Virgo O3 111
2C.1.1. The gravitational wave catalogs 111
2C.1.2. Search time window 112
2C.1.3. Run selection 112
2C.1.4. Background characterization 113
2C.1.5. Analysis principle 114
2C.1.6. Results 116
2C.2. GRB 221009A: the Brightest γ-ray burst Of All Times 121
2C.2.1. GRB 221009A 121
2C.2.2. Search method 122
2C.2.3. Results 123

2A. Origin and detection of CCSN neutrinos

2A.1. Supernova neutrinos

Supernovae (SNe) are explosive phenomena ending the life of some massive stars. They release a huge amount of energy in different forms, such as the ejection of matter with very high kinetic energy (up to 10^{51} erg) and the emission of neutrinos. Their peak luminosity reaches the same order of magnitude as entire galaxies. Supernovae are known to be facilities producing heavy elements that are essential in a lot of chemical processes, including life.

2A.1.1. First observations of supernovae

Supernovae that have exploded in our Galaxy have been documented throughout history [54]. Between the 2nd and 11th century of the current era, Chinese astronomers reported objects suddenly appearing in the sky and dimming away after some time, naming them "guest stars" (Chinese: 客星; pinyin: kèxīng). The brightest supernova ever recorded has been observed in 1006 by cultures all over the globe. Its brightness reached one-quarter of the brightness of the Moon, according to the Egyptian astronomer Ali ibn Ridwan. Another widely observed event happened in 1054, where the supernova remained visible for 23 days during daylight and for 653 days during the night. The explosion created the Crab Nebula, which was the first astronomical object identified as the remnant of a historically-recorded supernova. The latest

supernovae that were seen in the Milky Way were in 1572 and 1604. They were studied extensively, respectively by Tycho Brahe and Johannes Kepler. The latter named the phenomenon "*Stella Nova*", Latin for "new star" [55].

2A.1.2. Supernovae types

Thanks to the development of astronomical telescopes, the first extragalactic supernovae were discovered in 1885 in the Andromeda Galaxy and in 1895 in NGC 5253, respectively 0.80 Mpc and 3.15 Mpc away. After these two observations and till the 1940s, supernovae were considered a new category of novae, another transient astronomical event that causes the appearance of a bright new star. The name "supernova" was coined by Walter Baade and Fritz Zwicky during their lectures and in [56]. Zwicky, along with Rudolph Minkowski, organized systematic searches which led to the knowledge of thousands of supernovae. Each observed supernova is labelled by the "SN" prefix followed by the year of discovery and a letter indicating the order of discovery for years with more than one supernova (*e.g.* historical SN185, newly seen SN1987A, etc).

The work of Minkowski and Zwicky led to the modern classification of SNe. They are divided into different types depending on the presence of absorption and emission lines in the spectra at maximum luminosity and the evolution properties of the light curves [57]. A SN is classified as type I if no hydrogen lines are present in the spectrum and as type II otherwise. Further subtypes are described in Table 2.1 and spectra examples of types Ia, Ic, Ib and II can be seen Figure 2.1.

However, the types defined in such way do not reflect the physical mechanisms behind the creation of SNe. Instead, the analysis of the light curves after about a year, once the ejecta becomes optically think, can give information on the elements produced during the explosion. Type Ia SNe show an inner region rich in iron, whereas type Ib, Ic and II all show a similar spectrum with oxygen and carbon emission lines, as seen Figure 2.1. Thermonuclear runaway of carbon-oxygen white dwarfs produce type Ia SNe and collapse of the stellar core gives birth to SNe of type Ib, Ic and II, at it will be discussed below.

2A.1.3. Mechanisms of Supernovae

Thermonuclear supernova Type Ia SNe are due to the thermonuclear runaway of white dwarfs. The stars that are not massive enough to reach the temperatures needed to fuse carbon reach a final state called white dwarf. As

Table 2.1.: Supernova taxonomy as a function of the different properties of the early spectrum. The mechansim of supernova formation is also indicated in the most right column.

<table>
<tr><th colspan="4">SN type</th><th>SN mechanism</th></tr>
<tr><td rowspan="3">Type I
no H</td><td colspan="3">Type Ia
Si II absorption line near peak light</td><td>Thermonuclear runaway</td></tr>
<tr><td rowspan="2">Type Ib/c
weak or no Si</td><td colspan="2">Type Ib
shows He I absorption</td><td rowspan="6">Core collapse</td></tr>
<tr><td colspan="2">Type Ic
weak or no He</td></tr>
<tr><td rowspan="4">Type II
shows H emission lines</td><td colspan="3">Type IIb
spectrum evolves towards Ib</td></tr>
<tr><td rowspan="3">Type IIP/L/n
keeps type II spectrum</td><td colspan="2">Type IIn
shows narrow lines</td></tr>
<tr><td rowspan="2">Type IIP/L
no narrow lines</td><td>Type IIP
presence of a “plateau” in the light curve</td></tr>
<tr><td>Type IIL
linear decrease in magnitude vs time of the light curve</td></tr>
</table>

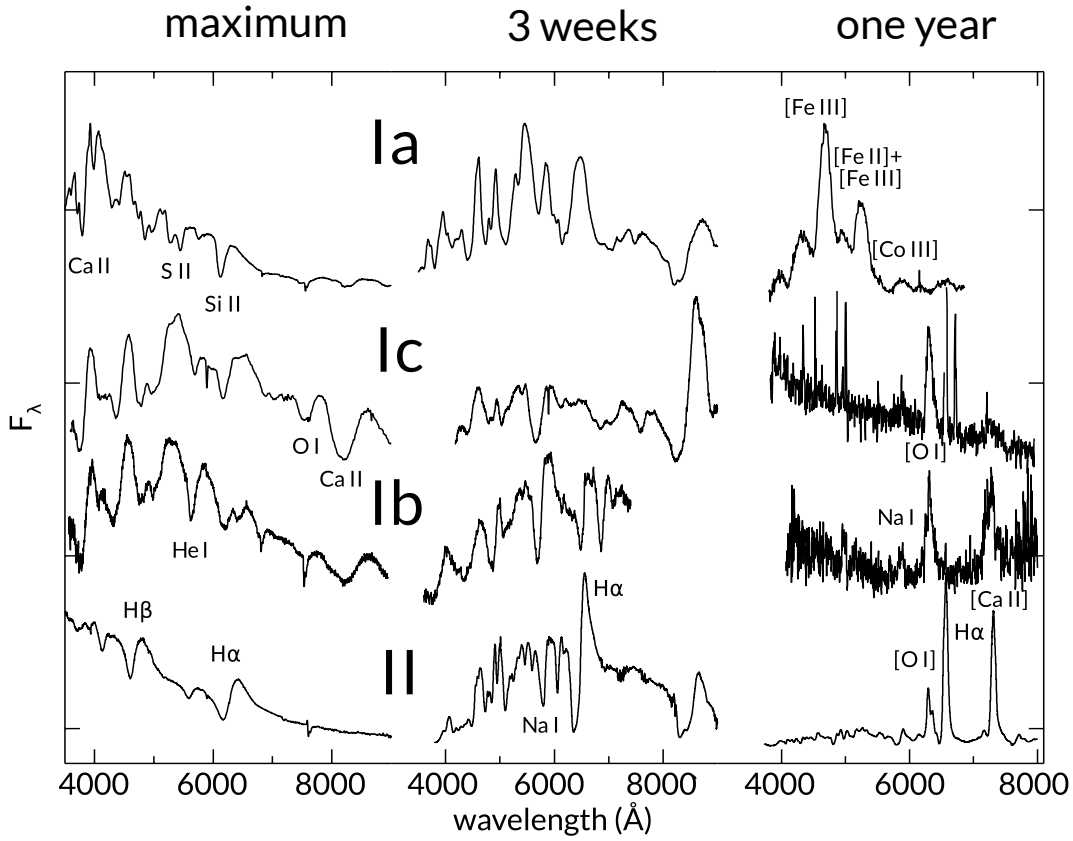

Figure 2.1.: Spectra of the main SN types at maximum, three weeks and one year after maximum luminosity [57].

such, a white dwarf main composition is usually oxygen and carbon, produced in the core by the triple-alpha process ($2\,{}^4\mathrm{He} \rightarrow {}^8\mathrm{Be}$, ${}^4\mathrm{He} + {}^8\mathrm{Be} \rightarrow {}^{12}\mathrm{C}$). As the star no longer produces energy through fusion, pressure from electron degeneracy is the only process ensuring the equilibrium against gravity. The equilibrium is only possible for a star with a mass below $1.4\,\mathrm{M}_\odot$, also known as the Chandrasekhar limit.

If the white dwarf orbits around a companion star, it can accrete matter and gain mass beyond the Chandrasekhar limit. Once the equilibrium is broken, the star begins to collapse. The core reaches a density high enough to start the fusion of carbon and oxygen to heavy nuclei. The released energy causes the thermonuclear explosion of the star, which expands to a nebula without a central compact object. Silicon is one of the products of carbon and oxygen fusion. Its absorption line is thus visible at maximum luminosity in Figure 2.1. The iron emission lines that can be seen after some months come from the ${}^{56}\mathrm{Ni} \rightarrow {}^{56}\mathrm{Co} \rightarrow {}^{56}\mathrm{Fe}$ nuclear decay chain.

Because of the constraint on the maximum mass of a white dwarf, type Ia SNe all show similar physical properties. In particular, Phillips discovered in 1993 [58] that the duration of the maximum light is correlated with the total luminosity. This makes type Ia SNe great standard candles for the measurement of cosmological distances. The Hubble Space Telescope was notably used with this method to measure the Hubble constant and discover the acceleration of the Universe expansion [59]. Systematic ground surveys like the Sloan Digital Sky Survey (SDSS) [60] and the Supernova Legacy Survey (SNLS) [61] further refined the measurement.

Contrary to core-collapse supernovae, the neutrino emission of thermonuclear supernovae is too low to be detected, even for close objects.

Core-collapse supernova Type Ib, Ic and II SNe are caused by the core-collapse of giant stars with a mass above 8–9 solar masses. A massive star from the main sequence goes through different stages of fusion (hydrogen, helium, carbon, neon, oxygen and silicon). The final stage from nuclear fusion is iron, as the synthesis of heavier elements does not produce energy. Those different elements organize from easier to fuse in the surface to harder to fuse in the core in an onion-like structure. The star structure is ensured by the equilibrium between gravity and the fusion processes.

Inside the iron core, the equilibrium is assured by the electron degeneracy pressure. The core has a mass of around $1\,\mathrm{M}_\odot$, a radius of about 10^3 km, a density in the order of $10^{10}\,\mathrm{g\,cm^{-3}}$ and a kinetic energy of around 1 MeV. Such

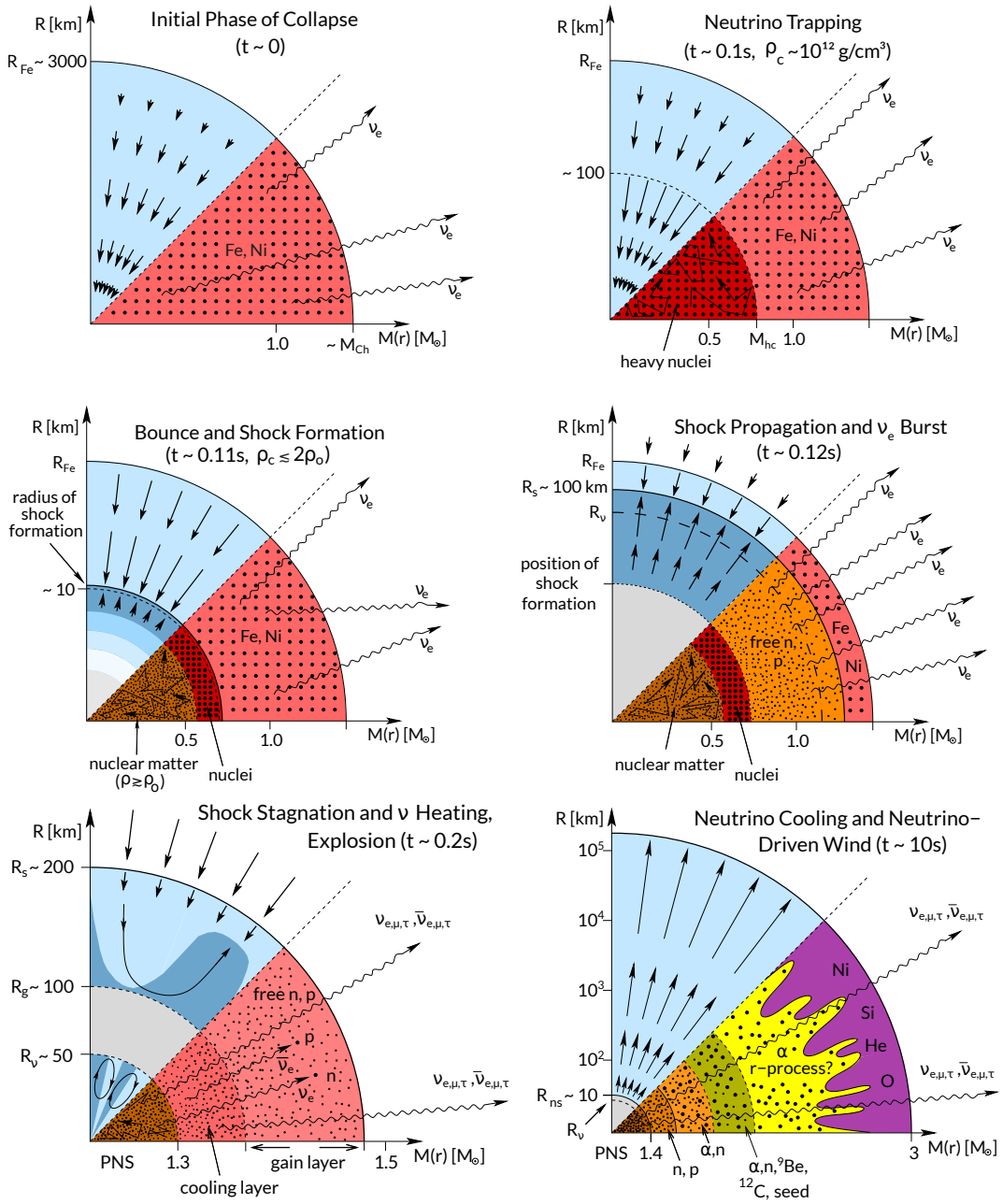

Figure 2.2.: The six phases of neutrino productions (from top left to bottom) [62]. Pointing arrows indicate respectively contraction and collapse and expansion or mass ejection. The radial distances R are indicated on the vertical axes and the corresponding enclosed masses M(r) are given on the horizontal axis.

extreme environment makes possible the photodissociation of iron

$$\gamma + {}^{56}\mathrm{Fe} \rightarrow 13\alpha + 4n, \tag{2.1}$$

which reduces the kinetic energy and thus pressure of the electrons. In addition, the high kinetic energy of electrons enables electron capture of free protons and nuclei,

$$e^- + p \rightarrow n + \nu_e, \tag{2.2}$$

$$e^- + \mathrm{N(Z,A)} \rightarrow \mathrm{N(Z-1,A)} + \nu_e, \tag{2.3}$$

which further reduces the electron degeneracy pressure. Once the electron pressure cannot compensate the gravitational pull, the collapse starts. The density inside the core increases which boosts the photodissociation and electron capture rates, lowering the electron pressure and rising the density in return. Such feedback loop accelerates the collapse. Initially, the produced neutrinos are able to escape the star freely. This is the initial phase of collapse, visible in the top left part of Figure 2.2.

Once the density of the inner core reaches around $3 \times 10^{11}\,\mathrm{g\,cm^{-3}}$, the neutrinos can no longer freely escape. The area dividing where the neutrinos can and cannot escape is called the *neutrinosphere*. Inside the neutrinosphere, the lepton number remains constant thus making matter in the inner core collapse in a subsonic and homologous (speed proportional to radius) manner. The matter in the outer core keeps falling in supersonic free-fall. This process, called neutrino trapping phase and shown in the top right part of Figure 2.2, lasts around 0.1 s.

When the inner density reaches nuclear density (about $10^{14}\,\mathrm{g\,cm^{-3}}$), the collapse is stopped abruptly. The pressure of the degenerate nucleons ensures the equilibrium against gravity and a proto-neutron star (PNS) is formed. The matter from the outer core, which falls at supersonic velocity, bounces against the surface of the PNS. A supersonic shock wave is created and is propagated outward through the outer iron core. The bounce and shock formation can be seen in the middle left part of Figure 2.2.

When free-falling matter encounters the shock wave, it decelerates and accretes around the PNS. Behind the shock wave, nuclei dissipate energy *via* photodissociation leaving mostly nucleons. Free protons capture electrons and produce electron neutrinos, which pile up at the shock. When the shock has sufficiently propagated to decrease matter density to $10^{11}\,\mathrm{g\,cm^{-3}}$, the neutrinos are all released in a few milliseconds. This process is called prompt electron neutrino burst and is drawn in the middle right part of Figure 2.2.

A lot of energy is dissipated during the last process. The photodissociation of nuclei and neutrino emission dissipates a lot of energy (10^{51} erg for each $0.1\,M_\odot$ of photodissociated matter), which weakens the shock. If the star has a mass over $10\,M_\odot$, the shock does not reach the outer parts of the star. This stalls the explosion and matter continues to fall towards the PNS. If the degenerate nucleons pressure is not high enough to stop the falling matter, the core collapses into a black-hole, stopping the supernova. Multiple mechanisms have been proposed to explain the revival of the shock propagation leading to the explosion. The most commonly accepted one is the energy deposition induced by the neutrino flux produced thermally. Those neutrinos are produced *via* thermal emission behind the shock, from matter falling and accreting around the PNS. This phase, called accretion phase, leads to the explosion taking place about 0.5 s after the bounce. The diagram in the bottom left part of Figure 2.2 illustrates the shock stagnation, neutrino heating and start of the explosion.

The different classification of core-collapse supernovae (CCSN), shown in Table 2.1, are due to the diversity of initial mass and metallicity of the progenitor. During the collapse, the high density leads to the nucleosynthesis of many heavy nuclei, which are expelled during the explosion, as visible in the bottom right part of Figure 2.2. This explains the emission lines of heavy nuclei that are shared between SNe of types Ib, Ic and II in Figure 2.1.

2A.1.4. Neutrino emission of core-collapse supernovae

A core-collapse supernova is one of the most energetic phenomenon of the Universe. The released gravitational energy is about 3×10^{53} erg in each supernova, of which 99 % is released as neutrinos, 1 % as the kinetic energy of expelled matter and 0.01 % as electromagnetic radiation. During the core-collapse, most of the emission of neutrinos happens in three phases [63]: the prompt electron neutrino burst, the accretion phase and the cooling phase. The neutrino luminosity is defined as the energy released per unit time in the neutrino form. It is shown as a function of time in Figure 2.3 where the three phases are visible.

Prompt ν_e burst The prompt electron neutrino burst happens a few ms after the bounce and lasts a few ms as well. Electron neutrino are produced through electron capture (Equation 2.2) during the neutrino trapping phase and pile-up behind the shock propagation. Once the density of the medium becomes sparse enough to become transparent, the neutrinos are released in a few

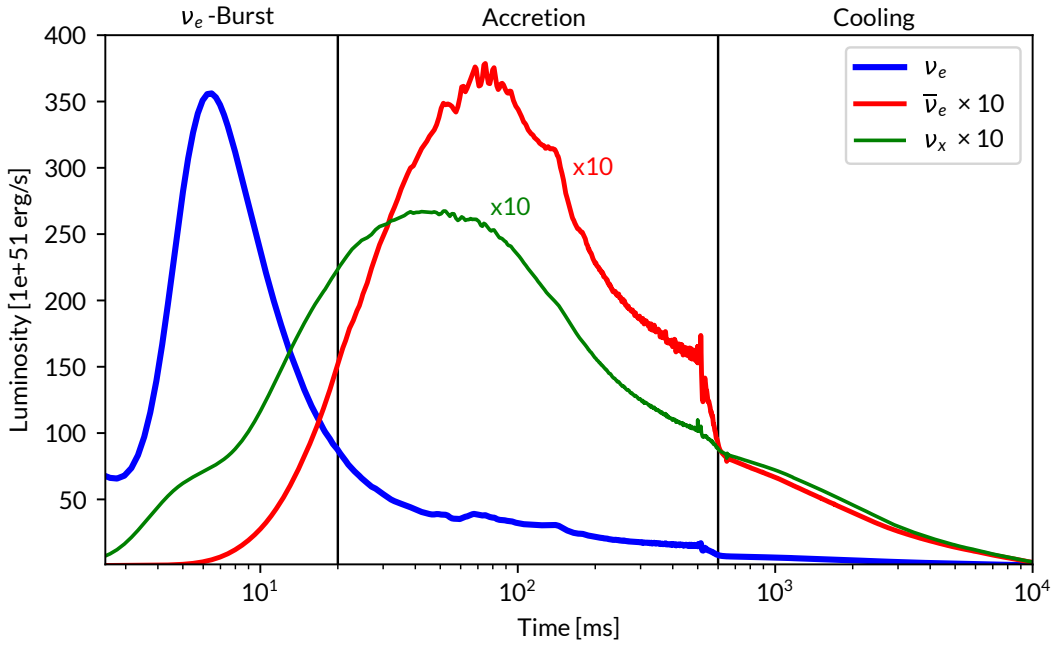

Figure 2.3.: Phases of emission in a typical CCSN [63]. The luminosity for $\bar{\nu}_e$ and ν_x is scaled up.

ms. The neutrino luminosity of the prompt burst reaches 3.5×10^{53} erg/s and dissipates a few 10^{51} erg.

Accretion Modern simulations show that during the accretion phase, neutrinos are emitted between 10 ms and 500 ms after the collapse. Neutrinos of all flavors are emitted by matter accreting around the PNS. The nuclei photodissociate and leave behind free protons. Both charged current (producing ν_e and $\bar{\nu}_e$) and thermal (producing all flavors of neutrinos) processes are involved with the neutrino production. Along with electron capture described in Equation 2.2, the main processes are:

$$\text{positron capture,} \quad e^+ + n \rightarrow p + \bar{\nu}_e, \tag{2.4}$$
$$\text{electron-positron pair annihilation,} \quad e^- + e^+ \rightarrow \nu + \bar{\nu}, \tag{2.5}$$
$$\text{electron-nucleon bremsstrahlung,} \quad e^\pm + \mathrm{N} \rightarrow e^\pm + \mathrm{N} + \nu + \bar{\nu}, \tag{2.6}$$
$$\text{nucleon-nucleon bremsstrahlung,} \quad \mathrm{N} + \mathrm{N} \rightarrow \mathrm{N} + \mathrm{N} + \nu + \bar{\nu}, \tag{2.7}$$
$$\text{plasmon decay,} \quad \gamma \rightarrow \nu + \bar{\nu}, \tag{2.8}$$
$$\text{and photoannihilation,} \quad \gamma + e^\pm \rightarrow e^\pm + \nu + \bar{\nu}, \tag{2.9}$$

with N being free nucleons and ν and $\bar{\nu}$ representing respectively neutrinos and antineutrinos of all flavors.

Cooling The accretion stops about 500ms after the bounce. The proto-neutron star keeps emitting neutrinos of all flavors until all the remaining gravitational energy is dissipated.

Three different neutrino luminosities curves can be seen Figure 2.3: one for ν_e, one for $\bar{\nu}_e$ and a common one for $(\nu, \bar{\nu})_{\mu,\tau}$ written as ν_x. The collapsing star is composed of protons, neutrons and electrons. The production of muons and taus is forbidden due to the energy of the produced neutrinos, in the order of the tens of MeV. Therefore, electron neutrinos and electron antineutrinos can interact both through charged current and neutral current processes, whereas the ν_x only interact through neutral current processes. As particles and antiparticles, for all flavors, interact identically through neutral current but not through charged current, all ν_x behave the same, while ν_e and $\bar{\nu}_e$ have independent behaviors.

The expected neutrino energy distribution f is flavor- and time-dependent but can be always approximated as a "pinched" thermal distribution [62],

$$f(E, \langle E \rangle, \alpha) = \left(\frac{1+\alpha}{\langle E \rangle}\right)^{1+\alpha} \frac{E^\alpha}{\Gamma(1+\alpha)} \exp\left(-(1+\alpha)\frac{E}{\langle E \rangle}\right), \tag{2.10}$$

where E is the neutrino energy, $\langle E \rangle$ the mean neutrino energy (we have $\langle E \rangle = \int f(E) E dE$), α the spectral shape (or pinching) parameter and Γ the Euler gamma function. The spectral shape parameter α is derived from the mean neutrino energy $\langle E \rangle$ and the energy variance Var(E) such as:

$$1 + \alpha = \frac{\langle E \rangle^2}{\mathrm{Var}(E)}. \tag{2.11}$$

Compared to a Maxwell-Boltzmann distribution ($\alpha = 2$) or a Fermi-Dirac distribution ($\alpha \approx 2.3$ for a null chemical potential), a higher spectral shape parameter will lead to a "pinched" spectrum with reduced contribution from low and high energies. This can be seen Figure 2.4, where spectra from electron antineutrinos have a narrower width than the associated Fermi-Dirac fits. The shape parameter ranges from $\alpha = 6$–7 for electron neutrinos around the ν_e burst and $\alpha = 2$–3 for all neutrinos starting around 200 ms after the bounce. The "pinched" spectra can be understood from the energy dependence of the neutrino interactions. Low-energy neutrinos have a smaller cross section and can escape at a smaller radius, where the temperature inside the star is higher. On the contrary, high-energy neutrinos escape at a larger radius, where the temperature is lower. This causes a reduction of low- and high-energy neutrinos on both sides of the spectral peak compared to a thermal spectrum

with the same mean energy.

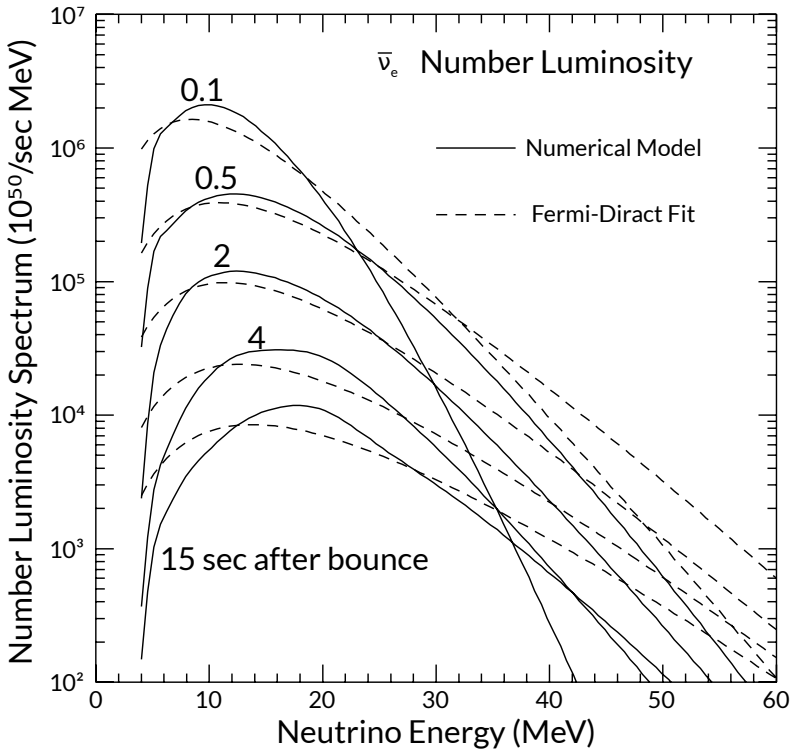

Figure 2.4.: Energy spectrum of $\bar{\nu}_e$ from numerical models [64]. The Fermi-Dirac fits have the same luminosity and average energy than the numerical curves.

The neutrino flux Φ_ν, defined as the rate of neutrinos across a unit area, is approximately isotropic. It can be derived from the neutrino luminosity $\mathrm{L}(t)$ and the distance from the CCSN d, such as

$$\Phi_\nu(\mathrm{E}, t) = \frac{\mathrm{L}(t)}{4\pi d^2} f(\mathrm{E}, \langle \mathrm{E} \rangle(t), \alpha(t)). \tag{2.12}$$

2A.1.5. Electromagnetic and gravitational wave emission

In addition to the emitted neutrinos, two other messengers can be observed to better characterize a CCSN: photons and gravitational waves (GW) [65]. Figure 2.5 is a combined plot showing the luminosity of neutrinos, GW and electromagnetic signals as a function of time after the bounce.

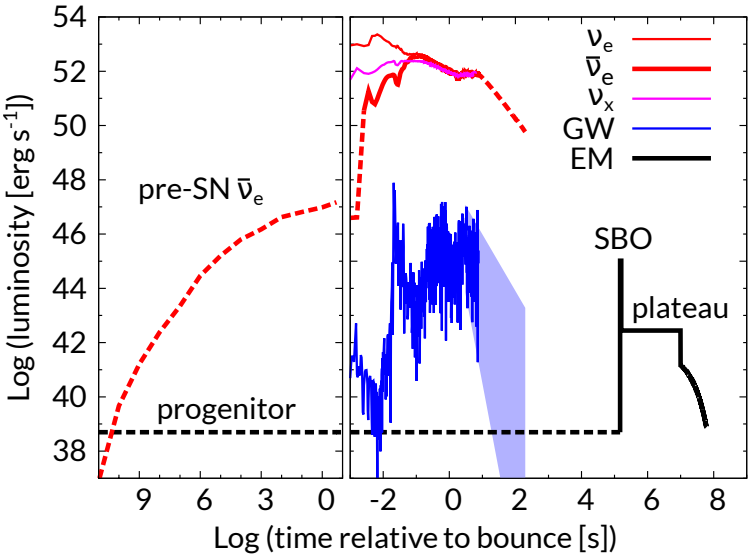

Figure 2.5.: Time evolution of the different messengers emitted by a CCSN [65]. The estimations come from the core-collapse simulation of a non-rotating star of 17 $M_\odot$.

The electromagnetic signal from a CCSN comes in two phases. The first happens when the shock breaks out from the star surface, releasing trapped photons in a UV and X-ray flash lasting from a few seconds to a few hours. This shock breakout (SBO) can take from a few minutes to a few days after the bounce depending on the size of the star. After the SBO, the expanding envelope cools down and emits photons in the UV and optical wavelengths. Depending on the type of supernova, the optical emission can either decrease linearly in time or stay on a plateau, as for the type IIP CCSN shown in Figure 2.5. The early observation of a CCSN light curve can give a lot of information on its size, composition, energy and velocity and is thus important for an accurate reconstruction.

Gravitational waves are propagation deformation of spacetime. They are generated by large asymmetric motions of very massive objects. During the collapse and after the bounce, complex three-dimensional are thought to happen. This causes an asymmetry in matter displacement, which in turn can lead to gravitational waves. Their observation can give precise knowledge on the inner movement of the star during the collapse. However, large uncertainties remain on the time- and frequency-profiles of gravitational waves generated by a CCSN.

2A.1.6. Motivations for the real-time detection of CCSN neutrinos

The past section gives an overview of the different mechanisms at play during a CCSN. However, more sophisticated analytical models and simulations are needed to reproduce the observations. In particular, one- and two-dimensional simulations cannot take into account the complex motions inside the star and to this day, even the most advanced three-dimensional simulations have difficulty to produce the explosion. The combined observation of neutrinos, gravitational waves and electromagnetic signal of a CCSN would give invaluable information to better understand and simulate the inner mechanisms.

But a CCSN could also probe other open physics questions, such as supernova nucleosynthesis and neutrino properties. Current nucleosynthesis models show discrepancies with respect to some observed ratios of heavy elements. A close-by observation of a CCSN would give insights on the type of process (*s*- *vs* *r*-processes) synthesizing elements and help constrain models. Moreover, the combination of the observations from the different neutrino detectors could bring a new measurement channel to the upper neutrino mass (time of flight difference between the heaviest and lightest neutrinos), to the neutrino mass hierarchy or bring to light beyond standard model physics phenomena [66].

The detection capabilities of current neutrino detectors is usually limited to the Milky Way (edge at 25 kpc) or satellite galaxies like the Large and Small Magellanic Clouds (around 50–60 kpc). It is possible to estimate the rate of Galactic CCSN with multiple measurements: the count of massive stars in the Solar neighborhood, extragalactic supernovae rates, the abundance of CCSN nucleosynthesis products, the birth rate of neutron stars and the age distribution of supernova remnants. A recent statistical study combining those measurements [67] estimates a Galactic CCSN rate of $1.63 \pm 0.46\,(100\text{yr})^{-1}$, usually abbreviated to 1.5 per century.

The first electromagnetic emission from a CCSN happens when the shock leaves the star surface, a few minutes to a few hours from the main neutrino emissions. As such, neutrinos can be used as an alert system to notify the observing facilities around the world and allow for early observations. SNEWS, the Supernova Early Warning System [68], is a network of neutrino detectors designed to give such a notification. A more detailed description of SNEWS and its ongoing upgrade is presented in a later section. An early neutrino alert can also be combined with the GW alert system from the Ligo-Virgo-Kagra (LVK) collaboration to refine the detection of unmodeled bursts associated with CCSN.

The rarity of a Galactic CCSN, the short duration of neutrino emission and the scientific potential of a full multi-messenger observation call for the need

of a fast, reliable and automatic detection system.

2A.2. Detection of MeV neutrinos with KM3NeT

2A.2.1. Interaction of MeV neutrinos in water

Neutrinos cannot be detected directly, but through the products of their interactions with electrons and nuclei. The kinematic threshold for charged current interactions is $E_\nu^{thr} \approx M_f - M_i + m_l$ where M_f and M_i are the initial and final state nuclear masses and m_l is the produced lepton mass. At CCSN energies, which ranges from 1 to 100 MeV, ν_μ and ν_τ are below the threshold and thus cannot interact. Four interaction processes are possible for CCSN neutrinos in water [69].

Inverse beta decay $\bar{\nu}_e + p \rightarrow n + e^+$ (2.13)
Inverse beta decay (IBD) is the most significant interaction in water. It is the charged-current interaction of electron neutrinos on free protons (hydrogen nuclei). The IBD kinematic threshold is $E_\nu^{thr} = 1.8\,\text{MeV}$. The positron energy is $E_{e^+} \approx E_\nu - 1.3\,\text{MeV}$ and its energy loss can typically be observed. The photon pair produced by the proton annihilation is not detectable in a water Cherenkov detector. As IBD has only a small energy-dependent anisotropy, the incoming direction of the neutrino is lost.

Elastic scattering on electrons $\nu + e^- \rightarrow \nu + e^-$ (2.14)
Elastic scattering on electrons (EES) can happen *via* neutral-current interactions for all flavors or *via* charged-current for electron neutrinos. The interaction has no kinematic threshold but has a much lower cross section than IBD. The scattering is directional and thus some low-background detectors can use the EES channel to point the direction of the source.

Charged-current interactions with oxygen (OCC)
$$\nu_e + {}^{16}\text{O} \rightarrow e^- + {}^{16}\text{F} \quad (2.15)$$
$$\bar{\nu}_e + {}^{16}\text{O} \rightarrow e^+ + {}^{16}\text{N} \quad (2.16)$$
Neutrinos can interact with nucleons in nuclei, even if the cross sections are usually smaller than for free nuclei. The kinematic thresholds are respectively 15.4 and 11.4 MeV.

Neutral-current interactions with oxygen (ONC) $\nu + {}^{16}\mathrm{O} \rightarrow \nu + {}^{16}\mathrm{O}^{*}$ (2.17)
The oxygen produces de-excitation photons which can Compton-scatter and eventually be observed.

The different cross sections for these interactions processes are taken from the SNOwGLoBES package and shown Figure 2.6. For the expected CCSN neutrino fluxes, the 97 % of the total interaction rate is due to IBD, 3 % due to EES and less than 1 % due to OCC and ONC. The main detection channel of KM3NeT for CCSN neutrinos is through inverse beta decay of the electron anti-neutrinos reaching Earth.

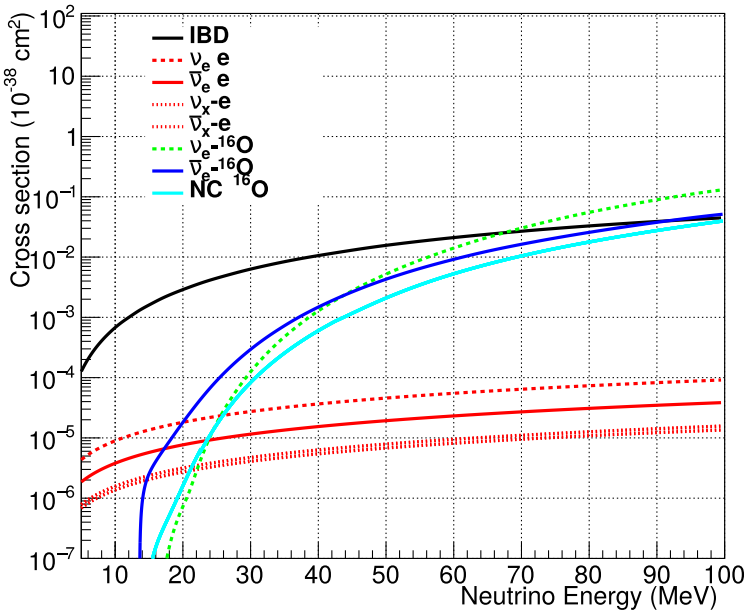

Figure 2.6.: Cross sections for neutrinos in water for energies between 8 and 100 MeV.

2A.2.2. Detection strategy

After neutrino interaction, the produced positron or electron is below 100 MeV. At this energy range, the lepton looses energy mainly *via* ionization and thermal excitation in collisions with molecules of water. Cherenkov radiation is emitted for a few cm, while the energy is above 0.8 MeV.

The KM3NeT detectors are optimized for the detection of neutrinos above the GeV scale. As such, the digital optical modules (DOMs) are spaced at

least tens of meters from each other. The probability of the photons reaching multiple DOMs is very low. In addition, the high optical background rate due to the natural radioactivity of seawater prevents the possibility to simply search for an increase of the global hit rate all over the detector. Figure 2.7 illustrates the single-DOM detection of neutrinos and the sources of optical background.

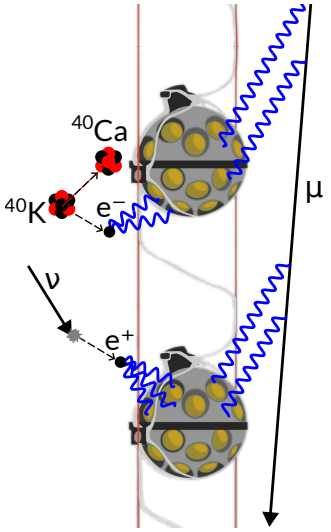

Figure 2.7.: Illustration of the optical background and signal. Neutrino interaction and radioactive decay can both lead to single-DOM coincidences, whereas a muon induces coincidences on multiple DOMs.

Instead, the strategy adopted for CCSN leptons detection is to search for an excess of coincidences between photomultipliers (PMTs) in single DOMs above the expected background of the detector. A coincidence is defined as a collection of hits (photon detection by a PMT) within a 10 ns time window. Technically, this can lead to events longer than 10 ns to be split in several coincidences and a cluster with highest coincidence being lost. With a maximal distance between PMTs of 0.2 m, the time difference between hits induced by MeV neutrinos is below 1 ns. As such, no coincidences due to signal events are lost. The coincidence time window of 10 ns is chosen to suppress the random background and to tolerate detection hit time uncertainties. On top of the time window condition, two consecutive hits must be in PMTs that are within 90 ° of each other. The number of unique PMTs inside a coincidence is called the multiplicity M.

2A.2.3. Description of the optical background

Both signal and background are counts randomly distributed in time. Their amount is convenient to present as a rate (Hz) which more strictly saying is the average number of counts in a period of observation (counts per second, cps). Both Hz and cps are have s^{-1} units so Hz is used everywhere.

Apart from the PMT dark rate (below 400 Hz), there are three main sources of optical background with KM3NeT: radioactive decay in the seawater and the glass spheres of the DOMs, bioluminescence and atmospheric muons. Radioactivity is dominated by the beta-decay of ^{40}K present naturally is salt, which emits electron of approximately 1.3 MeV. Every radioactivity contributions causes a constant background in every PMT with a hit rate of about 6–8 kHz. Bioluminescence leads to a localized increase of the hit rates up to the MHz range. Finally, atmospheric muons generate long, downgoing tracks, inducing Cherenkov radiation detected by multiple DOMs, making it possible to identify them most of the time.

The average DOM coincidence rate as a function of the multiplicity is shown Figure 2.8. For low multiplicities, the background is dominated by radioactive decays, whereas for multiplicity 7 and above, the dominant contribution is atmospheric muons. The difference of high-multiplicity rates is due to the depth difference between ARCA (3500 m) and ORCA (2500 m), which impacts the number of muons reaching the detectors.

2A.2.4. Optical background filtering

The typical energy scale for a CCSN neutrino is at least ten times higher than the electrons produced by beta decay. As such, a simple cut on the low-multiplicity coincidences can reduce a lot of background due to radioactivity while still preserving the CCSN signal.

Emission of bioluminescence is noncoherent. As such, the associated rate is dropping rapidly for multiplicity above 2 and is negligible. However, the high rate measured by single PMTs can saturate the data acquisition system. As a result, PMTs with rates above 20 kHz are vetoed with the embedded electronics of the DOMs.

Atmospheric muons cause coincidences that are distributed along the DOMs intercepting the light of the moving Cherenkov cone. The coincidences are time-correlated between the DOMs for the duration that a muon takes to cross the detector, typically a few microseconds. Those coincidences need to be suppressed, both to reduce the optical background rate and to ensure that the expected number of background events among all DOMs in the detector

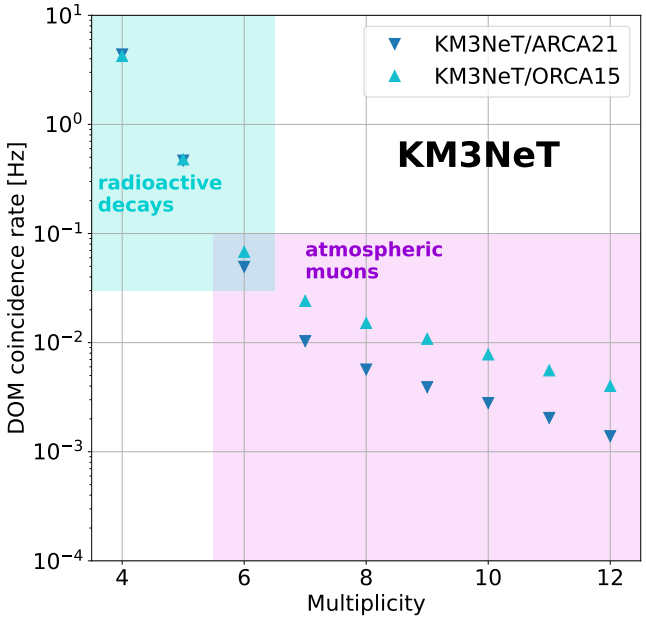

Figure 2.8.: Average DOM coincidence rate as a function of multiplicity for ARCA21 and ORCA15. The main contribution to the coincidence rate is indicated with the colored areas.

follows a Poisson distribution.

Atmospheric muons are routinely reconstructed by the KM3NeT detectors as the detectors are optimized for GeV energies and above. Thus, filtering of the triggered events is implemented to suppress this background. While detectors are at construction their early configurations are less efficient to detect the muons, especially at low energies. The alternative filter is based on correlation between coincidences.

Triggered events This filter uses the information contained in the triggered events produced by the KM3NeT physics triggers. Each triggered events contains a collection of triggered hits that are causally correlated and match an event topology (spherical or cylindrical). Coincidences are removed on every DOM detecting at least one triggered hit for the duration of the triggered event.

Coincidence correlation This filter checks if coincidences are distributed on multiple DOMs in a given time window. When a coincidence is recorded at a time $t = 0$, all coincidences from the detector until $t = \tau_{\text{veto}}$ are merged

with the initial coincidence. The duration τ_{veto} are 3 µs for ARCA and 1 µs for ORCA. They are typical duration of a muon crossing the detector. If a global coincidence is spread on multiple DOMs, all associated coincidences are removed.

An summary and illustration in the case of a muon crossing the detector for the two rejection methods is shown Figure 2.9.

Due to the design of the data acquisition (DAQ) software, coincidences are computed in groups of 100 ms, called *timeslices*. To maximize the detection sensitivity, the coincidences are summed over five sliding timeslices. Five timeslices contain 500 ms of coincidences, the approximate duration of the electron anti-neutrino emission (see Figure 2.3).

The number of coincidences in the five timeslices is called the coincidence level. In one sentence, the coincidence level is the number of coincidences – collections of single DOMs hits within 10 ns and 90 ° of each other – within an optimal multiplicity range and that have survived the muon veto, in time windows of 500 ms computed every 100 ms.

2A.2.5. Detection sensitivity

The sensitivity is estimated for three different signal computed by three-dimensional CCSN models from the MPA Garching group [70, 71]. The first two neutrino flux are simulated for progenitors of respective mass 11 $M_\odot$ and 27 $M_\odot$. The last flux comes from the model of a 40 $M_\odot$ progenitor collapsing into a black hole. The neutrino luminosity of the last model is considerably higher, whereas the first two flux can be respectively considered as a pessimistic and realistic detection cases.

The expected number of unfiltered coincidences as a function of multiplicity is given Table 2.2 for the three progenitors. Even for the pessimistic case, multiple hundreds of neutrinos are detected. The high number of signal events is one of the characteristic of water and ice Cherenkov detectors, compared to low-background experiments. It is, of course, at the price of a large background contamination.

The multiplicity distribution of filtered background and expected signal at 10 kpc for the three models can be seen Figure 2.10. Contrary to the non-filtered optical background shown Figure 2.8, the optical background is much more suppressed for the ORCA detector than for the ARCA detector. This is due to the geometry differences of the two detectors, which improves the trigger performance for muons for the most compact one, ORCA. The optimal sensitivity is obtained for a multiplicity range between 7 and 11. Figure 2.11

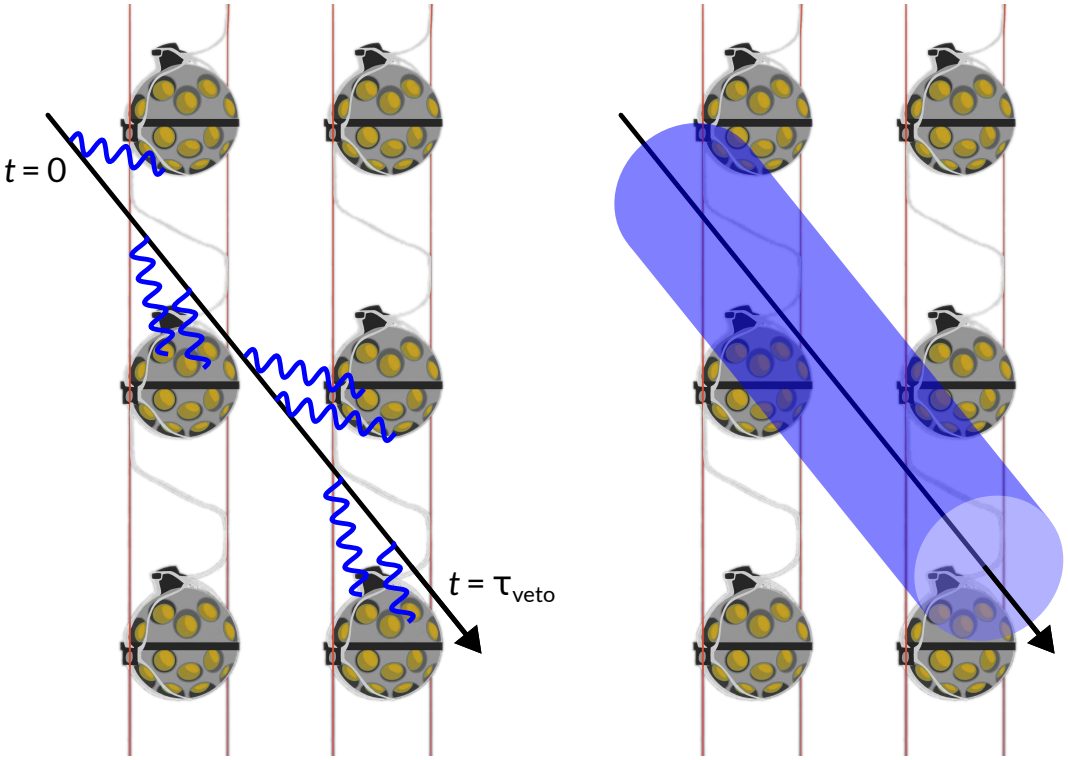

Figure 2.9.: Illustration of the two muon filters applied to a crossing muon, represented as the black arrow.
Left, coincidence correlation: A muon crosses the detector in a time τ_{veto}. The coincidences associated to the Cherenkov emission are all aggregated in a single global coincidence. Since the coincidences are distributed on multiple DOMs, all coincidences are vetoed.
Right, triggered events: The triggered event matches the cylindrical topology of the propagating muon. All hits and associated coincidences recorded during the triggered events are vetoed.

Table 2.2.: Expected number of coincidences as a function of multiplicity for one KM3NeT building block (2070 DOMs) for the three different progenitors considered at 10 kpc. The errors on the expected values come from the statistical uncertainty of the Monte Carlo simulation.

Model	**Multiplicity**			
	4	**5**	**6**	**7**
$11\,M_\odot$	100.4 ± 0.8	48.9 ± 0.5	25.8 ± 0.4	13.3 ± 0.3
$27\,M_\odot$	442 ± 3	218 ± 2	116.0 ± 1.5	64 ± 1
$40\,M_\odot$	1449 ± 8	723 ± 6	399 ± 4	226 ± 3
	8	**9**	**10**	**11**
$11\,M_\odot$	7.2 ± 0.2	3.4 ± 0.1	1.29 ± 0.08	0.50 ± 0.05
$27\,M_\odot$	35.2 ± 0.8	19.4 ± 0.6	8.0 ± 0.4	1.9 ± 0.2
$40\,M_\odot$	127 ± 2	69.5 ± 1.8	36.6 ± 1.3	15.0 ± 0.8

shows the sensitivity of the combined KM3NeT detectors as a function of the distance of the CCSN. In the most conservative scenario (progenitor of mass $11\,M_\odot$), KM3NeT is able to observe 95 % of the Milky Way, and can go up to the Large Magellanic Cloud. At the date of the writing of the manuscript, respectively 32 and 24 detection units are deployed within ARCA and ORCA. The current detectors combined sensitivity reaches 3σ for the Galactic edge in the realistic scenario.

The detection sensitivity can be compared to the ones of other neutrinos detector. IceCube, an ice Cherenkov detector in operation, reaches the Large and Small Magellanic Clouds [72]. Super-Kamiokande is a low-background Cherenkov detector and offers currently the best sensitivity with hundreds of kpc [73]. However, 90 % of possible CCSN progenitors are predicted to occur within 20 kpc of Earth. Overall, all neutrino detectors currently built are limited to the detection of a Galactic CCSN.

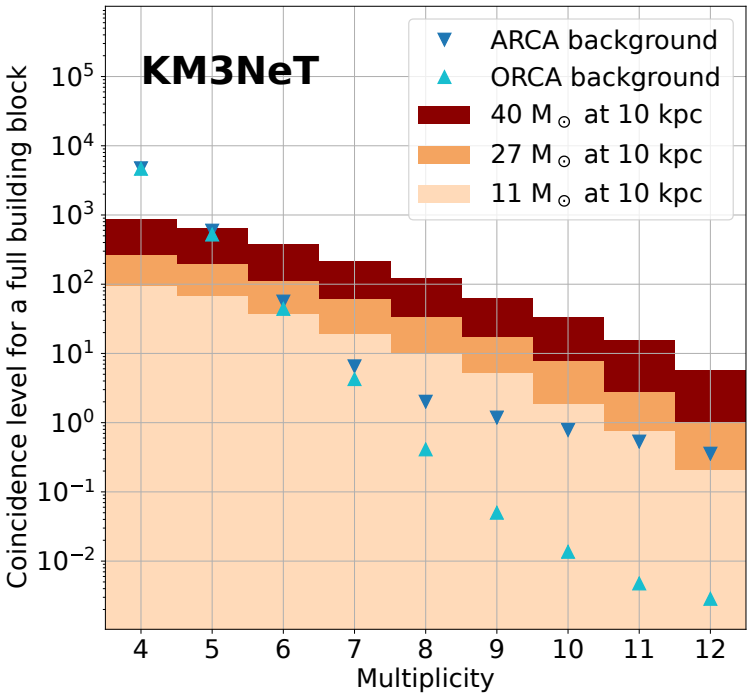

Figure 2.10.: Expected coincidence level in a KM3NeT building block as a function of the multiplicity. The background is shown with markers in light blue for ORCA and dark blue for ARCA. The signal is represented with colored bars in orange shades for the different models: light for $11\,M_\odot$, intermediate for $27\,M_\odot$, dark for $40\,M_\odot$.

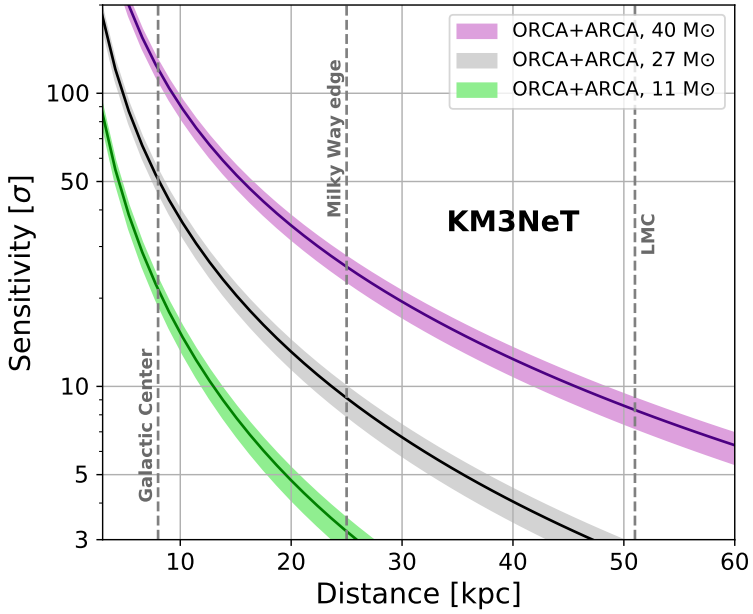

Figure 2.11.: KM3NeT detection sensitivity as a function of the distance to the CCSN for the three progenitors considered: 11 $M_\odot$ (green), 27 $M_\odot$ (gray) and 40 $M_\odot$ (purple).

2B. The KM3NeT CCSN online pipeline

Ya deux choses que j'déteste : le ^{40}K et le CAC40.

Gau'd'cho

The KM3NeT CCSN online pipeline aims to apply the detection strategy presented before in a fast and automatic capability. It consists of multiple modules which are small independent programs running on a common server to both detectors. The modules are organized in three groups, each with a main objective.

The purpose of the real-time CCSN search pipeline is to send a fast alert in the event of a Galactic CCSN. The alert is sent when the coincidence level reaches a significant excess over expected background, with a given false alarm rate. The quasi-online pipeline implements the retrieval of coincidences with a lower threshold. It is activated in the event of an alert to perform longer additional analyses with the increased statistics. Finally, the triggered follow-up pipeline re-analyzes past data following an external multi-messenger alert. Its goal is to provide a fast and quasi-automatic response with sub-threshold

data.

An overview of the CCSN online pipeline is given in Figure 2.12. The modules of the real-time CCSN search, quasi-online and triggered are color-coded respectively in blue, red and yellow.

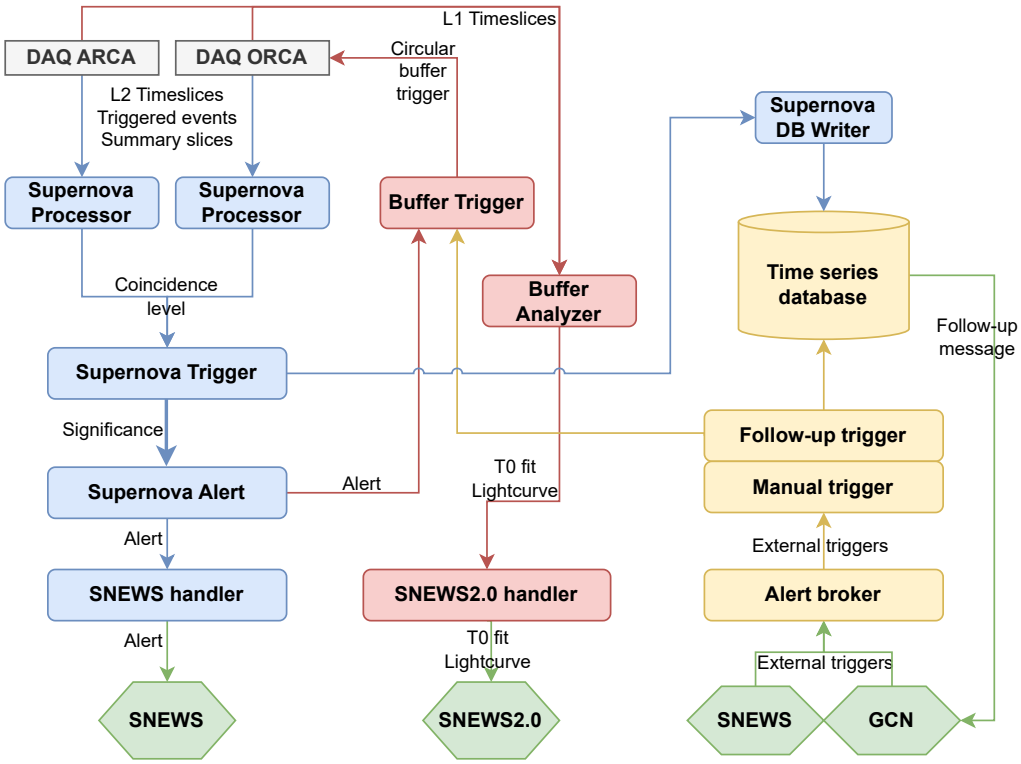

Figure 2.12.: Diagram describing the dataflow of the CCSN online pipeline. The modules of the real-time CCSN search, quasi-online and triggered are color-coded respectively in blue, red and yellow. The green hexagons represent external alert system, to which information is sent to or received.

2B.1. Real-time CCSN search pipeline

The real-time CCSN search pipeline is made of four modules. The *supernova processor* processes real-time DAQ data and computes the coincidence level. The *supernova trigger* merges the data from the two detectors and computes the associated significance. Finally, the *supernova alert* module applies a threshold and formats the alert message, before sending it to a network of neutrino telescope through the *SNEWS handler*.

2B.1.1. Coincidence level computation and detector combination

On the shore station of each detector, the *supernova processor* computes the coincidence level described previously (subsection 2A.2.4). To do so, coincidences, triggered events and summary information such as the number of active DOMs are aggregated for each timeslice in a priority queue. The queue allows waiting for possible late data to arrive and be processed. The length of the queue can be changed to prioritize latency or data integrity.

Once processed, the *supernova processor* outputs a message in the JSON format. An example output is shown Listing 2.1. The message contains, in the order of the example, a unique ID for the detector; an ID for the current run; an ID for the current timeslice; the starting time of the 500 ms window; the number of active DOMs in the detector; the number of active PMTs in the detector; the total hit rate of the detector at the given time and a dictionary. The dictionary contains, for both muon suppression methods, the coincidence level and the number of DOMs detecting at least one coincidence. The message is propagated to a common dispatcher, which receives the data from both the ARCA and ORCA detectors.

The combination of the two detector streams is done by the *supernova trigger* module on the common platform. To ensure that the significance is computed in the event of the downtime of one detector and to accommodate for the variations of delay between the two detectors, the incoming data is queued for a configurable maximum amount of time, at the end of which the module computes the significance for only one detector. If data from the second detector arrives after this delay, it is stored for a potential triggered follow-up analysis, but is not considered in the realtime computation of the significance.

Listing 2.1: Example output of the *supernova processor* module.

```
{
  "detid": 234,
  "run_number": 23223,
  "frame_index": 87681,
  "daq_time": "1739640368:0006250000",
  "active_doms": 415,
  "active_pmts": 12454,
  "detector_rate_MHz": 163,
  "trigger": {
    "cc": {"c": 7, "m": 7},
    "ev": {"c": 6, "m": 6}
  }
}
```

2B.1.2. Quality score

In some cases, a large number of coincidences in a few hundreds of milliseconds can be observed on a single DOM. Those coincidences are usually due to noisy or sparking PMTs. To avoid counting this transient behavior as significant, a quality score, called qscore, is introduced.

The qscore depends on the coincidence level n, the total number of DOMs in the detector m and the number of unique DOMs k on which those n coincidences are distributed. The probability of having k unique DOMs on which n coincidences are distributed is called $p_{n,m}(k)$. This probability is the ratio of the number of ways to distribute n coincidences on k DOMs (favorable outcome) and the number of ways to distribute n coincidences on m DOMs (total number of possible outcomes).

The number of possibilities to distribute n coincidences on k DOMs is:

- for the first coincidence, m possible DOMs;
- for the second, $m-1$;
- ...;
- for the last, $m-k+1$;

times the number of ways to partition the n coincidences into the k DOMs, which is given by the Stirling number of the second kind $S(n,k)$.

Finally, the total number of possible distribution of n coincidences among m DOMs is m^n, as there is m possibilities for the first coincidence, m possibilities for the second coincidence, etc, thus giving the following probability:

$$p_{n,m}(k) = \frac{m(m-1)\dots(m-k+1) \times \mathrm{S}(n,k)}{m^n} \tag{2.18}$$

The qscore is the cumulative distribution of this probability:

$$\text{qscore} = \sum_{i=1}^{k} p_{n,m}(i) = \mathrm{P}(\mathrm{X} \leq k) \tag{2.19}$$

A low quality score indicates that one or a few DOMs are producing an anomalous number of coincidences, a behavior not compatible with the hypothesis of an evenly distributed background or signal population of events. A threshold on the quality score is implemented to veto the alert generation, whose value is 0.05. As a result, around 5 % of timeslices without issues are dropped.

2B.1.3. Significance computation for constant background

The expected optical background is expected to follow a Poisson distribution. The significance of observing a coincidence level n while expecting a constant background b is represented by the one-tailed p-value p. The p-value is the probability of observing a number of events $\mathrm{X} \geq n$ with only background and no signal. As p decreases, the probability of the n coincidences originating only from the optical background decreases as well, and the significance of seeing a signal increases. For a Poisson variable, the p-value for observing n coincidences is given by:

$$p(n) = 1 - \sum_{0 \leq i < n} \mathrm{P}_{\text{Poisson}}^{\text{exp bkg}=b}(\mathrm{X} = i) = \mathrm{P}(\mathrm{X} \geq n). \tag{2.20}$$

A more convenient representation of the significance is the Gaussian significance, written as zscore. It is the value above which the integral of the normal distribution with centered mean and unit variance is equal to the p-value:

$$p = \int_{\text{zscore}}^{+\text{inf}} \mathrm{P}_{\text{Gaussian}}(x)\,\mathrm{d}x, \tag{2.21}$$

also written as:

$$\text{zscore} = \text{inverted survival function}(p). \tag{2.22}$$

The zscore can be interpreted as the number of standard deviation that the observed coincidence level deviates from the expected background.

In the real-time search pipeline, the coincidence level is evaluated every 100 ms from the previous 500 ms. When multiple observations are performed, a trial factor needs to be applied to the statistical significance for it to remain relevant. For a real-time search, the trial factor is infinite and only a false alarm rate (FAR) can be defined, by multiplying the observation frequency f to the p-value:

$$\text{FAR} = f \times p \tag{2.23}$$

A common unit for the FAR is "per day", which can be interpreted as the number of times per day the same coincidence level would be observed.

2B.1.4. Significance combination

The two detectors don't have the same rate. As such, they are treated as individual experiments before combining their significance. The combination of significance is an unresolved problem within data analysis, and each chosen method has benefits and drawbacks.

Currently, the combination of the significance of both detectors is done by summing the coincidence levels and the expected backgrounds, such as:

$$p = 1 - \sum_{0 \leq i}^{i < n_{\text{ARCA}} + n_{\text{ORCA}}} \text{P}_{\text{Poisson}}^{\text{exp bkg} = b_{\text{ARCA}} + b_{\text{ORCA}}}(\text{X} = i). \tag{2.24}$$

This is made possible by the fact that the sum of two Poisson variables follows a Poisson distribution. This method has the benefit of simplicity, but only works for comparable optical background. The detector with a higher background has a higher weight in the combination.

Two other combination methods are also considered: Fisher and Stouffer's methods [74]. Fisher's method consists of multiplying the two p-values and computing a χ^2 test used to determine the significance:

$$\chi^2 = -2\left(\ln p_{\text{ARCA}} + \ln p_{\text{ORCA}}\right) \tag{2.25}$$

Here each experiment is treated equally, which is a drawback for two detectors of different sizes and rates. Stouffer's method computes the significance with

Listing 2.2: Example output of the *supernova trigger* module.

```
{
  "time": "2025-02-15T17:22:15.400",
  "dets": [236, 234],
  "zscore": 1.2602785177162388,
  "FARday": 89669.76771278463,
  "qscore": 1.0,
  "data": {
    "236": {"c": 2, "m": 2, "b": 1.5},
    "234": {"c": 12, "m": 12, "b": 8.0}
  }
}
```

a weighted linear combination of the individual significances:

$$\text{zscore} = \frac{\sum_i w_i \, \text{zscore}_i}{\sqrt{w_i^2}}. \tag{2.26}$$

The weight, w, is chosen as the detection sensitivity at a reference distance of 10 kpc for a benchmark flux model. Stouffer's method has the benefit of taking into accounts the response of the two detectors. The drawback is that a high significance could be reached with only one of the two detectors reaching a high significance, in the case of an uncontrolled background event. Discussion are still ongoing between the choice of methods to use.

2B.1.5. CCSN alerts

Once the two detectors have been combined, a JSON message containing the starting time of the 500 ms time window, the quality score and the combined significance and associated FAR is transmitted to the common dispatcher. An example can be seen Listing 2.2. The *supernova alert* module tags the message according to different thresholds.

Four thresholds are defined: `test`, alerts with an hourly FAR; `snews-low`, alerts with a FAR below one per day; `snews`, alerts with a FAR below one every eight days and `high-Z`, alerts with a FAR below one per year. The naming reflects the conditions defined by the SNEWS network. The `test` and `snews-low` threshold are defined internally for testing purposes. The `snews` and `high-Z` are

Listing 2.3: Example output of the *supernova alert* module.

```
{
  "phys": "ccsn",
  "qualifier": "snews",
  "data": {
    "time": "2025-02-10T10:51:22.400",
    "dets": [236, 234],
    "zscore": 5.181283371095192,
    "FARday": 0.09519742719594765,
    "qscore": 0.33866199369846944,
    "data": {
      "236": {"c": 7, "m": 6, "b": 1.5},
      "234": {"c": 20, "m": 20, "b": 6.5}
    }
  }
}
```

respectively threshold beyond which a message is transmitted respectively to the SNEWS network and as a GCN notice for public advertising. A snews-level alert example is shown Listing 2.3.

2B.2. Adaptive background expectation

In the sea, bioluminescence may lead to a localized increase of the hit rates up to the MHz range per PMT, causing the need to veto rates above kHz with the embedded electronics of the DOMs. This leads to a non-constant number of active PMTs over the whole detector, which also causes variation in the expected background. The effect is more pronounced in the ORCA detector than in the ARCA detector. The difference comes from the bioluminescence activity, which is stronger in the French site. The distribution for the number of active PMTs for both detectors for one month of data is shown Figure 2.13.

In order to properly compute the significance for every timeslice, this phenomenon needs to be properly characterized. In the following, an adaptive background (AB) characterization for the ORCA detector is shown.

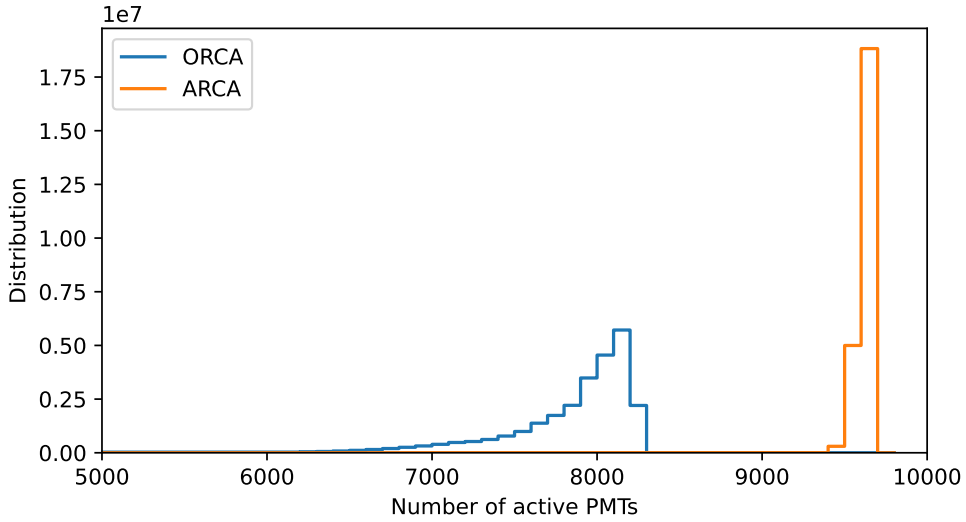

Figure 2.13.: Distribution of number of active PMTs for the ARCA and ORCA detectors for a one-month period.

2B.2.1. Previous AB method

Two previous characterizations of the expected background as a function of number active PMTs have been done in the past, respectively for ORCA4 and ORCA6. The first one, visible Figure 2.14, considers a variable called instrumentation efficiency, defined as the ratio between the expected background measured with a given fraction of active PMTs and the expected background measured with a fully active detector. The second one, which can be seen Figure 2.15, considers directly the expected background (mean rate on the plot) as a function of active PMTs. For both plots, a linear relationship is found between the expected background and the number of active PMTs.

The issue of the previous method is its shortcoming to take into account the short time variability of the number of active PMTs. This effect is illustrated when drawing a scatter plot of values averaged over groups of ten minutes, instead of applying a binning to the number of active PMTs, as done with Figure 2.16. This plot shows the coincidence level from the optical background as a function of the number of active PMTs. Each dot represents 10 minutes of timeslices averaged. The color represents the mean number of active DOMs during those 10 minutes. As seen on the figure, the relationship is no longer linear: the relationship between the two variables seems to be quadratic, with multiple quadratic parameters depending on the number of active DOMs.

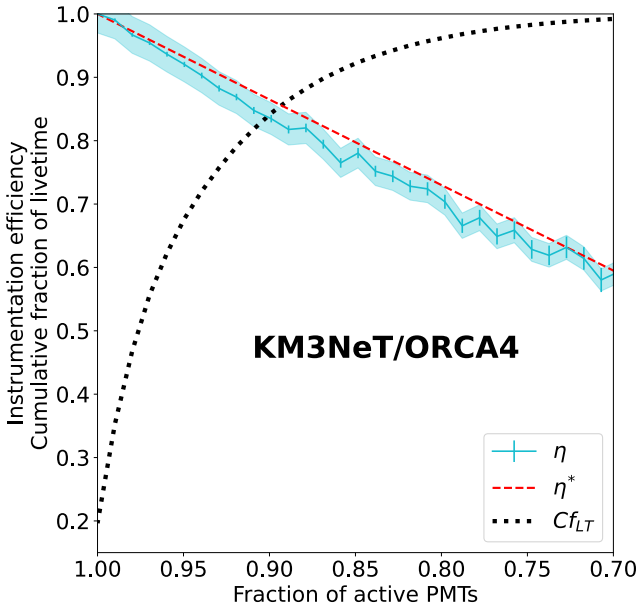

Figure 2.14.: Measured instrumentation efficiency as a function of the fraction of active PMTs in ORCA4 detector.

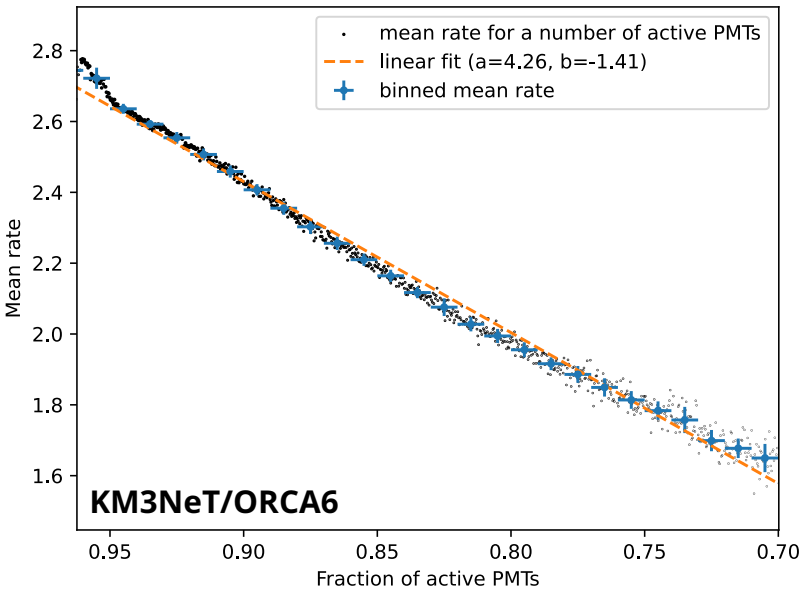

Figure 2.15.: Mean rate of the coincidence level as a function of the fraction of active PMTs for ORCA6.

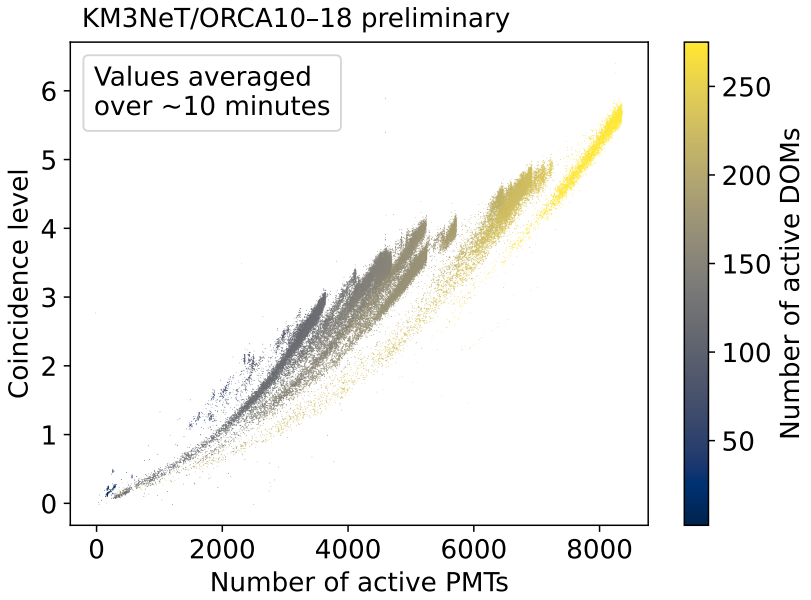

Figure 2.16.: Scatter plot of coincidence level vs number of active PMTs averaged over groups of ten minutes for ORCA10 and above. The data spans from December 2021 to July 2023.

2B.2.2. New AB method and application to 1.5 year of data

The behavior seen Figure 2.16 can easily be explained by the fact that the detector with all lines working and half of the PMTs active does not behave the same way as the detector with half of the lines working and all PMTs active. The solution is to normalize both the coincidence level and the number of active PMTs by the number of active DOMs. On Figure 2.17, where data from all PHYSICS runs since the beginning of ORCA10 (December 2021) to middle of June have been processed, the coincidence level follows a single quadratic function, with a non negligible variability.

2B.2.3. Refined AB method with monthly fits

The goal of the following analysis is to show that a new quadratic fit is needed regularly in order to insure a good estimation of the significance.

To set this new strategy, 20 months of ORCA data (from December 2021 to July 2023) have been analyzed, where data has been grouped in blocks of 30 days. The 30 days period was chosen to have enough data to be able to have a variation in the number of active PMTs to perform the fit and to take into

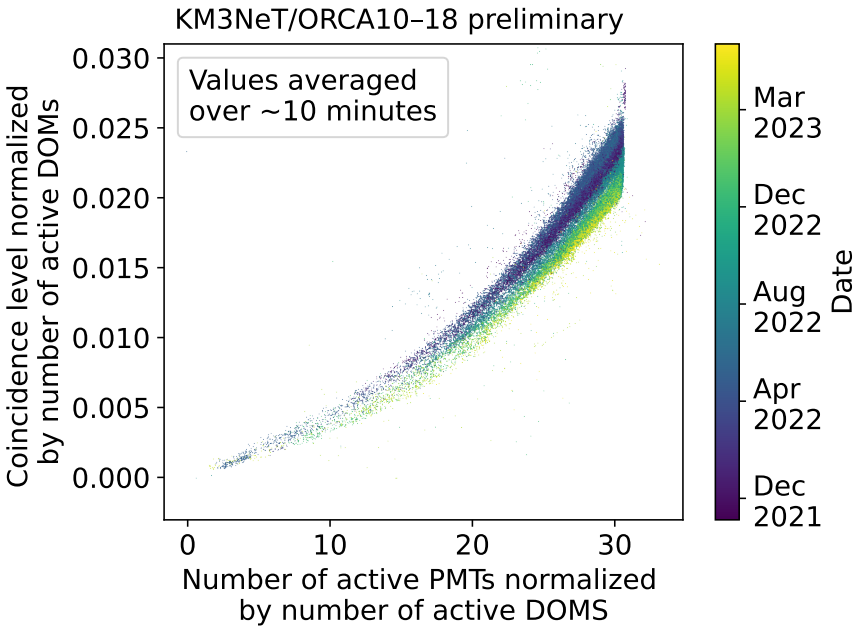

Figure 2.17.: Scatter plot of coincidence level vs number of active PMTs both normalized by number of active DOMs averaged over groups of ten minutes for ORCA10 and above. The data spans from December 2021 to July 2023.

account the most recent behavior of the detector. For example a period of 90 days gives slightly worse result with the relative error distribution.

Four examples of fits are shown in Figure 2.18. The fits were done using the `curve_fit` function from `scipy.optimize` and a quadratic function with no term of order 0, $f(x) = ax^2 + bx$, with forced $a \geq 0$ and $b \geq 0$. In order to test the quality of the fit, two histograms are computed (Figure 2.19): the relative error between the data points and the first fit (December 2021) in blue and the relative error between the data points and the closest previous fit in orange. The closest previous fit was chosen in order to emulate what would be done in the online pipeline. The relative error for multiple fits is centered in zero with a single population, and is overall much better than the relative error for one single fit.

2B.2.4. Effect of the refined AB method on the zscore

The zscore is computed for all data and compared to an expected zscore distribution, both for the single fit method and for multiple fits.

The coincidence level follows a mixed Poisson distribution: each timeslice

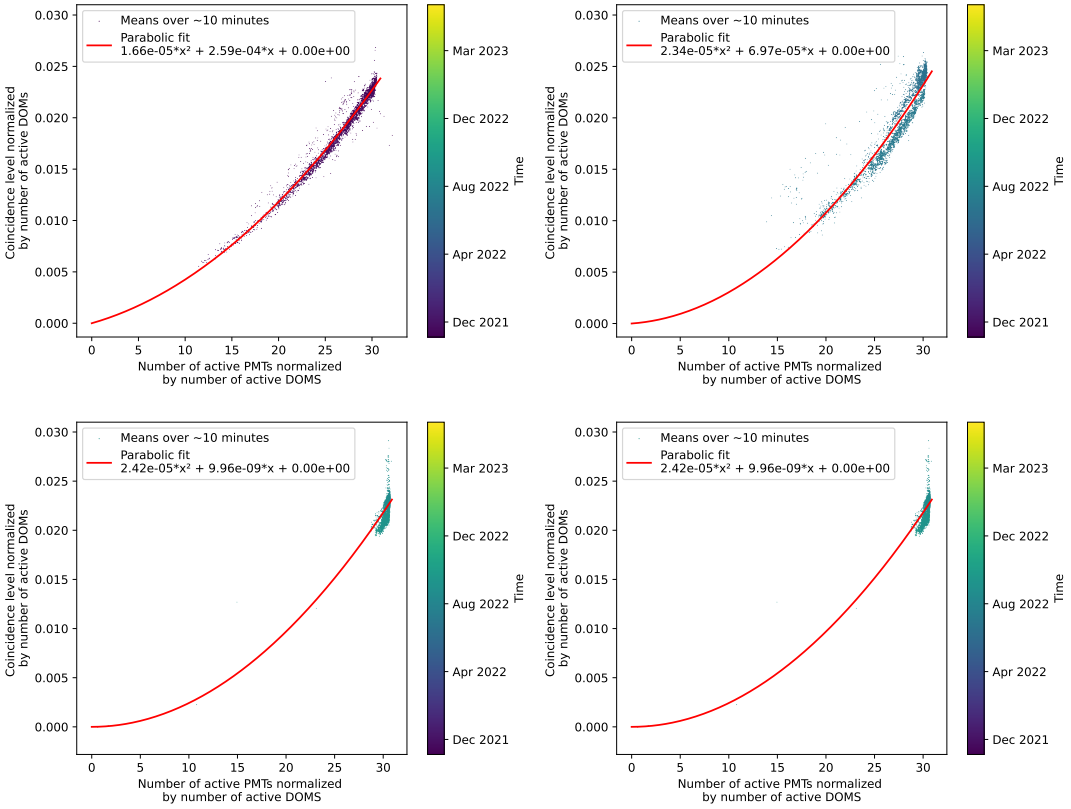

Figure 2.18.: Four example of fits performed on ORCA data. The four fits were chosen to illustrate different spreads of number of active PMTs normalized by number of active DOMs and the associated quality of each fit.

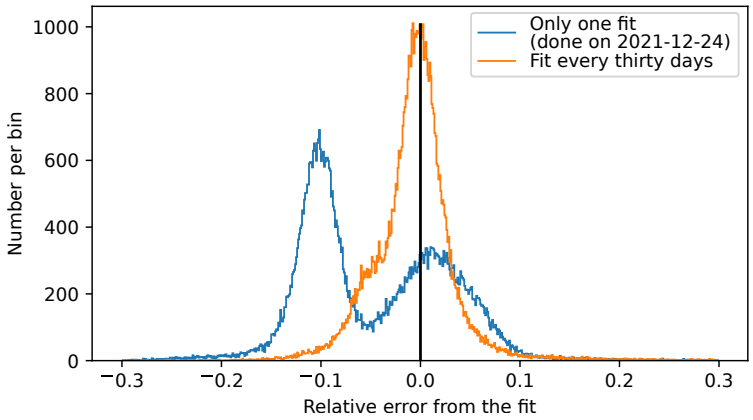

Figure 2.19.: Histogram of the relative error between the average data point (in blue) and the one expected provided by the closest monthly fit (in orange).

contributes to the distribution with a varying expected background. For every timeslice, the following method is applied:

- the timeslice is vetoed if the number of active PMTs or the number of active DOMs is equal to 0 or if the qscore is below 0.05;
- the expected background is estimated with b = number of active DOMs $\times$ f(number of active PMTs / number of active DOMs);
- the p-value and zscore are computed from the coincidence level n and the computed expected background b following a Poisson expectation. The zscore is added to the *data* histogram;
- the probability mass function of a Poisson distribution with expected background b is added to the *expected* histogram.

For a given zscore threshold $\mathrm{Z}_{\mathrm{threshold}}$, the number of alerts sent within the 20 months span of data ($\mathrm{N}_{\mathrm{tot}}$ timeslices) is

$$\mathrm{N}_{\mathrm{tot}} \times \mathrm{P}(z > \mathrm{Z}_{\mathrm{threshold}}). \tag{2.27}$$

This value corresponds to the anti-cumulative distribution, which will be used to check the effects of the refined AB method.

A toy-experiment for a mixed Poisson variable z_k is given as a reference Figure 2.20. A value of 1 is added to the anti-cumulative distribution to visualize correctly the high zscore values, which are low in statistics. For reference, the distribution of a zscore following a normal distribution is also drawn in pink. The vertical lines represent the different thresholds used with KM3NeT. The gray and green horizontal lines are the number of alerts sent for the `test` threshold respectively for the Poisson and normal distributions. A mixed Poisson distribution is expected to always be below the normal distribution.

The anti-cumulative zscore distributions for a single fits and monthly fits are presented respectively Figure 2.21 and Figure 2.22, along with the relative comparison. The two vertical lines represent the two threshold levels `test` and `snews`, with the horizontal lines showing the number of timeslices above the `test` threshold for the expected distribution (in dash-dotted) and from data (full line). Table 2.3 and Table 2.4 show the obtained FAR for the different thresholds both for the single fit method and the monthly fits method. The bottom plots of Figure 2.21 and Figure 2.22 clearly show that for zscore below 4, the agreement between data and expected is much better when doing a monthly fit that with a single fit. For zscore above, the statistical uncertainty starts to be predominant.

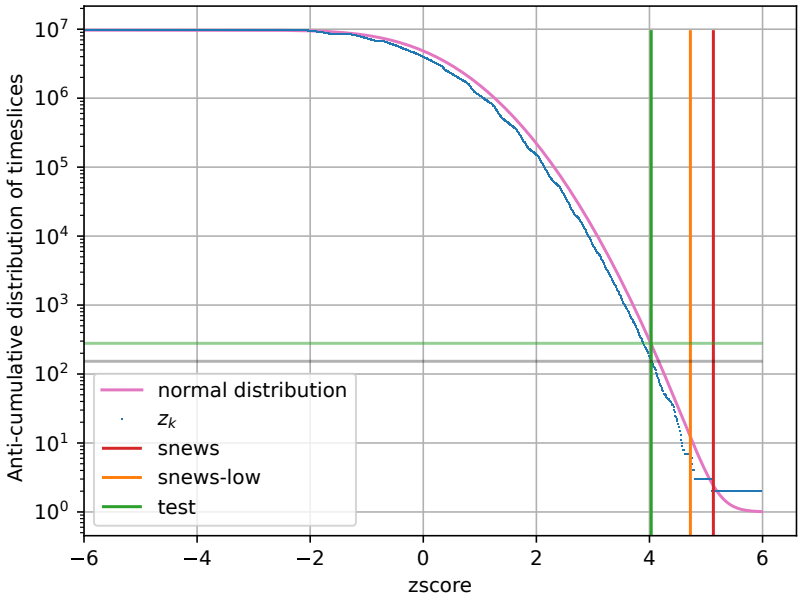

Figure 2.20.: Anti-cumulative distribution as a function of zscore for a variable z_k following a mixed Poisson distribution (blue) and a variable following a normal distribution (pink). The vertical lines represent the different thresholds used with KM3NeT. The gray and green horizontal lines are the number of alerts sent for the `test` threshold respectively for the Poisson and normal distributions.

Table 2.3.: Computed FAR for the three different thresholds for data from December 2021 to July 2023 based on a single fit.

level	wanted FAR [d^{-1}] (number of timeslices)	expected FAR [d^{-1}] (number of timeslices)	obtained FAR [d^{-1}] (number of timeslices)
snews	0.125 (45.91)	0.05 (20.14)	0.05 (18)
snews-low	1.0 (367.25)	0.52 (189.74)	0.43 (157)
test	24.0 (8814.11)	12.53 (4601.12)	9.60 (3525)

Table 2.4.: Computed FAR for the three different thresholds for data from December 2021 to July 2023 with AB taking into account monthly fits.

level	wanted FAR [d^{-1}] (number of timeslices)	expected FAR [d^{-1}] (number of timeslices)	obtained FAR [d^{-1}] (number of timeslices)
snews	0.125 (45.91)	0.06 (20.79)	0.08 (29)
snews-low	1.0 (367.25)	0.49 (181.76)	0.60 (222)
test	24.0 (8814.11)	12.36 (4539.54)	12.62 (4633)

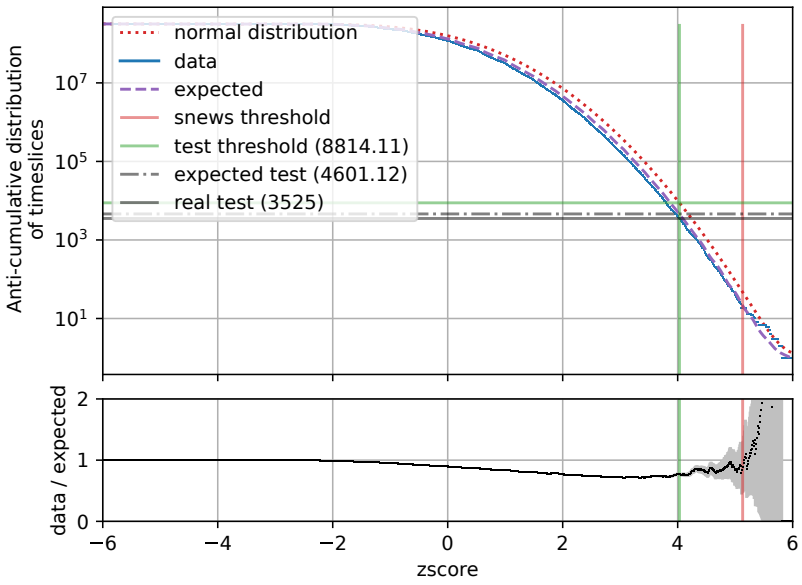

Figure 2.21.: Anti-cumulative distribution of zscore computed for data from December 2021 to July 2023 based on a single fit.

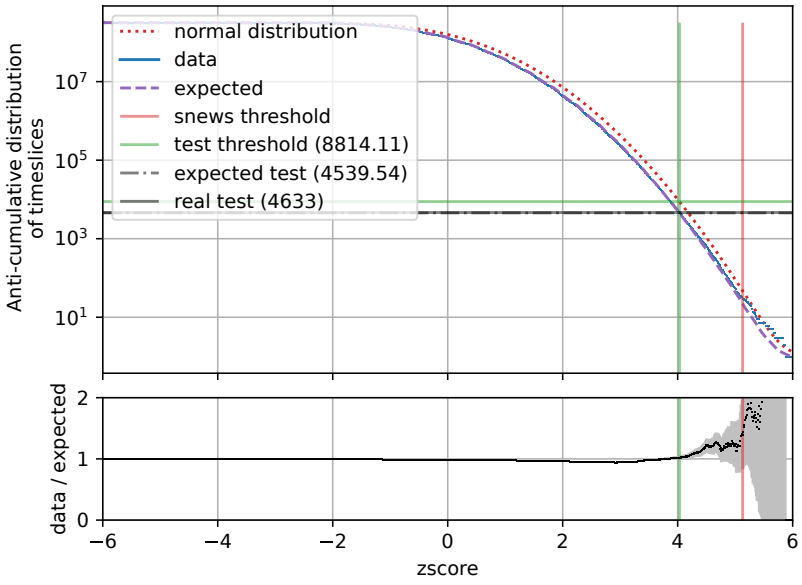

Figure 2.22.: Anti-cumulative distribution of zscore computed for data from December 2021 to July 2023 with AB taking into account monthly fits.

Despite the good agreement, Table 2.4 shows there is still a factor 2 between the wanted and obtained number of timeslices. The difference arises from the nature of the mixed Poisson distribution. A solution would be to decrease the threshold to meet the target number of alerts. However, an issue arises when trying to combine significance with other detectors. Should it be done with the zscore associated with a given timeslice, or with the resulting expected rate of timeslices at the threshold? Discussion are ongoing to solve this issue.

2B.3. Quasi-online pipeline

2B.3.1. Goals of the quasi-online pipeline

The real-time analysis combined with the SNEWS network enables the detection of CCSNe before any optical observation is possible. However, this process only indicates the presence of a CCSN, without any precision concerning its position or other physical mechanisms. Additional information can be gained by the study of the time-profile of the neutrino signal.

The determination of the arrival time of the neutrino signal for different detectors can be used to triangulate the source. The triangulation would allow optical telescopes to observe the collapsing star before the supernova being visible, making it possible to collect as much data as possible to understand this phenomenon [75].

Due to the large background in water Cherenkov detectors, the detection pipeline requires strict constrains on coincidences, described previously (subsection 2A.2.2). For the refined studies of the neutrinos time profile, a higher number of coincidences is needed to improve statistics. As such, all coincidences with hits within 5 ns are considered, without constraints on the coincidence geometry or multiplicity. A simulated time distribution for such relaxed coincidences is shown left of Figure 2.23. The simulation is made for the full ARCA detector ($2 \times 18 \times 115$ DOMs) for a CCSN with a progenitor of mass $20\,M_\odot$ at 5 kpc. Such distribution is often called a "neutrino light curve", as a reference to the light curves (light intensity as a function of time) recorded with light telescopes.

The measurement of the neutrinos arrival time T0 is made from an exponential fit on the obtained neutrino light curve (see Figure 2.23 right). With this method, the uncertainty on T0 is estimated between 3 ms in the best cases and 70 ms in the worst cases, depending on the distance and the CCSN model used.

The goal of the quasi-online analysis is to compute the neutrino light curves

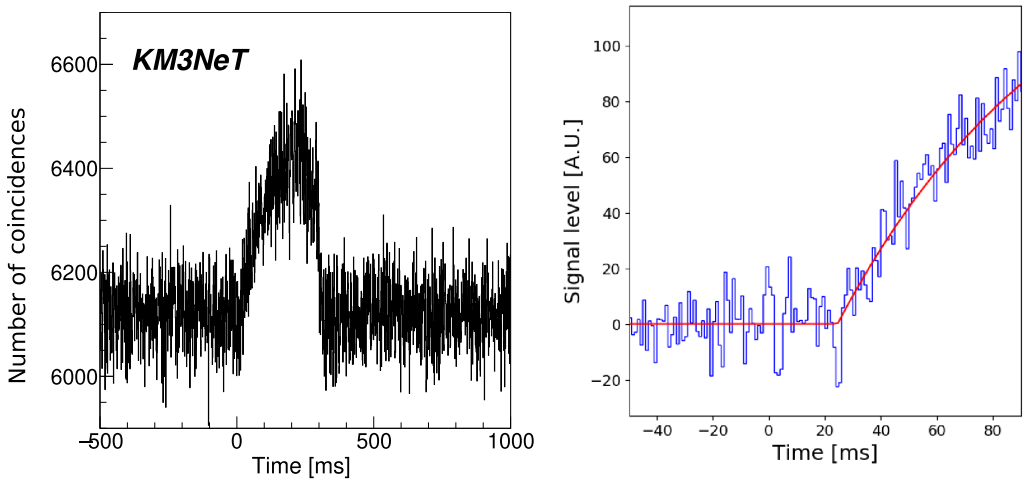

Figure 2.23.: Simulated neutrino light curve for the full ARCA detector, considering a source at 5 kpc and a CCSN progenitor of mass 20 $M_\odot$. The left plot shows all coincidences detected by the detector. The right plot shows the coincidences averaged over windows of 23 ms, with subtracted background and with an exponential fit applied.

and the associated T0. It is triggered in two instances. Internally, when the real-time analysis detects a significance reaching the `snews`-level. The data is further transmitted to the SNEWS network to enable the triangulation between detectors. And externally, from a possible CCSN signal provided by SNEWS or other channels to look for a sub-threshold signal in KM3NeT data. The implementation of the quasi-online pipeline is described in the next section.

2B.3.2. Implementation of the quasi-online pipeline

Three modules compose the quasi-online pipeline (shown in red Figure 2.12). The *buffer trigger* is responsible to trigger the data acquisition on the reception of an alert message to write to disk the past five minutes of coincidences, retrieve the generated files and transmit them to the *buffer analyzer*. The *buffer analyzer* processes the file to output a neutrino light curve and fit the arrival time of the first neutrinos. Finally, the *SNEWS handler* formats the data and transmits it to the SNEWS network.

The *buffer trigger* is activated when the supernova alert module transmits an alert on the multi-messenger dispatcher, or when an “interesting” external trigger is received. The external trigger currently activating the buffer are

CCSN alerts from SNEWS or Super-Kamiokande in the neutrino channel and burst and compact binary coalescence involving at least one neutron star alerts from LVK in the gravitational wave chanel.

At activation, the *buffer trigger* sends a message to the DAQ dispatcher to prompt the data filters to dump the last 5 minutes of unconstrained coincidences to disk. Those coincidences cannot all be stored to disk due to data size issues and are only written with this specific trigger. The *buffer trigger* then listens to the logs output of each data filter to determine when each file is completed. Finally, the files are retrieved from the shore station to the common online platform and a JSON message containing the alert content and the locations of each file is sent to the *buffer analyzer*.

The *buffer analyzer* merges the files written by the data filters and cuts around the time of the alert to optimize processing times. The coincidences are then ordered to generate the neutrino light curve. The T0 fit happens in two steps: a first estimation is made by looking for a 2.5σ excess over background, before using the value to perform an exponential fit.

Finally, the neutrino light curve and T0 fit are both transmitted to the *SNEWS2.0 handler*, which formats and sends the relevant data.

2B.4. Transmitting data to the SNEWS network

2B.4.1. SNEWS

SNEWS, for Supernova Early Warning System, is a neutrino detector network aiming to report an early alert for a Galactic CCSN. The principle is simple: if two or more detectors report an alert within a ten second window, a public alert from SNEWS is sent. The false alarm rate required for every neutrino detectors is once per eight day, which leads to a global false alarm rate of less than one per century.

Since SNEWS's start in 2005, the multi-messenger community has evolved considerably. False positive detection, with an associated false alarm rate, are now more accepted. Follow-up are better organized and more observation facilities are able to operate automatically and in real-time. To improve the scientific output from the next Galactic CSSN, an ongoing effort is made to update the alert system. SNEWS2.0 [76] has multiple goals, including reducing the threshold for alerts for better sensitivity, combining the pointing and timing information from the different detectors and preparing a follow-up strategy.

Three tiers of data sharing are planned, as indicated Figure 2.24. The alert tier is similar to the one running with the current version of SNEWS,

with a coincidence based system of alerts presenting a FAR of less than once per 8 days. The significance tier aims to perform sub-threshold analysis, by organizing the combination of the significance of the detectors if one of them measures a significance rise. Finally, the timing tier aims to communicate timing information, such as the neutrino light-curve and T0 fit described in the quasi-online pipeline section.

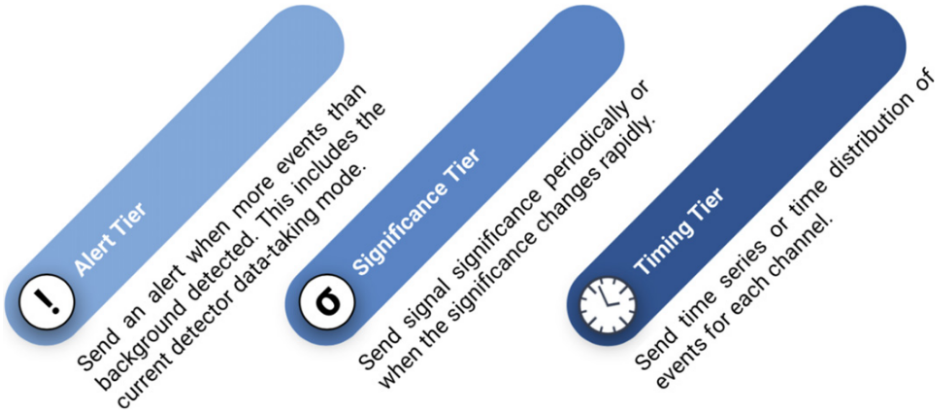

Figure 2.24.: Data sharing policies of SNEWS2.0, describing the different tiers of data collection, increasing in complexity from left to right [76].

2B.4.2. Data transmission

Data is transmitted to the new SNEWS network in the format of JSON messages. The infrastructure is based on the Apache Kafka streaming platform, already extensively used in the industry. It guarantees strong delivery (messages are transmitted at least once) with high reliability and allows for authentication and permissions. The different format for the different tiers of alerts have recently been defined can be found [77]. Sending a message relies on two Python libraries: `hop-client` and `snews_pt`. `hop-client` interfaces with a specific Kafka instance dedicated for multi-messenger astrophysics called HOPSKOTCH. The library allows both to publish (send) and to subscribe (receive) to specific data channels. The SNEWS publishing tools, or `snews_pt`, are built on top of `hop-client` to facilitate data exchange specific to the neutrino detectors and the SNEWS server. The integration of the KM3NeT real-time CCSN search pipeline to those two libraries is implemented and operational. The alert tier is ready to start running in production on the SNEWS side soon, which should supersede the legacy SNEWS coincidence software.

2B.5. Triggered follow-up searches

The triggered analysis pipeline aims to follow-up external multi-messenger triggers by recomputing the significance for the KM3NeT detector around the time of the measured transient events.

2B.5.1. Design of the database

Coincidence levels are stored alongside triggered events in offline files, written at the end of each run. However, retrieving files to recompute a significance would be too slow to be able to answer within minutes. As such, a *time series* database has been implemented to store the output of both the *supernova processor* modules and the *supernova trigger*, in two separate tables.

After testing different technologies, the time series database relies on `PostgreSQL` and the `TimescaleDB` plugin. This allows for complex SQL queries while not degrading performance as more data is stored, and to perform rolling deletion of older than one year data to save disk space.

The database structure is shown Figure 2.25. On the top left, the two tables containing all outputs from the real-time modules are shown. The fields follow the same structures as the JSON messages shown Listing 2.1 and Listing 2.2. Only the first table is strictly necessary for the triggered follow-up searches, but the second table is also used for monitoring purposes. Additionally, summary tables containing reduced data are automatically generated to speed up queries. On the bottom left, the two tables contain the ten minutes averages for the coincidence levels, the number of active DOMs, the number of active PMTs and the qscore, and the ten minutes maximum for the zscore. Those summary tables are used both for monitoring purposes and to be able to compute the AB characterization presented previously (subsection 2B.2.2). Finally, histogram tables are computed for the number of active PMTs, the number of active DOMs, the number of active PMTs normalized by the number of active DOMs, the expected background and the zscore. The histogram tables are presented in the right section of Figure 2.25.

2B.5.2. Principle of the search

At the reception of a selected external trigger by the broker, a query to the time series database is made. The principle of the search is to look for the maximum significance during a given time-window, which differs according to the type of alert: $[0, 2\,\mathrm{s}]$ for GW detection and $[-5\,\mathrm{s}, 5\,\mathrm{s}]$ for external CCSN alerts. The

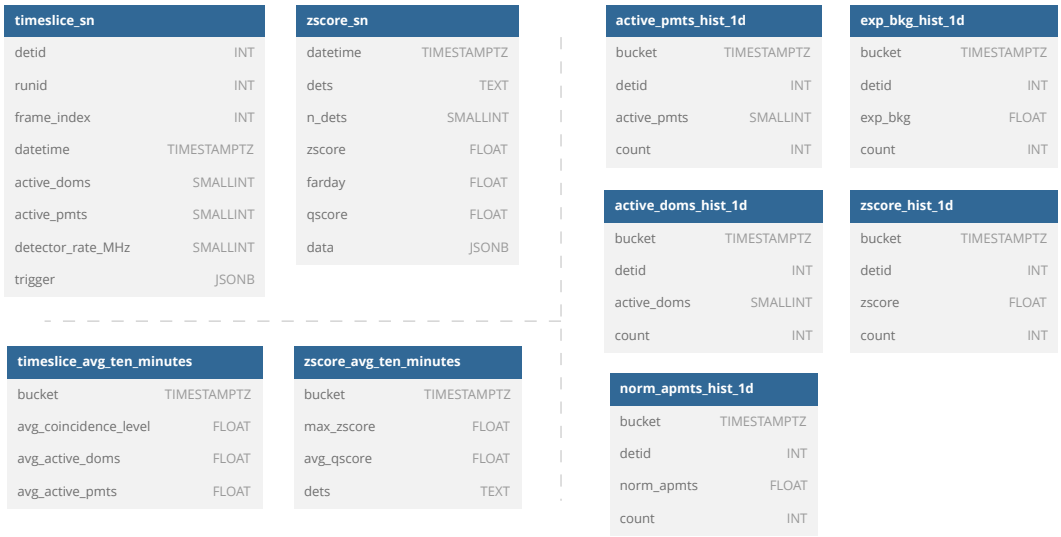

Figure 2.25.: Database diagram for the KM3NeT CCSN online pipeline. The tables are separated according to their type of contents and functions. On the top left are the two tables containing the full time series of the output of the *supernova processors* and *supernova trigger* modules. On the bottom left, the two tables contain reduced data (average or maximum) over time buckets of ten minutes. The tables on the right are histograms for all the variables of interest.

2 s time window for the GW was chosen assuming a prompt emission of MeV neutrinos at the same time of gravitational wave, and the duration to account for the possible time of flight difference due to the neutrino mass. The 10 s for the external CCSN alerts is a bit larger to account for uncertainties in the arrival time of neutrinos with other detectors.

For both detectors, the coincidence level, number of active DOMs and number of active PMTs inside the time window are retrieved. The quality score and significance from the adaptive background expectation are computed, before being combined in the same way as within the real-time search pipeline.

2B.5.3. Significance computation

Coincidence levels are computed every 100 ms. As such, the number of coincidence levels inside the search time window is two times the length of the time window in seconds. For a single coincidence level, the one-sided p-value and the associated Gaussian significance can be computed simply from the estimated expected background and the Poisson distribution. For multiple coincidence levels, a more complex distribution is needed,

$$\mathrm{P}\left(\max_{i=1,n}(\mathrm{X}_i) = k\right), \tag{2.28}$$

where each X_i follows a Poisson distribution.

This distribution can be simply approximated with toy experiments containing Poisson variables, but an analytical expression can be derived. Let's consider n variables X, all following a Poisson distribution with the same expected background. The maximum value reached by one or more variables is k.

- If there is only 1 variable equal to k, there is 1 among n variables to choose from, or $\binom{n}{1}$. The probability of this variable to reach k is $\mathrm{P}(\mathrm{X} = k)$, with a Poisson distribution. Since there is only one variable equal to k, all other variables are strictly below k, and the associated probability is $\mathrm{P}(\mathrm{X} < k)^{n-1}$.

- If there are 2 variables equal to k, there are 2 among n variables to choose from, or $\binom{n}{2}$. The probability for those two variables to reach k is $\mathrm{P}(\mathrm{X} = k)^2$. Since only two variables are equal to k, the associated probability for the remaining variables is $\mathrm{P}(\mathrm{X} < k)^{n-2}$.

- And so forth, until n variable equal to k.

Summing all those probabilities gives the following distribution:

$$\mathrm{P}\left(\max_{i=1,n}(\mathrm{X}_i) = k\right) = \sum_{i=1}^{n} \binom{n}{i} \mathrm{P}(\mathrm{X} = k)^i \, \mathrm{P}(\mathrm{X} < k)^{n-i}. \tag{2.29}$$

A sanity check can be made by comparing the obtained distribution from the toy experiments and from the analytical expression. The comparison of the two methods is shown Figure 2.26 for an expected background $b = 5$ and a number of coincidence levels $n = 20$, showing a good agreement.

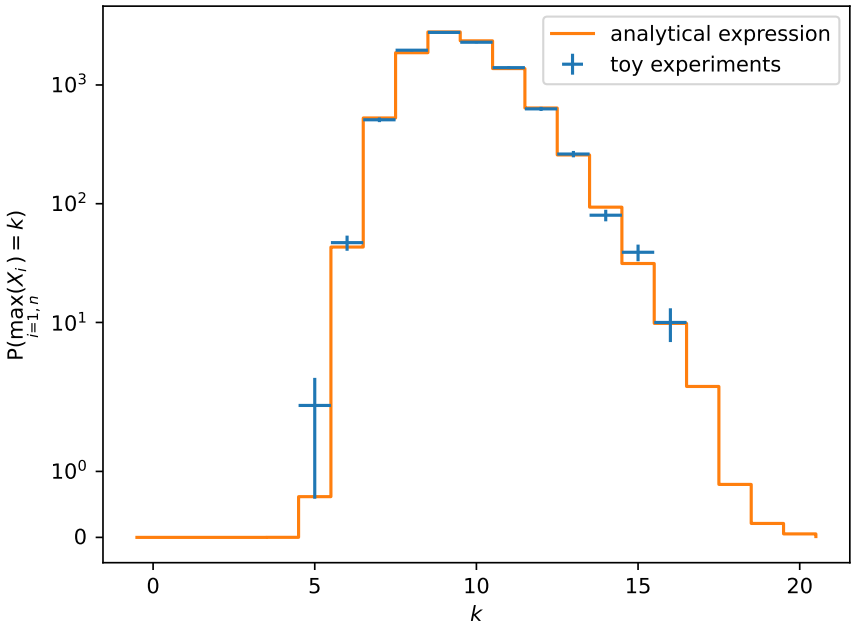

Figure 2.26.: Distribution for the maximum among 20 Poisson variables with expected background $b = 5$. The blue points are the results of 10 000 toy experiments, along with the statistical uncertainties. The orange line is the analytical expression derived in Equation 2.29.

2B.5.4. Results report

The results of the follow-up search are automatically reported on a website dedicated to the KM3NeT online infrastructure. The website, called shifter-tools, will be further presented in the next chapter. The results report contains the active detectors at the time of the trigger, the expected Poisson background, the maximum coincidence level within the search time window, the

associated qscore, zscore and FAR and the one-sided p-value computed from Equation 2.29. Additional plots are also reported (Figure 2.27). The different plots report respectively the time evolution of the coincidence levels and of quality scores, the variability of the number of active DOMs, number of active PMTs and normalized number of active PMTs and the expected background distribution during the search time window.

The time profiles (two top plots) allow shifters to compare the maximum coincidence level to those outside the time window and to make sure that the quality score does not indicate an erratic behavior. The shifter can also check whether the maximum coincidence level corresponds to a maximum in both detectors or in only one. The time variability plots (two middle plots and bottom left plot) allow to check whether the detectors were stable during the last 4 hours and during the time window. Finally, the expected background distribution shows whether the obtained maximum coincidence level is a statistical outlier or not.

The specific plots of Figure 2.27 correspond to a weekly SNEWS test alert. The maximum coincidence level corresponds to a local maximum for both detectors, with a good quality score and stable variables during the search time window, but is not at all a statistical outlier.

To this day, no significant observation was made following an external trigger. But the system is ready and shifters are being trained to report any detection of a MeV neutrino burst in coincidence with other messengers.

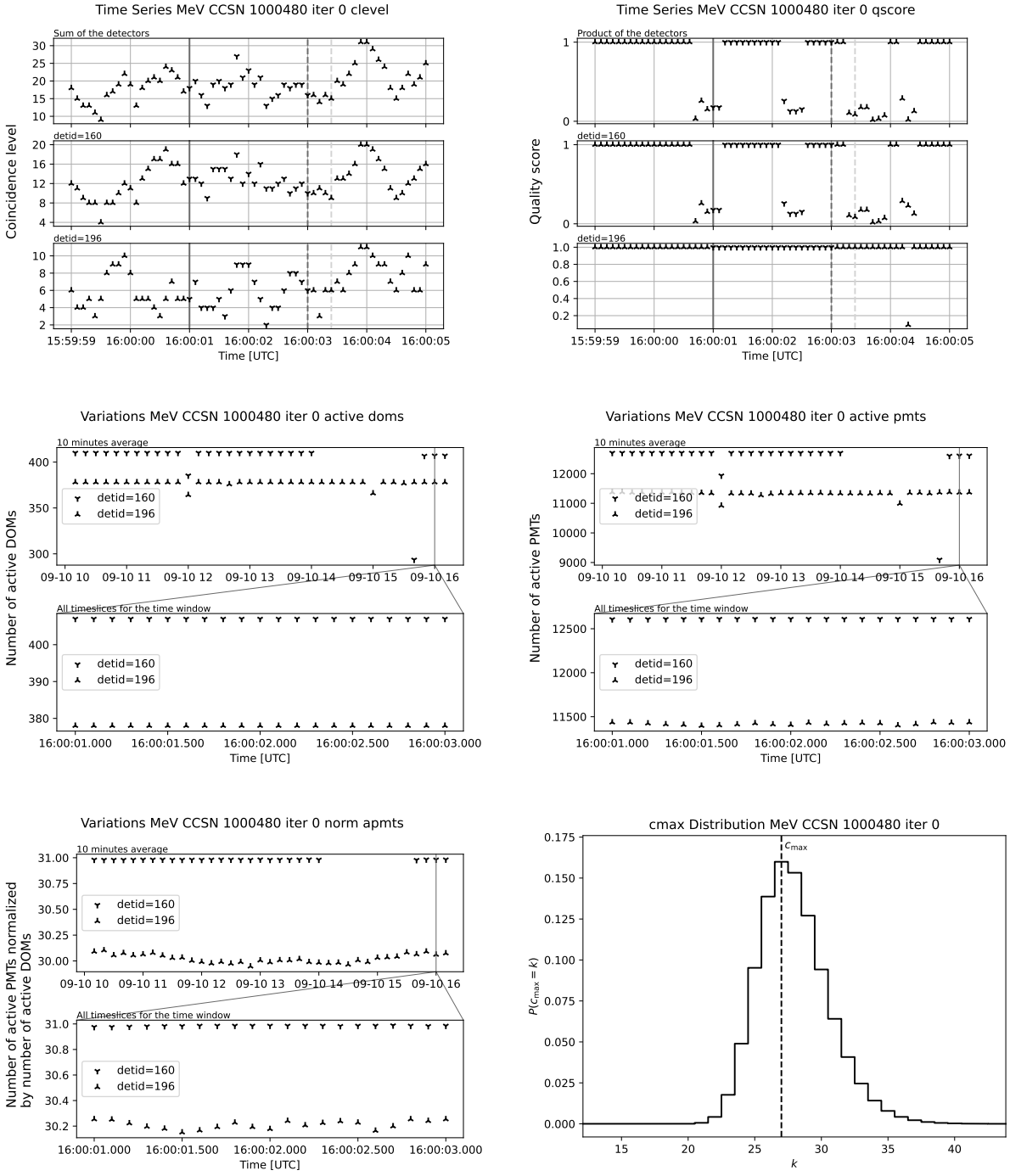

Figure 2.27.: Results reports for the triggered follow-up searches. Time series distribution for the coincidence levels and quality score during the search time window (top), time distributions for the averaged number of active DOMs, number of active PMTs and normalized number of active PMTs (middle and bottom left) and c_{max} distribution for the expected background (bottom right).

2C. Searches for MeV neutrino burst counterparts

> Jpp: the software that should make you happy, alternatively « j'en peux plus », french for "I cannot anymore".

Alongside the development of the triggered follow-up search pipeline, the method was applied to offline data to search for counterparts to specific events. The first analysis is the search for a correlation between neutrinos and gravitational waves for the ORCA detector between July 2019 and March 2020. The second analysis is the follow-up of GRB 221009A, the brightest gamma-ray burst ever observed.

2C.1. Gravitational waves from the LIGO/Virgo third observing run

Some models predict the production of neutrinos during the compact mergers of binary neutron stars (BNS) [78], neutron star-black hole (NSBH) [79] and even binary black holes (BBH) [80]. The predicted energies are above the GeV range, but the production of thermal neutrinos in the MeV range is also possible [81].

The GW detectors LIGO and Virgo were performing their third observing run (O3) in 2019 and 2020. During O3, the ORCA detector went through three configuration. The detector was taking data with two lines (ORCA2) before July 1, with four lines (ORCA4) during the period from July 1, 2019 to January 17, 2020, and with six lines (ORCA6) after until 2021. The ORCA2 configuration is not large enough to perform a proper search, and the ARCA detector was not taking data available for physics analysis.

2C.1.1. The gravitational wave catalogs

Candidate binary mergers detected during O3 by the LIGO and Virgo GW detectors are reported in three catalogs:

- GWTC-2 [82] reports 39 significant detections from April to September 2019;
- GWTC-2.1 [83] updates the previous catalog with eight additional events;

– GWTC-3 [84] reports 35 significant detections from November 2019 to March 2020 and seven marginal candidates. Out of those candidates, GW200105_162426 was identified as a possible NSBH and is therefore included in the analysis.

The data from the catalogs contains information for each GW event including the timing t_{GW}, the localization skymap $P(\Omega)$, luminosity distance D_L, masses m_1 and m_2 and total radiated energy in GWs E_{GW} (defined as the difference between the final object mass and the sum of the masses of the initial objects). Each event is categorized as a BNS, NSBH or BBH from the estimated individual masses of the objects. An arbitrary boundary $m = 3\,M_\odot$ separates the neutron stars and the black holes.

The ORCA4 data-taking period overlaps with 19, 6, and 17 GW events, respectively in the GWTC-2, GWTC-2.1, and GWTC-3 catalogs ORCA6 overlaps with 19 GW events from the GWTC-3 catalog. This leads to a total of 61 GW events.

2C.1.2. Search time window

Models for prompt MeV neutrino emission from binary mergers predict the most of the signal to be emitted in tens of milliseconds after the merger [81, 85]. As such, the only delay between the GW and neutrino detection considered is the time-of-flight difference ΔT_{flight} between the two. Assuming that GW propagate at the speed of light,

$$\Delta T_{flight} < D_{max}\left(\frac{1}{v_\nu} - \frac{1}{c}\right) = \frac{D_{max}}{c}\left(\sqrt{1 + \frac{m_\nu^2 c^4}{p_\nu^2 c^2}} - 1\right) \approx \frac{1}{2}\frac{D_{max}}{c}\frac{m_\nu^2 c^4}{E_\nu^2}, \quad (2.30)$$

where D_{max} is the estimated upper distance of the farthest GW source, v_ν, m_ν, p_ν, and E_ν are respectively the speed, mass, momentum, and energy of the neutrino. The current constraints on the absolute neutrino mass [86, 87] give an upper limit for the heavier neutrino in the order of 0.1 eV. With an upper distance D_{max} of around 1 Gpc and a neutrino energy in the tens of MeV, the maximum time-of-flight difference is $\Delta T_{flight} \lessapprox 1\,s$. The chosen search time window is $[0, +2\,s]$ to be a bit more conservative.

2C.1.3. Run selection

The KM3NeT detectors take data in consecutive runs of a few hours. For each GW event, data for the full run is retrieved with a custom software based

on the *supernova processor* module. Data acquisition issues prevented the retrieval of five runs. One additional GW event was removed because of a low quality score during the 2 s time window. The analysis is thus done on the 55 remaining GW events.

2C.1.4. Background characterization

The GW analysis was performed before the development of the new adaptive background method presented previously (subsection 2B.2.2). As such, the characterization relies on the expected background as a function of the fraction of active PMTs. The relation between these quantities is shown in Figure 2.28 for the two detector configurations. Every dot is the computed background averaged for the whole detector, for a given range of fraction of active PMTs The data is taken from around 200 runs, uniformly distributed in the ORCA4 and ORCA6 data-taking periods.

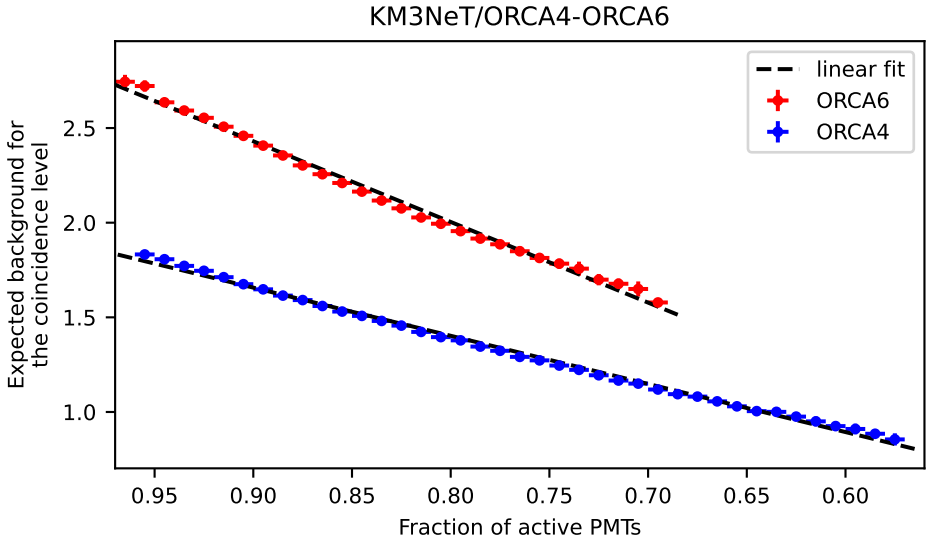

Figure 2.28.: Expected background of the coincidence level as a function of the fraction of active PMTs for ORCA4 (blue) and ORCA6 (red). The crosses indicate averaged values over the full periods, and the dashed lines are linear fits to these points.

The expected background for each run is inferred from the fraction of active PMTs and the linear fits shown Figure 2.28. The coincidence level distribution from each run (removing the search time window) is compared to the expected coincidence level distribution. The agreement is found sufficient for most of

the runs. The six runs between December 19, 2019 and January 25, 2020 show however a disagreement. The cause is a network issue between the ORCA detector and the shore station at the beginning of the ORCA6 data taking. For the six runs, the fraction of active PMTs is relatively stable and the expected background is taken directly from data.

2C.1.5. Analysis principle

The analysis is identical to the one done in real time (see triggered follow-up search, section 2B.5). The 20 coincidence levels in the $[0, +2\,\mathrm{s}]$ time window and the associated maximum c_{max} are retrieved for each GW event. An example coincidence level time distribution is given left of Figure 2.29. The expected background $\bar{b}_c$ for each timeslice is inferred from the averaged fraction of active PMTs during the 2 s time window. Figure 2.30 shows an example of time distribution and distribution of fraction of active PMTs for the full run and for the time window. The high stability of fraction of active PMTs ensures that the right expected background is computed.

Pseudo-experiments are used to estimate the expected distribution of c_{max} assuming only background and background + signal. Multiple c_{max} distribution for different $\bar{b}_c$ are shown right of Figure 2.29. From the measured c_{max} and the obtained distributions, the p-value p and the upper limit are computed. The 90 % confidence level upper limit on the number of coincidences due to a neutrino signal $\mu_{\mathrm{sig}}^{90\%}$ is estimated using the Feldman-Cousins [88] statistical approach.

Two physical upper limits are computed: the total neutrino fluence $\Phi^{90\%}$ and the total energy emitted in MeV neutrinos by the source $E_{\mathrm{tot},\nu}^{\mathrm{iso},90\%}$. The two values are computed from the number of expected signal events $\mu_{\mathrm{sig,\ full\ det}}(E_0, D_{L,0})$ for a reference CCSN and a full ORCA detector (115×18 DOMs). The reference CCSN is at a distance $D_{L,0}$, with a neutrino fluence Φ_0 and a total released neutrino energy E_0. The detector is considered to be working with perfect efficiency with perfect efficiency ($\eta = 1$, where η is the ratio of the measured expected background to the one when all PMTs are active). The upper limits are obtained by scaling the obtained upper limit $\mu_{\mathrm{sig}}^{90\%}$ with the reference

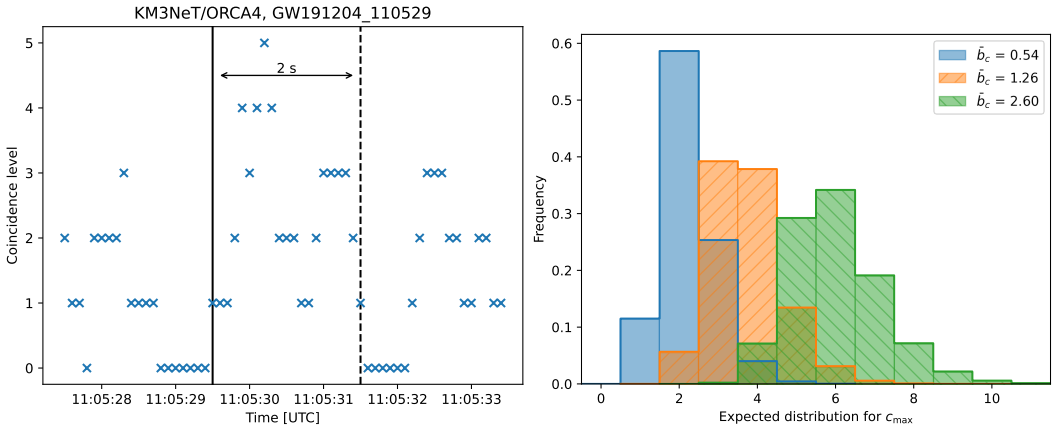

Figure 2.29.: Time distribution of the coincidence levels around GW101204_110529 (left) and distribution of the maximum coincidence level c_{max} for different values of the expected background $\bar{b}_c$ (right). On the left, the solid black line indicates the GW event time, and the dashed black line is the end of the 2 s time window during which the search is made.

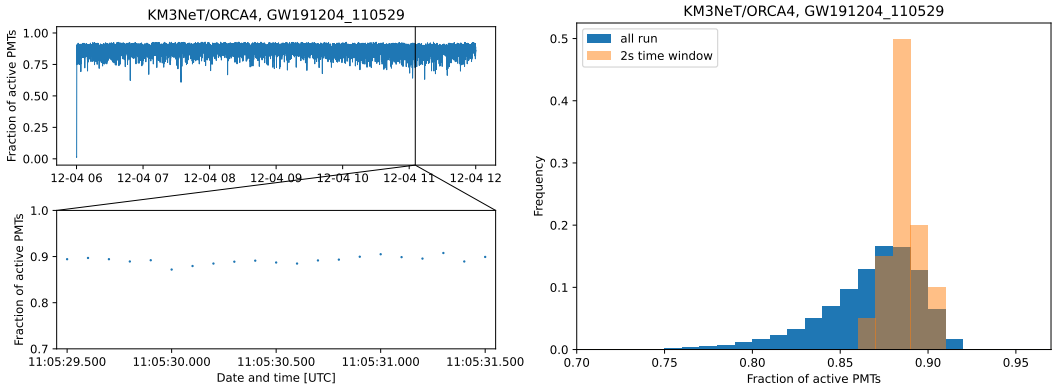

Figure 2.30.: Time series (left) and distribution (right) of the fraction of active PMTs for the run covering GW191204_110529. On the left, the top plot shows the variability of the fraction of active PMTs during the run while the bottom plot is a zoom on the 2 s time window starting from the GW event time. On the right, the distribution of the fraction of active PMTs is shown in blue for every timeslice of the run and in orange for the 20 timeslices inside the 2 s time window.

values:

$$\Phi^{90\%} = \frac{115 \times 18}{n_{\text{active DOMs}}} \times \frac{1}{\eta} \times \frac{\mu_{\text{sig}}^{90\%}}{\mu_{\text{sig, full det}}(E_0, D_{L,0})} \times \Phi_0 \tag{2.31}$$

$$E_{\text{tot},\nu}^{\text{iso},90\%} = \frac{115 \times 18}{n_{\text{active DOMs}}} \times \frac{1}{\eta} \times \frac{\mu_{\text{sig}}^{90\%}}{\mu_{\text{sig, full det}}(E_0, D_{L,0})} \times \frac{D_L^2}{D_{L,0}^2} \times E_0 \tag{2.32}$$

The values are computed from refined simulations based on the work done in [89, 90], assuming a quasi-thermal emission of electron anti-neutrinos: $\mu_{\text{sig, full det}}(E_0, D_{L,0}) = 132.5$, $D_{L,0} = 10\,\text{kpc}$, $\Phi_0 = 8.2 \times 10^{10}\,\text{cm}^{-2}$, and $E_0 = 3 \times 10^{53}\,\text{erg}$.

2C.1.6. Results

The results are presented Table 2.5 and Table 2.6. Only four events have a p-value lower than 0.2, with a minimum of 0.02, which is fully compatible with the background expectation. For the considered 2 s time window, the upper limits on the neutrino fluence range between 10^{10} and $10^{11}\,\text{cm}^{-2}$. The total energies emitted in neutrinos range between 10^{60} and $10^{63}\,\text{erg}$, as reported in Figure 2.31.

The search for neutrino counterparts to the GW events of the O3 catalog was also performed in the GeV–TeV energy range. No excess was found either, but upper limits were also reported in a joint publication [46]. The ranges of upper limits are reported Figure 2.32, along with the limits found by the ANTARES [91], IceCube [92] and Super-Kamiokande [93] collaborations. In the MeV range, the obtained limits are of the same order as the ones reported by KamLAND [94], although one to two orders of magnitude worse than Super-Kamiokande's. However, the sensitivity is directly proportional to the size of the detector (see Equation 2.31) and KM3NeT will reach a similar sensitivity as Super-Kamiokande at the end of its construction.

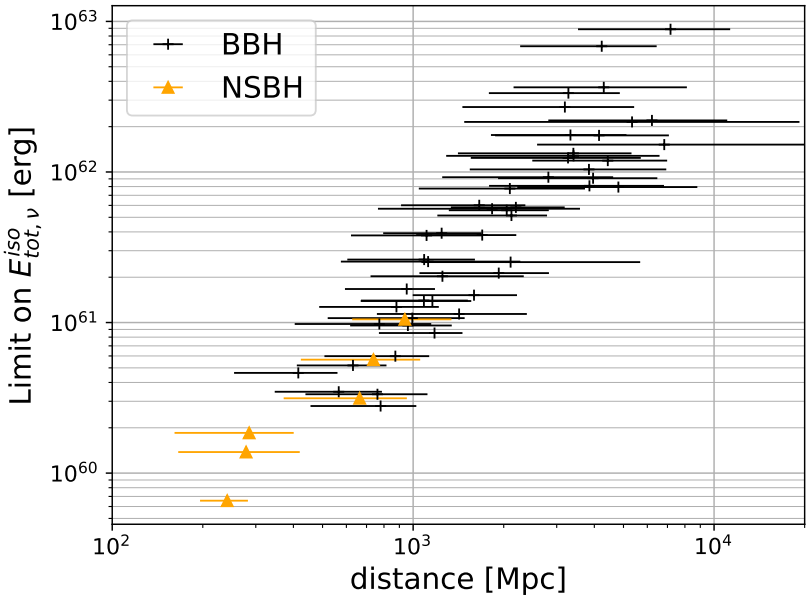

Figure 2.31.: 90% upper limits on the total energy $E^{iso}_{tot,\nu}$ emitted in neutrinos, as a function of the source luminosity distance, assuming a quasi-thermal distribution centered at 13 MeV and isotropic emission.

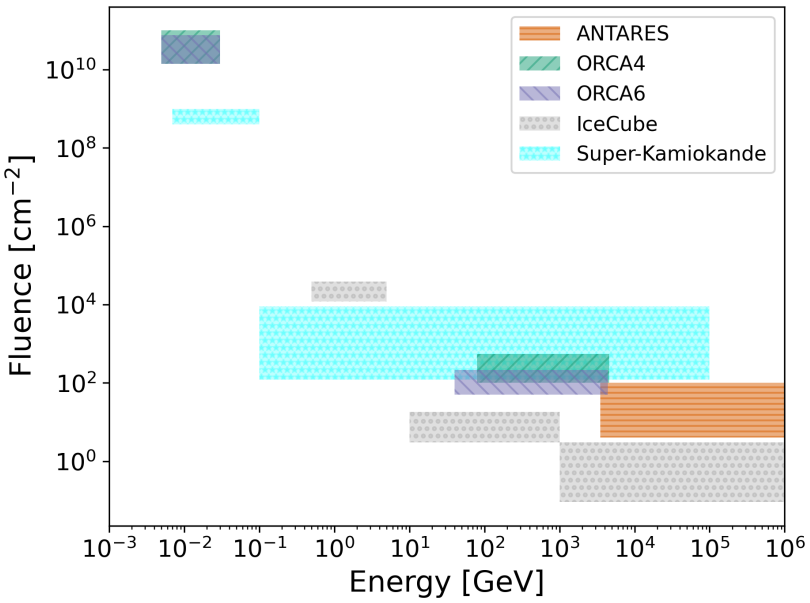

Figure 2.32.: Range of 90% upper limits on the total neutrino fluence for ORCA4, ORCA6, ANTARES, IceCube and Super-Kamiokande. The horizontal widths of the bands delimit the central energy range expected to contain 90% of the signal events (except for the IceCube and Super-Kamiokande results where the full sensitive range is shown) [46].

Table 2.5.: Results for the search for MeV neutrino bursts as counterparts for gravitational waves from O3. For each GW event, the third and fourth columns give the expected background $\bar{b}_c$ and the maximum observed coincidence level $c_{\max}$ during the 2 s window after the GW event. The next two columns report the False Alarm Rate (FAR, number of times per day one expects to observe $c_{\max}$ coincidences originating only from background) and the p-value. The last two columns provide the obtained upper limits on the neutrino emission, in terms of the incoming fluence and the total energy emitted in neutrinos.

GW name	Merger type	$\bar{b}_c$	$c_{\max}$	FAR [d^{-1}]	p	$\Phi^{90\%}$ [cm^{-2}]	$E^{iso,90\%}_{tot,\nu}$ [erg]
ORCA4 period							
GW190701_203306	BBH	1.44	4	5.04×10^4	0.70	3.6×10^{10}	5.6×10^{61}
GW190706_222641	BBH	1.63	3	1.94×10^5	0.99	1.7×10^{10}	1.2×10^{62}
GW190707_093326	BBH	1.75	5	2.84×10^4	0.49	4.5×10^{10}	9.8×10^{60}
GW190708_232457	BBH	1.76	5	2.90×10^4	0.50	4.5×10^{10}	1.3×10^{61}
GW190719_215514	BBH	1.70	3	2.10×10^5	1.00	1.6×10^{10}	9.1×10^{61}
GW190725_174728	BBH	0.84	4	9.24×10^3	0.19	9.4×10^{10}	3.8×10^{61}
GW190727_060333	BBH	0.94	4	1.34×10^4	0.27	8.4×10^{10}	3.3×10^{62}
GW190728_064510	BBH	1.26	3	1.16×10^5	0.94	2.2×10^{10}	6.0×10^{60}
GW190731_140936	BBH	1.66	4	7.54×10^4	0.84	3.1×10^{10}	1.2×10^{62}
GW190805_211137	BBH	1.55	7	9.64×10^2	0.02	8.6×10^{10}	8.9×10^{62}
GW190814	NSBH	1.66	4	7.54×10^4	0.84	3.1×10^{10}	6.6×10^{59}
GW190828_063405	BBH	1.67	4	7.67×10^4	0.84	3.1×10^{10}	5.1×10^{61}
GW190828_065509	BBH	1.68	3	2.05×10^5	1.00	1.6×10^{10}	1.5×10^{61}
GW190909_114149	BBH	1.23	1	6.11×10^5	1.00	2.0×10^{10}	1.0×10^{62}
GW190917_114630	NSBH	1.73	4	8.44×10^4	0.87	3.0×10^{10}	5.7×10^{60}
GW190924_021846	BBH	1.77	4	8.98×10^4	0.89	2.9×10^{10}	3.5×10^{60}
GW190925_232845	BBH	1.71	4	8.18×10^4	0.86	3.0×10^{10}	9.6×10^{60}
GW190926_050336	BBH	1.79	3	2.30×10^5	1.00	1.5×10^{10}	7.9×10^{61}
GW190929_012149	BBH	1.79	3	2.30×10^5	1.00	1.5×10^{10}	2.5×10^{61}
GW190930_133541	BBH	1.72	3	2.14×10^5	1.00	1.6×10^{10}	3.3×10^{60}
GW191103_012549	BBH	1.73	4	8.44×10^4	0.87	3.0×10^{10}	1.1×10^{61}
GW191105_143521	BBH	1.80	4	9.39×10^4	0.90	2.9×10^{10}	1.4×10^{61}
GW191109_010717	BBH	1.24	4	3.23×10^4	0.53	4.2×10^{10}	2.5×10^{61}
GW191113_071753	BBH	1.75	4	8.71×10^4	0.88	3.0×10^{10}	2.0×10^{61}
GW191126_115259	BBH	1.26	5	8.14×10^3	0.17	6.3×10^{10}	6.0×10^{61}

Table 2.6.: Continuation of Table 2.5.

GW name	Merger type	$\bar{b}_c$	$c_{\max}$	FAR [d^{-1}]	p	$\Phi^{90\%}$ [cm^{-2}]	$E^{iso,90\%}_{tot,\nu}$ [erg]
ORCA4 period (continued)							
GW191127_050227	BBH	1.71	4	8.18×10^4	0.86	3.0×10^{10}	1.3×10^{62}
GW191129_134029	BBH	1.78	1	7.18×10^5	1.00	1.1×10^{10}	2.4×10^{60}
GW191204_110529	BBH	1.64	5	2.24×10^4	0.41	4.8×10^{10}	5.7×10^{61}
GW191204_171526	BBH	1.54	4	6.11×10^4	0.77	3.4×10^{10}	5.2×10^{60}
GW191215_223052	BBH	1.74	3	2.19×10^5	1.00	1.6×10^{10}	2.1×10^{61}
GW191219_163120	NSBH	0.96	2	2.16×10^5	1.00	2.8×10^{10}	3.1×10^{60}
GW191222_033537	BBH	0.97	2	2.19×10^5	1.00	2.8×10^{10}	9.2×10^{61}
GW191230_180458	BBH	1.05	5	3.88×10^3	0.09	1.0×10^{11}	6.8×10^{62}
GW200105_162426	NSBH	1.14	4	2.49×10^4	0.44	6.9×10^{10}	1.9×10^{60}
GW200112_155838	BBH	1.15	4	2.56×10^4	0.45	6.9×10^{10}	3.9×10^{61}
GW200115_042309	NSBH	1.15	3	9.49×10^4	0.90	4.5×10^{10}	1.4×10^{60}
ORCA6 period							
GW200128_022011	BBH	1.21	3	1.06×10^5	0.93	6.4×10^{10}	2.7×10^{62}
GW200129_065458	BBH	1.23	3	1.10×10^5	0.93	3.3×10^{10}	9.8×10^{60}
GW200202_154313	BBH	0.54	1	3.61×10^5	1.00	7.5×10^{10}	4.6×10^{60}
GW200208_130117	BBH	1.27	3	1.18×10^5	0.95	3.2×10^{10}	5.8×10^{61}
GW200208_222617	BBH	1.30	4	3.72×10^4	0.59	5.9×10^{10}	3.7×10^{62}
GW200209_085452	BBH	1.29	2	3.19×10^5	1.00	3.2×10^{10}	1.3×10^{62}
GW200210_092254	NSBH	1.25	2	3.07×10^5	1.00	3.3×10^{10}	1.1×10^{61}
GW200216_220804	BBH	2.39	2	5.96×10^5	1.00	1.5×10^{10}	8.1×10^{61}
GW200219_094415	BBH	1.86	4	1.02×10^5	0.92	4.2×10^{10}	1.8×10^{62}
GW200220_061928	BBH	2.43	4	1.97×10^5	0.99	1.7×10^{10}	2.2×10^{62}
GW200220_124850	BBH	2.58	5	1.03×10^5	0.92	3.0×10^{10}	1.8×10^{62}
GW200224_222234	BBH	2.17	5	5.99×10^4	0.76	3.6×10^{10}	3.8×10^{61}
GW200225_060421	BBH	2.18	6	2.07×10^4	0.38	5.4×10^{10}	2.6×10^{61}
GW200302_015811	BBH	2.57	3	4.10×10^5	1.00	1.6×10^{10}	1.3×10^{61}
GW200306_093714	BBH	2.45	6	3.35×10^4	0.55	4.8×10^{10}	7.8×10^{61}
GW200308_173609	BBH	2.56	3	4.07×10^5	1.00	1.4×10^{10}	1.5×10^{62}
GW200311_115853	BBH	2.39	4	1.89×10^5	0.99	1.7×10^{10}	8.5×10^{60}
GW200316_215756	BBH	2.53	5	9.75×10^4	0.91	3.1×10^{10}	1.4×10^{61}
GW200322_091133	BBH	2.60	6	4.24×10^4	0.63	4.5×10^{10}	2.2×10^{62}

2C.2. GRB 221009A: the Brightest γ-ray burst Of All Times

After the ratification of the Partial Test Ban Treaty in 1963, the Soviet Union, United Kingdom and United States were prohibited to test nuclear weapons in the atmosphere, in outer space and under water. To monitor the upholding of the treaty, the United States launched satellites to monitor signature gamma radiation on Earth. However, the *Vela 3* and *Vela 4* satellites detected for the first time a gamma-ray burst from a direction outside of the solar system.

Gamma-ray bursts are among the most luminous objects in the Universe. The gamma-ray emission can last between 0.01 and 10 000 s. After the initial flash, an afterglow can usually be observed in the other frequencies. Gamma-ray bursts are classified in two categories depending on the gamma emission length. Events with a duration below 2 s are classified as short GRBs. They account for 30 % of all observed GRBs. The nature of short GRBs was proved through the multi-messenger observation of GW170817 to come from the merger of binary neutron stars and the production of a kilonova [30]. The remaining 70 % are long GRBs. They are almost always linked to galaxies with high rate of star formations and often to CCSN. The origin of long GRBs is most likely related to the death of massive stars.

2C.2.1. GRB 221009A

GRB 221009A is the brightest gamma-ray burst ever observed. Its detection was first reported by the Fermi gamma telescope on October 9, 2022 at 13:16:59.0 UTC (T_0 hereafter) through a GCN Notice before being confirmed by the Swift telescope [95]. A large follow-up campaign was conducted to characterize the afterglow in X-ray [96], optical [97, 95] and radio [98]. Its origin is most likely an extra-galactic CCSN [99].

The event has been called by the scientific community the brightest of all time, or BOAT [100]. GRB 221009A is the brightest ever detected in term of peak flux and fluence. The Fermi telescope detected for the first time photons close to 99 GeV, and the brightness caused the saturation of most of its instruments. The LHAASO Water Cherenkov Detector Array even reported photons up to 13 TeV [101]. By extrapolation of GRB distribution, the BOAT appears to be a once-in-10000-year event [100].

The light curve measured by the Fermi telescope is presented Figure 2.33. As a comparison, the light curve for the second brightest GRB ever measured, GRB 130427A is shown in green. The brightest portion of the light curve

are reconstructed from the saturation observed by the Fermi instruments. The light curve is composed from a first isolated peak followed by multiple pulses of emission. The 90 % central emission of the GRB is comprised within $T_{90} = 327\,s$.

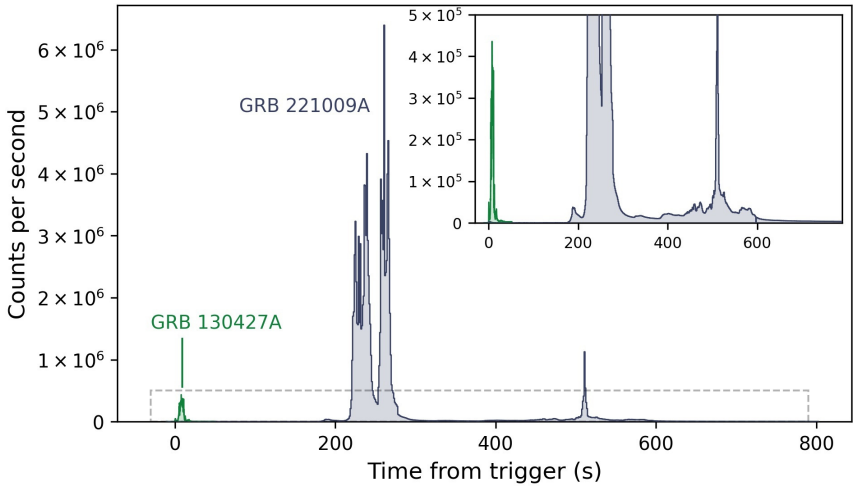

Figure 2.33.: Fermi Gamma-Ray Burst Monitor light curves of the two brightest GRBs ever recorded. [102]

2C.2.2. Search method

At the time of GRB 221009A, ARCA and ORCA were respectively operating with 21 and 10 DUs. The KM3NeT Collaboration performed a real-time search for neutrino emission in the $[T_0 - 50\,s,\ T_0 + 5000\,s]$ time window. No candidate events were detected, and the results were reported in [103].

A refined search was performed from offline files and additional time windows. The following presents the methods and results for the search of MeV neutrinos.

The method follows the same principle as the triggered follow-up searches (section 2B.5) and GW follow-up. The search for MeV neutrinos is made considering two time windows: $[T_0,\ T_{90}]$ and $[T_0 - 50\,s,\ T_0 + 5000\,s]$, the latter covering the high-energy emission seen by Fermi and LHAASO [104]. The background is characterized from the new AB method (subsection 2B.2.2) using 30 days of data of both detectors around T_0. The expected background and coincidence levels of ARCA and ORCA are summed, and the maximum coincidence level is searched directly on the sum of the two detectors. Toy

experiments are used to compute the distribution of maximum coincidence level. The associated p-value and upper limits are computed with the same method used in the GW follow-up.

2C.2.3. Results

The results are shown Table 2.7. Contrary to the GW follow-up, the expected background reported is the mean of the distribution of maximum coincidence levels. The time distributions for the coincidence level are reported Figure 2.34 and Figure 2.35, respectively for the two time windows. The maximum is reached 5 times for the T_{90} time window. No significant excess is found and upper limits are reported. The results were published in [47].

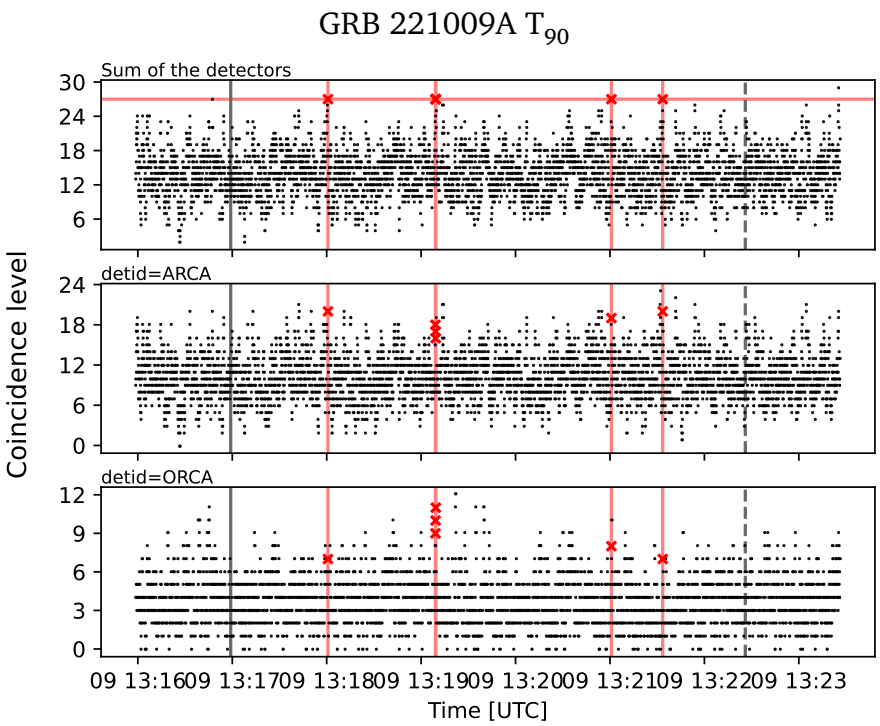

Figure 2.34.: Time distribution for the coincidence level during the [T_0, T_{90}] time window after GRB 221009A. The red lines indicate the found maxima.

Table 2.7.: Results for the MeV counterpart search to GRB 221009A.

Time window	Maximum coincidence level	Expected background	p-value	Total $\bar{\nu}_e$ flux [cm^{-2}]	$E^{iso,90\%}_{tot,\nu}$ [erg]
T_{90}	27	29	0.99	2.5×10^9	5.1×10^{62}
T_0 [−50 s, 5000 s]	32	33	0.79	4.8×10^9	9.7×10^{62}

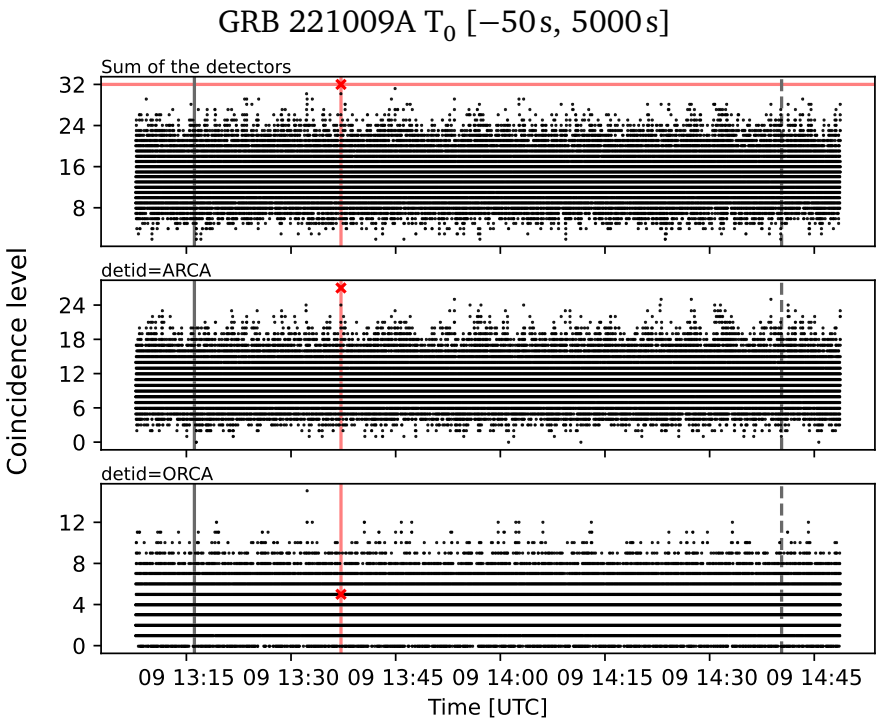

Figure 2.35.: Time distribution for the coincidence levels during the [−50 s, 5000 s] time window around GRB 221009A. The red line indicate the found maximum.

Conclusion and prospects

Despite partial detectors, KM3NeT is currently sensitive to the detection of a CCSN within the Galactic edge. Within the next years, the detectors will grow and the sensitivity will reach the Large Magellanic Cloud. To this day, the KM3NeT CCSN online pipeline is running and monitoring the sky. In the event of a CCSN, an internal alert would be registered. The alerts will be transmitted to the SNEWS network as soon as the new coincidence system is deployed. The full data at disposal for the water Cherenkov detectors would be retrieved, to be analyzed to further characterize the CCSN. Triggered follow-up searches are also performed for every GW event thought to involve a neutron star and for every alert related to CCSN detection. Those events also trigger the retrieval of the full detector data. The design and implementation of the CCSN online pipeline led to a publication describing it in *Eur. Phys. J. C* [90].

I was personally responsible for the development and maintenance of the CCSN online pipeline. In particular I:

- deployed the *supernova processor* module to the ARCA shore station;
- rewrote the combination algorithms between the two detectors data queues;
- investigated the impact of the quality score on data;
- devised a new method to properly characterize the optical background for the different detectors configurations;
- developed the trigger and retrieval of coincidences with higher statistics;
- represented KM3NeT to the SNEWS collaboration;
- overall maintained all the different software and adapted them with each detector upgrade.

The work was presented in multiple conferences (LIA-ERIDANUS Virtual Workshop 2021, Neutrino 2022, Neutrinos in the Multi-Messenger Era, Transient Universe Summer School and ICRC 2023), as oral communications, posters and proceedings.

Building on top of the infrastructure in place, further improvement will come in the near future. New dedicated observables built from DOM coincidences improve the KM3NeT distance horizon by 23 % [105]. This new method is currently implemented within the CCSN pipeline for commissioning purposes.

Work is also being done on tuning the alert threshold to reach a rate closer to 1 per 8 days.

The first searches for MeV burst counterparts to GW events were also performed and described for the first time in a publication to *J. Cosmol. Astropart. Phys.* [46]. A follow-up search was also made for the exceptional event GRB 221009A, and the results were also published to *J. Cosmol. Astropart. Phys.* [47]. Both MeV analyses were conducted entirely by me.

As SNEWS2.0 further develops, KM3NeT will participate to alerts with multiple false alarm rate. The combination of temporal information will also enable the triangulation to potential CCSN, which will improve the coordinated response in the astronomy community. Let's prepare a future where everyone is ready for the event of the century!

Chapter 3.

Neutrino alerts within the KM3NeT Online Program

Introduction

This chapter first presents some context about the key players and the used methods in the observation of multi-messenger transients, in section 3A.

The KM3NeT Online Multi-Messenger Program is then presented in section 3B. The Online Multi-Messenger Program aims to process events in real-time to be able to respond as fast as possible to external observations and to broadcast neutrino alerts. Events from both ARCA and ORCA can be reconstructed and classified in less than 10 s. All events and associated data are stored in a database, which can be used to perform ON/OFF searches triggered by external observations.

The work performed on the KM3NeT neutrino alerts is presented section 3C. Some context is first given on neutrino alerts transmitted by other detectors. Compared to them, the strategy chosen for the KM3NeT alerts consists of selecting neutrinos both on the neutrino properties and the properties of the potential sources of origin. Two neutrino selection methods are introduced: one to select high-energy track-like events with the ARCA detector, and one to detect neutrino multiplets with the ORCA detector. Finally, a prototype for the retrieval of astronomical data is presented.

Contents

3A. Real-time strategies for multi-messenger transient observations . . 129
3A.1. Observation facilities 129
3A.1.1. Neutrino telescopes 129
3A.1.2. GW detection 130

3A.1.3. Very high energy γ-ray telescopes . . . 131
3A.1.4. γ- and X-ray telescopes . . . 132
3A.1.5. Robotic telescopes . . . 133
3A.1.6. Radio telescopes . . . 134
3A.2. Communication methods . . . 134
3A.2.1. General Coordinates Network . . . 134
3A.2.2. Alert brokers . . . 135
3A.2.3. Additional methods . . . 136
3A.3. Prospects for the near future of astronomy alerts . . . 136

3B. The KM3NeT Online Multi-Messenger Program . . . 136
3B.1. Online GeV-PeV event processing . . . 137
3B.1.1. Database storage . . . 139
3B.1.2. Monitoring tools . . . 141
3B.2. Automatic follow-up pipeline . . . 141
3B.2.1. Principle of the ON/OFF method . . . 142
3B.2.2. Selection of external triggers . . . 143
3B.2.3. Follow-up results . . . 144

3C. KM3NeT neutrino alerts . . . 147
3C.1. Context within the multi-messenger landscape . . . 147
3C.1.1. ANTARES . . . 147
3C.1.2. IceCube . . . 148
3C.2. Strategy for the KM3NeT neutrino alerts . . . 150
3C.2.1. Strengths of KM3NeT . . . 150
3C.2.2. Maximizing the scientific interest of alerts . . . 151
3C.2.3. Selecting alerts and false alarm rates . . . 152
3C.3. Pure neutrino alert selection . . . 154
3C.3.1. High-energy selection . . . 154
3C.3.2. Search for multiplets . . . 159
3C.4. Multi-wavelength correlation . . . 160
3C.4.1. Proof of concept . . . 161
3C.4.2. Available multi-wavelength data . . . 162
3C.4.3. Prototype module . . . 165
3C.4.4. Example application to KM3-230213A . . . 167

3A. Real-time strategies for multi-messenger transient observations

The diverse nature of cosmic messengers leads to an important variety of observation methods and facilities. Coordination is necessary to collect as much data as possible to study and discriminate the physical processes present in the sources.

3A.1. Observation facilities

The following presents some key players in past and present multi-messenger observations. The experiments are chosen subjectively and do not constitute an exhaustive list. Additionally, some future observation facilities are discussed.

3A.1.1. Neutrino telescopes

Neutrino astronomy was marked during the last decade by the results of the IceCube neutrino telescope. The IceCube neutrino telescope is a km^3 volume of ice instrumented with 10 inches single-PMT optical modules. The sensors are located under the Antarctic Ice, at the South Pole. The IceCube collaboration announced in 2013 the detection of the first astrophysical neutrinos with energies between 30 and 1200 TeV [14]. The first measurement of the diffuse astrophysical neutrino flux and the first observation of a neutrino in coincidence with a celestial object were also performed by IceCube. Both are presented in more details in chapter 1.

The ANTARES neutrino telescope also participated in the search for cosmic neutrinos. ANTARES is a first-generation telescope which operated in the Mediterranean Sea until 2022. Despite its smaller volume compared to IceCube, it was able to constrain the neutrino diffuse flux [106] and to give a hint of the galactic diffuse flux [107].

In addition to KM3NeT, another water Cherenkov neutrino telescope is being built in the Baikal lake, in Russia. The Baikal Gigaton Volume Detector (Baikal-GVD) aims to instrument one km^3 of water with around two thousand 37 cm photo-multipliers. KM3NeT and Baikal-GVD are expected to have a higher angular resolution than IceCube thanks to the lower scattering length of water. This will be useful to further probe the regions of neutrino emission of the already identified sources.

An approximate timeline for the instrumented volume of neutrino telescope is presented Figure 3.1. Over the next decade, the volume could be multiplied by 20. The Pacific Ocean Neutrino Explorer (P-ONE) is a planned water Cherenkov neutrino telescope off the west coast of Canada [108]. The principle is quite similar to KM3NeT, with lines of multi-PMT optical modules and a buoy attached at the top. The first instrumented line is planned to be deployed and tested within 2025. Other projects like TRIDENT [109] or HUNT [110] have the goal to reach volumes in the tens of km^3 but are currently only in the detector conception phase.

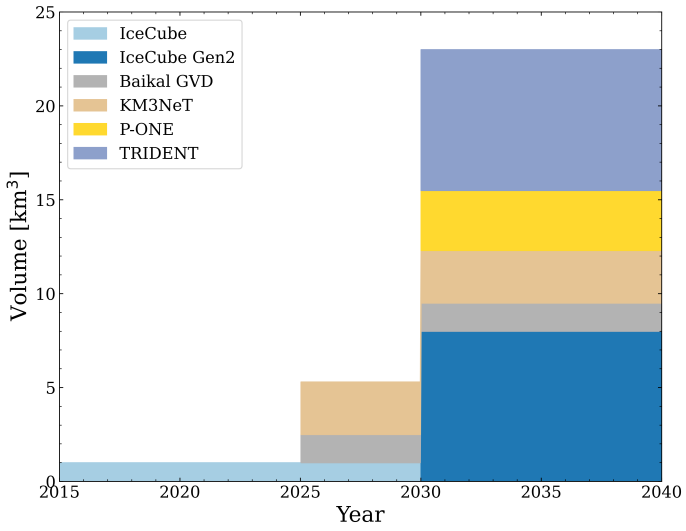

Figure 3.1.: Projection of the volume of ice/water high-energy neutrino telescope as a function of time. [111]

Finally, the IceCube collaboration plans to upgrade its current detector in the following years. Seven new strings with new multi-PMTs optical modules should be added in December 2025 [112]. IceCube-Gen2 will go further with 120 further spaced strings and a radio array [113]. The radio array is designed to detect Askaryan radiation [114], a coherent radio emission associated with neutrinos above 10 PeV.

3A.1.2. GW detection

As discussed in chapter 1, the only current detectors sensible to gravitational waves are the two LIGO detectors in the USA, Virgo in Italy and KAGRA in Japan. The LIGO-Virgo-KAGRA (LVK) collaboration schedules detectors operation

in observing runs limited in time. Between each observing run, operation is stopped to upgrade and commission every detector. Figure 3.2 shows the timeline for the different observing runs with the associated sensitivities of each detector. Compared to the third observing run in 2019 and 2020, the sensitivity and associated number of sent public alerts could more than double by 2030.

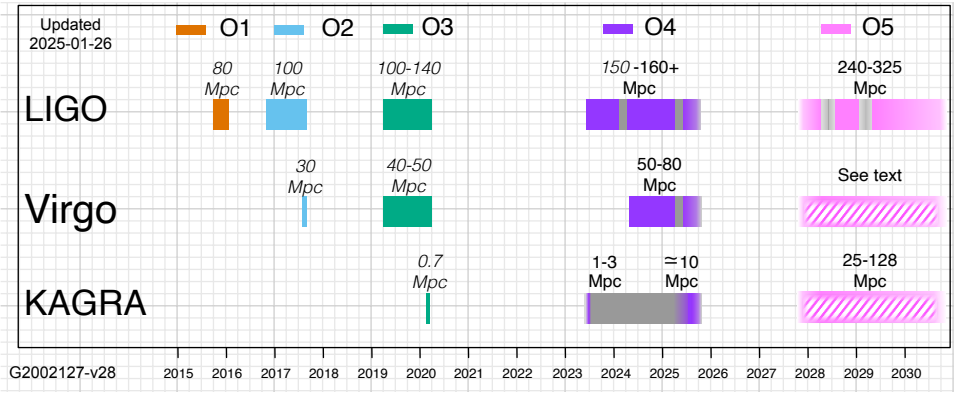

Figure 3.2.: Planned sensitivity evolution and observing runs of the LIGO, Virgo and KAGRA detectors over the coming years. The colored bars show the observing runs with the associated observed or planned sensitivities. [115]

The localization of the objects involved in GW emission rely on a triangulation performed by the different GW detectors. As such, the localization is often imprecise, with an 90 % containment region reaching sometimes more than half the sky.

3A.1.3. Very high energy γ-ray telescopes

Above 100 GeV energy, cosmic- and γ-ray induce particle showers when entering the atmosphere. The so-called *air showers* can be detected to retrieve the incoming particle's energy and direction. Two main detection methods are currently used: the detection of the secondary particles from the air shower and the imaging air Cherenkov technique.

The HAWC [116], Pierre Auger [117] and LHAASO [118] observatories all detect secondary particles from air showers. They consist of an array of tanks of water spread over large areas (*e.g.* around 3000 km^3 for Pierre Auger) containing PMTs. The secondary particles are detected through their associated Cherenkov emission. In addition, the Pierre Auger Observatory can

observe air showers structure from the side during moonless nights. Inside air showers, nitrogen molecules from the atmosphere get excited and emit UV light through fluorescence. The light can be collected from different locations to better reconstruct the shower geometry. This enables improved energy resolution.

Imaging air Cherenkov telescopes detect the Cherenkov radiation emitted by the air shower particles as they propagate. To do so, multiple telescopes collect light under different viewing angles. The combination of multiple telescopes increases the effective detection area and facilitates the rejection of optical background. HESS [119] is an example of such telescope with four 12 m mirrors and one 28 m mirror. The Cherenkov Telescope Array (CTA) [120] plans to apply the same detection technique with more than 100 telescopes spanning both hemispheres. The resulting sensitivity would be increased by a factor of 10.

3A.1.4. γ- and X-ray telescopes

The detection of photons in the gamma and X-ray range relies on space telescopes, as the Earth atmosphere is opaque to them. Most detectors are satellites and have two main instruments: one with a wide field of view but a low pointing accuracy to maximize detection opportunities, and the other with a lower point of view but added precision.

Three examples of such telescopes are INTEGRAL, the Fermi Gamma-ray Space Telescope (usually called Fermi) and the Neil Gehrels Swift Observatory (usually called Swift). INTEGRAL is a European telescope sensitive to photons in the MeV energy range, at the border between X- and γ-rays. It is retired since February 2025. Fermi is the main γ-ray telescope currently in operation. The Gamma-ray Burst Monitor (GBM) is able to detect photons from the 8 keV to 1 MeV energy range. It can detect gamma-ray bursts across the whole sky. The Large Area Telescope (LAT) cat detect photons between 20 MeV and 300 GeV with a field of view of around 20 % of the sky. Swift's main scientific goal is the study of gamma-ray bursts in the X-ray and UV range. The two X-ray instruments are the Burst Alert Telescope (BAT) and X-ray Telescope (XRT). BAT is able to monitor around 20 % of the sky to locate events with an accuracy between 1 and 4 arcminutes. XRT follows BAT detections to perform a spectral analysis and reduce the pointing accuracy to 2 arcseconds.

In addition, MAXI monitors the full sky with an X-ray telescope mounted on the International Space Station.

The SVOM telescope is a new X-ray telescope, launched since June 2024.

It is equipped with respectively two large field of view and two narrow field of view instruments. It aims to complement Swift's observation of GRBs and GRB afterglows but will also participate in the observation of other transient events.

3A.1.5. Robotic telescopes

For optical telescopes, an increase of magnification causes a worse field of view. As a result, optical (and near-optical) telescopes usually don't have a field of view as big as X- and γ−rays instruments.

The characterization of transient astrophysical sources in the optical range is thus usually done with automatic or semi-automatic robotic telescopes. TAROT is such a network of automatic telescopes. It is made of three fast moving telescopes installed in metropolitan France, Chile and the French Reunion island. Their fields of view are around 4, 4 and 18 square degrees respectively. Thanks to the fast acceleration and movement of the telescopes, 50 square degrees of the sky can be observed within 10 minutes. The MASTER project [121] is another example of automatic robotic telescopes frequently involved in observations of transient events.

With the increased number of public alerts associated with the detection of gravitational waves, collaborations of telescopes and telescope networks have also organized in the past years. For example, the GRANDMA [122] project coordinates over 30 telescopes to follow-up transient events such as GRBs and search for sources emitting multiple messengers.

Another approach to the optical observation of transient object is to scan the full sky with wide-field telescopes. Two such examples are the Zwicky Transient Facility (ZTF) and the Vera C. Rubin Observatory (VRO). ZTF [123] can cover an area of 47 square degrees and can image the entire northern sky in three nights. It is sensitive to a magnitude down to 20.5. Alerts are being sent every time a difference of 5σ is measured compared to template reference images. The resulting typical nightly rates of alerts reach two hundred thousands. VRO [124], formerly named LSST, is planned to start observations in 2025. It has a smaller field of view of 9.6 square degrees. However, the lower limit on magnitude (24.7) causes the planned number of alerts to rise to ten millions per night.

3A.1.6. Radio telescopes

In the lower part of the energy spectrum, radio telescopes are usually used for follow-up of transients detected at other wavelengths. Examples of such telescopes are LOFAR and Nenufar in France, the MWA, Parkes and ASKAP observatory in Australia and MeerKAT in South Africa. Most of the previously cited observatories are precursors to the Square Kilometre Array (SKA) [125], a radio telescope which should be able to survey the sky much faster.

The CHIME telescope [126], located in Canada, is a radio telescope with no moving parts. It is able to detect Fast Radio Bursts (FRBs) in real-time. However, the localization capabilities of CHIME are not as good as detectors like ASKAP.

3A.2. Communication methods

The diversity of the different types of astronomical instruments is reflected in the number of communities and practices within the astronomers. As such, multiple tools exist to coordinate observations. The following presents some of these methods.

3A.2.1. General Coordinates Network

The GCN (General Coordinates Network) [127] is a platform created by NASA to send and receive alerts related to astronomical transients. Historically, the network was born from the recorder failure of a gamma-ray telescope. Since all events needed to be transmitted to ground, the opportunity for real-time follow-up arose. In 1994, the Gamma-ray burst Coordinates Network was born, originally to coordinate the observation of GRB afterglows. The observation of new transients such as GW events and high-energy neutrinos led in 2022 to the network being renamed to its current name.

Two kinds of data can be sent and received through GCN. GCN Notices are made by and for machines with a fixed and predefined format. They are usually sent automatically by experiments. GCN Circulars are instead usually written by humans to be read by other humans, with a free-form text.

GCN alerts can be sent *via* multiple formats: text, custom binary format and VOEvent. VOEvent [128] is a data format made for the information about a transient celestial event. A message is organized in different categories:

– “Who” to identify the alert emitter;

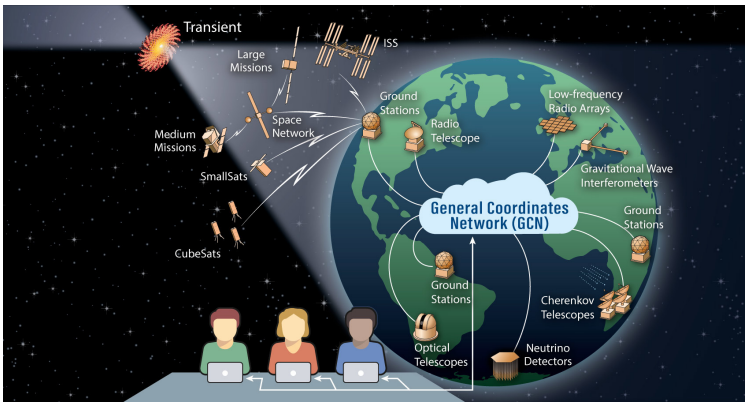

Figure 3.3.: Illustration of the General Coordinates Network: distribution of alerts between space- and ground-based observatories, physics experiments, and thousands of astronomers around the world [127].

– “What” to describe the measurement;

– “WhereWhen” to provide a sky location and event time;

– “How” for specific information about the instrument;

– “Why” to communicate an assessment of the importance of the alert.

The development of new technologies and internet standards have led the GCN to modernize and use the industry-standard Kafka protocol. Over the next few years, the JSON format should also replace the different formats currently used.

3A.2.2. Alert brokers

Not all experiments communicate through the Global Coordinates Network. For example, the CHIME detector relies on the COMET [129] broker to transmit FRB alerts in the VOEvent format.

ZTF and VRO rely on selected external brokers for their alert transmission [130]. The brokers are responsible to ingest data from the telescopes but also to add functionalities. Examples of such functionalities are to cross-match with existing catalogs, to do classification from the obtained light curves or to offer filters to the scientific community. FINK [131] is an example of such broker, used in the following alert section.

3A.2.3. Additional methods

Some other methods are used to communicate between astronomers. The Astronomer's Telegram (ATel) [132] is a publication service for reporting short bulletins related to astronomy observations. The published bulletins can be cited, such as the follow-up performed by KM3NeT in response to GRB 221009A [103].

Finally, a very common practice for experiments is to make agreements with chosen partners to exchange private alerts. It was the case for the ANTARES neutrino telescope [133], which was sending 25 alerts per year to optical telescopes and 6 alerts per year to the Swift satellite.

3A.3. Prospects for the near future of astronomy alerts

The number of astronomy alerts is knowing an increase in importance over the last decade. With the update of GCN to handle more alerts, the growing number of neutrino telescopes, the improvement in sensitivity for GW detectors and the new electromagnetic observation facilities, the number of alerts will explode over the next few years. A manual follow-up of all those alerts will not be possible. Section 3B presents the KM3NeT Online Multi-Messenger Program, which aims to automatize the processing of events, the follow-up of external triggers and the dispatch of neutrino alerts. Section 3C presents in further details the planned KM3NeT neutrino alerts.

3B. The KM3NeT Online Multi-Messenger Program

> Okay, here we go. Focus. Speed. I am speed. One winner. 42 losers. I eat losers for breakfast. Breakfast? Wait, maybe I should have had breakfast? A little breaky could be good for me. No, no, no, stay focused. Speed!
>
> *Flash McQueen*

The KM3NeT online pipeline is organized as multiple modules, each with a specific function. The modules are organized in two groups. The Real Time Analysis (RTA) platforms are responsible for the real-time reconstruction and classification of events captured by each detector. Two RTA platforms,

respectively for the ARCA and the ORCA detectors, are running independently. The second group of modules receives the processed events, which are used in the follow-up of external triggers and the selection for neutrino alerts. It is the Multi-Messenger (MM) platform. The MM platform currently runs on the ORCA shore station for prototyping, but should be moved in the near future to a new third independent location.

Figure 3.4 is a simplified diagram of the KM3NeT online pipeline. The RTA platform is shown on the left side, with the different modules connected to the RTA dispatchers. The MM platform, on the right, contains:

- modules to write the processed events (*event writer*);
- modules to receive, store and perform follow-up analysis on external triggers (*GCN alert handler* and *online analysis pipeline*);
- modules related to neutrino alerts (*neutrino alerts* and *alert sending*).

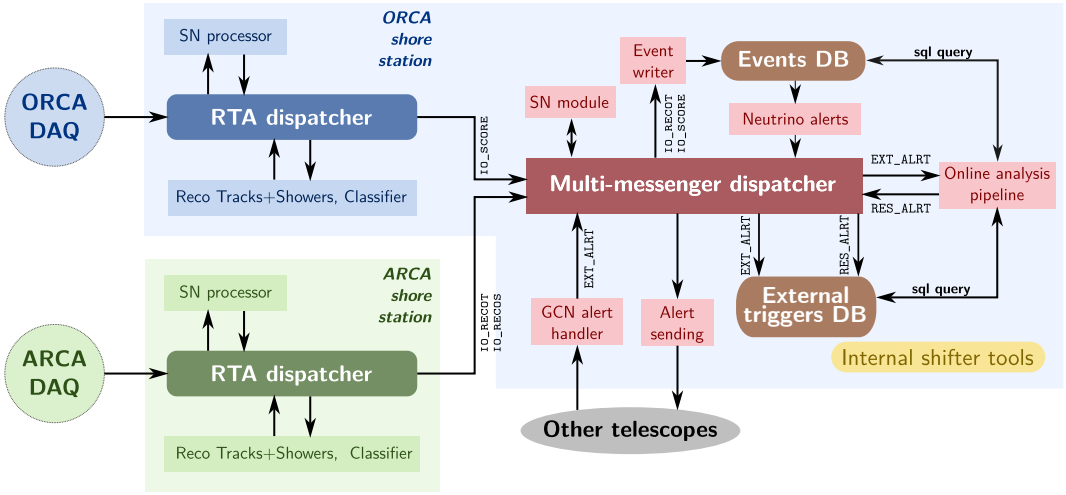

Figure 3.4.: Diagram describing the dataflow of the KM3NeT online pipeline. The modules of the real-time analysis platforms are shown in green and in blue, respectively for ARCA and ORCA. The modules of the multi-messenger platform are shown in red and the databases are shown in brown.

3B.1. Online GeV-PeV event processing

The KM3NeT detectors follow an *all-data-to-shore* approach. The Data Acquisition (DAQ) System searches for specific conditions in data. When met, the

associated set of hits is tagged as a triggered event. All triggered events, as well as periodic summary information about the detector status, are transmitted to the RTA platforms.

The reconstruction of events takes longer than the time between two triggered events. As such, multiple workers (software modules) are running in parallel and events are dispatched among them. The reconstruction software chains are identical to the ones performed for offline analyses. The only difference arises from the calibration process. With the offline analyses, the reconstruction algorithms take into account the DUs displacement caused by the sea current. The DUs are considered perfectly vertical during the online processing.

Online processing includes three steps: reconstruction assuming the event is a track, reconstruction assuming the event is a shower and classification of the event. Those three steps are performed differently for ARCA and ORCA events. With ORCA, the two reconstruction steps and the classification step happen sequentially. With ARCA, the three steps are performed in parallel. The difference comes from design philosophy differences between the development teams. ARCA events are processed faster, at the expense of added software infrastructure complexity.

The classification method is also different between ARCA and ORCA. Both rely on machine learning algorithms to discriminate between atmospheric muons (noise) and neutrinos (signal). For a given event, a neutrino score is computed. The higher the neutrino score, the more likely an event is a neutrino and not a muon.

ARCA The method used for ARCA is Graph Neural Networks (GNN). The raw event structure is converted into a graph where the nodes are hits and the links are the spatial and temporal correlations between hits. A neural network computes the neutrino score from the resulting graph. An example neutrino score distribution for ARCA28 is given Figure 3.5. As a GNN relies only on the geometric distribution of all hits, multiple advantages arise. A maximum number of information is available to the neural network. Moreover, the classifier can be applied directly to triggered events without needing to get reconstructed first. This allows the ARCA RTA platform to perform the classification in parallel to the reconstruction. However, the inner workings of a specific GNN are very difficult to understand.

ORCA ORCA events are classified with Boosted Decision Trees (BDT). The use of Boosted Decision Trees (BDT) is made for ORCA events. BDT rely on a given

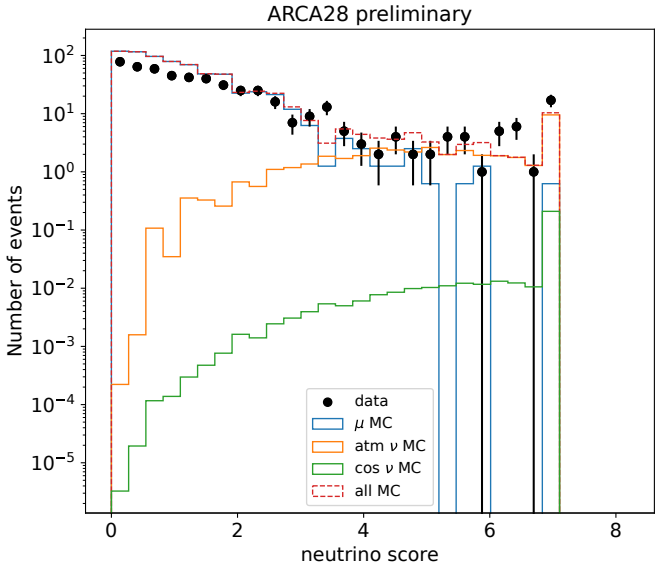

Figure 3.5.: Neutrino score distribution of online processed data and Monte-Carlo events for the ARCA28 detector.

number of input variables. The input variables are organized in a decision tree, in which all leaves are the variables and all branches are conditions on the parent variable. The end of the tree gives the neutrino score. Boosted trees are a specific training method where each new decision tree learns from the previously created one. In the case of ORCA, the input variables are obtained from the track and shower reconstruction steps. Figure 3.6 shows the neutrino score distribution for the ORCA18 detector. BDT inner workings are easier to understand than GNN, but are still subject to interpretation issues.

3B.1.1. Database storage

Once the triggered events are reconstructed and classified, they are transmitted to the MM platform where they are stored. The events between ARCA and ORCA are dispatched in two tables with identical structures. The experience gained in building the CCSN pipeline database was reused for the events database. As such, the `PostgreSQL` software and `TimescaleDB` plugins are used. The tables diagram is shown Figure 3.7.

The five-tuple `detid`, `runid`, `trigger_mask`, `frame_index` and `trigger_counter` describes each triggered event and is a unique identifier. The `online_data` field contains all the data output from the reconstruction and classifier steps. The

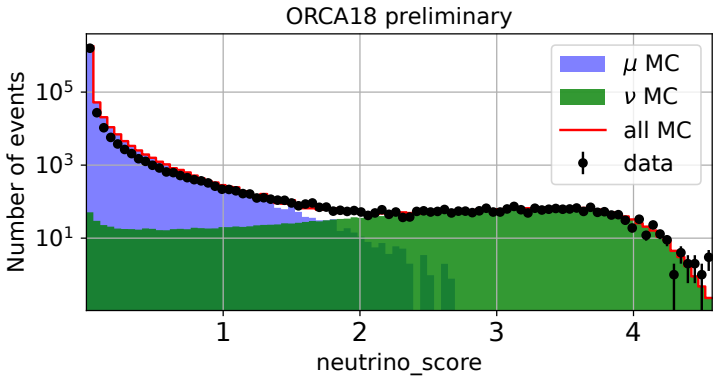

Figure 3.6.: Neutrino score distribution of online processed data and Monte-Carlo events for the ORCA18 detector.

field is formatted in JSON, to allow for a flexible number of fields for future upgrades. Finally, some metadata fields contain the configuration and version used for the whole processing chain. The metadata fields ensure that a stored event can be reprocessed identically in the future.

event_arca	
detid	INT
runid	INT
trigger_mask	INT
frame_index	INT
trigger_counter	INT
datetime	TIMESTAMPTZ
online_data	JSONB
per_event_metadata	JSONB
metadata_id	INT

event_orca	
detid	INT
runid	INT
trigger_mask	INT
frame_index	INT
trigger_counter	INT
datetime	TIMESTAMPTZ
online_data	JSONB
per_event_metadata	JSONB
metadata_id	INT

Figure 3.7.: Diagram for the two tables containing events processed online by the RTA platform. Each event is uniquely identified by the variables `detid`, `runid`, `trigger_mask`, `frame_index` and `trigger_counter`.

3B.1.2. Monitoring tools

A set of different monitoring tools ensures that no issues arise within the real-time processing of events. The monitoring is done through a website for easy access from anywhere and any platform. A `Grafana` dashboard is used to monitor the running state of every module in the pipeline.

The monitoring of some "high-level" variables is also performed. The event rates at different cut levels (*e.g.* anti-noise, anti-noise up-going…) is monitored between runs. If a discrepancy higher than 20 % is observed, an error is displayed.

Finally, the processing time distribution is also monitored. Figure 3.8 shows the time distribution of the full processing pipeline for 24 hours, for ARCA on the left and ORCA on the right. The median processing times are respectively around 3 and 10 s.

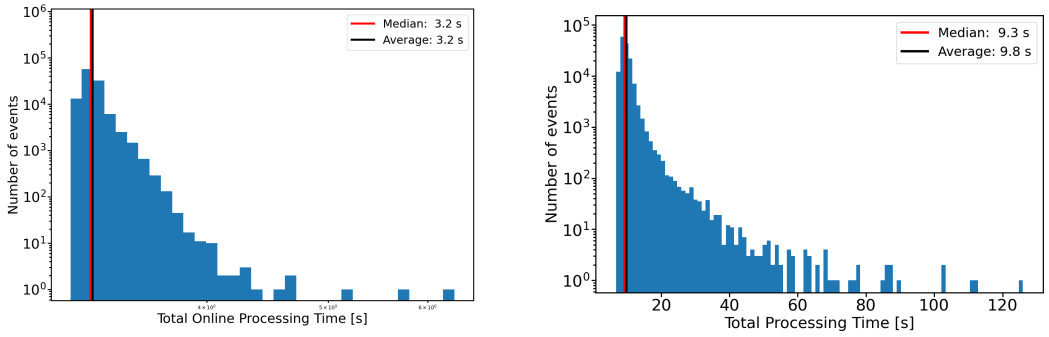

Figure 3.8.: Distribution for the processing time of the full online processing pipeline for ARCA on the left and ORCA on the right. The distribution is plotted for 24 h of triggered events.

In less than 10 seconds, triggered events are reconstructed and classified. The reconstruction performance is almost identical to offline analyses performed with refined calibration data. With the ARCA28 configuration, the median angular resolution for track-like events reaches 0.1° for events above 10 PeV [134]. All events with sufficient reconstruction quality are stored within a database to be used for further analyses.

3B.2. Automatic follow-up pipeline

The goal of the follow-up pipeline is to perform an automatic time-dependent search for neutrinos in the direction of transient astrophysical objects. The

real-time detection of transient astrophysical objects relies on alerts sent by external detectors. The external alerts received by KM3NeT are called in the following external triggers. The idea is to be able, in the event of a found excess in the direction of the object, to immediately organize the observation in multiple wavelengths to characterize a potential neutrino source. The high and growing number of astronomical alerts requires the search to be fully automatic.

3B.2.1. Principle of the ON/OFF method

The number of detected events with the KM3NeT detectors is background dominated by muons and atmospheric neutrinos. As such, a full suppression of background events would reduce too much the possibility to observe any signal. The binned ON/OFF technique [135] is used instead. The principle of this technique is to compare the number of events in an ON region compared to the expected background computed from an OFF region. Both regions have a spatial and time extension. The spatial distribution of the ON region is described by the convolution of the angular error associated with the external trigger and the angular uncertainty of KM3NeT events. The used time window is different for the different types of triggers. The ON region moves in the local sky because of the Earth rotation. The OFF region is therefore made of multiple local zenith bands, which are used accordingly to the ON region's position. Each zenith band has the ON region subtracted. The zenith bands and ON regions for different times are shown Figure 3.9. The OFF time window covers the two weeks prior to the trigger.

The expected number of background events n_{bkg} is estimated by re-scaling in time T and solid angle Ω:

$$n_{\mathrm{bkg}} = \sum_{i \in \mathrm{bands}} \frac{\mathrm{T}_{\mathrm{ON}}}{\mathrm{T}_{\mathrm{OFF}}} \frac{\Omega^i_{\mathrm{ON}}}{\Omega^i_{\mathrm{OFF}}} \mathrm{N}^i_{\mathrm{OFF}} \tag{3.1}$$

The ON/OFF search is not performed on the whole set of events triggering the KM3NeT detectors. A first set of pre-cuts is applied to reduce the number of background events. Additionally, a selection is made on the track reconstruction quality for ARCA and the classifier neutrino score for ORCA. An optimization is made on the expected number of background events to ensure a sufficient significance in the case of a detected event in the ON region.

As of beginning of 2025, the median angular error considered for ARCA and ORCA are respectively 2° and 4°. The event directions are only obtained

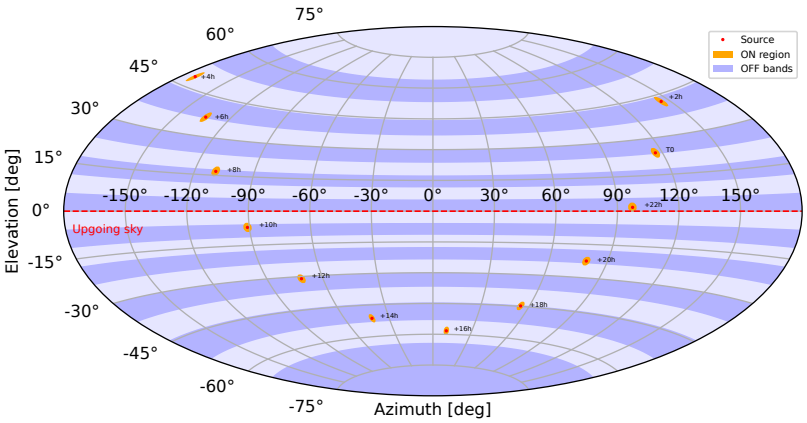

Figure 3.9.: Skymap illustrating the movement of a circular ON region (orange) across multiple local elevation OFF bands (blue). The expected atmospheric background is different in each elevation band. [136]

from the track-like reconstruction. An implementation with data from the shower-like reconstruction is planned shortly.

3B.2.2. Selection of external triggers

The time window during which a signal is searched is different for the different possible types of triggers. Follow-ups are performed for:

- Neutrino events shared by the IceCube neutrino telescope;
- GW events shared by the LVK collaboration;
- GRBs detected by γ-ray satellites;
- general transient events;
- fast radio bursts (FRB), reported by radio telescopes;
- micro-quasars, triggered when X-ray flares are detected with associated objects from a selected list.

Most triggers are communicated through the GCN. The association between the detector and the type of event the trigger is tagged as is shown Table 3.1. Some selection criteria are also applied to filter some triggers and classify

between GRB and transient. Table 3.2 shows the time window for each type of events. In the case of multiple time windows, the analyses are run multiple times.

3B.2.3. Follow-up results

The follow-up pipeline is running since June 2023, for the beginning of the third GW observing run from LVK. Figure 3.10 shows the cumulative number of external triggers to which a follow-up analysis has been performed. Filters on trigger parameters are usually implemented after some commissioning time, resulting in the steep rise followed by linear growth visible on Figure 3.10. Overall, more than 1000 follow-up analyses have been performed.

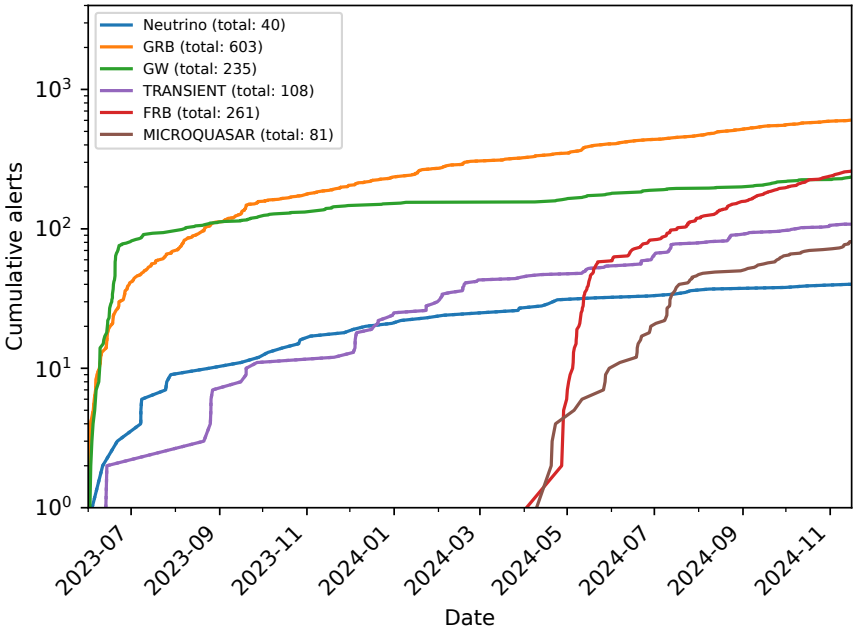

Figure 3.10.: Cumulative number of analyzed alerts by the KM3NeT real-time platform, in the period from June 2023 to December 2024. The different colors denote the kind of alert analyzed. Updated from [136].

The *p*-value for each analysis, as a function of the time of the trigger, is shown Figure 3.11. Overall, a higher number than predicted has reached a significance higher than 2.5σ and 3σ. However, some investigations showed that the excess might come from duplicated events in the ON region for some analyses.

Table 3.1.: Experiments used as triggers for the follow-up analyses and associated trigger tag with the required condition.

Detector	Conditions	Event type
IceCube	–	Neutrino
LVK	if tagged as significant and probability of terrestrial origin < 0.5	GW
INTEGRAL	–	GRB
Fermi-GBM	if most likely a GRB with probability > 0.5	GRB
	otherwise	TRANSIENT
Fermi-LAT		TRANSIENT
Swift-BAT	if identified as GRB	GRB
	otherwise	TRANSIENT
Swift-XRT	if source not in Swift catalog	TRANSIENT
MAXI	–	TRANSIENT
HAWC	–	TRANSIENT
Chime	–	FRB
TNS	if tagged as FRB	FRB

Table 3.2.: Time-windows used for the different trigger tags of the follow-up analyses.

Event type	HE analysis time-window
Neutrino	-1 hour to $+1$ hour -1 day to $+1$ day
GW	-500 seconds to $+500$ seconds -500 seconds to $+6$ hours
GRB	-500 seconds to $+500$ seconds -1 hour to $+1$ hour -1 day to $+1$ day
Transient	transient duration (or ± 500 s if lower) -1 day to $+1$ day
FRB	-500 seconds to $+500$ seconds -1 hour to $+1$ hour -1 day to $+1$ day
Microquasar	transient duration (or ± 500 s if lower)

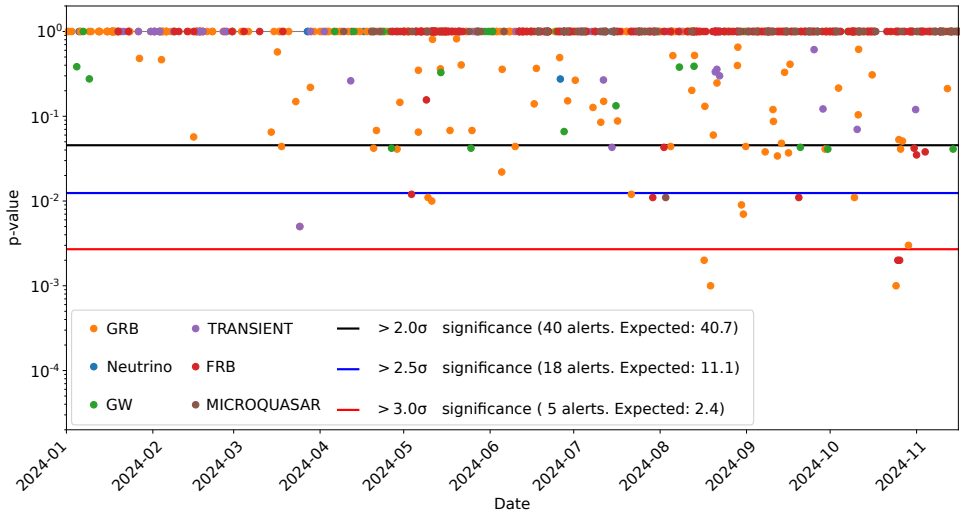

Figure 3.11.: Pre-trial p-values for all analyses performed during the year 2024. The different colors correspond to the different tags of external triggers. Updated from [136].

No follow-up results from KM3NeT has been shared in real-time to the astronomical community as of beginning of 2025. However, shifters have been trained to monitor the state of the online processing pipeline and to report the result of follow-ups internally. The KM3NeT collaboration is ready to communicate in the event of a found excess in correlation with a transient astronomical event.

3C. KM3NeT neutrino alerts

3C.1. Context of neutrino alerts within the multi-messenger landscape

3C.1.1. ANTARES

The ANTARES neutrino telescope communicated private alerts between 2009 and the decommissioning in 2022 [133]. The events were reconstructed in real-time with a fast and robust online algorithm. From the results, a cut on up-going events and reconstruction quality reduced the event rate from around 3 Hz to 0.01 Hz. From the reduced rate of events, a refined reconstruction of events was applied to refine the angular resolution. The dynamic position of the ANTARES lines was not taken into account and alerts were vetoed for high current speed, resulting in an 85 % duty cycle. Despite this, the median angular resolution reached around 0.5°, with alerts distributed in less than ten seconds.

From the reconstructed events, the TAToO (Telescopes-Antares Target of Opportunity) system defined four criteria of alerts:

- the High Energy (HE) trigger was selecting single neutrinos with estimated energy higher than 5 TeV. The associated rate was around 1 per month.
- The Very High Energy (VHE) trigger was a sub-sample of the HE trigger, with a selection on neutrinos higher than 30 TeV. Between 3 and 5 events were sent per year.
- The Directional trigger aimed to enhance the chances to detect a local (within 20 Mpc) CCSN. Neutrinos within 0.4° of a local galaxy of the Gravitational Wave Galaxy Catalog [137] were selected, resulting in a rate of 1 per month.
- The Doublet trigger built coincidences of neutrinos within 15 min and 3° of each other. No doublet was ever found in the lifetime of the detector.

All alerts (around 25 per year) were automatically transmitted to partner optical telescopes. A subset of alerts (6 per year) were also communicated to the Swift X-ray telescope to perform a follow-up observation. Additionally, some follow-ups were performed by the MWA radio telescope and the HESS γ-ray telescope

3C.1.2. IceCube

The IceCube neutrino telescope is issuing real-time alerts since 2016 [138]. Events are reconstructed in real-time in the South Pole station. A first selection on the reconstructed parameters is applied. From selected events, two messages are transmitted to the IceCube data center in the Northern Hemisphere. The first message contains the key information such as event time, run information, direction and energy to be communicated to follow-up partners. The second message transmits the light arrival information, which is used for a refined reconstruction of the event. This reconstruction step is needed due to the non-uniformity of the ice scattering properties. The inclusion of the properties causes the computation to be too heavy to be performed at the South Pole.

A refined selection is made to the incoming events before being transmitted through the General Coordinates Network. Overall, an alert is issued within 30 to 40 s of the detection. The refined reconstruction information is sent after few hours.

Alerts are organized in multiple channels. Among the public alerts channels, one is dedicated for track events, one for cascade events and one for coincidence between neutrino and gamma. IceCube also transmits private alerts to preferred partners with Two private channels based on neutrino clustering are also a search for clustered events. The following describes the current (as of 2025) categories of alerts transmitted.

Public track event alerts Track event alerts are organized since 2019 in a single channel including three different event selections [139]. The selections are optimized to reach a high "signalness" parameter. The signalness is defined as

$$\text{signalness}(E,\delta) = \frac{N_{\text{signal}}(E,\delta)}{N_{\text{signal}}(E,\delta) + N_{\text{background}}(E,\delta)}, \tag{3.2}$$

where E is the reconstructed event energy, δ is the event declination, $N_{\text{signal}}(E,\delta)$ and $N_{\text{background}}(E,\delta)$ are the expected number of signal and background events at declination δ and above energy E. The expected number of events are obtained from simulations assuming an astrophysical neutrino spectrum of $E^{-1.19}$. The signalness can be interpreted as the probability of the event being of astrophysical origin. Alerts are tagged as "Bronze" when the signalness is between 30 and 50 % and "Gold" for signalness above 50 %.

The performed selections are the following:

– the Gamma-ray Followup Event (GFU) selection was initially based on a

selection optimized for follow-up by gamma-ray air Cherenkov telescopes. Two boosted decision trees, one for the Northern Hemisphere and one for the Southern Hemisphere, are applied to the event. The resulting score is cut to reach the signalness requirement. As a result, only the highest energy events (hundreds of TeV) are selected.

– The High-Energy Starting Event (HESE) selection only selects events which interaction vertex is contained within the detector. An additional threshold on number of photo-electrons and track length is added to favor astrophysical events and reject poorly reconstructed ones.

– The Extremely High-Energy Event (EHE) selection is optimized to detect neutrino events between 500 TeV and 10 PeV. Atmospheric background is reduced thanks to a 2D cut on reconstructed zenith and deposited energy.

Each of those selections is optimized to reach the 30 % and 50 % threshold, but no selection is actually made on signalness.

Public cascade event alerts Cascade event alerts are sent through the GCN since 2020 [140]. From events which interaction vertex is contained inside the detector, a deep neural network selects a majority of cascade events. A second deep neural network reconstructs the cascade events to reach an angular resolution below 9° for 68 % of the events.

Neutrino-gamma coincidence alerts The final public channel searches for coincidences between track-like events from IceCube and γ-ray observation from HAWC. The coincidence search is assured by the Astrophysical Multimessenger Observatory Network (AMON) [141]. The HAWC observatory transmits to AMON around 800 "hotspots" per day, defined as an excess above the estimated cosmic-ray background level. Track-like neutrinos are searched within the gamma transient time window and within 3.5° of the hotspot. A combined p-value is obtained from a chi-square using Fischer's method:

$$\chi^2_{6+2n_\nu} = -2\ln(p_\lambda\, p_{\mathrm{HAWC}}\, p_{\mathrm{cluster}}\, \Pi_i^\nu\, p_{\mathrm{IC},i}), \tag{3.3}$$

where p_λ is the overlap between the events, p_{HAWC} is the associated p-value of the HAWC event, p_{cluster} is the probability of seeing more than one neutrino from background in the HAWC transit period and $p_{\mathrm{IC},i}$ are the associated p-values of the IceCube events. A cut on χ^2 is made to transmit through GCN 4 alerts per year due to background.

Clustering searches The clustering program aims to search for bursts of neutrino-like events. If a burst is identified, the location is communicated to telescopes to search for a counterpart. In contrast to the previous channels, the cluster locations are communicated privately to partners following agreements. Two types of alerts are defined:

- the Optical Followup (OFU) selection is limited to the northern sky (only up-going events). A neutrino multiplet requires at least two events within 100 s and within 3.5° of each other. Multiplets higher than three are immediately transmitted to optical and X-ray telescopes. For doublets, a cut is made on a quality factor depending on the angular radius to reach the agreed alert rates.
- The Gamma-ray Followup (GFU) selection is identical to the one used for track-like events. Neutrino clusters are searched near a predefined list of sources, mainly gamma sources. If a significant cluster is observed, IceCube shares the location with air Cherenkov telescopes to search for a coincident gamma flare.

3C.2. Strategy for the KM3NeT neutrino alerts

From the ten years experience in neutrino alerts of ANTARES and IceCube, some conclusions can be drawn. The low number of observed astrophysical neutrinos is a difficult limit to work with. As such, alerts are one of the best strategy to identify them and characterize their sources. The follow-up observations to neutrinos play a necessary role and bring:

- an enhancement to the scientific output for every detected neutrinos;
- an inquiry into the source dynamics and population, even in the case of non-observations;
- high chances to identify high-energy astrophysical neutrinos sources.

However, the follow-up capabilities of the different observation facilities are limited. The growing number of alerts in the following years increases the need to make every follow-up as interesting as possible.

3C.2.1. Strengths of KM3NeT

KM3NeT shows many strengths in the landscape of multi-messenger alerts. The extended energy range, from GeV to above hundreds of TeV, allows

probing multiple populations of sources. The location of the two detectors is complementary to the one of IceCube and brings a full coverage of the neutrino sky. Moreover, all neutrino flavors can be detected and reconstructed within seconds. This makes it possible to enhance the detection capabilities and provide multiple channels. Finally, KM3NeT/ARCA is able to reconstruct with an excellent angular resolution the track-like events at high-energy. This is particularly important for the identification of new sources, as the field of view of telescopes is usually limited.

3C.2.2. Maximizing the scientific interest of alerts

The conditions for the issuing of alerts for ANTARES and IceCube relies only on the neutrino properties. Once a neutrino is selected and the alert is sent, a common practice is to search for possible counterparts sources. In the event of "interesting" sources found within the neutrino angular uncertainty, the sharing of information often happens with handwritten messages such as GCN circulars. This method is illustrated left of Figure 3.12.

A new method is proposed for the KM3NeT neutrino alerts. Instead of applying a hard selection on neutrino properties to send one or two alerts per month, the selection is loosened to few events per day. For every event, an automatic counterparts search is performed. The properties of the potential sources are retrieved, both with catalogs for spatial correlation and with light-curves retrieval for temporal selection. If a source is considered sufficiently interesting, an alert is sent. The right part of Figure 3.12 depicts this ν-EM mix selection method.

Many advantages arise from this method. A low energy cosmic neutrino which could not normally be discriminated from an atmospheric muon can be more easily identified. Moreover, communicating automatically potential counterparts facilitates the follow-up. Telescopes indeed no longer need to scan inside the uncertainty region and can start characterizing sources directly. A first estimation of the object magnitude also helps telescopes to attribute observing time to alerts they are able to follow up.

The main difficulty comes from the possible bias towards some given sources. An associated concern is the reduced potential to discover new sources. To avoid those issues, a selection based only on neutrino properties is kept. Figure 3.13 describes the selection pipeline developed for the KM3NeT alerts.

For both detectors, a first preselection is applied to reduce the event rates. Specialized selection pipelines are run to further select based on different objectives. Two such pipelines are described section 3C.3: one optimized for

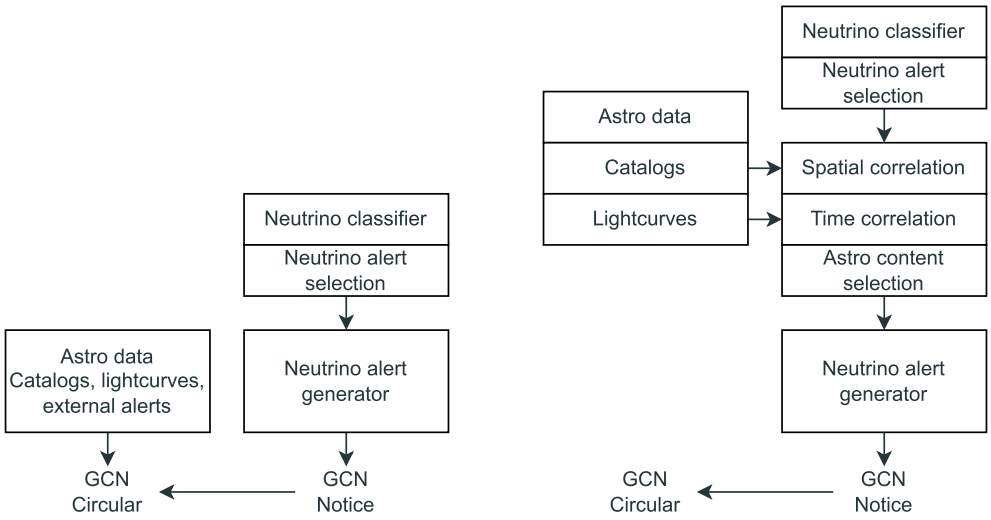

Figure 3.12.: The two selection methods for neutrino alerts. Left: "classical" method with selection only on neutrino properties. Once the alert is sent, manual or semi-automated search for source candidates. Right: proposed new method, selection on a mix of the neutrino properties and the electromagnetic properties of the possible astrophysical sources of emission.

the detection of track-like high energy ARCA events and the second based on a search for multiplets with ORCA events. A false alarm rate (FAR) is computed for every event passing the selections. All events are aggregated within a module which searches for astronomical counterparts. If the neutrino event is significant enough on its own, it is communicated with the astronomical content. Otherwise, a combined neutrino-astro FAR is computed. An alert is sent if the FAR reaches a given threshold.

All work related to the "astro" module is presented section 3C.4.

3C.2.3. Selecting alerts and false alarm rates

Due to the high background when searching for cosmic neutrinos, an efficient approach is to define for every event a false alarm rate (FAR). If the selection is made with only one parameter, the FAR is simply the rate of events multiplied by the one-dimensional p-value. The FAR computation for two or more parameters is more complicated. In the case of independent parameters, p-value can be combined using different methods. This is what is done for the FAR combination of the CCSN pipeline. However, the different properties of a neutrino or a celestial object are not independent.

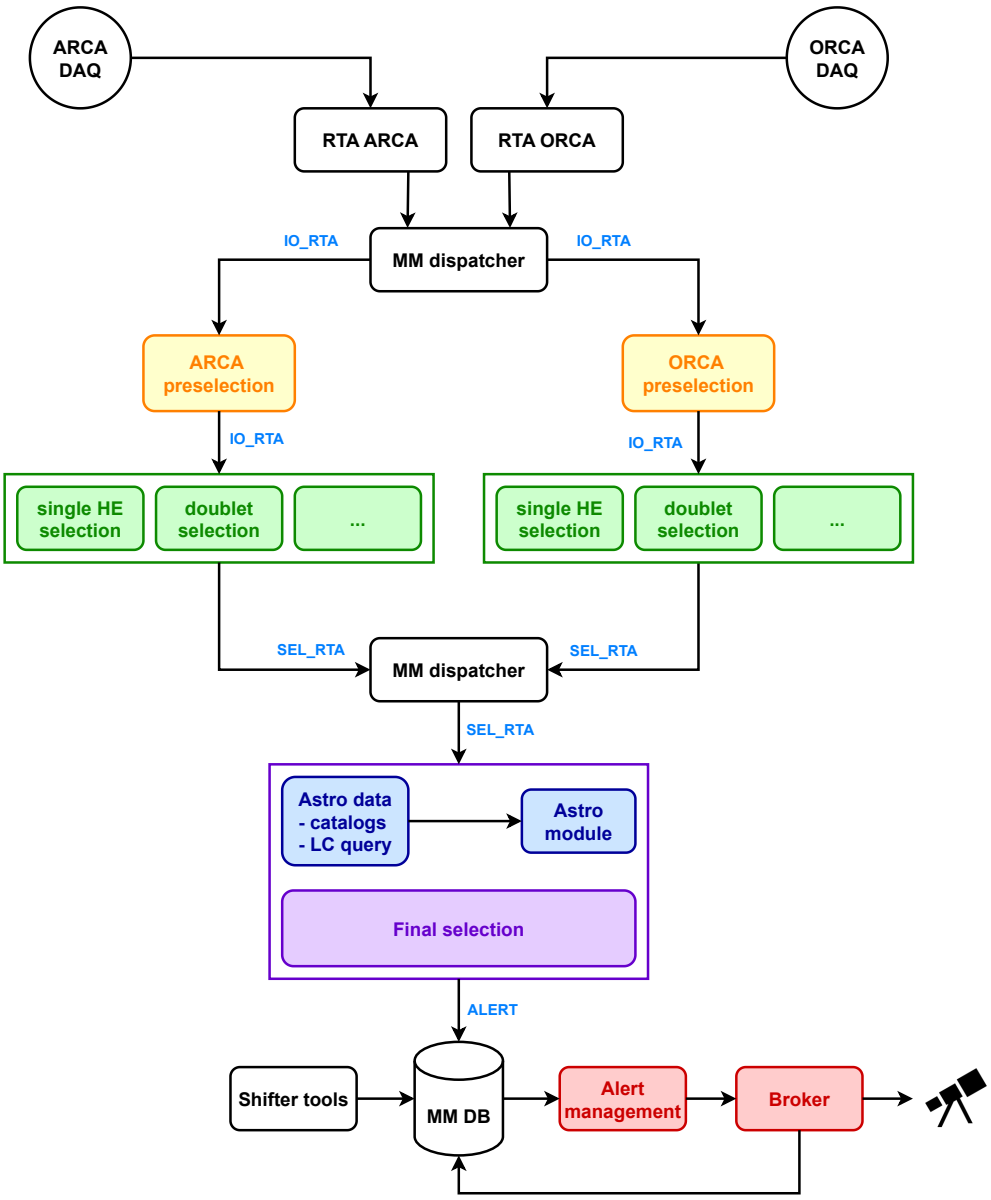

Figure 3.13.: Diagram describing the dataflow of the alert pipeline. From the MM dispatcher, given selections are applied on the events from ARCA and ORCA. For every event, an astronomical counterpart is searched. From all data available, a final selection is made before storing the alert inside a database and transmitting it to the astronomy community.

The one-dimensional FAR can be generalized in higher dimensions. For example, the FAR associated for on event with the properties $A = A^*$ and $B = B^*$ is

$$\mathrm{FAR}(A^*, B^*) = \text{rate of events} \times \int_{A^*}^{+\infty} \int_{B^*}^{+\infty} N(A,B)\,dA\,dB, \tag{3.4}$$

where $N(A,B)$ is the distribution of events as a function of A and B. The resulting FAR is illustrated on the top left of Figure 3.14. It corresponds to the expected rate of background events with parameters above A^* and B^*. However, the FAR parameter is degenerate. The same rate of background events could be found with parameters above another set of variables, such as A^{**} and B^{**} on the top right of Figure 3.14.

This means that, if a threshold is set on the FAR parameter, more events than wanted will be selected. A new parameter, hyperFAR[1] is introduced. The hyperFAR for an event with properties A^* and B^* is defined as the number of background events with FAR equal or lower than $\mathrm{FAR}(A^*, B^*)$:

$$\mathrm{hyperFAR}(A^*, B^*) = \iint_{\mathrm{FAR}(A,B)<\mathrm{FAR}(A^*,B^*)} N(A,B)\,dA\,dB. \tag{3.5}$$

The hyperFAR parameter is illustrated at the bottom of Figure 3.14.

The hyperFAR method is used for the selection of high-energy track-like events. Further discussions are ongoing whether to use the hyperFAR method further down the selection pipeline.

3C.3. Pure neutrino alert selection

3C.3.1. High-energy selection

The following section describes the prototype method for the selection of high-energy track-like events with the ARCA detector. It is made from a simulation of events made specifically for the online platform. As a result, the statistics of some events (such as atmospheric muons badly reconstructed as up-going) might be insufficient. It is however enough to define the method, which can be iterated on later.

A first preselection is made to reduce the event rate from around 15 Hz to around 15 per day. The preselection consists of:

– a minimal muon energy of 10 GeV;

[1]Called so because the FAR iso-curve is a hyperplane in the parameters space.

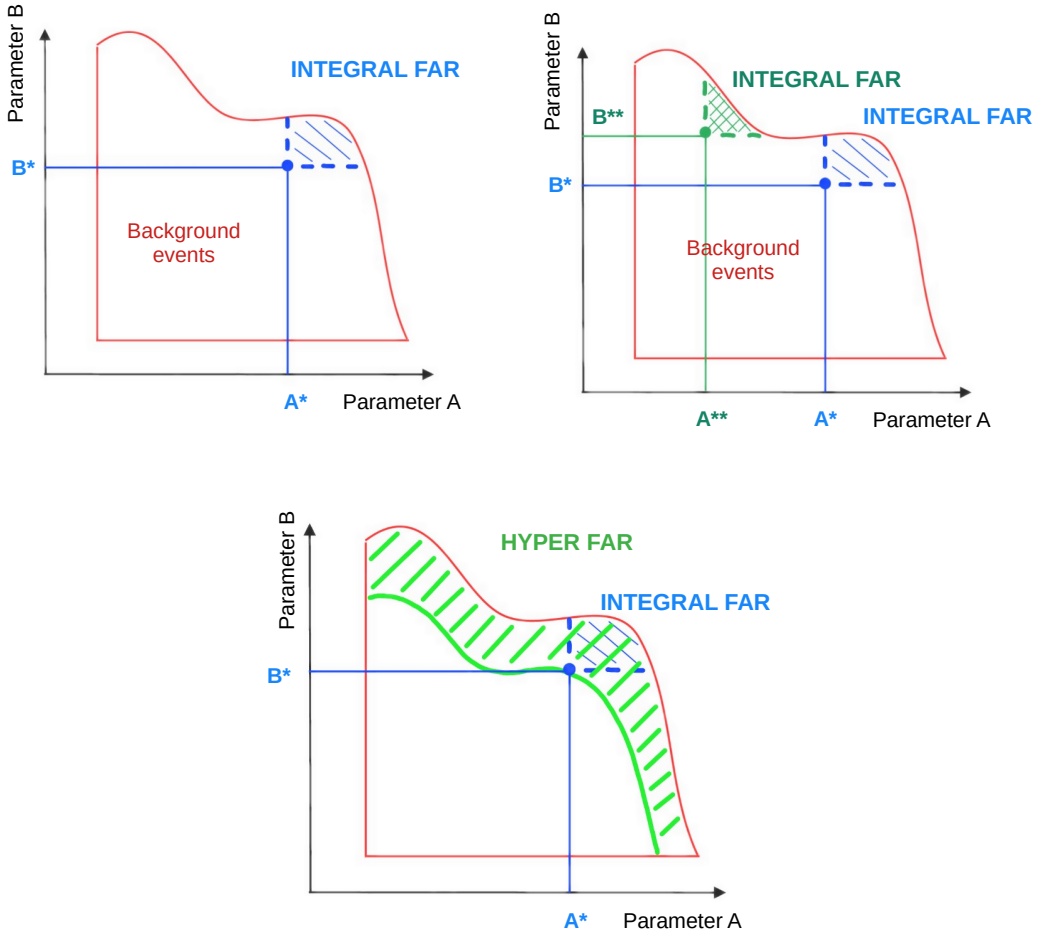

Figure 3.14.: Illustration in 2D of the FAR parameter (named integral FAR in the drawing) and the hyperFAR parameter. The green line in the bottom plot is where associated FAR are equal to the FAR of the blue point [142].

– an uncertainty on the muon direction below 0.6° (0.01 rad);

– a zenith angle around 5° below horizon.

The preselection aims to select up-going or near-horizontal track-like events. The selection on zenith is made to remove the atmospheric muons which cannot cross the Earth or big enough body of water. Table 3.3 shows the expected number of cosmic neutrinos, atmospheric neutrinos and atmospheric muons. Around one fourth of the events are atmospheric muons wrongly reconstructed as up-going.

Table 3.3.: Estimated number of events in 30 days from simulations after the preselection.

Cosmic neutrinos	3.5954 ± 0.0160
Atmospheric neutrinos	296.8110 ± 3.5057
Atmospheric muons	117.5360 ± 41.5553
Total background	414.3470 ± 41.7029
Total	417.9424 ± 41.7029

From the preselected events, the FAR is computed from three parameters: reconstruction quality (called reco quality), reconstructed energy and length of the contained track within the detector (called track length). Those three values are chosen to make a compromise between properly reconstructed events (reco quality), number of cosmic neutrinos (energy) and low angular error. A higher track length indeed reduces the angular error, as the associated lever arm is bigger. The following added requirements are added to ensure better selection performances:

– muon energy above 1 TeV;

– track length above 225 m;

– number of hits used in the reconstruction above 30;

– reconstruction quality above 50.

Figure 3.15 shows the 2D distributions, respectively of energy vs reco quality, energy vs track length and reco quality vs track length. For a given event, the FAR is computed from integrating the expected events over the three

variables. This is shown as an example in two dimensions in the red surface of Figure 3.16. The hyperFAR, or number of expected background events with FAR equal or below, is computed as well and shown as the green surface in Figure 3.16.

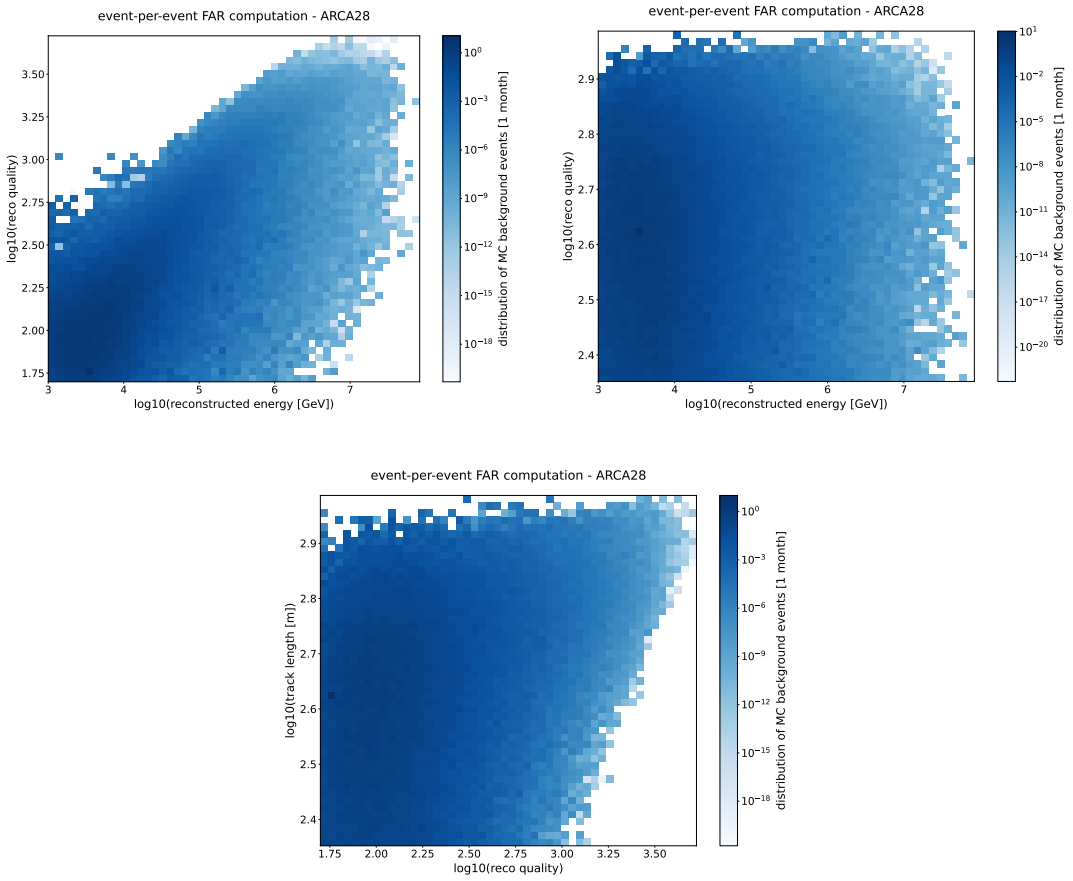

Figure 3.15.: 2D distribution of background events, respectively for energy vs reco quality (top left), energy vs track length (top right) and reco quality vs track length (bottom).

The chosen threshold on high-energy events to be transmitted to the astro module is 30 per month. At this level and for this set of simulations, no atmospheric muons are selected, as shown Table 3.4. The requirements on track length ensure a good angular resolution. Figure 3.17 shows that 68 % of cosmic neutrinos are reconstructed within at least 0.26° and 90 % within 4.79°.

All events with hyperFAR below 30 per month are considered to be correlated

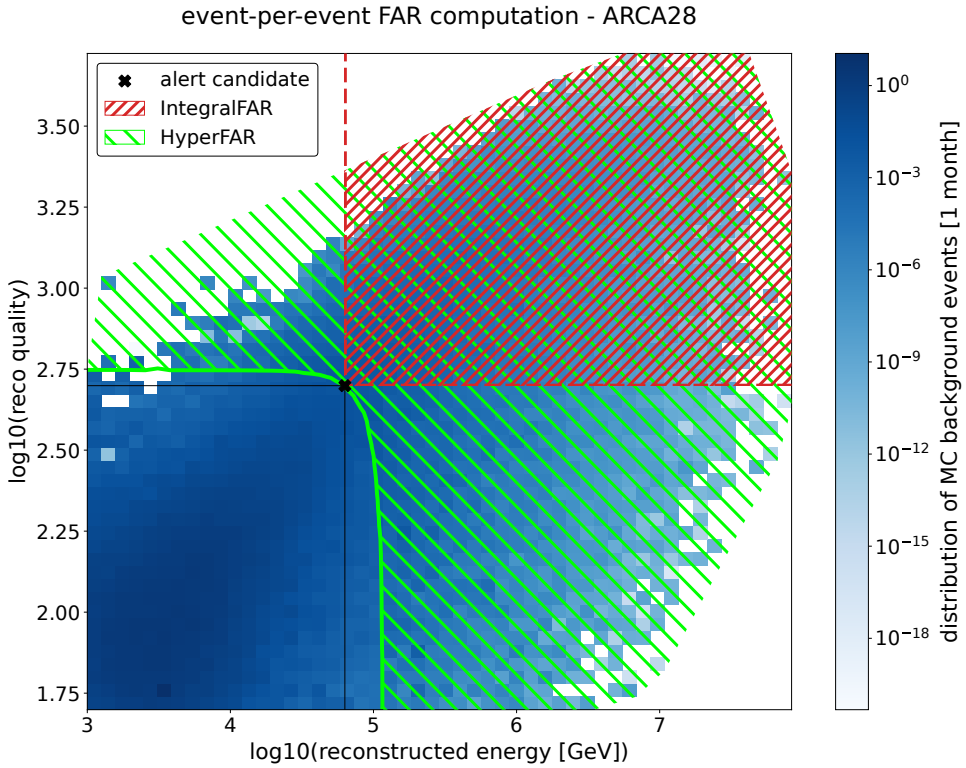

Figure 3.16.: FAR and hyperFAR surfaces drawn as an example for the 2D distribution of energy vs reco quality.

Table 3.4.: Estimated number of events in 30 days from simulations after the 30 events per month selection on hyperFAR.

Cosmic neutrinos	1.2167 ± 0.0072
Atmospheric neutrinos	29.7247 ± 0.7164
Atmospheric muons	–
Total background	29.7247 ± 0.7164
Total	30.9414 ± 0.7165

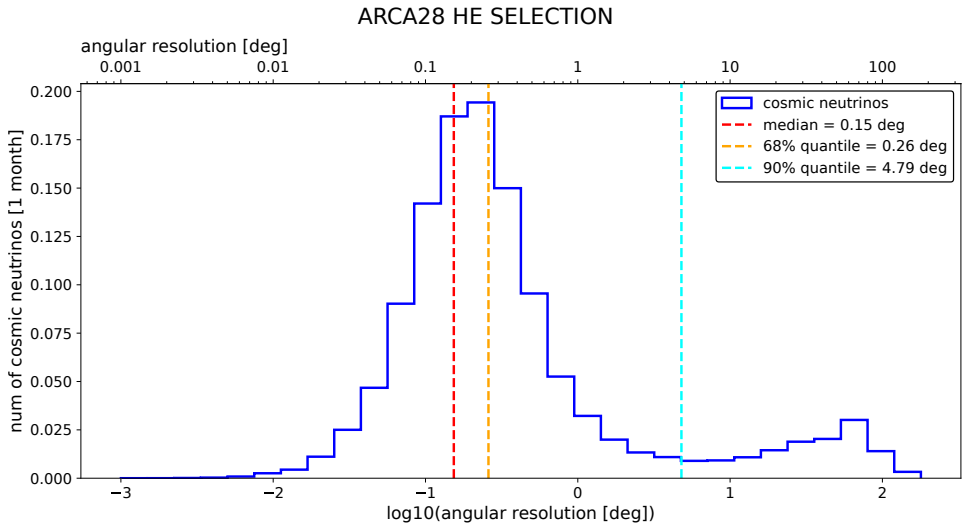

Figure 3.17.: Angular errors on the cosmic neutrino events after the 30 events per month selection on hyperFAR.

with astronomy information. Events with hyperFAR below 1 per month are automatically tagged as alerts to be sent. The high-energy neutrino alert pipeline is thus able, based only on neutrino properties, to identify a cosmic neutrino one in three times. The estimated number of events for the pure high-energy neutrino pipeline is shown Table 3.5.

Table 3.5.: Estimated number of events in 30 days from simulations after the 1 event per month selection on hyperFAR.

Cosmic neutrinos	0.4207 ± 0.0040
Atmospheric neutrinos	0.9800 ± 0.0561
Atmospheric muons	–
Total background	0.9800 ± 0.0561
Total	1.4007 ± 0.0562

3C.3.2. Search for multiplets

The multiplet pipeline is currently in development for the ORCA detector. The principle is identical to the multiplet search of ANTARES and the clustering

searches of IceCube. The BDT classifier used in the ORCA processing pipeline is able to discriminate atmospheric muons from neutrinos.

From the atmospheric and cosmic neutrinos, the temporal and spatial correlation is computed between each event. The temporal search is based on [143] and requires data to be Poisson distributed, which is verified. The probability to find two events within a time window τ is given by

$$P(\Delta t \leq \tau \,|\, N, T) = 1 - \left(1 + \frac{2\tau}{T}\right)^{-(N+1)}, \tag{3.6}$$

where N is the observed number of events over a wider time window T.

The spatial correlation between two events is computed from the two respective uncertainty region in the sky. From the sky split in a high number of pixels, the probability for two events to be spatially correlated is

$$p_{\text{loc}} = 1 - \left(\frac{N_{\text{overlap}}}{N_{\text{union}}} \times \left(1 - \frac{N_{\text{union}}}{N_{\text{total}}}\right)\right), \tag{3.7}$$

where N_{overlap} is the number of overlapping pixels between the two events, N_{union} is the number of pixels within the union of the two events regions and N_{total} is the total number of pixels within the sky.

From the two probabilities, the combined probability can be computed with

$$p_{\text{combined}} = 1 - \left((1 - p_{\text{time}}) \times (1 - p_{\text{loc}})\right). \tag{3.8}$$

The former describes the principle of the multiplet search. The pipeline is still a work in progress, notably to define the probability threshold for events to transmit to the astro module and to be selected as multiplet-only alerts.

3C.4. Multi-wavelength correlation

A set of events arrives to the astro module with a given rate. For every event, a list of potential sources needs to be retrieved as well as their properties. This section presents the preliminary work performed for the astro module and the planned method to be implemented. A first example is also applied to a specific event.

3C.4.1. Proof of concept

AGNs in a 1° cone The first approach of the conception of the astro module was to search for a specific type of objects. To do so, the SIMBAD Astronomical Database [144] from the Strasbourg astronomical Data Center (CDS) was used. The SIMBAD database is a meta-compilation of all properties from astronomical objects obtained from publications. All objects in SIMBAD are classified with a type, which describes the nature of the object. The classification is hierarchical, meaning that some galaxies (G) are also be classified as AGN, and some AGN can be classified as radio galaxies (rG) and so on.

A random set of galactic coordinates is generated. For every coordinate, a one degree region of the sky is probed to look for AGNs. The query is made using the `astroquery` library. This is made for 100 queries, and the number of AGNs within the one degree region is shown Figure 3.18. The high number of AGNs found within 1° illustrates the difficulty to select objects.

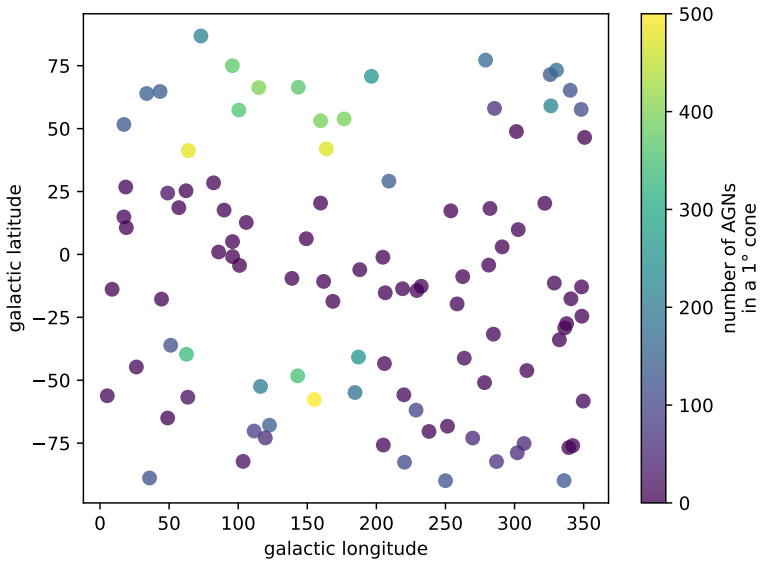

Figure 3.18.: Scatter plot for the number of found AGNs within one degree of the galactic coordinate.

Optical transients in a 1° cone To reduce the number of objects, a constraint on variability can be added. The FINK broker, which serves as an interface for the ZTF observatory, can automatically search for an association with the

SIMBAD database [131]. For 1000 randomly generated coordinates, ZTF alerts associated with an "interesting" object are searched within a 1° cone. ZTF alerts are issued when a 5σ difference with a template image is found. Object tagged as "interesting" are AGNs, AGN subcategories and ultra-luminous X-ray sources. Again the number of objects found within 1° is high.

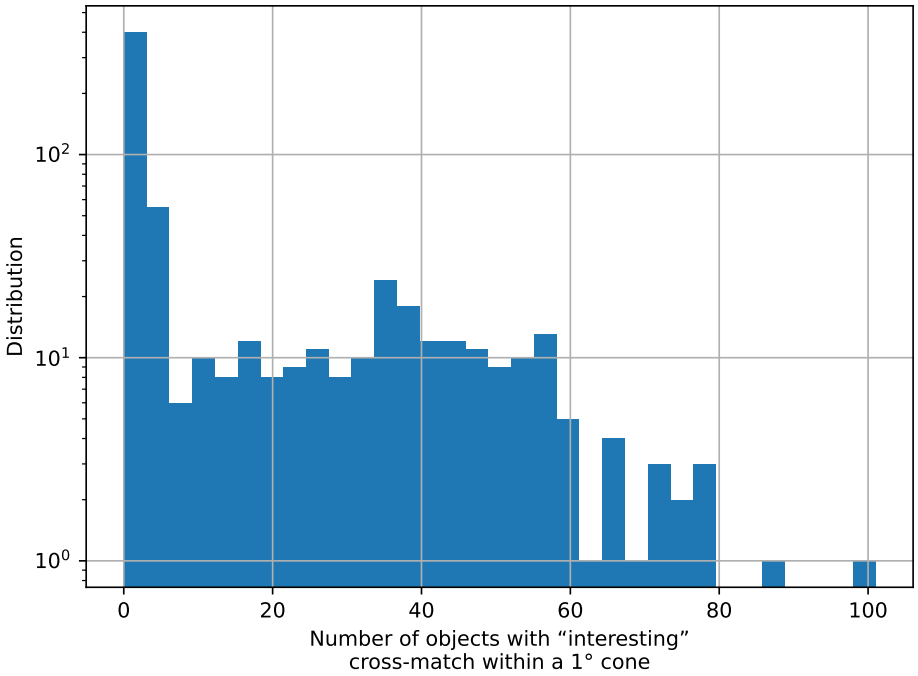

Figure 3.19.: Distribution of "interesting" objects cross-matched to ZTF alerts within 1000 1° search cones. An interesting object is defined as either an AGN and subcategories or an ultra-luminous X-ray source.

The two searches described above show the need to start from a reduced selection of objects. The following section describes the investigation performed on the possible sources of data for different wavelengths.

3C.4.2. Available multi-wavelength data

γ-rays The Fermi-LAT source catalog is a standard list of gamma-ray sources [145]. Its latest iteration (as of early 2025) is the data release 4 of the fourth catalog, named 4FGL-DR4 [146]. The catalog is made from 14 years of observation in the energy range from 50 MeV to 1 TeV and includes 194 gamma-ray sources.

Around one fourth of the observed sources is found to vary significantly on timescales of one year.

An initial goal of the astro module was to compute the variability in gamma emission in the search cone, independently of known gamma-ray sources. To do so, significant time was spent on studying the FlaapLUC tool [147]. FlaapLUC aims to detect early fast gamma transient to trigger follow-up searches. It has been developed using a simple aperture photometry approach, without considering the spectral shape of sources. An example light-curve obtained with FlaapLuc for the blazar PKS0736+01 is chown Figure 3.20. However, the tool is made to follow a given list of sources, and adapting it for given arbitrary regions of the sky proved to be difficult. In addition, some technical issues drove to choose a different method.

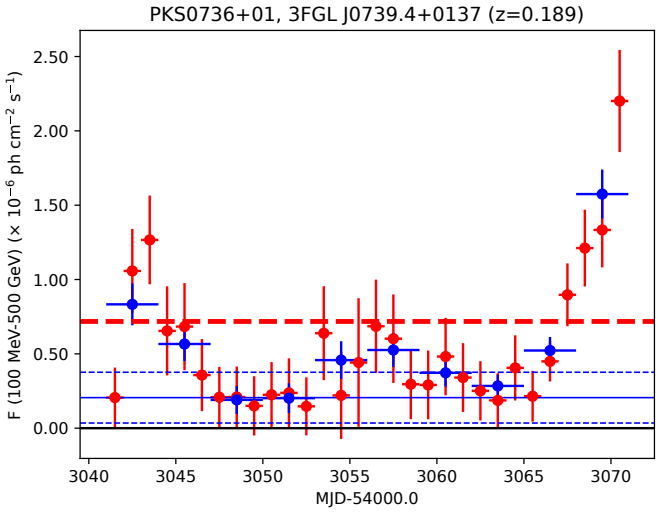

Figure 3.20.: FLaapLUC light curve output on PKS 0736+01 issued on Feb. 18, 2015. [147]

The Fermi-LAT Lightcurve Repository (LCR) is a publicly available library of gamma-ray light-curves for over 1500 sources [148]. Bins of either 3 days, 1 week or 1 month can be chosen when querying the light-curve for a given object. The queries can be made to a web API, simplifying significantly the process. One downside of the Fermi LCR is that the last bin, for the last few days for example, is missing. However, the objects present in the repository are mostly AGNs, which usually have a variability higher than months due to their sizes.

Finally, a last considered option is forced aperture photometry. The light-

curves of the Fermi LCR are computed using likelihood analysis, which leads to more accurate flux measurements. However, aperture photometry is model independent and easier to perform. It can also be performed with the Fermi tools, which simplifies the process [149]. The application of forced photometry is considered for sources which light-curves are not part of the Fermi LCR.

Optical The FINK broker [131] is one of the chosen brokers to aggregate ZTF and VRO alerts. As of early 2025, only the ZTF observatory is performing observations. Every time a significant difference is found between observations and template images, an alert is issued and retrieved by the FINK broker. Every alert is classified, either from cross-matches with the SIMBAD database or from homemade classifiers.

The data can be accessed in real-time from two different methods. The first method is a web API where alerts can be searched by sky position, by date or by classification. The second method is a real-time stream of filtered alerts, where only a subset of alerts is transmitted depending on the classification. An example light-curve in the green and red bands is shown Figure 3.21. The light-curve was queried from the FINK web API in the direction of the gamma source 4FGL J2116.2+3339 (chosen randomly). One downside from the web API search is that the current night cannot be queried due to the high flux of data being ingested. As such, a real-time stream containing the alerts of the current night for a given subset of objects is also necessary to obtain the latest data.

Additionally, ATLAS ("Asteroid Terrestrial-impact Last Alert System") [150, 151] is able to survey the full sky between 1 and 2 days. Originally designed for the detection of dangerous near-Earth asteroids, it is also possible to use the observations for transient surveys. ATLAS makes available with a web API a forced photometry service, with access over the full history of observation. This service is useful to obtain past data points before refined observations are made through the follow-up.

X-rays The Swift/BAT instrument monitors the full sky in the hard X-ray range, between 15 and 50 keV. Thanks to its wide field of view, over 1000 sources flux can be measured daily [152]. For each source, the daily light-curves can be directly retrieved from the Swift website.

The eROSITA telescope performed a survey of the sky between December 2019 and June 2020 with unprecedented depth [153]. The resulting catalog 1eRASS contains over 900 000 objects detected mostly in the soft X-ray band of 0.2–2.3 keV. A smaller catalog is also available in the harder 2.3–5 keV band,

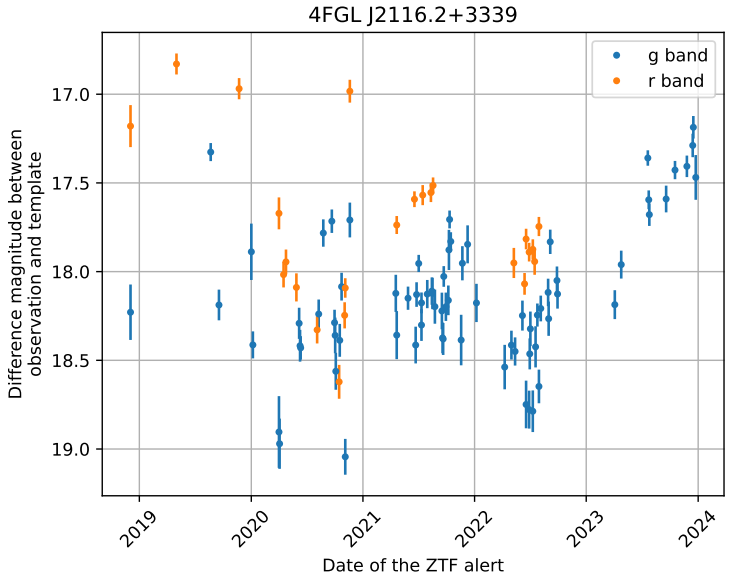

Figure 3.21.: Optical light-curves for the 4FGL J2116.2+3339 gamma sources retrieved from the ZTF observatory with the FINK broker.

containing a bit over 5000 sources.

Radio The Radio Fundamental Catalog (RFC), published in January 2025, is an all-sky catalog of radio sources [154]. It aggregates all very long baseline interferometry observations in the radio range between 2 and 23 GHz. Overall, around 22000 sources are identified with their flux at different bands. All objects are cross-matched with 14 large surveys, from all wavelengths: radio (NVSS, VLASS, SUMSS, TGSS, AT20G), optical and infrared (Gaia EDR3, Pan-STARRS, ALLWISE, 2MASS, Galaxy Evolution Explorer (GALEX)), X-ray (2RXS, XMMSL, 1eRASS) and gamma (Fermi-LAT). Additionally, the eventual jet angle and redshift are also given.

No easy method was found to retrieve automatically radio light-curves. A possible source could be to use surveys such as the ASKAP Variables and Slow Transient (VAST) [155], but further work is needed on that front.

3C.4.3. Prototype module

From the tests performed previously and the available data described beforehand, the following protocol is chosen for the astro module:

– within the uncertainty cone of origin from the neutrino, search for objects within the eROSITA, RFC and Fermi catalogs;

– for each object found, search for an associated light-curve if possible;

– if no known gamma source is found, apply a forced photometry method within the cone search;

– from the obtained flux and variability, select on the brightest radio and X-ray sources;

– for every selected object, retrieve the associated light-curve in the optical range from FINK and ATLAS forced photometry service.

No selection is made on the intensity of the gamma flux to avoid a bias towards sources with high absorption. However, radio and X-ray emissions are directly correlated to the source magnetic field, which plays a direct role in the acceleration of charged particles and thus the production of neutrinos. The planned astro module method is summarized Figure 3.22.

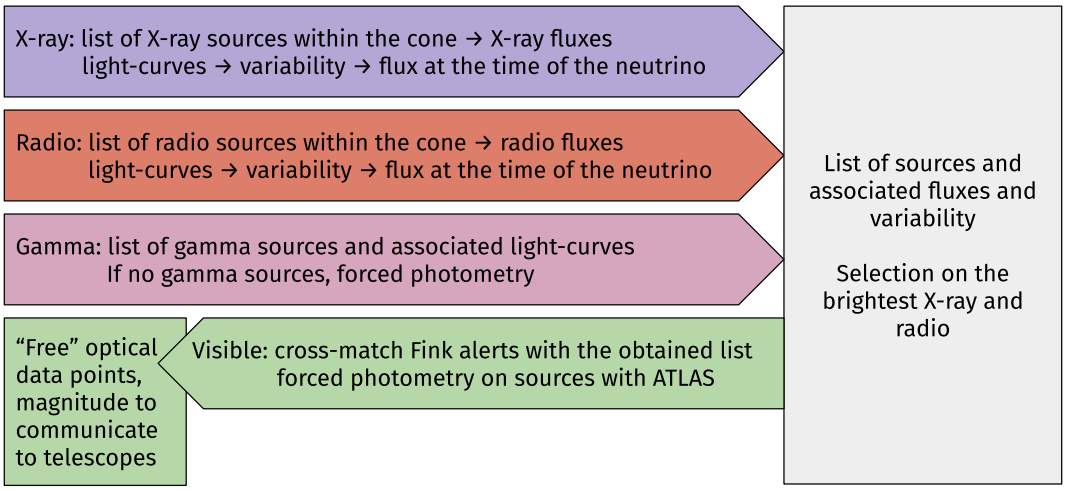

Figure 3.22.: Diagram describing the planned method to be applied to select astronomical sources in the KM3NeT alert sending program.

The current prototype of the astro module includes a cross-match with the three chosen catalogs and the retrieval of associated optical light-curves from the FINK broker. Compared to the high-energy selection, more variables need to be considered: flux in the different bands (soft and hard X-ray for eROSITA, 5 radio bands for RFC), physical quantity describing the variability and state

at the time of the neutrino, distance from the center of the cone search, etc. The selection method is under discussion within the KM3NeT collaboration.

3C.4.4. Example application to KM3-230213A

On February 13th 2023, an event was observed with the KM3NeT/ARCA detector. This event triggered 3672 PMTs, around 35 % of the active PMTs of the detector at the time. Named KM3-230213A, the event is identified as a near horizontal muon crossing the detector. The muon energy is estimated from the number of triggered PMTs as 120^{+110}_{-60} PeV. Because of the near horizontal nature of the event, the muon can only originate from a neutrino interaction. Indeed, a muon with this direction would have to cross around 300 km of water, which is impossible for an atmospheric muon. As such, KM3-230213A is the most energetic neutrino ever observed [156].

The celestial coordinates (J2000) associated with KM3-230213A are RA = 94.3°, dec = −7.8° with a 3° uncertainty cone for the 99 % quantile. Most of the uncertainty comes from the absolute orientation of the detector. A search of counterpart candidates was made in the uncertainty cone, and the method and results is described in [156].

Despite the searches already performed, KM3-230213A is a good candidate to test the astro module on. Counterparts are searched within the 3° uncertainty cone. The catalogs used are the Fermi 4FGL-DR4, the eROSITA (1eRASS) main catalog containing X-ray sources detected in the 0.3–2.3 keV band, the eROSITA hard catalog in the 2.3–5.0 keV band and the RFC catalog. Respectively, 3 sources are found in 4FGL-DR4 (see Table 3.6), 648 sources are found in main 1eRASS, 4 sources are found in hard 1eRASS (see Table 3.7) and 24 sources are found in RFC (see Table 3.8). The table of X-ray sources found with the main eROSITA catalog are not shown due to the high number. The associated flux is given for gamma and X-ray sources. For radio sources, the number of association found in other surveys is shown instead of the flux in the four bands.

Table 3.6.: Sources found within the uncertainty origin region of KM3-230213A in the 4FGL-DR4 catalog.

Source name	RA [deg]	Dec [deg]	Integral photon flux from 1 to 100 GeV [photons/s/cm^2]
4FGL J0608.0-0835	92.0101	-8.5857	1.7624×10^{-9}
4FGL J0616.2-0653	94.0570	-6.8983	1.8956×10^{-10}
4FGL J0624.8-0735	96.2239	-7.5891	3.8454×10^{-10}

Table 3.7.: Sources found within the uncertainty origin region of KM3-230213A in the hard 1eRASS catalog.

Source name	RA [deg]	Dec [deg]	Source flux in 2.3–5.0 keV band [erg/s/cm^2]
1eRASS J060759.7-083448	91.9994	−8.5804	1.7152×10^{-12}
1eRASS J061542.2-072344	93.9263	−7.3958	5.8674×10^{-12}
1eRASS J061235.9-064417	93.1498	−6.7382	3.1652×10^{-12}
1eRASS J062405.9-093849	96.0251	−9.6474	2.5014×10^{-12}

Table 3.8.: Sources found within the uncertainty origin region of KM3-230213A in the RFC catalog.

Source name	RA [deg]	Dec [deg]	Catalogs with found counterparts
RFC J0606-0724	91.6814	-6.5916	NVSS, VLASS, TGSS, AT20G, Gaia, PS1, WISE, 1eRASS
RFC J0607-0733	91.6814	-6.5916	NVSS, VLASS, PS1
RFC J0607-0834	91.6814	-6.5916	NVSS, VLASS, TGSS, AT20G, Gaia, PS1, WISE, 1eRASS, FERMI
RFC J0608-0727	91.6814	-6.5916	NVSS, VLASS, TGSS, AT20G
RFC J0608-1028	91.6814	-6.5916	NVSS, VLASS, TGSS
RFC J0609-0615	91.6814	-6.5916	NVSS, VLASS, TGSS, Gaia, PS1
RFC J0610-0959	91.6814	-6.5916	NVSS, VLASS, TGSS, AT20G, Gaia, PS1, WISE
RFC J0611-1155	91.6814	-6.5916	NVSS, VLASS, TGSS, AT20G, WISE
RFC J0611-0800	91.6814	-6.5916	NVSS, VLASS, TGSS
RFC J0614-1045	91.6814	-6.5916	NVSS, VLASS, Gaia, PS1, WISE, 1eRASS
RFC J0614-0918	91.6814	-6.5916	NVSS, VLASS
RFC J0615-0934	91.6814	-6.5916	NVSS, VLASS
RFC J0616-1041	91.6814	-6.5916	NVSS, VLASS, TGSS, AT20G, Gaia, PS1, WISE, 1eRASS, FERMI
RFC J0617-0822	91.6814	-6.5916	NVSS, VLASS, TGSS, Gaia, PS1, WISE, 2MASS, 1eRASS
RFC J0617-1134	91.6814	-6.5916	NVSS, VLASS, TGSS, AT20G, PS1, WISE, 1eRASS
RFC J0618-0954	91.6814	-6.5916	NVSS, VLASS, AT20G
RFC J0619-1140	91.6814	-6.5916	NVSS, VLASS, TGSS, AT20G, PS1, WISE, 1eRASS, FERMI
RFC J0620-1036	91.6814	-6.5916	NVSS, VLASS, TGSS, AT20G
RFC J0620-0638	91.6814	-6.5916	NVSS, VLASS, TGSS, Gaia, PS1
RFC J0621-0609	91.6814	-6.5916	NVSS, VLASS, TGSS, AT20G, Gaia, PS1, WISE, 2MASS
RFC J0622-0846	91.6814	-6.5916	NVSS, VLASS, TGSS, AT20G
RFC J0625-1017	91.6814	-6.5916	NVSS, VLASS, TGSS, AT20G, PS1, WISE, 1eRASS
RFC J0626-1041	91.6814	-6.5916	NVSS, VLASS, TGSS, PS1, WISE, 1eRASS
RFC J0629-0838	91.6814	-6.5916	NVSS, VLASS, TGSS, AT20G

Conclusion and prospects

Over the past years, the KM3NeT Online Multi-Messenger Program grew from a real-time processing prototype to the actual running system. The event processing pipeline is running and is being monitored by a rolling team of shifters. Follow-up searches are being performed from a growing list of external observations. The first iteration of the selection method for the KM3NeT neutrino alerts is also ready.

I was personally part of the team of experts developing the Online Multi-Messenger Program. In particular, I:

- shared my expertise gained in the CCSN online pipeline for the global development of the online platform;
- took part in the development of the global follow-up software framework, mostly the MeV part;
- performed numerous shifts to monitor the processing pipelines and the results of the follow-up;
- participated in the maintenance of the monitoring tools;
- devised in cooperation with Martina Marconi the method to select neutrinos based on their properties and the computation of the associated false alarm rates;
- researched the different sources of data available for the astro module;
- implemented the first prototype of the astro module, able to search for sources and retrieve optical light-curves.

The continuous work made on the online program was presented at multiple occasions, both by colleagues and by me (Second KM3NeT Town Hall Meeting and Neutrinos in the Multi-Messenger Era).

In the near future, the KM3NeT collaboration with start reporting the results of the follow-up searches. Neutrino alerts will also start to be issued, at first with chosen partners to refine the selection methods. With the growing detectors and the continuous improvement in all fronts, KM3NeT will play in the following years a key role within the multi-messenger community.

Bibliography

[1] Johannes Albrecht et al. “The Muon Puzzle in Cosmic-Ray Induced Air Showers and Its Connection to the Large Hadron Collider”. In: *Astrophysics and Space Science* 367.3 (Mar. 9, 2022), p. 27. ISSN: 1572-946X. DOI: 10.1007/s10509-022-04054-5 (cit. on p. 23).

[2] M. G. Aartsen et al. “Astrophysical Neutrinos and Cosmic Rays Observed by IceCube”. In: *Advances in Space Research*. Origins of Cosmic Rays 62.10 (Nov. 15, 2018), pp. 2902–2930. ISSN: 0273-1177. DOI: 10.1016/j.asr.2017.05.030 (cit. on p. 25).

[3] Thomas K. Gaisser, Ralph Engel, and Elisa Resconi. *Cosmic Rays and Particle Physics*. 2nd ed. Cambridge University Press, June 2, 2016. ISBN: 978-0-521-01646-9 978-1-139-19219-4. DOI: 10.1017/cbo9781139192194 (cit. on p. 25).

[4] D. Kagan et al. “Relativistic Magnetic Reconnection in Pair Plasmas and Its Astrophysical Applications”. In: *Space Science Reviews* 191.1 (Oct. 1, 2015), pp. 545–573. ISSN: 1572-9672. DOI: 10.1007/s11214-014-0132-9 (cit. on p. 26).

[5] L. Sironi, U. Keshet, and M. Lemoine. “Relativistic Shocks: Particle Acceleration and Magnetization”. In: *Space Science Reviews* 191.1–4 (Oct. 2015), pp. 519–544. ISSN: 0038-6308, 1572-9672. DOI: 10.1007/s11214-015-0181-8 (cit. on p. 26).

[6] Frank M. Rieger. “An Introduction to Particle Acceleration in Shearing Flows”. In: *Galaxies* 7.3 (3 Sept. 2019), p. 78. ISSN: 2075-4434. DOI: 10.3390/galaxies7030078 (cit. on p. 26).

[7] Karl G. Jansky. “Radio Waves from Outside the Solar System”. In: *Nature* 132.3323 (July 1933), pp. 66–66. ISSN: 1476-4687. DOI: 10.1038/132066a0 (cit. on p. 26).

[8] The Event Horizon Telescope Collaboration et al. “First M87 Event Horizon Telescope Results. I. The Shadow of the Supermassive Black Hole”. In: *The Astrophysical Journal Letters* 875.1 (Apr. 10, 2019), p. L1. ISSN: 2041-8205, 2041-8213. DOI: 10.3847/2041-8213/ab0ec7 (cit. on p. 27).

[9] I. Heywood et al. “The 1.28 GHz MeerKAT Galactic Center Mosaic”. In: *The Astrophysical Journal* 925.2 (Feb. 2022), p. 165. ISSN: 0004-637X. DOI: 10.3847/1538-4357/ac449a (cit. on p. 27).

[10] A. A. Abdo et al. “FERMI LARGE AREA TELESCOPE OBSERVATIONS OF MARKARIAN 421: THE MISSING PIECE OF ITS SPECTRAL ENERGY DISTRIBUTION”. In: *The Astrophysical Journal* 736.2 (July 2011), p. 131. ISSN: 0004-637X. DOI: 10.1088/0004-637X/736/2/131 (cit. on pp. 28, 30).

[11] Gabriele Ghisellini. *Radiative Processes in High Energy Astrophysics*. Vol. 873. Lecture Notes in Physics. Heidelberg: Springer International Publishing, 2013. ISBN: 978-3-319-00611-6 978-3-319-00612-3. DOI: 10.1007/978-3-319-00612-3 (cit. on pp. 29, 30).

[12] Edoardo Vitagliano, Irene Tamborra, and Georg Raffelt. “Grand Unified Neutrino Spectrum at Earth: Sources and Spectral Components”. In: *Reviews of Modern Physics* 92.4 (Dec. 9, 2020), p. 045006. DOI: 10.1103/RevModPhys.92.045006 (cit. on pp. 31, 33).

[13] IceCube Collaboration et al. “Characterization of the Astrophysical Diffuse Neutrino Flux Using Starting Track Events in IceCube”. In: *Physical Review D* 110.2 (July 2, 2024), p. 022001. DOI: 10.1103/PhysRevD.110.022001 (cit. on p. 33).

[14] IceCube Collaboration. “Evidence for High-Energy Extraterrestrial Neutrinos at the IceCube Detector”. In: *Science* 342.6161 (Nov. 22, 2013), p. 1242856. DOI: 10.1126/science.1242856 (cit. on pp. 32, 129).

[15] IceCube Collaboration et al. “Multimessenger Observations of a Flaring Blazar Coincident with High-Energy Neutrino IceCube-170922A”. In: *Science* 361.6398 (July 13, 2018), eaat1378. DOI: 10.1126/science.aat1378 (cit. on pp. 32, 39, 41).

[16] Alexander Plavin et al. “Observational Evidence for the Origin of High-energy Neutrinos in Parsec-scale Nuclei of Radio-bright Active Galaxies”. In: *The Astrophysical Journal* 894.2 (May 2020), p. 101. ISSN: 0004-637X. DOI: 10.3847/1538-4357/ab86bd (cit. on p. 32).

[17] IceCube Collaboration et al. “Evidence for Neutrino Emission from the Nearby Active Galaxy NGC 1068”. In: *Science* 378.6619 (Nov. 4, 2022), pp. 538–543. DOI: 10.1126/science.abg3395 (cit. on p. 32).

[18] IceCube Collaboration. “Observation of High-Energy Neutrinos from the Galactic Plane”. In: *Science* 380.6652 (June 30, 2023), pp. 1338–1343. DOI: 10.1126/science.adc9818 (cit. on p. 32).

[19] LIGO Scientific Collaboration and Virgo Collaboration et al. “Observation of Gravitational Waves from a Binary Black Hole Merger”. In: *Physical Review Letters* 116.6 (Feb. 11, 2016), p. 061102. DOI: 10.1103/PhysRevLett.116.061102 (cit. on p. 32).

[20] Maurizio Spurio. *Particles and Astrophysics: A Multi-Messenger Approach*. Astronomy and Astrophysics Library. Cham: Springer International Publishing, 2015. ISBN: 978-3-319-08050-5 978-3-319-08051-2. DOI: 10.1007/978-3-319-08051-2 (cit. on p. 35).

[21] Floyd W Stecker. *Cosmic Gamma Rays*. Scientific and Technical Information Office, National Aeronautics and Space Administration, Jan. 1, 1971. 266 pp. URL: http://archive.org/details/cosmicgammaraysn0000floy (cit. on p. 36).

[22] Imre Bartos and Marek Kowalski. *Multimessenger Astronomy*. IOP Publishing, Apr. 1, 2017. ISBN: 978-0-7503-1369-8. URL: https://iopscience.iop.org/book/mono/978-0-7503-1369-8 (cit. on p. 37).

[23] *IAUC 4316: 1987A; N Cen 1986*. URL: http://www.cbat.eps.harvard.edu/iauc/04300/04316.html (cit. on p. 37).

[24] K. S. Hirata et al. “Observation in the Kamiokande-II Detector of the Neutrino Burst from Supernova SN1987A”. In: *Physical Review D* 38.2 (July 15, 1988), pp. 448–458. DOI: 10.1103/PhysRevD.38.448 (cit. on p. 37).

[25] R. M. Bionta et al. “Observation of a Neutrino Burst in Coincidence with Supernova 1987A in the Large Magellanic Cloud”. In: *Physical Review Letters* 58.14 (Apr. 6, 1987), pp. 1494–1496. DOI: 10.1103/PhysRevLett.58.1494 (cit. on p. 37).

[26] E. N. Alekseev et al. “Possible Detection of a Neutrino Signal on 23 February 1987 at the Baksan Underground Scintillation Telescope of the Institute of Nuclear Research”. In: *Soviet Journal of Experimental and Theoretical Physics Letters* 45 (May 1, 1987), p. 589. ISSN: 0021-3640. URL: https://ui.adsabs.harvard.edu/abs/1987JETPL..45..589A (visited on 02/01/2025) (cit. on p. 37).

[27] M. Aglietta et al. “On the Event Observed in the Mont Blanc Underground Neutrino Observatory during the Occurrence of Supernova 1987a”. In: *Europhysics Letters* 3.12 (June 1987), p. 1315. ISSN: 0295-5075. DOI: 10.1209/0295-5075/3/12/011 (cit. on p. 37).

[28] Georg G. Raffelt. “PARTICLE PHYSICS FROM STARS”. In: *Annual Review of Nuclear and Particle Science* 49 (Volume 49, 1999 Dec. 1, 1999), pp. 163–216. ISSN: 0163-8998, 1545-4134. DOI: 10.1146/annurev.nucl.49.1.163 (cit. on p. 38).

[29] Christian Spiering. “Finale mit Knall: Neutrinos aus Supernovae”. In: *Neutrinoastronomie*. Berlin, Heidelberg: Springer Berlin Heidelberg, 2021, pp. 89–118. ISBN: 978-3-662-63293-2 978-3-662-63294-9. DOI: 10.1007/978-3-662-63294-9_5 (cit. on p. 38).

[30] B. P. Abbott et al. “Multi-Messenger Observations of a Binary Neutron Star Merger”. In: *The Astrophysical Journal Letters* 848.2 (Oct. 20, 2017), p. L12. ISSN: 2041-8205, 2041-8213. DOI: 10.3847/2041-8213/aa91c9 (cit. on pp. 39, 40, 121).

[31] Albino Perego, David Radice, and Sebastiano Bernuzzi. “AT 2017gfo: An Anisotropic and Three-component Kilonova Counterpart of GW170817”. In: *The Astrophysical Journal Letters* 850.2 (Dec. 1, 2017), p. L37. ISSN: 2041-8205, 2041-8213. DOI: 10.3847/2041-8213/aa9ab9 (cit. on p. 39).

[32] IceCube Collaboration et al. “Neutrino Emission from the Direction of the Blazar TXS 0506+056 Prior to the IceCube-170922A Alert”. In: *Science* 361.6398 (July 13, 2018), pp. 147–151. DOI: 10.1126/science.aat2890 (cit. on pp. 39, 41).

[33] S. Garrappa et al. “Investigation of Two Fermi-LAT Gamma-Ray Blazars Coincident with High-energy Neutrinos Detected by IceCube”. In: *The Astrophysical Journal* 880.2 (July 2019), p. 103. ISSN: 0004-637X. DOI: 10.3847/1538-4357/ab2ada (cit. on p. 41).

[34] M.A. Markov and I.M. Zheleznykh. “Large-Scale Cherenkov Detectors in Ocean, Atmosphere and Ice”. In: *Nuclear Instruments and Methods in Physics Research Section A: Accelerators, Spectrometers, Detectors and Associated Equipment* 248.1 (July 1986), pp. 242–251. ISSN: 01689002. DOI: 10.1016/0168-9002(86)90522-X (cit. on p. 42).

[35] J. A. Formaggio and G. P. Zeller. “From eV to EeV: Neutrino Cross Sections across Energy Scales”. In: *Reviews of Modern Physics* 84.3 (Sept. 24, 2012), pp. 1307–1341. ISSN: 0034-6861, 1539-0756. DOI: 10.1103/RevModPhys.84.1307 (cit. on p. 43).

[36] Víctor B. Valera, Mauricio Bustamante, and Christian Glaser. “The Ultra-High-Energy Neutrino-Nucleon Cross Section: Measurement Forecasts for an Era of Cosmic EeV-neutrino Discovery”. In: *Journal of High Energy Physics* 2022.6

(June 20, 2022), p. 105. ISSN: 1029-8479. DOI: 10.1007/JHEP06(2022)105 (cit. on pp. 44, 45).

[37] Roshan Mammen Abraham et al. "First Measurement of the Muon Neutrino Interaction Cross Section and Flux as a Function of Energy at the LHC with FASER". In: *Physical Review Letters* 134.21 (May 27, 2025). ISSN: 0031-9007, 1079-7114. DOI: 10.1103/physrevlett.134.211801 (cit. on pp. 44, 45).

[38] I. Frank and Ig. Tamm. "Coherent Visible Radiation of Fast Electrons Passing Through Matter". In: *Proceedings of the USSR Academy of Sciences* 14.3 (1937). DOI: 10.1007/978-3-642-74626-0_2 (cit. on p. 44).

[39] G Riccobene et al. "Deep Seawater Inherent Optical Properties in the Southern Ionian Sea". In: *Astroparticle Physics* 27.1 (Feb. 2007), pp. 1–9. ISSN: 09276505. DOI: 10.1016/j.astropartphys.2006.08.006 (cit. on p. 46).

[40] S. Adrián-Martínez et al. "Letter of Intent for KM3NeT 2.0". In: *Journal of Physics G: Nuclear and Particle Physics* 43.8 (June 2016), p. 084001. ISSN: 0954-3899. DOI: 10.1088/0954-3899/43/8/084001 (cit. on p. 49).

[41] M. Ageron et al. "ANTARES: The First Undersea Neutrino Telescope". In: *Nuclear Instruments and Methods in Physics Research Section A: Accelerators, Spectrometers, Detectors and Associated Equipment* 656.1 (Nov. 11, 2011), pp. 11–38. ISSN: 0168-9002. DOI: 10.1016/j.nima.2011.06.103 (cit. on p. 49).

[42] S. Aiello et al. "Astronomy Potential of KM3NeT/ARCA". In: *The European Physical Journal C* 84.9 (Sept. 2, 2024), p. 885. ISSN: 1434-6052. DOI: 10.1140/epjc/s10052-024-13137-2 (cit. on pp. 49, 51).

[43] S. Aiello et al. "The KM3NeT Multi-PMT Optical Module". In: *Journal of Instrumentation* 17.07 (July 2022), P07038. ISSN: 1748-0221. DOI: 10.1088/1748-0221/17/07/P07038 (cit. on p. 50).

[44] G. Mul et al. "A Vertical Electro-Optical Data Cable for KM3NeT". In: *Nuclear Instruments and Methods in Physics Research Section A: Accelerators, Spectrometers, Detectors and Associated Equipment* 725 (Oct. 2013), pp. 230–233. ISSN: 01689002. DOI: 10.1016/j.nima.2012.12.099 (cit. on p. 51).

[45] R. S. Muller. *Getting to the Point: First Cosmic Neutrino Source Search with the KM3NeT / ARCA Detector*. 2023. ISBN: 978-94-6469-422-2. URL: https://dare.uva.nl/search?identifier=20b0aa27-83ee-42a4-aeaa-a4f0a13f56ae (cit. on p. 52).

[46] S. Aiello et al. “Searches for Neutrino Counterparts of Gravitational Waves from the LIGO/Virgo Third Observing Run with KM3NeT”. In: *Journal of Cosmology and Astroparticle Physics* 2024.04 (Apr. 1, 2024), p. 026. ISSN: 1475-7516. DOI: 10.1088/1475-7516/2024/04/026 (cit. on pp. 52, 116, 118, 126).

[47] S. Aiello et al. “Search for Neutrino Emission from GRB 221009A Using the KM3NeT ARCA and ORCA Detectors”. In: *Journal of Cosmology and Astroparticle Physics* 2024.08 (Aug. 1, 2024), p. 006. ISSN: 1475-7516. DOI: 10.1088/1475-7516/2024/08/006 (cit. on pp. 52, 123, 126).

[48] KM3NeT Collaboration et al. “Atmospheric Muons Measured with the KM3NeT Detectors in Comparison with Updated Numeric Predictions”. In: *The European Physical Journal C* 84.7 (July 15, 2024), p. 696. ISSN: 1434-6052. DOI: 10.1140/epjc/s10052-024-13018-8 (cit. on p. 52).

[49] The KM3NeT collaboration et al. “Probing Invisible Neutrino Decay with KM3NeT/ORCA”. In: *Journal of High Energy Physics* 2023.4 (Apr. 19, 2023), p. 90. ISSN: 1029-8479. DOI: 10.1007/JHEP04(2023)090 (cit. on p. 54).

[50] KM3NeT Collaboration et al. *First Searches for Dark Matter with the KM3NeT Neutrino Telescopes*. Nov. 15, 2024. DOI: 10.48550/arXiv.2411.10092. arXiv: 2411.10092 [astro-ph]. Pre-published (cit. on p. 54).

[51] T. Chiarusi and M. Spurio. “High-Energy Astrophysics with Neutrino Telescopes”. In: *The European Physical Journal C* 65.3 (Feb. 1, 2010), pp. 649–701. ISSN: 1434-6052. DOI: 10.1140/epjc/s10052-009-1230-9 (cit. on p. 55).

[52] Simone Biagi et al. “The Data Acquisition System of the KM3NeT Detector”. In: *Proceedings of The 34th International Cosmic Ray Conference — PoS(ICRC2015)*. The 34th International Cosmic Ray Conference. The Hague, The Netherlands: Sissa Medialab, Aug. 18, 2016, p. 1172. DOI: 10.22323/1.236.1172 (cit. on p. 56).

[53] Karel Melis et al. “KM3NeT/ARCA Event Reconstruction Algorithms”. In: *Proceedings of 35th International Cosmic Ray Conference — PoS(ICRC2017)*. 35th International Cosmic Ray Conference. Bexco, Busan, Korea: Sissa Medialab, Aug. 16, 2017, p. 950. DOI: 10.22323/1.301.0950 (cit. on p. 58).

[54] David H. Clark and F. Richard Stephenson. *The Historical Supernovae*. Elsevier, 1977. ISBN: 978-0-08-020914-2. DOI: 10.1016/C2013-0-10100-6 (cit. on p. 63).

[55] Johannes Kepler. *De Stella Nova in Pede Serpentarii*. 1606 (cit. on p. 64).

[56] Walter Baade and Fritz Zwicky. “On Super-Novae”. In: *Proceedings of the National Academy of Sciences* 20.5 (May 1934), pp. 254–259. ISSN: 0027-8424, 1091-6490. DOI: 10.1073/pnas.20.5.254 (cit. on p. 64).

[57] Massimo Turatto. “Classification of Supernovae”. In: *Supernovae and Gamma-Ray Bursters*. Ed. by Kurt W. Weiler. Red. by R. Beig et al. Vol. 598. Berlin, Heidelberg: Springer Berlin Heidelberg, 2003, pp. 21–36. ISBN: 978-3-540-44053-6 978-3-540-45863-0. DOI: 10.1007/3-540-45863-8_3 (cit. on pp. 64, 66).

[58] M. M. Phillips. “The Absolute Magnitudes of Type IA Supernovae”. In: *The Astrophysical Journal* 413 (Aug. 1, 1993), p. L105. ISSN: 0004-637X. DOI: 10.1086/186970 (cit. on p. 67).

[59] Adam G. Riess et al. “Observational Evidence from Supernovae for an Accelerating Universe and a Cosmological Constant”. In: *The Astronomical Journal* 116.3 (Sept. 1998), pp. 1009–1038. ISSN: 00046256. DOI: 10.1086/300499 (cit. on p. 67).

[60] Masao Sako et al. “THE SLOAN DIGITAL SKY SURVEY-II SUPERNOVA SURVEY: SEARCH ALGORITHM AND FOLLOW-UP OBSERVATIONS”. In: *The Astronomical Journal* 135.1 (Dec. 2007), p. 348. ISSN: 1538-3881. DOI: 10.1088/0004-6256/135/1/348 (cit. on p. 67).

[61] A. Conley et al. “SUPERNOVA CONSTRAINTS AND SYSTEMATIC UNCERTAINTIES FROM THE FIRST THREE YEARS OF THE SUPERNOVA LEGACY SURVEY*”. In: *The Astrophysical Journal Supplement Series* 192.1 (Dec. 2010), p. 1. ISSN: 0067-0049. DOI: 10.1088/0067-0049/192/1/1 (cit. on p. 67).

[62] Hans-Thomas Janka. “Neutrino Emission from Supernovae”. In: *Handbook of Supernovae*. Ed. by Athem W. Alsabti and Paul Murdin. Cham: Springer International Publishing, 2017, pp. 1575–1604. ISBN: 978-3-319-21845-8 978-3-319-21846-5. DOI: 10.1007/978-3-319-21846-5_4 (cit. on pp. 68, 72).

[63] Rasmus S. L. Hansen, Manfred Lindner, and Oliver Scholer. “Timing the Neutrino Signal of a Galactic Supernova”. In: *Physical Review D* 101.12 (June 16, 2020), p. 123018. ISSN: 2470-0010, 2470-0029. DOI: 10.1103/PhysRevD.101.123018 (cit. on pp. 70, 71).

[64] Carlo Giunti and Chung W. Kim. *Fundamentals of Neutrino Physics and Astrophysics*. Oxford University Press, Mar. 15, 2007. ISBN: 978-0-19-850871-7. DOI: 10.1093/acprof:oso/9780198508717.001.0001 (cit. on p. 73).

[65] Ko Nakamura et al. “Multimessenger Signals of Long-Term Core-Collapse Supernova Simulations: Synergetic Observation Strategies”. In: *Monthly Notices of the Royal Astronomical Society* 461.3 (Sept. 21, 2016), pp. 3296–3313. ISSN: 0035-8711, 1365-2966. DOI: 10.1093/mnras/stw1453 (cit. on pp. 73, 74).

[66] Meriem Bendahman et al. “Prospects for Realtime Characterization of Core-Collapse Supernova and Neutrino Properties”. In: *Journal of Cosmology and Astroparticle Physics* 2024.02 (Feb. 1, 2024), p. 008. ISSN: 1475-7516. DOI: 10.1088/1475-7516/2024/02/008 (cit. on p. 75).

[67] Karolina Rozwadowska, Francesco Vissani, and Enrico Cappellaro. “On the Rate of Core Collapse Supernovae in the Milky Way”. In: *New Astronomy* 83 (Feb. 1, 2021), p. 101498. ISSN: 1384-1076. DOI: 10.1016/j.newast.2020.101498 (cit. on p. 75).

[68] Pietro Antonioli et al. “SNEWS: The SuperNova Early Warning System”. In: *New Journal of Physics* 6 (Sept. 2, 2004), pp. 114–114. ISSN: 1367-2630. DOI: 10.1088/1367-2630/6/1/114 (cit. on p. 75).

[69] Kate Scholberg. “Supernova Neutrino Detection”. In: *Annual Review of Nuclear and Particle Science* 62 (Volume 62, 2012 Nov. 23, 2012), pp. 81–103. ISSN: 0163-8998, 1545-4134. DOI: 10.1146/annurev-nucl-102711-095006 (cit. on p. 76).

[70] Laurie Walk et al. “Neutrino Emission Characteristics of Black Hole Formation in Three-Dimensional Simulations of Stellar Collapse”. In: *Physical Review D* 101.12 (June 11, 2020), p. 123013. ISSN: 2470-0010, 2470-0029. DOI: 10.1103/PhysRevD.101.123013 (cit. on p. 81).

[71] Irene Tamborra et al. “Neutrino Emission Characteristics and Detection Opportunities Based on Three-Dimensional Supernova Simulations”. In: *Physical Review D* 90.4 (Aug. 25, 2014), p. 045032. ISSN: 1550-7998, 1550-2368. DOI: 10.1103/PhysRevD.90.045032 (cit. on p. 81).

[72] R. Abbasi et al. “IceCube Sensitivity for Low-Energy Neutrinos from Nearby Supernovae”. In: *Astronomy & Astrophysics* 535 (Nov. 1, 2011), A109. ISSN: 0004-6361, 1432-0746. DOI: 10.1051/0004-6361/201117810 (cit. on p. 83).

[73] M. Ikeda et al. “Search for Supernova Neutrino Bursts at Super-Kamiokande”. In: *The Astrophysical Journal* 669.1 (Nov. 1, 2007), p. 519. ISSN: 0004-637X. DOI: 10.1086/521547 (cit. on p. 83).

[74] Robert D. Cousins. *Annotated Bibliography of Some Papers on Combining Significances or P-Values*. Dec. 20, 2008. DOI: 10.48550/arXiv.0705.2209. arXiv: 0705.2209 [physics]. Pre-published (cit. on p. 90).

[75] A. Coleiro et al. “Combining Neutrino Experimental Light-Curves for Pointing to the next Galactic Core-Collapse Supernova”. In: *The European Physical Journal C* 80.9 (Sept. 2020), p. 856. ISSN: 1434-6044, 1434-6052. DOI: 10.1140/epjc/s10052-020-8407-7 (cit. on p. 101).

[76] S Al Kharusi et al. “SNEWS 2.0: A next-Generation Supernova Early Warning System for Multi-Messenger Astronomy”. In: *New Journal of Physics* 23.3 (Mar. 1, 2021), p. 031201. ISSN: 1367-2630. DOI: 10.1088/1367-2630/abde33 (cit. on pp. 103, 104).

[77] M. Kara et al. *The SNEWS 2.0 Alert Software for the Coincident Detection of Neutrinos from Core-Collapse Supernovae*. Version 2. 2024. DOI: 10.48550/ARXIV.2406.17743. Pre-published (cit. on p. 104).

[78] Shigeo S. Kimura et al. “Transejecta High-Energy Neutrino Emission from Binary Neutron Star Mergers”. In: *Physical Review D* 98.4 (Aug. 24, 2018), p. 043020. ISSN: 2470-0010, 2470-0029. DOI: 10.1103/PhysRevD.98.043020 (cit. on p. 111).

[79] Shigeo S. Kimura et al. “High-Energy Neutrino Emission from Short Gamma-Ray Bursts: Prospects for Coincident Detection with Gravitational Waves”. In: *The Astrophysical Journal Letters* 848.1 (Oct. 10, 2017), p. L4. ISSN: 2041-8205, 2041-8213. DOI: 10.3847/2041-8213/aa8d14 (cit. on p. 111).

[80] Kumiko Kotera and Joseph Silk. “ULTRAHIGH-ENERGY COSMIC RAYS AND BLACK HOLE MERGERS”. In: *The Astrophysical Journal Letters* 823.2 (June 1, 2016), p. L29. ISSN: 2041-8205, 2041-8213. DOI: 10.3847/2041-8205/823/2/L29 (cit. on p. 111).

[81] Koutarou Kyutoku and Kazumi Kashiyama. “Detectability of Thermal Neutrinos from Binary Neutron-Star Mergers and Implications for Neutrino Physics”. In: *Physical Review D* 97.10 (May 1, 2018), p. 103001. ISSN: 2470-0010, 2470-0029. DOI: 10.1103/PhysRevD.97.103001 (cit. on pp. 111, 112).

[82] R. Abbott et al. “GWTC-2: Compact Binary Coalescences Observed by LIGO and Virgo during the First Half of the Third Observing Run”. In: *Physical Review X* 11.2 (June 9, 2021), p. 021053. ISSN: 2160-3308. DOI: 10.1103/PhysRevX.11.021053 (cit. on p. 111).

[83] R. Abbott et al. “GWTC-2.1: Deep Extended Catalog of Compact Binary Coalescences Observed by LIGO and Virgo during the First Half of the Third Observing Run”. In: *Physical Review D* 109.2 (Jan. 5, 2024), p. 022001. ISSN: 2470-0010, 2470-0029. DOI: 10.1103/PhysRevD.109.022001 (cit. on p. 111).

[84] R. Abbott et al. “GWTC-3: Compact Binary Coalescences Observed by LIGO and Virgo during the Second Part of the Third Observing Run”. In: *Physical Review X* 13.4 (Dec. 4, 2023), p. 041039. ISSN: 2160-3308. DOI: 10.1103/PhysRevX.13.041039 (cit. on p. 112).

[85] Yuichiro Sekiguchi et al. “Gravitational Waves and Neutrino Emission from the Merger of Binary Neutron Stars”. In: *Physical Review Letters* 107.5 (July 27, 2011), p. 051102. ISSN: 0031-9007, 1079-7114. DOI: 10.1103/PhysRevLett.107.051102 (cit. on p. 112).

[86] Nathalie Palanque-Delabrouille et al. “Neutrino Masses and Cosmology with Lyman-alpha Forest Power Spectrum”. In: *Journal of Cosmology and Astroparticle Physics* 2015.11 (Nov. 6, 2015), pp. 011–011. ISSN: 1475-7516. DOI: 10.1088/1475-7516/2015/11/011 (cit. on p. 112).

[87] Francesco Capozzi et al. “Unfinished Fabric of the Three Neutrino Paradigm”. In: *Physical Review D* 104.8 (Oct. 26, 2021), p. 083031. ISSN: 2470-0010, 2470-0029. DOI: 10.1103/PhysRevD.104.083031 (cit. on p. 112).

[88] Gary J. Feldman and Robert D. Cousins. “Unified Approach to the Classical Statistical Analysis of Small Signals”. In: *Physical Review D* 57.7 (Apr. 1, 1998), pp. 3873–3889. ISSN: 0556-2821, 1089-4918. DOI: 10.1103/PhysRevD.57.3873 (cit. on p. 114).

[89] S. Aiello et al. “The KM3NeT Potential for the next Core-Collapse Supernova Observation with Neutrinos”. In: *The European Physical Journal C* 81.5 (May 24, 2021), p. 445. ISSN: 1434-6052. DOI: 10.1140/epjc/s10052-021-09187-5 (cit. on p. 116).

[90] S. Aiello et al. “Implementation and First Results of the KM3NeT Real-Time Core-Collapse Supernova Neutrino Search”. In: *The European Physical Journal C* 82.4 (Apr. 11, 2022), p. 317. ISSN: 1434-6052. DOI: 10.1140/epjc/s10052-022-10137-y (cit. on pp. 116, 125).

[91] A. Albert et al. “Search for Neutrino Counterparts to the Gravitational Wave Sources from LIGO/Virgo O3 Run with the ANTARES Detector”. In: *Journal of Cosmology and Astroparticle Physics* 2023.04 (Apr. 1, 2023), p. 004. ISSN: 1475-7516. DOI: 10.1088/1475-7516/2023/04/004 (cit. on p. 116).

[92] R. Abbasi et al. “IceCube Search for Neutrinos Coincident with Gravitational Wave Events from LIGO/Virgo Run O3”. In: *The Astrophysical Journal* 944.1 (Feb. 1, 2023), p. 80. ISSN: 0004-637X, 1538-4357. DOI: 10.3847/1538-4357/aca5fc (cit. on p. 116).

[93] K. Abe et al. “Search for Neutrinos in Coincidence with Gravitational Wave Events from the LIGO–Virgo O3a Observing Run with the Super-Kamiokande Detector”. In: *The Astrophysical Journal* 918.2 (Sept. 1, 2021), p. 78. ISSN: 0004-637X, 1538-4357. DOI: 10.3847/1538-4357/ac0d5a (cit. on p. 116).

[94] S. Abe et al. “Search for Low-energy Electron Antineutrinos in KamLAND Associated with Gravitational Wave Events”. In: *The Astrophysical Journal* 909.2 (Mar. 1, 2021), p. 116. ISSN: 0004-637X, 1538-4357. DOI: 10.3847/1538-4357/abd5bc (cit. on p. 116).

[95] Maia A. Williams et al. “GRB 221009A: Discovery of an Exceptionally Rare Nearby and Energetic Gamma-Ray Burst”. In: *The Astrophysical Journal Letters* 946.1 (Mar. 1, 2023), p. L24. ISSN: 2041-8205, 2041-8213. DOI: 10.3847/2041-8213/acbcd1 (cit. on p. 121).

[96] Michela Negro et al. “The IXPE View of GRB 221009A”. In: *The Astrophysical Journal Letters* 946.1 (Mar. 1, 2023), p. L21. ISSN: 2041-8205, 2041-8213. DOI: 10.3847/2041-8213/acba17 (cit. on p. 121).

[97] D. A. Kann et al. “GRANDMA and HXMT Observations of GRB 221009A: The Standard Luminosity Afterglow of a Hyperluminous Gamma-Ray Burst—In Gedenken an David Alexander Kann”. In: *The Astrophysical Journal Letters* 948.2 (May 1, 2023), p. L12. ISSN: 2041-8205, 2041-8213. DOI: 10.3847/2041-8213/acc8d0 (cit. on p. 121).

[98] Tanmoy Laskar et al. “The Radio to GeV Afterglow of GRB 221009A”. In: *The Astrophysical Journal Letters* 946.1 (Mar. 1, 2023), p. L23. ISSN: 2041-8205, 2041-8213. DOI: 10.3847/2041-8213/acbfad (cit. on p. 121).

[99] M. D. Fulton et al. “The Optical Light Curve of GRB 221009A: The Afterglow and the Emerging Supernova”. In: *The Astrophysical Journal Letters* 946.1 (Mar. 1, 2023), p. L22. ISSN: 2041-8205, 2041-8213. DOI: 10.3847/2041-8213/acc101 (cit. on p. 121).

[100] Eric Burns et al. “GRB 221009A: The BOAT”. In: *The Astrophysical Journal Letters* 946.1 (Mar. 1, 2023), p. L31. ISSN: 2041-8205, 2041-8213. DOI: 10.3847/2041-8213/acc39c (cit. on p. 121).

[101] The LHAASO Collaboration. “Very High-Energy Gamma-Ray Emission beyond 10 TeV from GRB 221009A”. In: *Science Advances* 9.46 (Nov. 17, 2023), eadj2778. ISSN: 2375-2548. DOI: 10.1126/sciadv.adj2778 (cit. on p. 121).

[102] Eric Burns and Adam Goldstein. *Focus on the Ultra-luminous Gamma-Ray Burst GRB 221009A*. The Astrophysical Journal Letters. URL: https://iopscience.iop.org/collections/apjl-230323-172_Focus-on-the-Ultra-luminous-GRB-221009A (cit. on p. 122).

[103] Damien Dornic. *GRB 221009A: Search for Neutrinos with KM3NeT*. GCN Circular. URL: https://gcn.nasa.gov/circulars/32741 (cit. on pp. 122, 136).

[104] LHAASO Collaboration et al. "A Tera–Electron Volt Afterglow from a Narrow Jet in an Extremely Bright Gamma-Ray Burst". In: *Science* 380.6652 (June 30, 2023), pp. 1390–1396. ISSN: 0036-8075, 1095-9203. DOI: 10.1126/science.adg9328 (cit. on p. 122).

[105] Isabel Goos et al. "Searching for Core-Collapse Supernova Neutrinos at KM3NeT". In: *Proceedings of 38th International Cosmic Ray Conference — PoS(ICRC2023)*. 38th International Cosmic Ray Conference. Nagoya, Japan: Sissa Medialab, July 25, 2023, p. 1160. DOI: 10.22323/1.444.1160 (cit. on p. 125).

[106] A. Albert et al. "Constraints on the Energy Spectrum of the Diffuse Cosmic Neutrino Flux from the ANTARES Neutrino Telescope". In: *Journal of Cosmology and Astroparticle Physics* 2024.08 (Aug. 1, 2024), p. 038. ISSN: 1475-7516. DOI: 10.1088/1475-7516/2024/08/038 (cit. on p. 129).

[107] A. Albert et al. "Hint for a TeV Neutrino Emission from the Galactic Ridge with ANTARES". In: *Physics Letters B* 841 (June 2023), p. 137951. ISSN: 03702693. DOI: 10.1016/j.physletb.2023.137951 (cit. on p. 129).

[108] Matteo Agostini et al. "The Pacific Ocean Neutrino Experiment". In: *Nature Astronomy* 4.10 (Sept. 8, 2020), pp. 913–915. ISSN: 2397-3366. DOI: 10.1038/s41550-020-1182-4 (cit. on p. 130).

[109] Z. P. Ye et al. "A Multi-Cubic-Kilometre Neutrino Telescope in the Western Pacific Ocean". In: *Nature Astronomy* 7.12 (Oct. 9, 2023), pp. 1497–1505. ISSN: 2397-3366. DOI: 10.1038/s41550-023-02087-6 (cit. on p. 130).

[110] Tian-Qi Huang et al. "Proposal for the High Energy Neutrino Telescope". In: *Proceedings of 38th International Cosmic Ray Conference — PoS(ICRC2023)*. 38th International Cosmic Ray Conference. Nagoya, Japan: Sissa Medialab, Aug. 5, 2023, p. 1080. DOI: 10.22323/1.444.1080 (cit. on p. 130).

[111] Liu Quinui. "Constraints on Heavy Asymmetric and Symmetric Dark Matter from the Glashow Resonance". TeVPA. 2024. URL: https://indico.uchicago.edu/event/427/contributions/1490/ (cit. on p. 130).

[112] Aya Ishihara and IceCube Collaboration. "The IceCube Upgrade - Design and Science Goals". In: *Proceedings of 36th International Cosmic Ray Conference — PoS(ICRC2019)*. 36th International Cosmic Ray Conference. Madison, WI, U.S.A.: Sissa Medialab, July 22, 2019, p. 1031. DOI: 10.22323/1.358.1031 (cit. on p. 130).

[113] M G Aartsen et al. “IceCube-Gen2: The Window to the Extreme Universe”. In: *Journal of Physics G: Nuclear and Particle Physics* 48.6 (June 1, 2021), p. 060501. ISSN: 0954-3899, 1361-6471. DOI: 10.1088/1361-6471/abbd48 (cit. on p. 130).

[114] G. A. Askaryan. “Excess Negative Charge of an Electron-Photon Shower and Its Coherent Radio Emission”. In: () (cit. on p. 130).

[115] David Shoemaker, Nicolas Arnaud, and Takahiro Sawada. *Observing Scenario Timeline Graphic, Post-O3*. URL: https://dcc.ligo.org/LIGO-G2002127-v28/public (cit. on p. 131).

[116] Andrew J. Smith and (forthe HAWC Collaboration). “HAWC: A next Generation All-Sky Gamma-Ray Telescope”. In: *Journal of Physics: Conference Series* 60.1 (Mar. 2007), p. 131. ISSN: 1742-6596. DOI: 10.1088/1742-6596/60/1/024 (cit. on p. 131).

[117] “The Pierre Auger Cosmic Ray Observatory”. In: *Nuclear Instruments and Methods in Physics Research Section A: Accelerators, Spectrometers, Detectors and Associated Equipment* 798 (Oct. 21, 2015), pp. 172–213. ISSN: 0168-9002. DOI: 10.1016/j.nima.2015.06.058 (cit. on p. 131).

[118] Xin-Hua Ma et al. “Chapter 1 LHAASO Instruments and Detector Technology”. In: *Chinese Physics C* 46.3 (Mar. 2022), p. 030001. ISSN: 1674-1137. DOI: 10.1088/1674-1137/ac3fa6 (cit. on p. 131).

[119] K Bernlöhr et al. “The Optical System of the H.E.S.S. Imaging Atmospheric Cherenkov Telescopes. Part I: Layout and Components of the System”. In: *Astroparticle Physics* 20.2 (Nov. 1, 2003), pp. 111–128. ISSN: 0927-6505. DOI: 10.1016/S0927-6505(03)00171-3 (cit. on p. 132).

[120] The CTA Consortium. *Science with the Cherenkov Telescope Array*. WORLD SCIENTIFIC, Mar. 2019. ISBN: 978-981-327-008-4 978-981-327-009-1. DOI: 10.1142/10986 (cit. on p. 132).

[121] Vladimir Lipunov et al. “Master Robotic Net”. In: *Advances in Astronomy* 2010.1 (Jan. 2010). Ed. by Taro Kotani, p. 349171. ISSN: 1687-7969, 1687-7977. DOI: 10.1155/2010/349171 (cit. on p. 133).

[122] S. Agayeva et al. “GRANDMA: A NETWORK TO COORDINATE THEM ALL”. In: *Revista Mexicana de Astronomía y Astrofísica Serie de Conferencias* 53 (Sept. 1, 2021), pp. 198–205. ISSN: 1405-2059. DOI: 10.22201/ia.14052059p.2021.53.39 (cit. on p. 133).

[123] Eric C. Bellm et al. “The Zwicky Transient Facility: System Overview, Performance, and First Results”. In: *Publications of the Astronomical Society of the Pacific* 131.995 (Jan. 1, 2019), p. 018002. ISSN: 0004-6280, 1538-3873. DOI: 10.1088/1538-3873/aaecbe (cit. on p. 133).

[124] Željko Ivezić et al. “LSST: From Science Drivers to Reference Design and Anticipated Data Products”. In: *The Astrophysical Journal* 873.2 (Mar. 10, 2019), p. 111. ISSN: 0004-637X, 1538-4357. DOI: 10.3847/1538-4357/ab042c (cit. on p. 133).

[125] Robert Braun et al. *Anticipated Performance of the Square Kilometre Array – Phase 1 (SKA1)*. Dec. 29, 2019. DOI: 10.48550/arXiv.1912.12699. arXiv: 1912.12699 [astro-ph]. Pre-published (cit. on p. 134).

[126] The CHIME/FRB Collaboration et al. “The CHIME Fast Radio Burst Project: System Overview”. In: *The Astrophysical Journal* 863.1 (Aug. 10, 2018), p. 48. ISSN: 0004-637X, 1538-4357. DOI: 10.3847/1538-4357/aad188 (cit. on p. 134).

[127] *GCN - General Coordinates Network*. URL: https://gcn.nasa.gov/ (cit. on pp. 134, 135).

[128] Rob Seaman et al. *Sky Event Reporting Metadata Version 2.0*. DOI: 10.5479/ADS/bib/2011ivoa.spec.0711S (cit. on p. 134).

[129] J. Swinbank. “Comet: A VOEvent Broker”. In: *Astronomy and Computing* 7–8 (Nov. 2014), pp. 12–26. ISSN: 22131337. DOI: 10.1016/j.ascom.2014.09.001 (cit. on p. 135).

[130] Maria T. Patterson et al. “The Zwicky Transient Facility Alert Distribution System”. In: *Publications of the Astronomical Society of the Pacific* 131.995 (Jan. 1, 2019), p. 018001. ISSN: 0004-6280, 1538-3873. DOI: 10.1088/1538-3873/aae904. arXiv: 1902.02227 [astro-ph] (cit. on p. 135).

[131] Anais Möller et al. “FINK, a New Generation of Broker for the LSST Community”. In: *Monthly Notices of the Royal Astronomical Society* 501.3 (Jan. 12, 2021), pp. 3272–3288. ISSN: 0035-8711, 1365-2966. DOI: 10.1093/mnras/staa3602 (cit. on pp. 135, 162, 164).

[132] Robert E. Rutledge. “The Astronomer’s Telegram: A Web-based Short-Notice Publication System for the Professional Astronomical Community”. In: *Publications of the Astronomical Society of the Pacific* 110.748 (June 1998), pp. 754–756. ISSN: 0004-6280, 1538-3873. DOI: 10.1086/316184 (cit. on p. 136).

[133] A. Albert et al. “Results of the Follow-up of ANTARES Neutrino Alerts”. In: *Journal of Cosmology and Astroparticle Physics* 2024.09 (Sept. 1, 2024), p. 042. ISSN: 1475-7516. DOI: 10.1088/1475-7516/2024/09/042 (cit. on pp. 136, 147).

[134] Alessandro Veutro. “Online Event Reconstruction and Classification in KM3NeT”. Seventeenth Marcel Grossman Meeting. July 9, 2024 (cit. on p. 141).

[135] T.-P. Li and Y.-Q. Ma. “Analysis Methods for Results in Gamma-Ray Astronomy”. In: *The Astrophysical Journal* 272 (Sept. 1983), p. 317. ISSN: 0004-637X, 1538-4357. DOI: 10.1086/161295 (cit. on p. 142).

[136] Juan Palacios Gonzalez et al. “Latest Multi-Messenger Results of the KM3NeT Real-Time Analysis Framework”. In: *Proceedings of 42nd International Conference on High Energy Physics — PoS(ICHEP2024)*. 42nd International Conference on High Energy Physics. Prague, Czech Republic: Sissa Medialab, Dec. 23, 2024, p. 667. DOI: 10.22323/1.476.0667 (cit. on pp. 143, 144, 146).

[137] Darren J White, E J Daw, and V S Dhillon. “A List of Galaxies for Gravitational Wave Searches”. In: *Classical and Quantum Gravity* 28.8 (Apr. 21, 2011), p. 085016. ISSN: 0264-9381, 1361-6382. DOI: 10.1088/0264-9381/28/8/085016 (cit. on p. 147).

[138] M.G. Aartsen et al. “The IceCube Realtime Alert System”. In: *Astroparticle Physics* 92 (June 2017), pp. 30–41. ISSN: 09276505. DOI: 10.1016/j.astropartphys.2017.05.002 (cit. on p. 148).

[139] R. Abbasi et al. “IceCat-1: The IceCube Event Catalog of Alert Tracks”. In: *The Astrophysical Journal Supplement Series* 269.1 (Nov. 1, 2023), p. 25. ISSN: 0067-0049, 1538-4365. DOI: 10.3847/1538-4365/acfa95 (cit. on p. 148).

[140] IceCube Collaboration. *IceCube High-Energy Neutrino Cascade Alerts*. July 31, 2020. URL: https://gcn.gsfc.nasa.gov/doc/High_Energy_Neutrino_Cascade_Alerts.pdf (cit. on p. 149).

[141] Hugo Ayala et al. “AMON: TeV Gamma and Neutrino Coincidence Alerts from HAWC and IceCube Subthreshold Data”. In: *Proceedings of 36th International Cosmic Ray Conference — PoS(ICRC2019)*. 36th International Cosmic Ray Conference. Madison, WI, U.S.A.: Sissa Medialab, July 22, 2019, p. 841. DOI: 10.22323/1.358.0841 (cit. on p. 149).

[142] Martina Marconi. “Event Selection and Direction Error for KM3NeT/ARCA Neutrino Alerts”. KM3NeT Astronomy Face-to-face Meeting, Kalamata. Sept. 12, 2024 (cit. on p. 155).

[143] Reed Essick, Geoffrey Mo, and Erik Katsavounidis. "A Coincidence Null Test for Poisson-distributed Events". In: *Physical Review D* 103.4 (Feb. 5, 2021), p. 042003. ISSN: 2470-0010, 2470-0029. DOI: 10.1103/PhysRevD.103.042003 (cit. on p. 160).

[144] M. Wenger et al. "The SIMBAD Astronomical Database: The CDS Reference Database for Astronomical Objects". In: *Astronomy and Astrophysics Supplement Series* 143.1 (Apr. 2000), pp. 9–22. ISSN: 0365-0138, 1286-4846. DOI: 10.1051/aas:2000332 (cit. on p. 161).

[145] S. Abdollahi et al. "Fermi Large Area Telescope Fourth Source Catalog". In: *The Astrophysical Journal Supplement Series* 247.1 (Mar. 1, 2020), p. 33. ISSN: 0067-0049, 1538-4365. DOI: 10.3847/1538-4365/ab6bcb (cit. on p. 162).

[146] J. Ballet et al. *Fermi Large Area Telescope Fourth Source Catalog Data Release 4 (4FGL-DR4)*. Version 4. 2023. DOI: 10.48550/ARXIV.2307.12546. Prepublished (cit. on p. 162).

[147] J.-P. Lenain. "FLaapLUC : A Pipeline for the Generation of Prompt Alerts on Transient Fermi -LAT γ -Ray Sources". In: *Astronomy and Computing* 22 (Jan. 2018), pp. 9–15. ISSN: 22131337. DOI: 10.1016/j.ascom.2017.11.002 (cit. on p. 163).

[148] S. Abdollahi et al. "The Fermi-LAT Lightcurve Repository". In: *The Astrophysical Journal Supplement Series* 265.2 (Apr. 1, 2023), p. 31. ISSN: 0067-0049, 1538-4365. DOI: 10.3847/1538-4365/acbb6a (cit. on p. 163).

[149] *Fermi LAT Aperture Photometry*. URL: https://fermi.gsfc.nasa.gov/ssc/data/analysis/scitools/aperture_photometry.html (cit. on p. 164).

[150] J. L. Tonry et al. "ATLAS: A High-cadence All-sky Survey System". In: *Publications of the Astronomical Society of the Pacific* 130.988 (June 1, 2018), p. 064505. ISSN: 0004-6280, 1538-3873. DOI: 10.1088/1538-3873/aabadf (cit. on p. 164).

[151] K. W. Smith et al. "Design and Operation of the ATLAS Transient Science Server". In: *Publications of the Astronomical Society of the Pacific* 132.1014 (Aug. 1, 2020), p. 085002. ISSN: 0004-6280, 1538-3873. DOI: 10.1088/1538-3873/ab936e (cit. on p. 164).

[152] H. A. Krimm et al. "THE *SWIFT* /BAT HARD X-RAY TRANSIENT MONITOR". In: *The Astrophysical Journal Supplement Series* 209.1 (Oct. 25, 2013), p. 14. ISSN: 0067-0049, 1538-4365. DOI: 10.1088/0067-0049/209/1/14 (cit. on p. 164).

[153] A. Merloni et al. “The SRG/eROSITA All-Sky Survey - First X-ray Catalogues and Data Release of the Western Galactic Hemisphere”. In: *Astronomy & Astrophysics* 682 (Feb. 1, 2024), A34. ISSN: 0004-6361, 1432-0746. DOI: 10.1051/0004-6361/202347165 (cit. on p. 164).

[154] L. Y. Petrov and Y. Y. Kovalev. “The Radio Fundamental Catalog. I. Astrometry”. In: *The Astrophysical Journal Supplement Series* 276.2 (Jan. 2025), p. 38. ISSN: 0067-0049. DOI: 10.3847/1538-4365/ad8c36 (cit. on p. 165).

[155] Tara Murphy et al. “VAST: An ASKAP Survey for Variables and Slow Transients”. In: *Publications of the Astronomical Society of Australia* 30 (2013), e006. ISSN: 1323-3580, 1448-6083. DOI: 10.1017/pasa.2012.006 (cit. on p. 165).

[156] S. Aiello et al. “Observation of an Ultra-High-Energy Cosmic Neutrino with KM3NeT”. In: *Nature* 638.8050 (Feb. 2025), pp. 376–382. ISSN: 1476-4687. DOI: 10.1038/s41586-024-08543-1 (cit. on p. 167).

Remerciements

Many thanks to the members of the jury, Prof. Anna Franckowiak, Prof. Sergio Navas, Dr. Alexis Coleiro, Prof. Alec Habig and Dr. Cristinel Diaconu for finding the time to read my thesis manuscript and to attend my defense.

Damien, je te remercie de m'avoir toujours confié des projets ambitieux sans jamais douter de mes capacités à les réussir. Merci pour ta patience lors des difficultés que j'ai rencontrées, et merci pour tous les bons souvenirs créés lors des différentes missions qu'on a pu faire ensemble.

Vladimir, merci d'avoir toujours été là pour m'aider à résoudre les problèmes qui semblaient impossibles mais qui s'avéraient juste difficiles. Merci de m'avoir accueilli à Gênes, d'où je revenais toujours revigoré. Merci aussi de m'avoir permis de prendre un peu de temps sur mon travail de postdoc pour finir ce manuscrit.

Au groupe de thésards de Marseille (oui vous resterez pour toujours des thésards dans mon cœur), ces trois (et quelques) années n'auraient simplement pas été possibles sans vous. On était tous dans la même galère, à prendre l'eau pas toujours aux mêmes moments, mais en étant là les uns pour les autres pour se sauver de la noyade. Merci d'avoir écouté mes théories farfelues (toutes vraies), d'avoir fait du toboggan avec moi sur les toits de Marseille, d'avoir réfléchi sérieusement à s'il y a plus de portes ou de roues dans le monde, de m'avoir accueilli dans vos différents bureaux et beaucoup d'autres. Merci aussi à tous les amis que j'ai pu rencontrer à Marseille.

Thanks to all the people that welcomed me in Genova and made it fell like my second house: Andrey, Julia, Hichem (oui je te mets dans la team og de Gênes), Clara, Leo and a special shout out to Martina, you really took me under your wing (PAPERE) and made my long-term installation so easier.

À Élise, Guillaume, Joa et Joel, merci beaucoup de m'avoir accompagné toutes ces années. Votre confiance en moi indéfectible m'a aidé à arriver où j'en suis.

Many thanks to the colleagues and friends of KM3NeT: Fraf, Juan, Thijs, Ila, Ale, Martina, Manu, Angela, Rasa, Bruno, Zineb and I probably forget some. Our work is highly collaborative by nature and everything presented before relies at least partly of some things you've made. Thanks also to the great fun we've had together over the different meetings.

J’aimerais aussi remercier les amis à qui je devrais donner plus souvent des nouvelles mais à qui je pense souvent: Marc, Zach, Nico, Léa, Emma, Aurélien…

Pour finir, j’aimerais remercier ma famille, spécialement mes parents et grands-parents pour avoir toujours encouragé ma curiosité et pour m’avoir permis d’étudier un sujet que j’aime. Un merci particulier à Clotilde, pour avoir pris suffisamment d’intelligence dans le ventre de ma mère pour que je ne sois pas trop bizarre.

And many thanks to you reader, who (I’m sure) just read the full manuscript front to back.